STRUCTURAL BEHAVIOUR OF COMPOSITE RC MEMBERS STRENGTHENED WITH UHPC SUBJECTED TO STATIC AND DYNAMIC LOADING

by

Hor YIN

A dissertation

submitted to the Hokkaido University

in partial fulfilment of the requirement for the degree of

Doctor of Philosophy

in the field of Architectural and Structural Design

August 20, 2018

北海道大学
HOKKAIDO UNIVERSITY

ACKNOWLEDGEMENTS

I would like to express my deepest appreciation to my supervisor, Dr. **Kazutaka SHIRAI**, Associate Professor at Hokkaido University, for his friendly guidance, expert advice and invaluable suggestion throughout all stages of this research program. His unfailing optimism and constant encouragement always prompted me to overcome the difficulties in completing this work. I would also wish to express my gratitude to Dr. **Wee TEO**, Associate Professor at Heriot Watt University Malaysia, for his support and constructive comments over the years.

I would like to extend my thanks to Dr. **Taichiro OKAZAKI**, Dr. **Masanori IIBA**, and Dr. **Osamu SENBU**, Professors at Hokkaido University, for serving as my co-supervisors. Their thoughtful comments and suggestions have greatly contributed to the completion of this dissertation.

I am grateful to all the members of the Building Structure Control Laboratory of Hokkaido University for their invaluable support and friendly help. My sincere thank is to Dr. **Masaru KIKUCHI**, Professor at Hokkaido University, who has created excellent research environment in the laboratory. I also thank Dr. **Ken ISHII**, research fellow in the laboratory, who has shared his helpful ideas contributed to the solution of my work.

Finally, I would like to give special thanks to my family for their continuous support, encouragement and understanding throughout this work.

ABSTRACT

Ultra-high performance concrete (UHPC), a mix of reactive powder concrete with steel fibres, is an advancement in concrete technology. It can be defined by its excellent properties of UHPC including high strength, strain hardening, low permeability and energy absorption. Over the last two decades, UHPC is commonly used in protective structures, as non-penetrable coverings and in elements that must be durable against aggressive environments and severe loadings such as earthquakes, impacts or blasts. In addition, strengthening reinforced concrete (RC) members with UHPC can be an emerging technique for design, strengthening and protecting new or existing structures. Moreover, UHPC has shown high bond strength and good adherence to normal-strength concrete (NSC) substrates. Recently, UHPC has been used for strengthening parts of structures where the outstanding properties of UHPC could be fully exploited in full-scale site applications. Although UHPC has been considered as a potential tool in retrofitting or repairing existing RC structures, investigation on the behaviour of UHPC-concrete composite members is very limited. In addition, research on non-composite UHPC structural members subjected to dynamic loading is relatively scarce, and dynamic response of composite UHPC-concrete members has not yet been performed in the previous literature.

This dissertation aims to further understand the structural behaviour of composite UHPC-concrete members under static and dynamic loading. In order to accomplish this aim, five specific objectives are carried out: (1) to investigate the structural behaviour of composite UHPC-concrete slabs under static loading through the experimental study; (2) to develop the finite element (FE) modelling for the flexural behaviour of UHPC members under static loading; (3) to predict the behaviour of UHPC-concrete slabs using FE modelling under static loading; (4) to figure out the numerical response of composite UHPC-concrete members subjected to dynamic loading; and (5) to evaluate the prediction method for the capacity of composite UHPC-concrete members. In this dissertation, for investigation of structural behaviour, experimental program was carried out. The experimental results were discussed. An FE modelling was developed and validated with the test results. For dynamic behaviour in this study, blast simulations were conducted to investigate the influence of UHPC strengthening layer on the blast resistance capacity of composite UHPC-concrete members. Calculation method of the structural capacity of composite UHPC-concrete members was proposed and verified with the experimental data.

TABLE OF CONTENTS

Chapter V (Paper IV): Behaviour of UHPC-concrete composite members subjected to static and dynamic loading: Numerical study

LIST OF FIGURES

Chapter II (Paper I): Experimental investigation on the behaviour of reinforced concrete slabs strengthened with ultra-high performance concrete

Chapter III (Paper II): Finite element modelling to predict the flexural behaviour of ultra-high performance concrete members

Chapter IV (Paper III): Numerical model for predicting the structural response of composite UHPC–concrete members considering the bond strength at the interface

Chapter V (Paper IV): Behaviour of UHPC-concrete composite members subjected to static and dynamic loading: Numerical study

Chapter VI (Paper V): Prediction of shear capacity of UHPC-concrete composite structural members based on existing codes

Chapter VII (Paper VI): Prediction of flexural strength of UHPC-concrete composite members based on existing design models

LIST OF TABLES

Chapter II (Paper I): Experimental investigation on the behaviour of reinforced concrete slabs strengthened with ultra-high performance concrete

Chapter III (Paper II): Finite element modelling to predict the flexural behaviour of ultra-high performance concrete members

Chapter IV (Paper III): Numerical model for predicting the structural response of composite UHPC–concrete members considering the bond strength at the interface

Chapter V (Paper IV): Behaviour of UHPC-concrete composite members subjected to static and dynamic loading: Numerical study

Chapter VI (Paper V): Prediction of shear capacity of UHPC-concrete composite structural members based on existing codes

Chapter VII (Paper VI): Prediction of flexural strength of UHPC-concrete composite members based on existing design models

ABBREVIATIONS

RE	UHPC rehabilitating
OV	UHPC overlay
RC	Reinforced concrete
NSC	Normal strength concrete
FRC	Fibre reinforced concrete
UHPC	Ultra-high-performance concrete
UHPC-concrete	RC members strengthened with UHPC
FE	Finite element
FEM	Finite element modelling
EOS	Equation of state
TNT	Trinitrotoluene (TNT is the standard measure of explosives.)
ANFO	Ammonium nitrate/fuel oil (0.82 TNT equivalence of ANFO)

Chapter I
Introduction

Introduction

1. Research background

Ultra-high-performance concrete (UHPC) is a relatively new type of cementitious concrete materials. UHPC is a mix of reactive powder concrete (RPC) with steel fibres [1]. Volume fractions of steel fibres of 1% to 5% are often used in the UHPC. UHPC can be defined by its high strength (> 150 MPa in compression and > 8 MPa in tension), high stiffness (Young's modulus of 45000−55000 MPa), extremely low permeability, and energy absorption [2-7]. Due to its excellent properties, UHPC is often used in protective structures under aggressive environments and severe loadings such as earthquakes, impacts or blasts.

In addition, the behaviour of UHPC structural members has been experimentally investigated through static, impact, and blast loading tests. Graybeal [8] tested full-scale UHPC bridge girders with different overall spans and shear spans. Voo et al. [9] conducted many structural UHPC tests. Yang et al. [10] and Yoo et al. [11] reported how the longitudinal steel ratio affects UHPC beams. Tests on reinforced UHPC members under static loading have shown that longitudinal rebar and steel fibres can effectively control the crack width and enhance ductility. Furthermore, studies on the drop-weight impact testing [12-14] and blast testing [15-18] of UHPC members have proven that the use of UHPC for structural elements is efficient and effective against dynamic loading because of the enhancement of the cracking response and strain hardening of UHPC relative to normal strength concrete (NSC).

Importantly, concrete is one of the most commonly used materials in buildings. During service life of reinforced concrete (RC) structures, insufficient strength problems due to, for example, the deterioration of concrete or excessive deformation of the structural members could occur. Therefore, repair or retrofitting of the RC structural members is one of primary needs. Recently, with its high performance including good adherence to NSC substrates, UHPC has been considered as a potential tool in the challenge of retrofitting or repairing existing RC members.

Concepts for using UHPC to strengthen parts of structures where the outstanding properties of UHPC could be fully exploited have been proposed by Brühwiler and Denarie [5]. To validate the concepts, four unique full-scale site applications were discussed: (1) rehabilitation and widening of a road bridge; (2) UHPC protection layer on a crash barrier wall; (3) rehabilitation of a bridge pier using prefabricated UHPC pannels; and (4) strengthening of an industrial floor. It showed that UHPC development is mature for use in either cast in-situ or precast applications using conventional standard concreting equipment.

To investigate the performance of the effect of UHPC strengthening, some experimental studies on the combination of UHPC and RC under static loading have been carried out [19-22]. Oesterlee [19], Habel et al. [20] and Noshiravani and Brühwiler [21] evaluated the behaviour of composite RC members strengthened with UHPC. Alaee and Karihaloo [22] used prefabricated CARDIFRC, a type of UHPC, to strengthen RC beams. Strips of CARDIFRC were attached to RC members using epoxy adhesive. The results showed that UHPC layer of composite UHPC-concrete members enhances the structural performance in terms of ultimate loads, stiffness and cracking behaviour.

Moreover, the interfacial bonding behaviour (between UHPC and NSC) of composite UHPC-concrete members has been reported through experimental investigations [20,21,23]. The premature failure of composite members can be caused by local failures such as the de-bonding

and/or fracture of UHPC in the interface zone [21]. According to Habel et al. [20], the bond between UHPC and NSC is stronger than the tensile strength of NSC at the level of the longitudinal rebar of the RC members. Noshiravani and Brühwiler [21] reported that the structural resistance of composite UHPC-concrete members depends on the bonding conditions in the interaction between the three materials in tension (longitudinal rebar, UHPC, and NSC). Al-Osta et al. [24] observed that no de-bonding but horizontally fine cracks appeared near the interface. Denarié et al. [23] showed that the bonding mechanism between UHPC and NSC is more efficient in terms of energy dissipation than the mechanism in the cracking of RC members.

Based on the above-mentioned literature, use of UHPC has demonstrated a great potential in strengthening RC structures. UHPC enhances the structural performance of composite UHPC-concrete members. However, studies in this area are very limited and remain challenges. Therefore, to further understanding the behaviour of composite RC members strengthened with UHPC, the present study was conducted. This study comprises experimental program, and numerical model of the composite members, and the structural capacity was computed using the applications of modification of existing design models.

2. Critical review

Although several studies were previously carried out [19-24], the behaviour of composite members influenced by a UHPC layer strengthening has not yet been fully clarified. In particular, the number of studies in the literature on composite members that include overlays onto which an additional UHPC overlay is applied to existing RC members is very limited. More importantly, there are several published studies of tests on UHPC overlay modes, but reports on rehabilitation schemes, in which UHPC is used to repair deteriorated concrete, are very few. Therefore, more experimental works in this research area are definitely needed.

In addition, studies on the behaviour of UHPC structural members using the finite element (FE) method, which is an effective tool for the effective enhancement of the structural performance, have been very limited in the past. According to previous studies [25-27], investigations on the application of FE analysis to UHPC behaviour have been very limited. Furthermore, the effect of the steel fibre length has not been yet clearly considered in existing FE models.

The experimental investigations in the previous studies [6,20,21,23,28] demonstrate that the strength of the bond between NSC and UHPC is a crucial factor in the performance of the composite. However, in the past, the FE models for predicting the behaviour of composite UHPC-concrete members did not involve the interfacial bond characteristic between UHPC and NSC and validate with test data [24,29-31].

Furthermore, dynamic behaviour of structural members particularly under explosions is usually more complex than static behaviour. Although accidental or intentional explosions rarely occur, blast damages of RC structures would become disastrous consequence. Blast loads with short duration can produce extremely large amount of energy to the structures and excite global or local responses. The excitement of the blast effect can cause immediate failure of structural members or executes the risk of structural progressive collapse. According to the past experimental studies [15,17,18,27], it demonstrated that UHPC structural members under blast loading significantly enhances the blast resistance capacity than the conventional RC members made of NSC. The use of UHPC layer onto RC members could be essential to mitigate the blast effect, because of the ductile behaviour of UHPC that could absorb large amount of blast energy.

However, the dynamic behaviour of composite RC members strengthened with UHPC under blast loading has not yet been investigated.

In addition to the experimental and numerical study, analytical methods of the structural capacity of composite UHPC-concrete members are certainly needed. According to Alaee and Karihaloo [22] and Habel et al. [32], the flexural strength of UHPC-concrete members was computed using the moment-curvature relationships. Noshiravani and Brühwiler [33] carried out analytical models for flexural-shear resistance of composite beams. An elastic-plastic fictitious composite hinge model was used for the cracking in RC members with consideration of interaction between the two elements of composite members. However, these studies required several steps in the analysis. Besides, design provisions have not yet been available to predict the structural capacity of UHPC-concrete sections. Use with modification of existing design models of RC such as ACI 318 [34] and/or fibre reinforced concrete (FRC) such as ACI 544 [35] structures may be useful because they are simple and easy to use.

3. Objectives

The main aim of the present study is to accomplish the overall understanding of the behaviour of composite RC members strengthened with UHPC. To achieve this aim, five specific objectives are made:

(1) To investigate the structural behaviour of composite UHPC-concrete slabs under static loading through the experimental study.

(2) To develop an FE modelling for the flexural behaviour of UHPC members under static loading.

(3) To predict the behaviour of composite UHPC-concrete slabs using FE modelling under static loading.

(4) To figure out the numerical response of composite UHPC-concrete members subjected to dynamic loading.

(5) To evaluate the prediction of composite UHPC-concrete members using existing design models.

4. Methodology

In this study, the research methodology consisted of:

- Conducting experiments on composite UHPC-concrete members.
- Developing an FE model for flexural behaviour of UHPC members.
- Proposing a new modelling technique for FE model of composite UHPC-concrete members.
- Investigating the numerical response of composite UHPC-concrete members subjected to dynamic loading.
- Adopting the existing design equations to predict the flexural and shear strength of UHPC-concrete members.

5. Research limitations

In this dissertation, the experimental investigation on the behaviour of composite UHPC-concrete members was investigated and limited to ten static slab specimens. Of ten specimens, seven slabs were composite UHPC-concrete members. The others were non-composite RC or UHPC members conducted for reference. The results of load-midspan deflection curves and longitudinal steel strains at the midspan were reported and discussed.

In addition, the FE model developed for flexural behaviour of non-composite UHPC members was validated with 21 experimental data, conducted in the present study and by previous researchers. Furthermore, a new modelling technique using equivalent beam elements to consider bond strength at NSC-UHPC interface was proposed and employed in the FE model of composite UHPC-concrete specimens. The numerical results were compared to the results of the seven composite UHPC-concrete slabs tested in the present study.

In the present study, no experiments for the dynamic behaviour were conducted. The dynamic behaviour was investigated through the numerical simulation of the specimens under blast loading. This blast simulation was performed to assess the effectiveness of UHPC strengthening layer of RC members on the blast resistance capacity of composite UHPC-concrete members.

Adopted methods to predict the structural capacity of composite UHPC-concrete members were based on the application of existing design models of non-composite members. For the sake of simplicity, some assumptions were made, although it may not fully capture the actual structural behaviour of the tested specimens. It could be suggested that more realistic and rational models are certainly needed to be further developed in the future.

6. Overview

In addition to the introductory chapter clarifying research background, critical review, and research objectives, the main body of this dissertation consists of six papers. The list of the papers includes:

- Paper I: Experimental investigation on the behaviour of reinforced concrete slabs strengthened with ultra-high performance concrete
- Paper II: Finite element modelling to predict the flexural behaviour of ultra-high performance concrete members
- Paper III: Numerical model for predicting the structural response of composite UHPC–concrete members considering the bond strength at the interface
- Paper IV: Behaviour of UHPC-concrete composite members subjected to static and dynamic loading: Numerical study
- Paper V: Prediction of shear capacity of UHPC-concrete composite structural members based on existing codes
- Paper VI: Prediction of flexural strength of UHPC-concrete composite members based on existing design models

This dissertation is structured into eight chapters, which can be summarised as follows.

Chapter I is the introductory chapter. This chapter clarifies the research background, critical review, and research objectives.

Chapter II (Paper I) presents the experimental program, and results and discussion. In this chapter, UHPC material was developed. After serval trials, the best performance of UHPC was

chosen and used for casting onto the tension zone of conventional RC members. A total of nine specimens of non-composite and composite RC slabs strengthened with various UHPC strengthening configurations were tested. Of nine specimens, seven slabs were composite UHPC-concrete members. The others were non-composite RC or UHPC members conducted for reference. All specimens were tested under static loading. To evaluate the behavioural response, the specimens were grouped into two series. The first, a rehabilitation series, tested UHPC as patch material for repairing deteriorated concrete structures. The second, a UHPC overlay series, was used to retrofit soffits of RC members. Results showed that UHPC layer, in rehabilitation series, prevented against the diagonal shear cracks shown in conventional RC slabs. The composite UHPC-concrete specimens revealed an excellent energy absorption with extensive deflection hardening and ductility during the post cracking range. In UHPC overlay series, each specimens showed diagonal shear cracks and debonding of UHPC. The ultimate capacity increased as the UHPC overlay thickness increased.

Chapter III (Paper II) addresses an FE model to predict the behaviour of UHPC members under static flexural loading. A concrete damage model based on plasticity constitutive model for concrete and an implicit solver in commercial FE software LS-DYNA were adopted in the numerical simulation. Experimental data for 21 UHPC flexural specimens tested in the present study and in previous works were used to validate the proposed FE model and modelling technique. Results revealed that the developed FE model was able to accurately predict the experimentally obtained ultimate strength, stiffness, and hardening and softening behaviours of the specimens.

Chapter IV (Paper III) focuses on an improved FE model developed for the prediction of the structural behaviour of RC members strengthened with UHPC. The model was validated using experimental data. Accurately representing the interfacial bond characteristics of composite UHPC-concrete members was the main challenge in developing the modelling technique. A novel technique using equivalent beam elements at the interface between UHPC and NSC substrate was proposed for this purpose. The material properties of the equivalent beam elements were defined to represent the equivalent bond characteristics of NSC. The structural response of composite UHPC-concrete members was effectively predicted with good accuracy using the developed FE model.

Chapter V (Paper IV) investigates the dynamic behaviour of RC strengthened with UHPC obtained using the developed FE modelling. For dynamic response, blast simulation was performed using explicit method. The blast model was validated with test data of non-composite RC or UHPC members available in the literature. For composite UHPC-concrete member, the blast simulations were carried out to investigate the influence of UHPC strengthening layer on the blast resistance capacity of the composite members. The effectiveness of UHPC layer of composite UHPC-concrete members was demonstrated through comparing the results with reference non-composite RC and UHPC members under same blast loading.

Chapters VI (Paper V) and VII (Paper VI) introduce methods based on application of existing design codes for predicting the shear and flexural capacity of composite UHPC-concrete members. Six different methods were individually investigated for shear strength. Three of them were adopted by converting the volume fraction of steel fibres used in UHPC as an equivalent longitudinal steel ratio. Other three methods computed the shear strength as a sum of two components of shear contributions provided by RC member and by UHPC layer; and each of the components was independently calculated. For flexural strength, a simple method was adopted based on the existing design models. The rectangular stress block diagrams for

compression and tension zone of the conventional concrete and UHPC layer in the composite section were assumed, respectively. The proposed methods were found to be able to fairly predict the structural capacity of composite UHPC-concrete members compared to the experimental results.

Chapter VIII is the conclusion and recommendation chapter. Through the results and discussion in the present study, it could be concluded that the understanding of the behaviour of composite RC members strengthened with UHPC was expanded. The influence of UHPC strengthening layer and the bond strength between UHPC and NSC were figured out. Importantly, it was found that the behaviour of composite UHPC-concrete could be effectively and efficiently predicted using the developed FE model. In addition to the conclusions, this chapter also lists some recommendations for future work.

7. Information details of the papers

Paper I:

The content of this Paper I (Chapter II) has been published in the following article.

Hor Yin, Wee Teo, Kazutaka Shirai, "Experimental investigation on the behaviour of reinforced concrete slabs strengthened with ultra-high performance concrete," Construction and Building Materials, vol. 155, pp. 463–474, 2017.

Paper II:

The content of this Paper II (Chapter III) has been submitted for consideration for publication as follows.

Hor Yin, Kazutaka Shirai, Wee Teo, "Finite element modelling to predict the flexural behaviour of ultra-high performance concrete members," Engineering Structures, (submitted date: 15 March 2018, under review).

Paper III:

The content of this Paper III (Chapter IV) has been submitted for consideration for publication as follows.

Hor Yin, Kazutaka Shirai, Wee Teo, "Numerical model for predicting the structural response of composite UHPC–concrete members considering the bond strength at the interface," Composite Structures, (submitted date: 25 April 2018, submitted).

Paper V:

The content of this Paper V (Chapter VI) has been submitted for consideration for publication as follows.

Hor Yin, Kazutaka Shirai, Wee Teo, "Prediction of shear capacity of UHPC–concrete composite structural members based on existing codes," Journal of Civil Engineering and Management, (submitted date: 25 May 2018, under review).

Papers IV (Chapter V) and VI (Chapter VII) in this dissertation have not yet been published or submitted to elsewhere. The preparation of these two papers for consideration for publication is in progress.

8. References

[1] P. Richard, M. Cheyrezy, Composition of reactive powder concretes, Cem. Concr. Res. 25 (7) (1995) 1501-1511.

[2] K. Wille, A.E. Naaman, G.J. Parra-Montesinos, Ultra-high performance concrete with compressive strength exceeding 150 MPa (22 ksi): a simpler way, ACI Mater. J. 108 (1) (2011) 46-54.

[3] T.M. Ahlborn, D.L. Misson, E.J. Peuse, C.G. Gilbertson, Durability and strength characterization of ultra-high performance concrete under variable curing regimes, in: Proc. 2nd Int. Symp. Ultra-high Performance Concrete, Germany, 05-07 March 2008.

[4] M. Alkaysi, S. El-Tawil, Z. Liu, W. Hansen, Effects of silica powder and cement type on durability of ultra high performance concrete (UHPC), Cem. Concr. Compos. 66 (2016) 47–56.

[5] E. Brühwiler, E. Denarie, Rehabilitation of concrete structures using ultra-high performance fibre reinforced concrete, in: Proc. 2nd Int. Symp. Ultra-high Performance Concrete, Kassel, Germany, 05-07 March 2008.

[6] B.A. Tayeh, B.A Bakar, M.M. Johari, Y.L. Voo, Mechanical and permeability properties of the interface between normal concrete substrate and ultra high performance fiber concrete overlay, Constr. Build. Mater. 36 (2012) 538-548.

[7] B.A. Graybeal, F. Baby, Development of direct tension test method for ultra-high-performance fiber-reinforced concrete, ACI Mater. J. 110 (2) (2013) 177-186.

[8] B.A. Graybeal, Characterization of the behavior of ultra-high performance concrete, PhD thesis, University of Maryland, USA, 2005.

[9] Y.L Voo, W.K. Poon, S.J. Foster, Shear strength of steel fiber-reinforced ultrahigh-performance concrete beams without stirrups, J. Struct. Eng. 136 (11) (2010) 1393-1400.

[10] I.H. Yang, C. Joh, B.S. Kim, Structural behavior of ultra high performance concrete beams subjected to bending, Eng. Struct. 32 (11) (2010) 3478-3487.

[11] D.Y. Yoo, N. Banthia, S.W. Kim, Y.S. Yoon, Response of ultra-high-performance fiber-reinforced concrete beams with continuous steel reinforcement subjected to low-velocity impact loading, Compos. Struct. 126 (2015) 233-245.

[12] K. Fujikake, T. Senga, N. Ueda, T. Ohno, M. Katagiri, Study on impact response of reactive powder concrete beam and its analytical model, J. Adv. Concr. Technol.;4 (1) (2006) 99-108.

[13] K. Habel, P. Gauvreau, Response of ultra-high performance fiber reinforced concrete (UHPFRC) to impact and static loading, Cem. Concr. Compos. 30 (10) (2008) 938-46.

[14] D.Y. Yoo, N. Banthia, S.W. Kim, Y.S. Yoon, Response of ultra-high-performance fiber-reinforced concrete beams with continuous steel reinforcement subjected to low-velocity impact loading, Compos. Struct. 126 (2015) 233-45.

[15] T. Ngo, P. Mendis, T. Krauthammer, Behavior of ultrahigh-strength prestressed concrete panels subjected to blast loading, J. Struct. Eng. 133 (11) (2007) 1582-90.

[16] C. Wu, D. Oehlers, M. Rebentrost, J. Leach, A. Whittaker, Blast testing of ultra-high performance fibre and FRP-retrofitted concrete slabs, Eng Struct 31 (9) (2009) 2060-69.

[17] N.H. Yi, J.H.J. Kim, T.S. Han, Y.G. Cho, J.H. Lee, Blast-resistant characteristics of ultra-high strength concrete and reactive powder concrete, Constr. Build. Mater. 28(1) (2012) 694-707.

[18] J. Li, C. Wu, H. Hao, An experimental and numerical study of reinforced ultra-high performance concrete slabs under blast loads, Mater. Des. 82 (2015) 64-76.

[19] C. Oesterlee, Structural response of reinforced UHPFRC and RC composite members, PhD thesis, École Polyechnique Fédérale de Lausanne, Switzerland, 2010.

[20] K. Habel, E. Denarié, E. Brühwiler, Experimental investigation of composite ultra-high-performance fiber-reinforced concrete and conventional concrete members, ACI Struct. J. 104 (1) (2007) 93-101.
[21] T. Noshiravani, E. Brühwiler, Experimental investigation on reinforced ultra-high-performance fiber-reinforced concrete composite beams subjected to combined bending and shear, ACI Struct. J. 110 (2) (2013) 251-261.
[22] F.J. Alaee, B.L. Karihaloo, Retrofitting of reinforced concrete beams with CARDIFRC, J. Compos. Constr. 7 (3) (2003) 174-186.
[23] E. Denarié, K. Habel, E. Briihwiler, Structural behavior of hybrid elements with Advanced Cementitious Materials (HPFRCC), In: 4th International RILEM Workshop on High Performance Fiber Reinforced Cement Composites (HPFRCC 4), 2003. p. 301.
[24] M. Al-Osta, M. Isa, M. Baluch, M. Rahman, Flexural behavior of reinforced concrete beams strengthened with ultra-high performance fiber reinforced concrete, Constr. Build. Mater. 134 (2017) 279-96.
[25] M. Singh, A. Sheikh, M.M. Ali, P. Visintin, M. Griffith, Experimental and numerical study of the flexural behaviour of ultra-high performance fibre reinforced concrete beams, Constr. Build. Mater. 138 (2017) 12-25.
[26] J. Magallanes, Y. Wu, J. Crawford, K. Morrill, Feasibility studies of a plasticity-based constitutive model for ultra-high performance fiber-reinforced concrete, In: Int Symp: Military Aspects of Blast and Shock. Jerusalem, Israel; 2010.
[27] L. Mao, S. Barnett, D. Begg, G. Schleyer, G. Wight, Numerical simulation of ultra high performance fibre reinforced concrete panel subjected to blast loading, Int. J. Impact. Eng. 64 (2014) 91-100.
[28] D.K. Harris, M.A.C. Muñoz, A. Gheitasi, T.M. Ahlborn, S.V. Rush, The challenges related to interface bond characterization of ultra-high-performance concrete with implications for bridge rehabilitation practices, Adv. Civil. Eng. Mater. 4 (2) (2014) 75-101.
[29] M. Safdar, T. Matsumoto, K. Kakuma, Flexural behavior of reinforced concrete beams repaired with UHPFRC, Compos. Struct. 157 (2016) 448-60.
[30] H. Sadouki, E. Denarié, E. Brühwiler, Validation of a FEA model of structural response of RC-cantilever beams strengthened with a (R-) UHPFRC layer, Constr. Build. Mater. 140 (2017) 100-8.
[31] A. Lampropoulos, S.A. Paschalis, O. Tsioulou, S.E. Dritsos, Strengthening of reinforced concrete beams using ultra high performance fibre reinforced concrete (UHPFRC), Eng. Struct. 106 (2016) 370-84.
[32] K. Habel, E. Denarié, E. Brühwiler, Structural response of elements combining ultrahigh-performance fiber-reinforced concretes and reinforced concrete, J. Struct. Eng. 132 (2006) 1793-800.
[33] T. Noshiravani, E. Brühwiler, Analytical model for predicting response and flexure-shear resistance of composite beams combining reinforced ultrahigh performance fiber-reinforced concrete and reinforced concrete, J. Struct. Eng. 140 (2013) 04014012.
[34] ACI Committee 318. Building code requirements for structural concrete (ACI 318M-08) and commentary. American Concrete Institute. 2008.
[35] ACI Committee 544. Design considerations for steel fiber reinforced concrete. ACI. Struct. J. 85 (1988).

Chapter II

Paper I

Experimental investigation on the behaviour of reinforced concrete slabs strengthened with ultra-high performance concrete

The content of this Chapter II has been published as follows.

Hor Yin, Wee Teo, Kazutaka Shirai, "Experimental investigation on the behaviour of reinforced concrete slabs strengthened with ultra-high performance concrete," Construction and Building Materials, vol. 155, pp. 463–474, 2017.

Experimental investigation on the behaviour of reinforced concrete slabs strengthened with ultra-high performance concrete

Abstract

Nine rectangular specimens were tested to investigate the behaviour of composite reinforced concrete (RC) slabs strengthened with ultra-high performance concrete (UHPC). The specimens were two series with various UHPC strengthening configurations. The first, a rehabilitation series, tested UHPC as patch material for repairing deteriorated concrete structures. The second, a UHPC overlay series, was used to retrofit soffits of RC members. The results showed that using the rehabilitation series, the UHPC reduced diagonal cracking and developed more flexural cracks as compared to RC slabs with no UHPC strengthening. The UHPC exhibited excellent energy absorption with extensive deflection hardening and ductility during the post cracking range. In the UHPC overlay series, each slab showed diagonal shear cracks and debonding modes. The UHPC overlay delayed the development of shear cracking. As the overlay thickness increased, the ultimate load increased; but the tendency for the UHPC to undergo fracture failure also increased.

Keywords: composite UHPC-concrete slabs; UHPC overlay; rehabilitation; structural behaviour; shear capacity; ductility.

1. Introduction

Ultra-high performance concrete (UHPC) is an advancement in concrete technology. It is a mix of reactive powder concrete (RPC) with steel fibres, which was firstly developed by Richard and Cheyrezy [1]. Typically, UHPC offers high compressive strength of from 150 to 200 MPa without heat curing [2]. In addition, UHPC or ultra-high performance fibre reinforced concrete (UHPFRC) exhibits excellent mechanical properties such as durability [3-5], low permeability [5,6] and energy absorption [7-11]. Therefore, UHPC is often used in protective structures, as non-penetrable coverings and in elements that must be durable against aggressive environments and severe loadings such as earthquakes, impacts or blasts.

Due to its superior properties, many researchers have expounded on the structural responses of UHPC members. Graybeal [12] conducted full-scale tests of UHPC bridge girders with different overall spans and shear spans. Voo et al. [13] conducted many structural UHPC tests. Their results showed that UHPC significantly improves ductile behaviour. Furthermore, Yang et al. [14] and Yoo et al. [15] reported how the longitudinal steel ratio affects UHPC beams. Their studies demonstrated that the rebar and steel fibres effectively control crack width and ductility.

Recently, UHPC has been considered as a potential tool in the challenge of retrofitting or repairing existing reinforced concrete (RC) members. Concepts for using UHPC to strengthen parts of structures where the outstanding properties of UHPC could be fully exploited have been proposed by Brühwiler and Denarie [5]. To validate the concepts, four unique full-scale site applications were discussed. Their findings were very encouraging. The use of UHPC has shown great potential and UHPC development is mature for use in either cast in-situ or precast applications using conventional standard concreting equipment.

To observe the performance of UHPC strengthening, some experimental studies that combine UHPC and RC have been carried out [16-21]. Oesterlee [16], Habel et al. [17], and Noshiravani

and Brühwiler [18] evaluated the behaviour of RC members strengthened with UHPC overlays when subjected to bending. The results showed that UHPC overlays enhance the structural performance in terms of ultimate loads, stiffness and cracking behaviour. Zohrevand et al. [19] reported the use of UHPC within critical punching shear area of the RC slabs. It was shown that the partial use of UHPC improves the shear capacity and significantly influences cracking patterns in punching shear area compared to the reference RC slab. Another investigation was carried out by Alaee and Karihaloo [20] using CARDIFRC, a type of UHPC, to strengthen RC beams. Strips of CARDIFRC were attached to RC members using epoxy adhesive. The maximum load carried by the strengthened beams was equal to or higher than that of the RC beams, but the load-deflection curves showed softening behaviour after reaching the maximum force. In addition, Kim et al. [21] tested RC beams repaired with the conventional ductile fibre reinforced cementitious composite (DFRCC). Two thicknesses of DFRCC for the concrete cover thickness and twice the cover thickness were adopted in their study. Results mainly showed that DFRCC delays the bond interface failure between DRFCC and the original RC beams. However, DFRCC has lower mechanical properties, especially load bearing capacity compared to UHPC.

Owing to the novel properties of UHPC, however, the behaviour of composite members influenced by a UHPC layer strengthening has not yet been fully clarified. In particular, the number of studies in the literature on composite members that include overlays onto which an additional UHPC overlay is applied to existing RC members is very limited. More importantly, there are published studies of tests on UHPC overlay modes, but to the best of the authors' knowledge, as yet there are no publish reports on rehabilitation schemes in which UHPC is used to repair deteriorated concrete. Therefore, more experimental work in this area is definitely needed.

The purpose of this study is to further understand the structural behaviour of composite UHPC-concrete slabs. To accomplish the objective, tests on various UHPC strengthening configurations applied in the tensile zone of RC slabs were conducted. New experimental features of rehabilitation strengthening modes and UHPC overlay modes are described. The experimental program, including details of the test parameters and equipment setup is described in section 2. In section 3, the mechanical properties of UHPC materials are provided. The test results and discussion are presented in section 4, focusing on the mechanical behaviour of load-deflection relationships, longitudinal steel strain, cracking development and failure modes. Section 5 summarises the research conclusions with recommendation of future research.

2. Experimental program

2.1. Description of test specimens and parameters

This experimental study used nine rectangular concrete slabs with various composite UHPC-concrete configurations. Two test series with distinct composite configurations were adopted. The first series used UHPC as rehabilitate material. It is labelled RE. The second, where UHPC is used as a retrofit material in overlays, is labelled OV. The RE series consisted of five slabs, while the OV series used four. Each slab was 1600 mm long with a clear span of 1200 mm. They were tested under a three-point load condition, as shown in Fig. 1. Full details of the various composite UHPC-concrete configurations adopted for the two series are illustrated in Fig. 2.

The RE series consisted of five slabs with 300 mm wide by 100 mm high cross sections. This series was designed to investigate the use of UHPC applied in the tension zone as patch material

for repair and rehabilitation of structural members. Often in practice, deteriorated concrete will be removed and high performance repair materials applied to the concrete substrate. In this series, different UHPC thicknesses were considered in order to reflect different extents of deterioration and repair. The slab specimens were designated according to the thickness of the UHPC applied to the concrete substrate. For example, slab specimen RE-32 featured a slab with deteriorated concrete removed and rehabilitated with a 32 mm thick layer of UHPC. All slabs in the RE series had five T12 mm diameter high tensile steel bars (5T12) at the top and bottom. No transverse shear reinforcement was provided, but to avoid anchorage failure at the end supports, three R6 mm diameter mild steel links were installed. Details of the reinforcement are shown in Figs. 1 and 2.

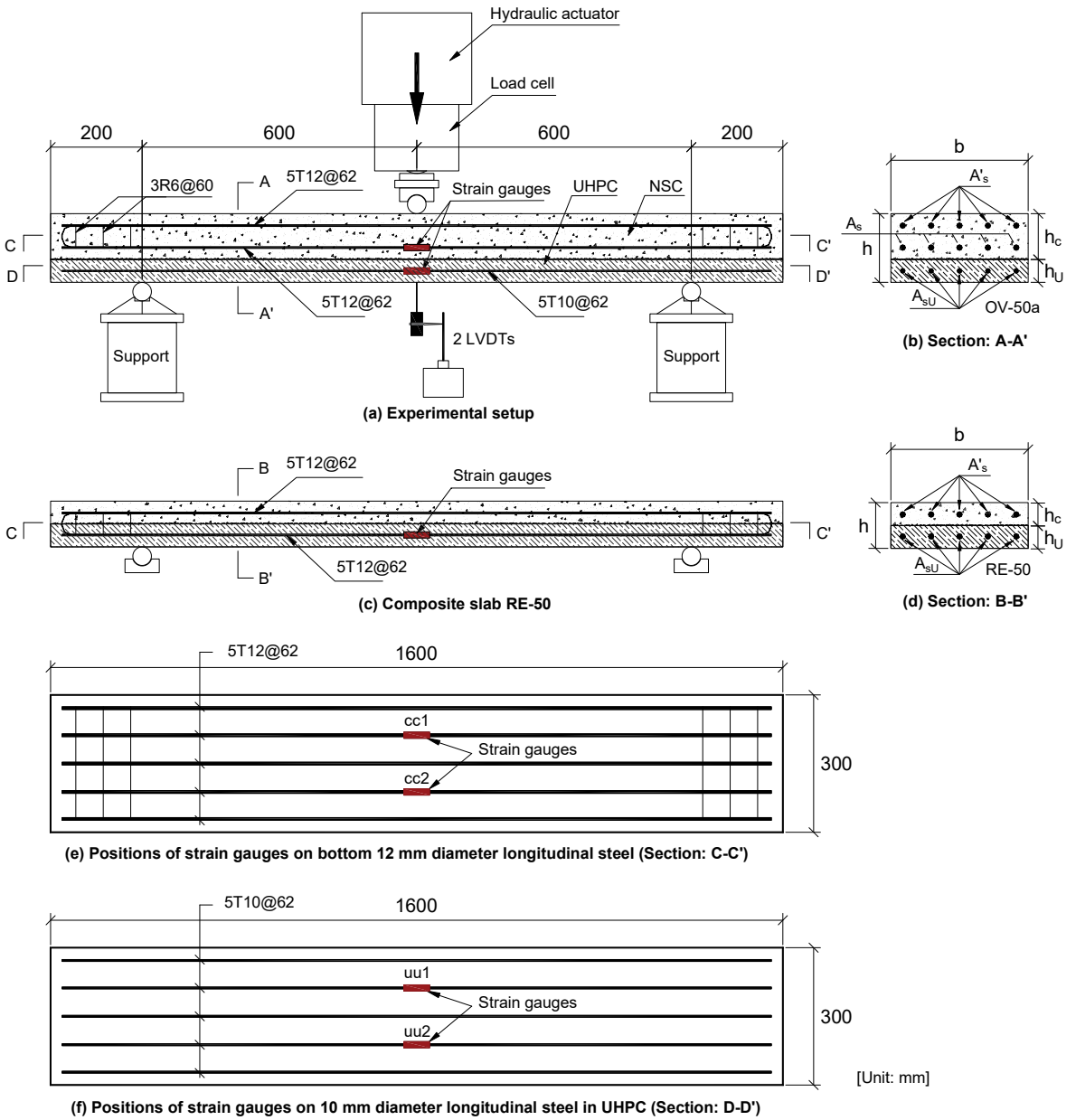

Figure 1: Experimental setup and test specimen instrumentation.

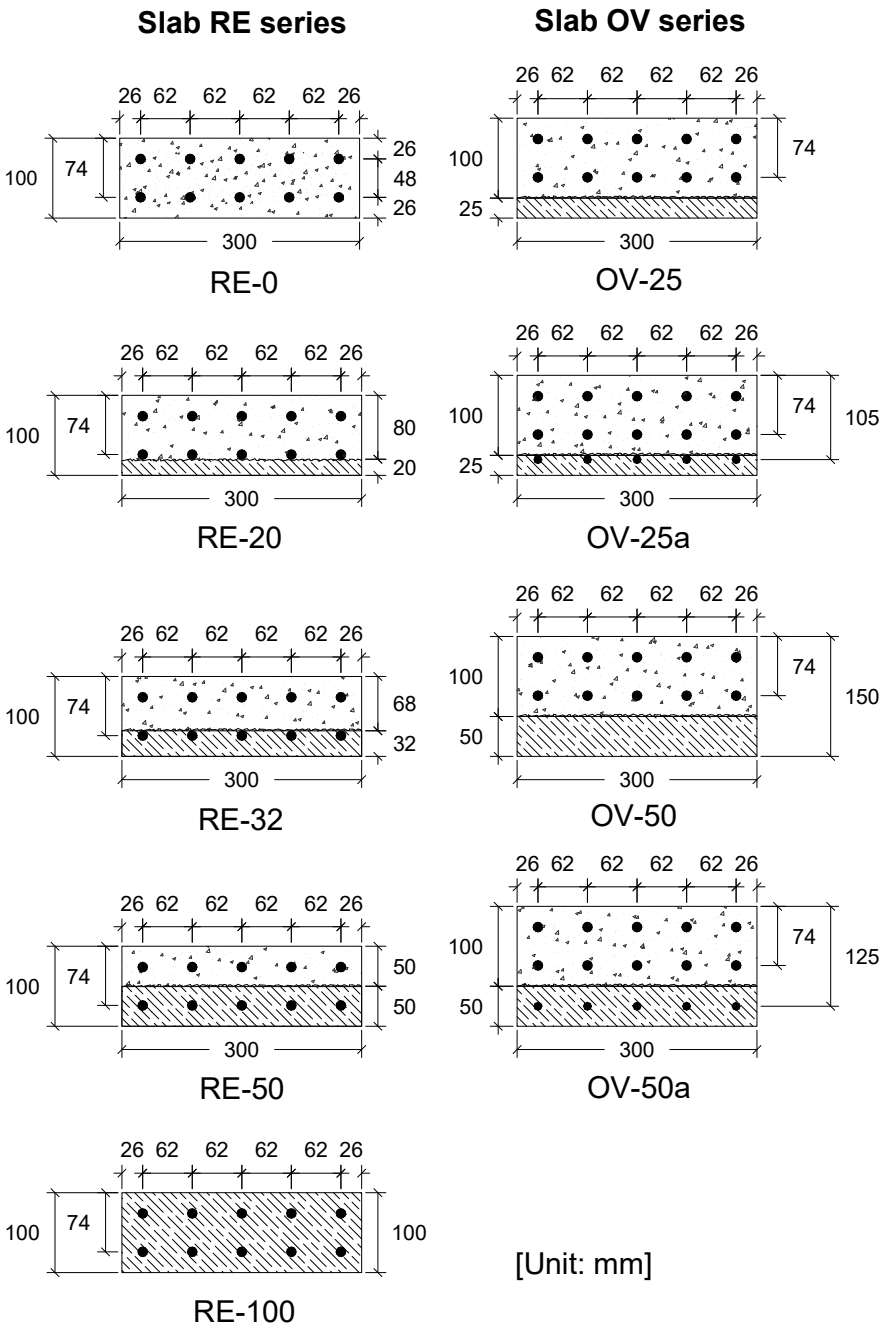

Figure 2: Details of RE and OV series composite UHPC-concrete configurations.

The OV series consisted of four slabs with similar cross-sectional dimensions as the RE series, but with different additional UHPC overlays strengthening the tension zone. Two thicknesses of UHPC overlay were considered, 25 mm and 50 mm. Two slab specimens of each overlay thickness were prepared. One was not reinforced, while the other had five T10 mm diameter high tensile steel bars as longitudinal reinforcement (5T10). The slab specimens were designated according to the thickness of UHPC overlay and longitudinal steel reinforcement. Slab specimens with a UHPC overlay and longitudinal reinforcement are denoted by "a". For example, slab specimen OV-50a had a 50 mm thick UHPC overlay and was reinforced with 5T10 longitudinal reinforcement. Geometric and reinforcement details of the experimental specimens are summarised in Table 1.

Table 1: Details of slab specimens.

Specimen	b (mm)	h (mm)	UHPC thickness, h_U (mm)	Longitudinal reinforcement						
				Top steel	Bottom steel		T12		T10	
				A'_s	A_s	A_{sU}	f_y (MPa)	f_{max} (MPa)	f_y (MPa)	f_{max} (MPa)
RE-0	300	100	-	5T12	5T12	-	501.6	564.7	-	-
RE-20	300	100	20	5T12	5T12	-	501.6	564.7	-	-
RE-32	300	100	32	5T12	-	5T12	501.6	564.7	-	-
RE-50	300	100	50	5T12	-	5T12	501.6	564.7	-	-
RE-100	300	100	100	5T12	-	5T12	501.6	564.7	-	-
OV-25	300	125	25	5T12	5T12	-	501.6	564.7	-	-
OV-25a	300	125	25	5T12	5T12	5T10	501.6	564.7	474.9	506.6
OV-50	300	150	50	5T12	5T12	-	501.6	564.7	-	-
OV-50a	300	150	50	5T12	5T12	5T10	501.6	564.7	474.9	506.6

The slab specimens for both series were prepared in two stages. First, the normal strength concrete (NSC) was cast, then the UHPC was mixed and cast onto the concrete substrate. The NSC was supplied by a local ready-mix supplier. Six 100 mm standard cubes and six 100 by 200 mm standard cylinders were prepared for compressive strength testing. All the slabs, cubes and cylinders were cured under identical conditions: under ambient temperature covered with wet hessian for 7 days followed by dry open air for the remainder of the period until the day of testing (day 28). The average compressive strength of the NSC at 28 days was 33 MPa for the cubes and 23 MPa for the cylinders.

After the NSC hardened, the top surface of the concrete was purposely roughened in order to create a good bonding surface for UHPC layer. This was done using chisel and hammer randomly throughout the NSC substrate. Before casting of UHPC, the surface of the concrete substrate was moistened for 10 min and wiped dry with a cloth. Unlike the NSC, UHPC was prepared manually in the laboratory. Because of the quantities, three separate UHPC mixes were prepared for the two series. Details of the UHPC mix proportions and mechanical properties are given in Tables 2 and 3. Fig. 3 shows the preparation of the slab specimens before and after casting of the UHPC layers.

Table 2: UHPC material properties and mix design proportions.

Constituent	Description	Specific density	Mix proportion by weight
Cement	Ordinary Portland cement Type I	3.15	1.00
Silica fume	Bulk density is 204.4 kg/m^3	3.15	0.25
Quartz powder	Minimum 97% pass through 325 mesh sieve	2.76	0.25
Quartz sand	P100/300 minimum 80% retained	2.71	0.48
River sand	0.3 – 0.8 mm	2.67	0.80
Steel fibre (%Vol.)	Straight fibres 13 mm long, 0.2 mm diameter, tensile strength > 2300 MPa	7.83	3%
Superplasticiser	Sika ViscoCrete 2044	-	0.05
W/C	Water to cement ratio	-	0.20

Table 3: Mechanical strength properties of UHPC mix designs used in this study.

Mix	Ultimate compressive strength of UHPC		Flexural strength: σ_f (MPa)	Spread (mm)
	Cube samples: $f_{cu,U}$ (MPa)	Cylinder samples: $f'_{c,U}$ (MPa)		
1st	166	156	27.4	233
2nd	156	151		215
3rd	184	152		224

(a) (b)

Figure 3: (a) RC slabs before UHPC layer casting and (b) composite UHPC-concrete slab specimens.

2.2. Test setup and instrumentation

All slab specimens were simply supported and subjected to the three-point load configuration shown in Fig. 1. Each slab had a clear span of 1200 mm and carried a concentrated load at mid-span, applied at a loading rate of 0.1 kN/sec. The shear span between the supports and load point is 600 mm, corresponding to a shear span-to-effective depth ratio (a/d) of 8.11 for slabs without UHPC overlays. Two types of instrumentation were used, linear variable differential transducers (LVDTs) to measure vertical mid-span deflection and electrical resistance strain gauges to measure internal longitudinal reinforcement steel strain. Fig. 4 shows a slab specimen with instrumentation ready for testing.

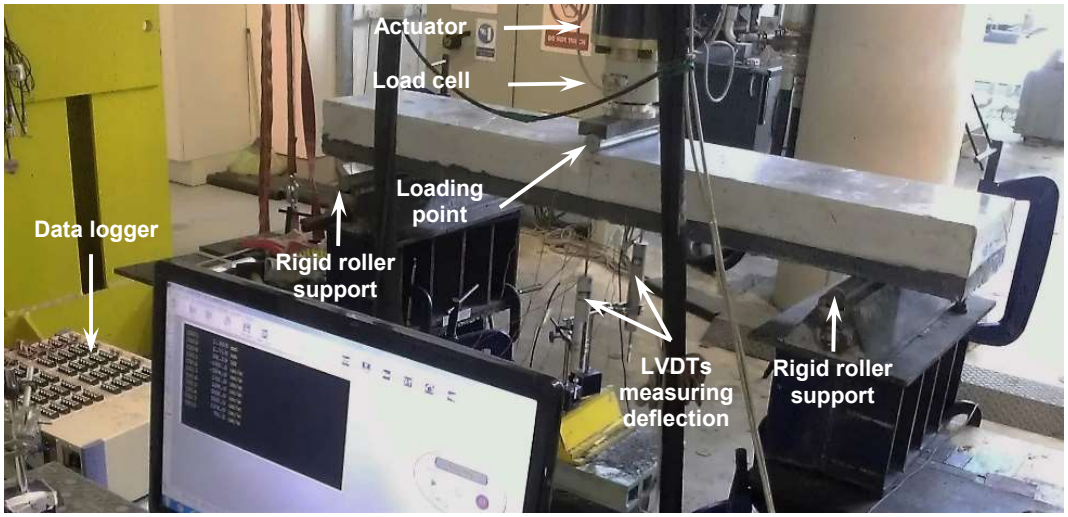

Figure 4: Test setup and specimen instrumentation system.

Two LVDTs were installed on each slab underneath the slab soffit at mid-span. The vertical deflections were plotted based on the average of the two LVDTs. For the slab specimens of the RE series, two strain gauges were installed at the mid-span of the bottom longitudinal reinforcement. For slabs OV-25a and OV-50a in the OV series, besides the two strain gauges on the bottom longitudinal reinforcements of the concrete substrate, two additional strain gauges were attached to their longitudinal reinforcements in the UHPC layer. Details of the positions of the strain gauges are shown in Fig. 1.

KYOWA waterproof strain gauges of 5 mm gauge length were used. Before a gauge was attached, the steel rebar was ground to a slightly flat surface for ease of gauge placement. The ground surface was then polished with sand paper and cleaned with acetone solvent before attaching the gauges using cement glue. To prevent strain gauge damage during concreting, all gauges were protected with an extra layer of silicone. Fig. 5 shows the placement of a waterproof strain gauge on the bottom longitudinal reinforcement before being protected with silicone.

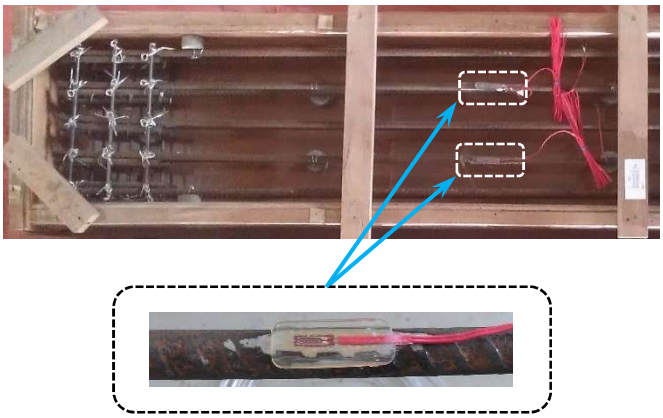

Figure 5: Strain gauges on longitudinal steel.

3. UHPC Material

The design strength of the UHPC in this study was targeted at 150 MPa. Several trial mixes were attempted. The mix proportion and constituents chosen for use in this study as a result of these trials are shown in Table 2. To obtain the rheology and mechanical properties of the UHPC mix, compressive strength testing, three-point flexural testing and flow testing were conducted. Details of the test results are explained in the following sub-sections.

3.1. Compressive strength

Four cube and cylinder samples were collected of each mixture to measure its compressive strength. After casting, all samples were cured and treated in the same environment as the slab specimens. In this study, three mixtures were prepared for the slab specimens of both the RE and OV series. The compressive strengths obtained at 28 days for each mixture are summarised in Table 3. After trying several different percentages of steel fibres, it was found that 3% of steel fibres achieved the best performance and was therefore chosen for this study.

3.2. Flexural strength

Three prism specimens 500 mm long with cross-sectional dimensions of 100 by 100 mm were prepared of each mixture for the three-point flexural strength tests. Flexural testing was conducted according to the BS EN 12390-5-2009 standard [22]. Fig. 6 shows the test setup and the final crack pattern of a UHPC specimen with 3% steel fibres after testing.

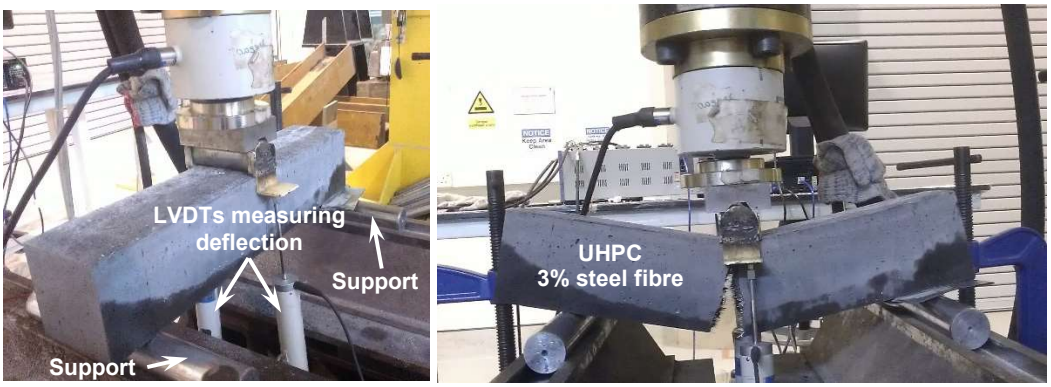

Figure 6: Three-point bending flexural test arrangement.

All the prism specimens were also instrumented to measure vertical deflection. Two LVDTs were installed at the top and on both sides of the specimen, as shown in Fig. 6. Such an arrangement ensured that the LVDTs were not damaged during or after the test. The deflection value was based on the average of the two LVDTs readings. Plots of load versus deflection for 0% steel fibre (plain UHPC) and 3% steel fibre are presented in Fig. 7.

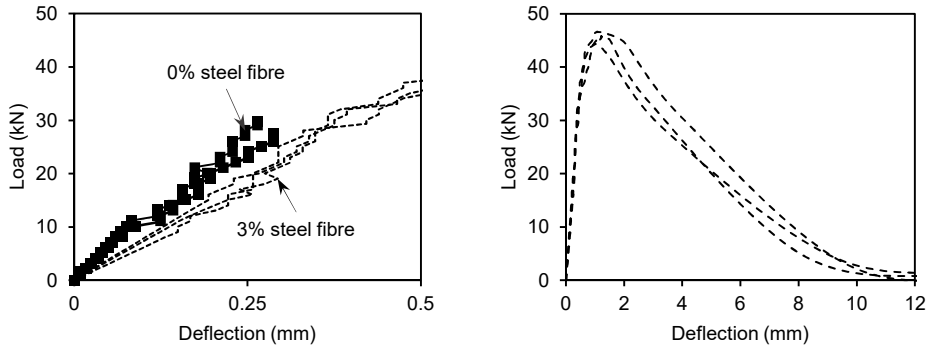

(a) Comparison between 0% and 3% by volume steel fibre (b) Full scale of 3% by volume steel fibre

Figure 7: Load-deflection curves of flexural tests.

According to BS EN 12390-5-2009 [22], flexural strength of the three-point bending test is as follows:

$$\sigma_f = \frac{3P_{\max}L}{2bh^2} \quad (1)$$

where P_{max} is the maximum load, L is the distance from support to support, b is the width of the specimen and h is the height of the specimen (b = h = 100 mm). The experimentally obtained average flexural strength for UHPC with 3% steel fibre is 27.4 MPa, as indicated in Table 3.

3.3. Workability

We carried out flow tests on fresh UHPC mixtures following EN 1015-3 [23]. Samples of fresh UHPC were obtained immediately before the slab specimens were cast. The flowability of the mixture was measured based on the average perpendicular diameter of the maximum spreads. According to Wille et al. [2], the acceptable spread limit for sufficient workability and optimum packing density should be between 200 mm and 300 mm. The average measured spreads are summarised in Table 3.

4. Experimental results and discussion

4.1. RE Series

4.1.1. Ultimate strength and failure modes

The ultimate experimental failure loads of the slabs in the RE series and their respective failure modes are summarised in Table 4. In addition, to illustrate the failure behaviour clearly, the crack patterns developed in each slab are shown in Fig. 8.

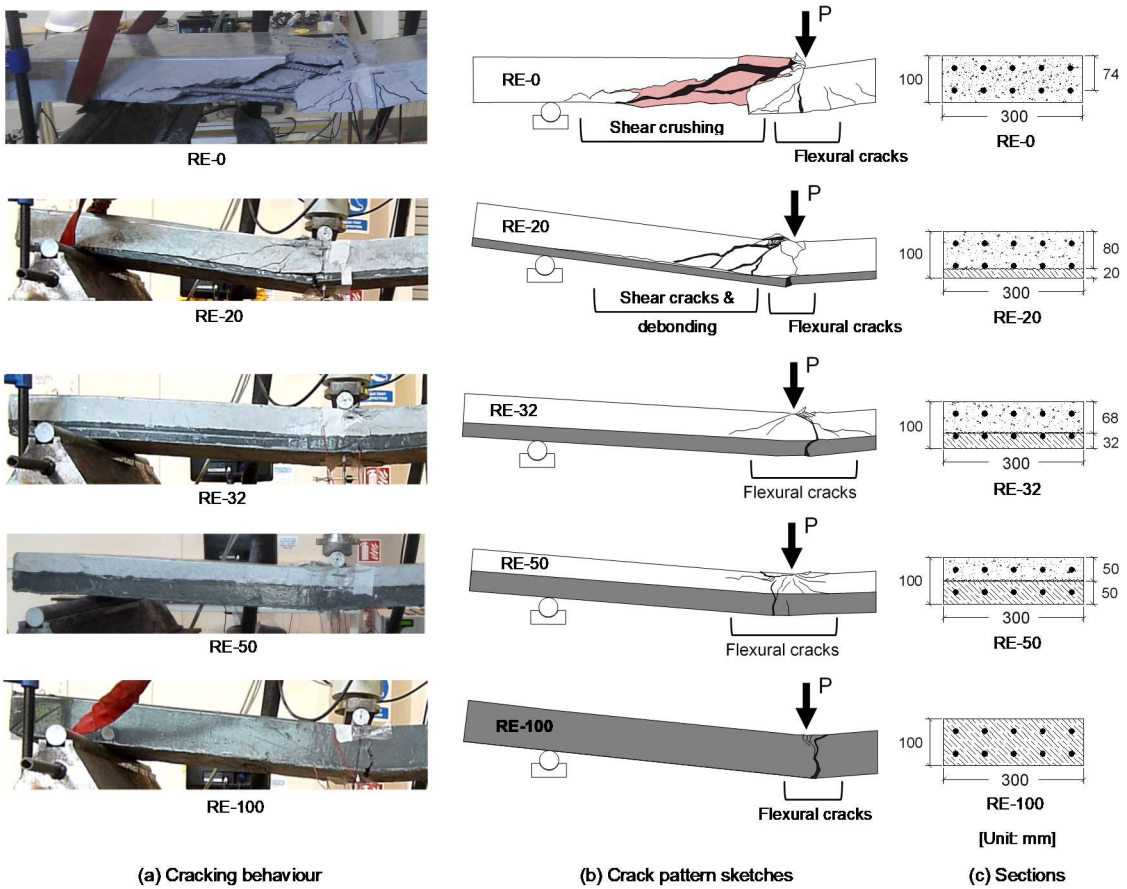

Figure 8: Failure modes and crack patterns of RE series.

Slab RE-0 is a reference specimen made of NSC. It failed at an ultimate load P_u equal to 61.08 kN, which corresponds to an ultimate moment $M_{u,exp}$ of 18.32 kNm. The calculated flexural moment capacity M_{fle} based on the exact material properties is equal to 15.51 kNm, so the failure load of slab RE-0 actually exceeded the full moment capacity of the section. Despite attaining such a load, however, slab RE-0 still failed in shear. The failure mode was brittle and sudden with diagonal tension cracks followed by spalling of the concrete cover along the longitudinal reinforcement.

Slab RE-20 simulated the repair of deteriorated concrete with a 20 mm thick UHPC cover. Its failure was not as sudden and devastating as that of slab RE-0. The strengthened UHPC concrete cover layer enhanced the tension zone and delayed the formation of diagonal shear cracks. The specimen suffered shear compression failure with concrete crushing and diagonal shear cracking, followed by fracture and debonding of the UHPC layer. Although the failure mode improved, there was no sign of strength enhancement. Slab RE-20 failed at an ultimate load P_u of 57.18 kN.

Slab RE-32 was strengthened with 32 mm thick UHPC to simulate the repair of deteriorated concrete with exposed reinforcement rebars. Unlike slab RE-20, no sign of UHPC layer debonding happened in slab RE-32. Its failure was purely flexural with concrete crushing at the compression zone. The slab behaved in a very ductile manner until the final fracture of the UHPC layer. Though a few inclined cracks were visible in the concrete substrate, no impending shear failure occurred. Similar to slab RE-20, no strength enhancement was observed compared with reference slab RE-0. On the contrary, slab RE-32 failed at the lowest load of the RE series, an ultimate P_u of only 43.68 kN.

Slab RE-50 was strengthened with 50 mm thick UHPC, which corresponds to half the thickness of the slab. There were neither signs of debonding of the UHPC layer nor inclined cracks in the concrete substrate. The mode of failure was a ductile flexural failure that featured concrete crushing at the compression zone, followed by a main flexural crack fracturing through the UHPC layer. Based on the observations from slabs RE-20, RE-32 and RE-50, it is evident that as the thickness of the tension zone enhanced by UHPC increased, the likelihood of diagonal shear failure diminished. Sllab RE-50 failed at an ultimate load P_u of 55.38 kN.

Slab RE-100 was a reference specimen formed of UHPC. It attained the highest ultimate failure load of the RE series (P_u = 112.95 kN). Throughout loading, no visible signs of major cracks were observed along the whole span. The final failure mode was ductile with a single flexural crack initiated at mid-span of the slab.

4.1.2. Mid-span deflection responses

Load versus mid-span deflection is plotted for the RE series slabs in Fig. 9. The curves are based on the average of the two LVDTs installed under the soffit at mid-span, as described earlier.

Slab RE-0 showed a quasi-linear load deflection response, which reflected typical characteristics for brittle shear failure behaviour with limited ductility. When the tension zone was strengthened with a UHPC layer, the overall behaviour of the strengthened slab changed completely. As can be seen in Fig. 9, all the composite UHPC-concrete slabs underwent extensive deflection hardening and ductility during the post cracking range. Although no sign of strength enhancement was found in any of the strengthened slabs as compared to reference slab RE-0, that could easily be offset by their excellent energy absorption capabilities. It is common to measure the extent of ductility of a structural element by a normalised factor known as the ductility index [24], which can be defined as the ratio of deflection at the ultimate state to deflection at the yielding of the longitudinal steel. The ductility indices calculated for each slab are summarised in Table 4.

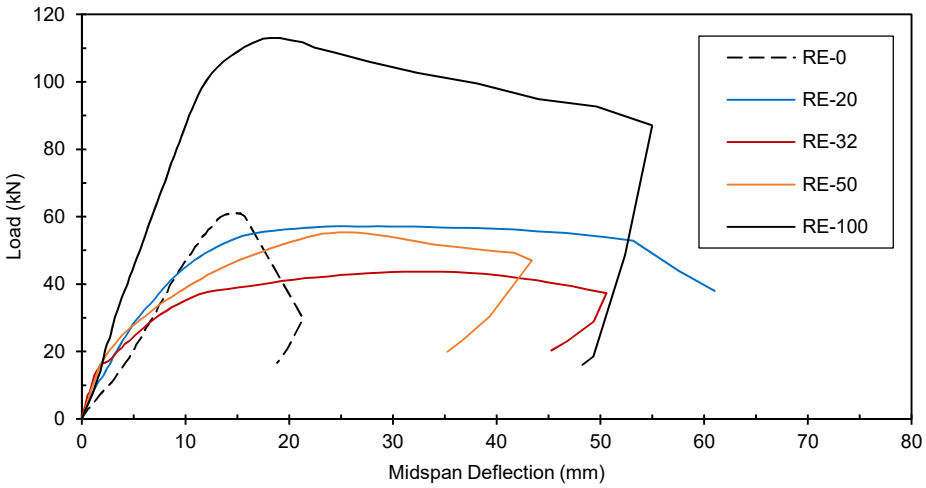

Figure 9: Load versus mid-span deflection curves of RE series.

The ductility index of the strengthened slabs decreased as the thickness of the UHPC layer increased. As demonstrated in Table 4, slab RE-20 had a ductility index of 2.85, whereas those of slabs RE-32 and RE-50 were 1.90 and 1.11, respectively. This implies that strengthening the tension zone with UHPC relieved the tensile forces acting on the longitudinal reinforcement. Therefore, greater deflection was required for the longitudinal reinforcement to reach its yield point. Ultimately, the failure of the strengthened slabs was limited by the strength of the concrete at the compression zone. As clearly observed from the experiment, slabs RE-32 and RE-50 failed in ductile flexure featuring concrete crushing at the compression zone. When the slab was a full UHPC section, like RE-100, the phenomena that occurred in slabs RE-20, RE-32 and RE-50 were inhibited. Slab RE-100 experience improved stiffness with the least deflection when the longitudinal reinforcement yielded, as shown in Fig. 9 and Table 4.

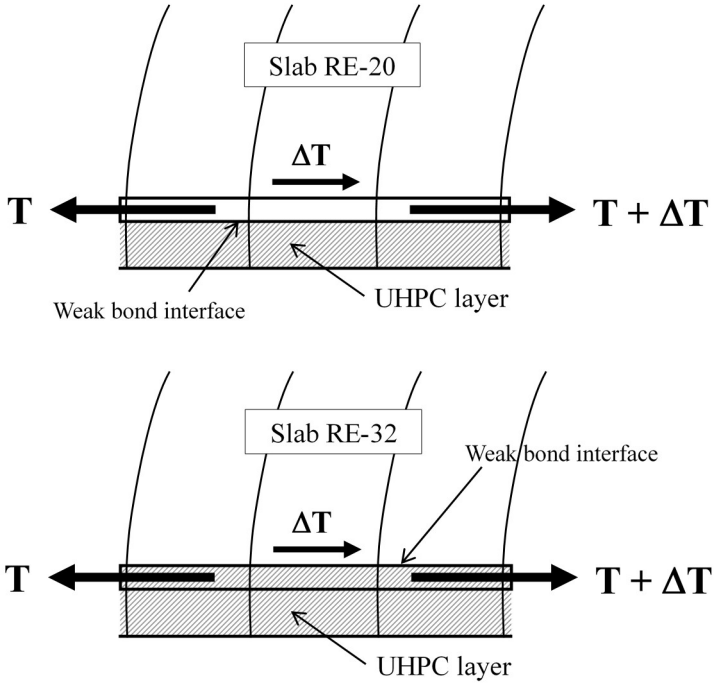

Figure 10: Shear transfer mechanism in slabs RE-20 and RE-32.

Partial strengthening of the tension zone with UHPC created a weak bond interface between the UHPC and NSC. This was even more critical when the interface happened to be located at the longitudinal reinforcement, as in the case of slab RE-32. Fig. 10 indicates the shear transfer mechanisms of slabs RE-20 and RE-32. As is commonly known (Kani [25], Teo and Müller [26]), shear in reinforced concrete arises due to the change of tensile forces (horizontal ΔT forces) along the longitudinal reinforcement. Shear (or ΔT forces) is transferred from the reinforcement to the concrete through the action of the bond between them. As can be seen in Fig. 10, slab RE-32, a UHPC layer that reaches up to the top of the reinforcement actually prevents effective shear transfer between the longitudinal reinforcement and the concrete. This inevitably weak bond interface caused the slab to fail at a lower loading than RE-20 or RE-50.

4.1.3. Longitudinal steel strain responses

The load versus longitudinal steel strain curves of the slabs of the RE series are shown in Fig. 11. Each slab was instrumented with two strain gauges at the longitudinal steel reinforcement, labelled "cc1" and "cc2" in Fig. 1(e). The steel strain curves plotted in Fig. 11 were based on the average values of the two strain gauges. The dashed vertical line in the figure shows the experimentally obtained yield strain of the steel, $\varepsilon_y = 2446.8$ με.

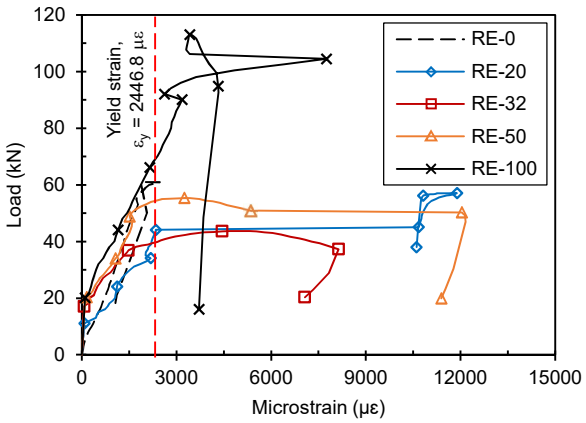

Figure 11: Load versus longitudinal steel strain curves of RE series.

Generally, yielding of the longitudinal reinforcement was observed in all slabs except RE-0. The experimental results indicated that UHPC provided at the tension zone could actually relieve the initial strain the longitudinal steel reinforcement underwent, compared with that in RE-0, as clearly observed in slabs RE-32 and RE-50. Similar to the mid-span deflection responses, all the strengthened slabs were found to undergo substantial hardening (strain) and ductility in the post cracking range.

It is of interest to note that at a load of approximate 45 kN, the strain sudden increased in slab RE-20 due to the breakdown (debonding) of the composite bond interface between the UHPC and NSC. Coincidently, slab RE-32 also experienced a comparative failure at that load level. It also experienced much less ultimate strain than slabs RE-20 or RE-50. This is mainly due to the weak bond interface between the longitudinal reinforcement and concrete, as discussed in the preceding section, which prevented effective full bond development and therefore failed prematurely.

Table 4: Summary of experimental results.

Specimen	Ultimate		Yield		Deflection ductility index $\mu_d = \Delta_u/\Delta_y$	Mode of failure
	P_u (kN)	Δ_u (mm)	P_y (kN)	Δ_y (mm)		
RE-0	61.08	14.78	-	-	-	Shear
RE-20	57.18	28.52	45.08	10.02	2.85	Flexure-shear
RE-32	43.68	34.65	40.38	18.25	1.90	Flexure
RE-50	55.38	25.68	54.98	23.17	1.11	Flexure
RE-100	113.05	19.09	72.07	8.22	2.32	Flexure
OV-25	73.47	14.70	69.87	10.02	1.47	Shear
OV-25a	77.97	14.42	76.07	11.16	1.29	Shear
OV-50	77.97	9.44	-	-	-	Shear
OV-50a	95.06	17.76	80.97	8.09	2.20	Shear

where:
P_u = ultimate load
P_y = load at yielding of the longitudinal steel
Δ_y = mid-span deflection at yielding of the longitudinal steel
Δ_u = mid-span deflection at ultimate load
μ_d = ductility index for deflection, given by the ratio Δ_u/Δ_y

4.2. OV Series

4.2.1. Ultimate strength and failure modes

As mentioned earlier, the OV series consisted of four slabs with similar cross-sectional dimensions as the RE series. The only difference is the additional UHPC overlays that strengthened the tension zone (see Fig. 2). Fig. 12 shows the final crack patterns and modes of failure exhibited for each slab in the OV series. Their ultimate failure loads are summarised in Table 4.

Regardless of the UHPC overlay thickness, all the strengthened slabs failed in shear in the NSC. Through all the loading stages, there were no apparent signs of distress or extensive cracking in the slabs. The UHPC overlay actually helped delay the development of diagonal shear cracks. Often, once a diagonal shear crack formed, ultimate failure prevailed. In some cases, the composite interface between the UHPC and NSC suffered debonding failure, as clearly indicated in Fig. 12.

Based on our observations, it appears that the thickness of the UHPC overlay did not significantly influence the ultimate strength and failure modes the slabs underwent. Slabs OV-25 and OV-50 both failed in comparatively similar ways at ultimate loads of 73.57 kN and 77.97 kN, respectively, only a 6% marginal difference. This is mainly because ultimate failure in both slabs was controlled by debonding failure at the composite interface. Despite that failure, the ultimate strengths of both slabs were about 24% higher than that of RE-0. It must also be noted that the tendency for fracture failure in the UHPC layer was higher with thicker overlays, as found in slabs OV-50 and OV-50a.

The experimental results showed that the presence of longitudinal steel bars within the UHPC layer increased the ultimate strength of the slab as long as sufficient cover was provided for effective bond development. For example, slab OV-50a achieved an ultimate load of 95.06 kN, an increase of 55.6% over that of slab RE-0. On the other hand, the strength of slab OV-25a

was only 6% greater than that of OV-25. This was likely due to the longitudinal reinforcement being placed adjacent to the composite interface, likely similar to slab RE-32 (illustrated in Fig. 10), which had a weak bond interface that did not encourage full bond development with the longitudinal reinforcement.

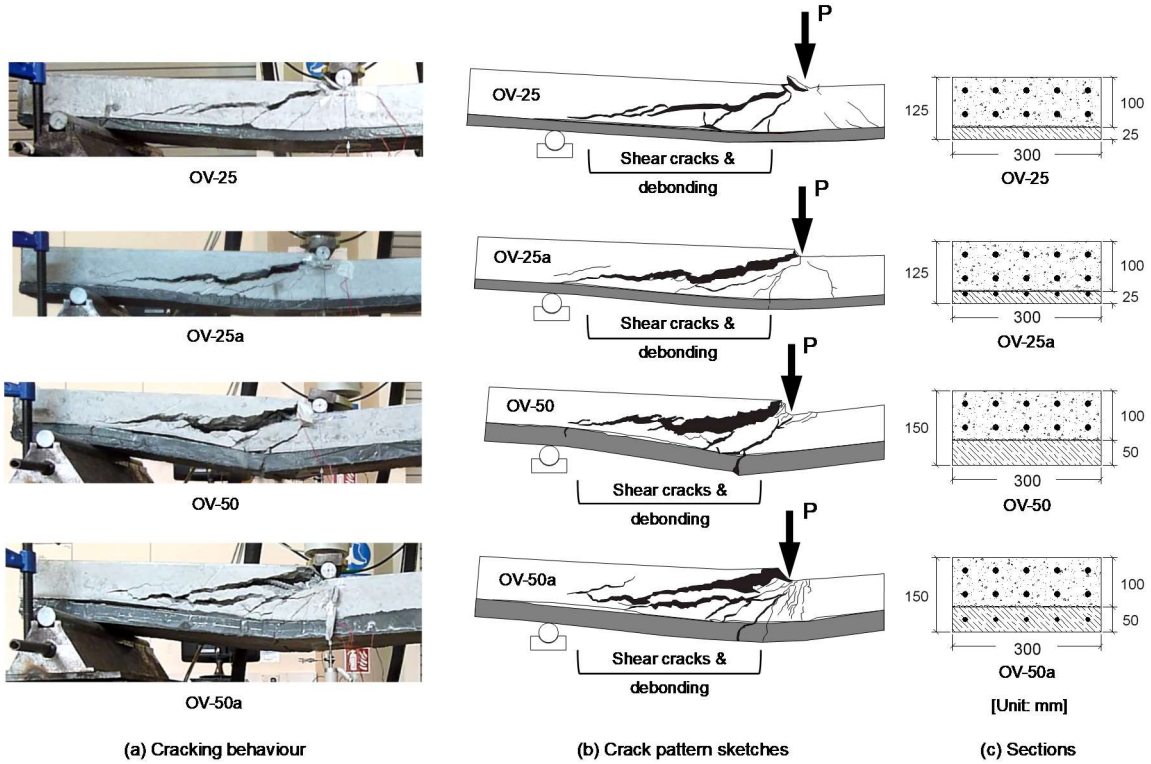

Figure 12: Failure modes and crack patterns of OV series.

4.2.2. Mid-span deflection responses

The load versus mid-span deflection curves of the slabs in OV series are shown in Fig. 13. Similar to the RE series, these deflection curves were based on the average response of the two LVDTs installed underneath the slab soffits at mid-span.

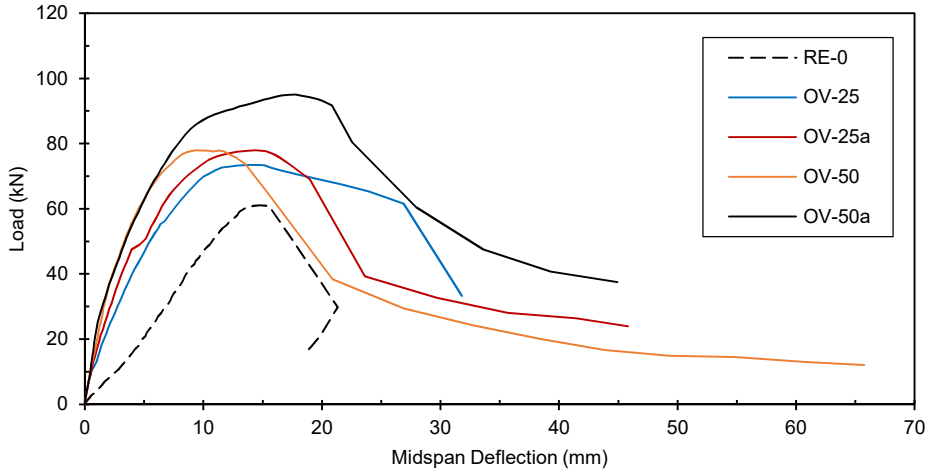

Figure 13: Load versus mid-span deflection curves of OV series.

Obviously, with UHPC overlays at the tension zone, the overall stiffness of the strengthened slabs improved significantly compared with reference slab RE-0. Extensive deflection hardening and ductility during the post cracking phase was seen in all strengthened slabs as well. As illustrated in Table 4, all the slabs, except OV-50, had ductility indices over 1.0. Slab OV-50a had the highest ductility index (2.20) in this series. Despite such behaviour, however, all the slabs were found to fail in diagonal shear in the NSC. It should be noted that no ductility index value was obtained for slab OV-50 mainly because its longitudinal reinforcement did not yield.

The thickness of the UHPC overlay greatly influenced the stiffness of the slabs. It was found that thicker UHPC layers lead to increased stiffness, as observed in slabs OV-25 and OV-50. Slab OV-50a, with its reinforced UHPC layer did not seem to differ from slab OV-50 in initial stiffness. However, the reinforcing bars in the UHPC layer helped to further extend the ultimate resistance capacity of the slab and led to smaller deflection when the longitudinal reinforcement yielded (refer to Table 4). Another important observation is that, similar to the findings of Habel et al. [27], the minimum thickness of the UHPC layer is limited by the size of the reinforcing bars and the UHPC cover over them, so that effective force transfer between the reinforcing bars and UHPC can be developed.

4.2.3. Longitudinal steel strain responses

Load versus longitudinal steel strain for the slabs in the OV series is plotted in Fig. 14. The strain curves were based on the average values of the two strain gauges. The curves are labelled as C1 and U1 based on their locations. The C1 strain curve was obtained from gauges cc1 and cc2 (see Fig. 1(e)) installed at the T12 mm longitudinal steel bars, similar to the RE series. The U1 strain curve came from gauges uu1 and uu2 (see Fig. 1(f)) installed at the T10 mm longitudinal steel bars in the UHPC layer. There is also a vertical line in Fig. 14 showing the yield strain of the longitudinal steel in the NSC, $\varepsilon_y = 2446.8\ \mu\varepsilon$.

The effect of UHPC thickness on longitudinal steel strain is illustrated in Fig. 14(a). It shows that thicker UHPC overlays decreased the strain experienced by the longitudinal steel reinforcement in the NSC. The UHPC overlays increased the flexural depth of the section and therefore reduced the tension action acting on the longitudinal steel reinforcement. This lowered the strains in the longitudinal steel reinforcement. The longitudinal steel strains of slab OV-25 exhibited very ductile behaviour with extensive yielding. When the thickness of the UHPC overlay was increased, as in slab OV-50, the slab experienced less steel strain with no yielding.

Interestingly, the addition of longitudinal steel bars in the UHPC layer did not appear to increase the overall stiffness of the slabs. Fig. 14(b) shows that the strain curve C1 for slab OV-25a follows a strongly similar trend to that of slab OV-25 before reaching yield. Slabs OV-50 and OV-50a behaved similarly as shown in Fig. 14(c). It should be noted that strain curve C1 for slab OV-25a did not exhibit extensive ductility after yielding like slab OV-25. This is partially due to the additional tensile resistance provided by the longitudinal steel bars in the UHPC layer. Neither curve for slab OV-25a reached yield. On the other hand, in slab OV-50a, because better effective force transfer between the rebar and the UHPC could be developed, both strain curves were able to exceed their full yield capacity.

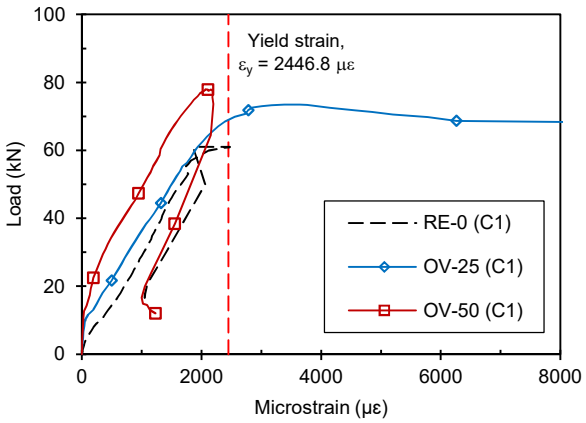

(a) Steel strain curves for slabs OV-25 and OV-50

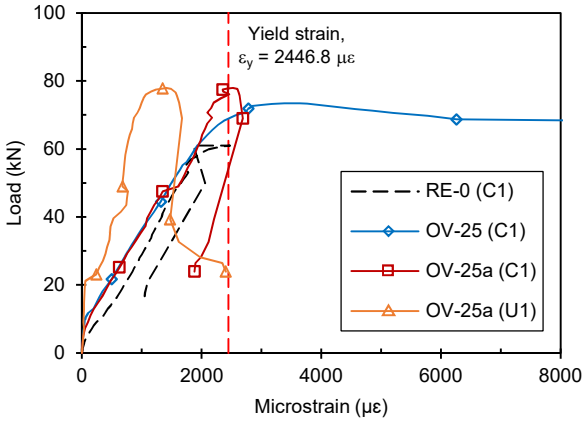

(b) Steel strain curves for slab OV-25a

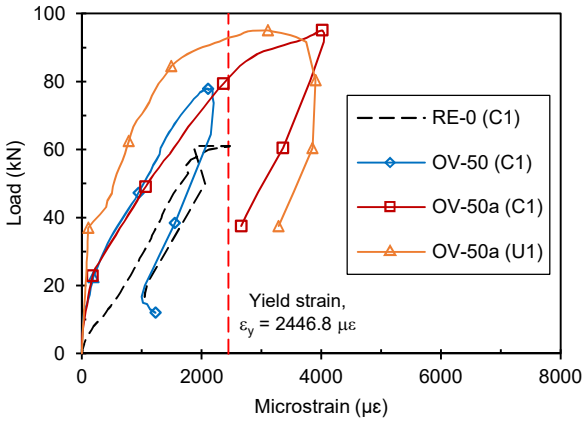

(c) Steel strain curves for slab OV-50a

Figure 14: Load versus longitudinal steel strain curves of OV series.

5. Conclusions

The following conclusions could be drawn from the results of experiments on RC slabs strengthened with UHPC in the tensile zone (composite UHPC-concrete slabs) presented in this study:

(1) In the RE series, the UHPC strengthening configuration greatly affects the failure modes and crack patterns of the composite UHPC-concrete slabs. It showed that as thickness of

UHPC layer increases, the failure mode changes from brittle diagonal shear failure to ductile flexure failure. Although no improvement in the ultimate strength was observed, all strengthened slabs exhibited excellent energy absorption capacity with extensive deflection hardening and ductility.

(2) In the OV series, all slabs strengthened with UHPC overlays at their soffits failed in shear. The slabs showed diagonal shear cracks in the NSC followed by debonding at the UHPC-concrete interface. The results indicated that the UHPC overlay improves the overall stiffness of the slabs and delays the development of shear cracks. With addition of reinforcing rebar in the UHPC layer, further enhancement could be observed in the ultimate strength. However, sufficient concrete cover is required to ensure effective full bond development.

(3) The results from this research were very promising and demonstrated the potential of UHPC as an excellent strengthening material for structural application.

Further research in this area is certainly needed. This study demonstrated that the bond interface between UHPC and original RC slabs is very critical. Therefore, a new analytical model that could reflect the actual bond interface behaviour needs to be proposed. This proposed model must accurately predict the resistance of the composite UHPC-concrete members. The development of such an analytical model will greatly assist in the design and advanced sectional analysis of the composite section, which would further encourage the acceptance of UHPC as a suitable strengthening material for deficient RC structures.

Acknowledgements

The authors gratefully acknowledge Universiti Teknologi PETRONAS (UTP) for providing financial support via a Yayasan UTP-Fundamental Research Grant (YUTP-FRG) Cycle 1/2013 and facilities for conducting experiments that contributed to this paper.

References

[1] P. Richard, M. Cheyrezy, Composition of reactive powder concretes, Cem. Concr. Res. 25 (7) (1995) 1501-1511.

[2] K. Wille, A.E. Naaman, G.J. Parra-Montesinos, Ultra-high performance concrete with compressive strength exceeding 150 MPa (22 ksi): a simpler way, ACI Mater. J. 108 (1) (2011) 46-54.

[3] T.M. Ahlborn, D.L. Misson, E.J. Peuse, C.G. Gilbertson, Durability and strength characterization of ultra-high performance concrete under variable curing regimes, in: Proc. 2nd Int. Symp. Ultra-high Performance Concrete, Kassel, Germany, 05-07 March 2008.

[4] M. Alkaysi, S. El-Tawil, Z. Liu, W. Hansen, Effects of silica powder and cement type on durability of ultra high performance concrete (UHPC), Cem. Concr. Compos. 66 (2016) 47–56.

[5] E. Brühwiler, E. Denarie, Rehabilitation of concrete structures using ultra-high performance fibre reinforced concrete, in: Proc. 2nd Int. Symp. Ultra-high Performance Concrete, Kassel, Germany, 05-07 March 2008.

[6] B.A. Tayeh, B.A Bakar, M.M. Johari, Y.L. Voo, Mechanical and permeability properties of the interface between normal concrete substrate and ultra high performance fiber concrete overlay, Constr. Build. Mater. 36 (2012) 538-548.

[7] B.A. Graybeal, F. Baby, Development of direct tension test method for ultra-high-performance fiber-reinforced concrete, ACI Mater. J. 110 (2) (2013) 177-186.
[8] S.D. Adhikary, B. Li, K. Fujikake, Strength and behavior in shear of reinforced concrete deep beams under dynamic loading conditions, Nucl. Eng. Des. 259 (2013) 14-28.
[9] K. Habel, P. Gauvreau, Response of ultra-high performance fiber reinforced concrete (UHPFRC) to impact and static loading, Cem. Concr. Compos. 30 (10) (2008) 938-946.
[10] L. Mao, S.J. Barnett, A. Tyas, J. Warren, G. Schleyer, S. Zaini, Response of small scale ultra high performance fibre reinforced concrete slabs to blast loading, Constr. Build. Mater. 93 (2015) 822-830.
[11] N.H. Yi, J.H.J. Kim, T.S. Han, Y.G. Cho, J.H. Lee, Blast-resistant characteristics of ultra-high strength concrete and reactive powder concrete, Constr. Build. Mater. 28 (2012) 694-707.
[12] B.A. Graybeal, Characterization of the behavior of ultra-high performance concrete, PhD thesis, University of Maryland, USA, 2005.
[13] Y.L Voo, W.K. Poon, S.J. Foster, Shear strength of steel fiber-reinforced ultrahigh-performance concrete beams without stirrups, J. Struct. Eng. 136 (11) (2010) 1393-1400.
[14] I.H. Yang, C. Joh, B.S. Kim, Structural behavior of ultra high performance concrete beams subjected to bending, Eng. Struct. 32 (11) (2010) 3478-3487.
[15] D.Y. Yoo, N. Banthia, S.W. Kim, Y.S. Yoon, Response of ultra-high-performance fiber-reinforced concrete beams with continuous steel reinforcement subjected to low-velocity impact loading, Compos. Struct. 126 (2015) 233-245.
[16] C. Oesterlee, Structural response of reinforced UHPFRC and RC composite members, PhD thesis, École Polyechnique Fédérale de Lausanne, Switzerland, 2010.
[17] K. Habel, E. Denarié, E. Brühwiler, Experimental investigation of composite ultra-high-performance fiber-reinforced concrete and conventional concrete members, ACI Struct. J. 104 (1) (2007) 93-101.
[18] T. Noshiravani, E. Brühwiler, Experimental investigation on reinforced ultra-high-performance fiber-reinforced concrete composite beams subjected to combined bending and shear, ACI Struct. J. 110 (2) (2013) 251-261.
[19] P. Zohrevand, X. Yang, X. Jiao, A. Mirmiran, Punching shear enhancement of flat slabs with partial use of ultrahigh-performance concrete. J. Mater. Civil Eng. 27 (9) (2014) 04014255.
[20] F.J. Alaee, B.L. Karihaloo, Retrofitting of reinforced concrete beams with CARDIFRC, J. Compos. Constr. 7 (3) (2003) 174-186.
[21] J.H.J. Kim, Y.M. Lim, J.P. Won, H.G. Park, K.M. Lee, Shear capacity and failure behaviour of DFRCC repaired RC beams at tensile region, Eng. Struct. 29 (2007) 121-131.
[22] BS EN 12390-5, Testing hardened concrete. Part 5: Flexural strength of test specimens, British Standards Institution, 2009.
[23] BS EN 1015-3, Methods of test for mortar for masonry. Part 3: Determination of consistence of fresh mortar (by flow table), British Standards Institution, 1999.
[24] S.W. Shin, S.K. Ghosh, J. Moreno, Flexural ductility of ultra-high-strength concrete members, Struct. J. 86 (4) (1989) 394-400.
[25] G.N.J. Kani, The riddle of shear failure and its solution, ACI J. 61 (4) (1964) 441–467.
[26] W. Teo, G. Müller, Shear effectiveness of shallow-angle bent-up bars for reinforced concrete beams, Proc. Inst. Civil Eng. Struct. Build. 167 (7) (2014) 398-413.
[27] K. Habel, E. Denarié, E. Brühwiler, Structural response of elements combining ultrahigh-performance fiber-reinforced concretes and reinforced concrete, J. Struct. Eng. 132 (11) (2006) 1793-1800.

Chapter III

Paper II

Finite element modelling to predict the flexural behaviour of ultra-high performance concrete members

The content of this Chapter III has been submitted for consideration for publication as follows.

Hor Yin, Kazutaka Shirai, Wee Teo, "Finite element modelling to predict the flexural behaviour of ultra-high performance concrete members," Engineering Strucutres, (submitted date: 15 March 2018, under review).

Finite element modelling to predict the flexural behaviour of ultra-high performance concrete members

Abstract

This paper presents a finite element (FE) modelling to predict the behaviour of ultra-high performance concrete (UHPC) members under static flexural loading. A plasticity-based constitutive model for concrete and an implicit solver in LS-DYNA were adopted in the numerical simulation. Experimental data for 21 UHPC specimens tested in the present study and in previous works were used to calibrate and validate the proposed FE model and modelling technique. The simulation was able to accurately predict the experimentally obtained ultimate strength, stiffness, and hardening and softening behaviours of the specimens. This demonstrates the effectiveness and adequacy of the developed FE model and modelling technique.

Keywords: Ultra-high performance concrete (UHPC); Steel fibres; Implicit analysis; LS-DYNA; Finite element model; Stiffness; Flexural response.

1. Introduction

Ultra-high performance concrete (UHPC) is a relatively new construction material with properties superior to those of conventional concrete. Its high strength, very low permeability, strain hardening behaviour, and energy absorption make this material exceptionally resistant against severe loading and environmental actions. Because of its excellent properties, UHPC is also attractive for use in protective structures and megastructures with slim and aesthetic designs. Over the last two decades, many studies have been conducted on the properties of UHPC after it was first developed by Richard and Cheyrezy [1]. These studies have mainly focused on the effects of the characteristics of the added steel fibres, such as their type [2], length [2–4], quantity [3–5], and distribution [6,7], on the properties of the UHPC.

To date, UHPC structural members have been experimentally investigated through static, impact, and blast loading tests. Tests on reinforced UHPC members under static loading have shown that longitudinal rebar and sufficient steel fibres can effectively control the crack width and enhance ductility [7–12]. Studies on the drop-weight impact testing [13–15] and blast testing [16–19] of UHPC members have proven that the use of UHPC for structural elements is efficient and effective against dynamic loading because of the enhancement of the cracking response and strain hardening of UHPC relative to conventional concrete.

Although the great potential of UHPC for structural applications has been demonstrated, few studies on finite element (FE) modelling to predict the flexural behaviour of the UHPC have been carried out [20,21]. A reliable numerical model would enable the effective enhancement of the structural performance and reductions in costs, testing and production time, and the required number of test specimens. Several types of commercial FE simulation software, such as LS-DYNA [22], are available with plasticity constitutive models for conventional concrete. The concrete damage model MAT_72R3 [23] in LS-DYNA has been commonly used to predict the behaviour of conventional concrete members [24–26]. However, the properties of UHPC are significantly different from those of conventional concrete. The parameters of the constitutive model for UHPC should therefore be defined according to the actual characteristics of UHPC.

Mao et al. [27] modified the concrete model parameters to model UHPC. The model was used to simulate the blast behaviour of four panels composed of UHPC containing short steel fibres of 13 mm in length and a mixture of fibres of 13 and 25 mm in length. Mao et al. [27] were able to accurately predict the response and failure mode using the FE model. Magallanes et al. [21] studied the feasibility of using MAT_72R3 to model UHPC under static and blast loading. They considered influential parameters related to the strain softening and tensile fracture energy characteristics through explicit analysis; however, the model showed only fair accuracy. Singh et al. [20] modelled the flexural behaviour of UHPC beams containing hooked-end steel fibres of 35 mm in length. They experimentally validated their numerical model; however, their study only considered very limited test data.

As demonstrated by the above discussion, investigations on the application of FE analysis to UHPC behaviour have been very limited. Furthermore, the effect of the steel fibre length has not been yet clearly considered in existing FE models. Although models for static and dynamic analysis have been established using an explicit solver [24,27], an implicit solver that is generally suitable for static simulations (e.g. one that allows the setting of larger time steps in the implicit analysis than in the explicit analysis) has not yet been employed to analyse UHPC members.

The aim of this study was to develop an accurate FE model and a corresponding modelling technique for the prediction of the flexural behaviour of UHPC members under static loading. The concrete damage model MAT_72R3 and an implicit solver in LS-DYNA software were used for the numerical simulation. To calibrate and validate the proposed FE model and modelling technique, the authors prepared UHPC mixtures and conducted static experiments on UHPC flexural members. The calibration of the concrete damage model, including stiffness correction and parameter determination, was carried out. Furthermore, validation was conducted using 18 additional numerical models of UHPC specimens tested by other researchers to investigate the effectiveness of the present FE model.

2. UHPC experiments

2.1. Overview

Section 2 describes the procedure and results of the experiments conducted in the present study. Several trials were conducted to investigate the material properties of UHPC and to use it to construct flexural members. The detailed mixing procedure and observations regarding the effect of the steel fibre contents added to the UHPC are presented. The flexural members made from the developed UHPC were used to calibrate and validate the FE model and modelling technique described in Sections 4 and 5.

All experimental results for specimens in Section 2 are original data obtained in this study, except for two of those described later in this section, namely 3-PL-3% and R-UHPC, which have been previously reported by the authors (Yin et al. [28]).

2.2. Material properties of UHPC

2.2.1. Mixing procedure

UHPC mixtures typically have several constituents, most of which are very fine particles. The UHPC mixtures used in this study were composed of Portland cement, silica fume, quartz powder, quartz sand, river sand, steel fibres, a superplasticizer admixture, and water. Detailed descriptions of the UHPC constituents and their properties are given in Table 1. The fine

particles can easily accumulate into chunks during the mixing process. To reduce the formation of chunks, all particles should be dry. The simple UHPC mixing procedure used in this study is illustrated in Fig. 1. Generally, the completion of each mixture took approximately 20 min.

Table 1: Properties of UHPC constituents.

	C	SF	QP	QS	RS	Steel fibres †	SP
Specific gravity	3.15	3.15	2.76	2.71	2.67	7.83	1.08

C: Ordinary Portland cement Type I
SF: Silica fume, bulk density of 204.4 kg/m^3
QP: Quartz powder, minimum of 97% passage through 325-mesh sieve
QS: Quartz sand, P100/300 minimum of 80% retained
RS: River sand, 0.3–0.8 mm in diameter
SP: Superplasticizer (Sika ViscoCrete 2044)
† Straight, smooth steel fibres of 13 mm in length and 0.2 mm in diameter

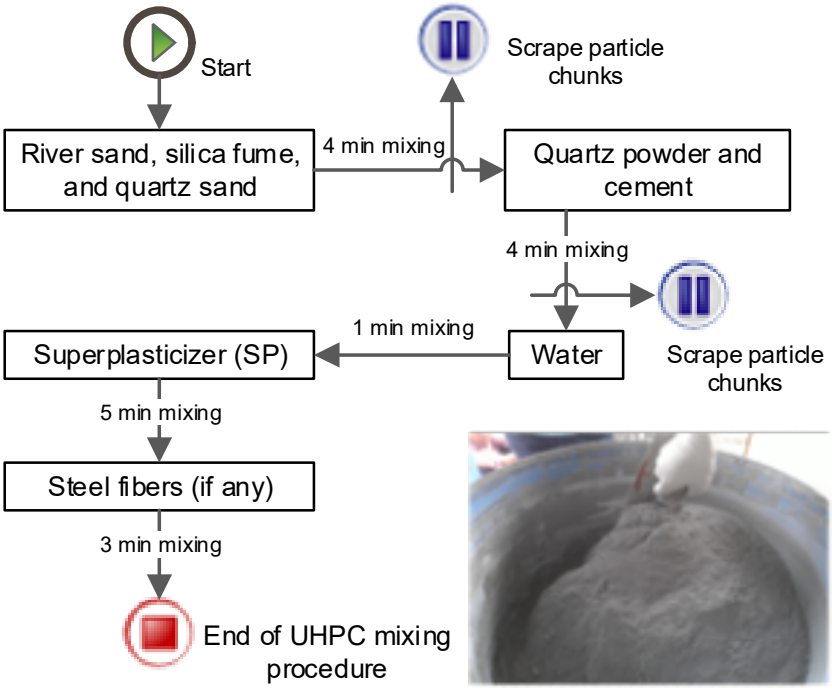

Figure 1: UHPC mixing procedure.

2.2.2. UHPC mixtures without steel fibres

Table 2 gives the compositions of different UHPC mixtures without steel fibres. Mixtures with several proportions were prepared to attain a target compressive strength of cubic or cylindrical samples of 150 MPa or greater. Three 100-mm standard cubes and three 100 mm × 200 mm standard cylinders were used for the compressive strength testing of each mixture. The samples were treated by conventional water curing in the laboratory. The average compressive strengths of cubic and cylindrical samples made from each UHPC mixture at day 28 are also given in Table 2. Among all the mixtures, the TM-11 mixture offered the most promising results with average strengths of 157 and 125 MPa achieved for the cubes and cylinders, respectively. TM-11 was thus selected to investigate the effect of steel fibres on the flexural strength, as described in Section 2.2.3, and was then used to make the UHPC flexural members in Section 2.3.

Table 2: Composition and compressive strength of UHPC without steel fibres.

Mixture	Proportion by weight normalized by cement weight								Compressive strength (MPa)	
	C	SF	QP	QS	RS	SP	W	W/B	Cube	Cylinder
TM-01	1.00	0.25	0.25	1.10	-	0.04	0.20	0.16	150.64	86.15
TM-02	1.00	0.25	-	1.10	-	0.04	0.20	0.16	129.60	68.03
TM-03	1.00	0.25	-	-	1.10	0.03	0.20	0.16	121.25	74.18
TM-04	1.00	0.25	0.15	-	1.10	0.03	0.20	0.16	130.10	82.44
TM-05	1.00	0.25	0.25	-	1.10	0.03	0.20	0.16	133.30	78.96
TM-06	1.00	0.25	0.15	0.40	0.80	0.03	0.20	0.16	149.75	80.31
TM-07	1.00	0.25	0.25	0.40	0.80	0.03	0.20	0.16	153.10	97.18
TM-08	1.00	0.25	0.25	0.80	0.40	0.03	0.20	0.16	131.80	78.77
TM-09	1.00	0.25	0.25	0.60	1.00	0.04	0.20	0.16	126.13	92.16
TM-10	1.00	0.25	0.25	0.54	0.90	0.04	0.20	0.16	139.67	108.52
TM-11	1.00	0.25	0.25	0.48	0.80	0.04	0.20	0.16	156.87	125.30
TM-12	1.00	0.25	0.25	0.42	0.70	0.04	0.20	0.16	142.40	119.07

W: Water
W/B: Water-to-binder ratio, where binder is composed of cement and silica fume

2.2.3. Mechanical properties of UHPC with steel fibres

To investigate the flexural strength, prismatic specimens with a length of 500 mm and cross-sectional dimensions of 100 mm × 100 mm were prepared. Three-point flexural tests were conducted according to the standard BS EN 12390-5:2009 [29]. The test setup of the UHPC specimen is shown in Fig. 2(a).

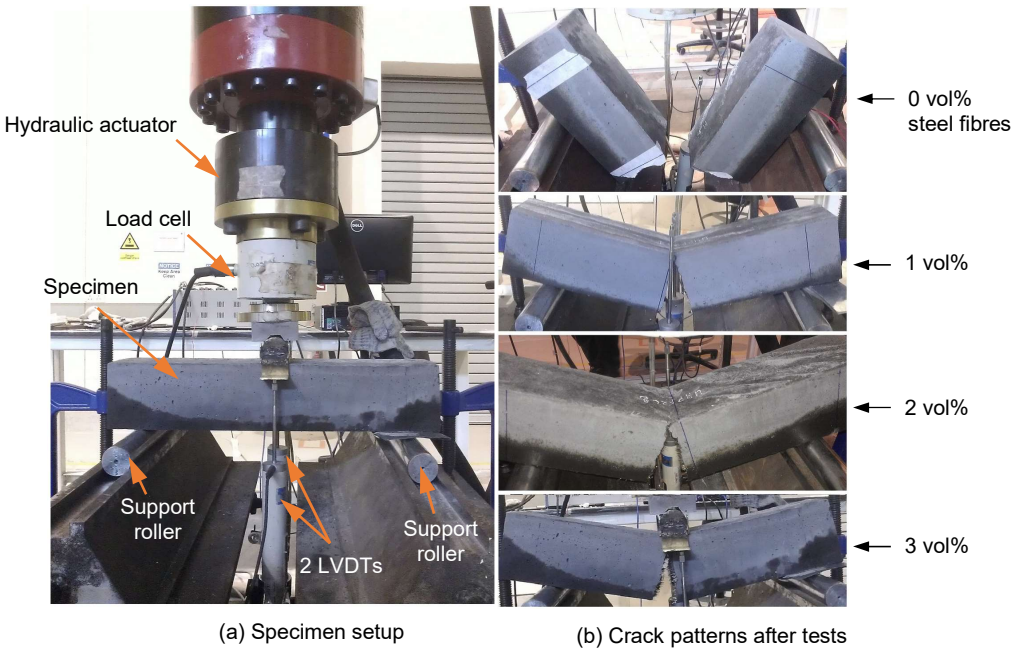

Figure 2: Three-point bending specimen setup and crack pattern results.

As previously mentioned, the effect of steel fibres on the flexural strength of UHPC was studied by adding different amounts of steel fibres to the TM-11 mixture (Table 2). Three volume fractions of steel fibres (1, 2, and 3 vol%) were considered. They are accordingly listed as mixtures UHPC-1, UHPC-2, and UHPC-3 in Table 3. The UHPC with no steel fibres (0 vol%

or UHPC-0) was also provided. Three specimens were prepared for each volume fraction. The specimen using UHPC-3 is referred to as 3-PL-3%. Fig. 2(b) shows examples of the crack patterns observed after the tests. The experimentally obtained load–deflection curves for the specimens made from the UHPC-0, UHPC-1, UHPC-2, and UHPC-3 are presented in Fig. 3. As shown in Fig. 3, increasing the steel fibre content resulted in larger peak loads in the load–deflection curves. Because of the bridging mechanism of steel fibres, the UHPC specimens showed excellent performance in comparison with the UHPC without fibres. The flexural strength σ_f under three-point bending was calculated following BS EN 12390-5-2009 [29] as

$$\sigma_f = \frac{3P_u L}{2bh^2} \tag{1}$$

where P_u is the maximum load, L = 400 mm is the distance between the supports, b = 100 mm is the width of the specimen, and h = 100 mm is the height of the specimen.

Table 3: Mechanical properties of UHPC with different steel fibre contents.

Mixture	Volume fraction of steel fibres (vol%)	Flexural strength (MPa)	Compressive strength (MPa)	
			Cube	Cylinder
UHPC-0 (TM-11)	0	16.65	156.87	125.30
UHPC-1	1	19.53	155.70	119.83
UHPC-2	2	20.75	151.27	145.27
UHPC-3	3	27.37	157.60	138.80

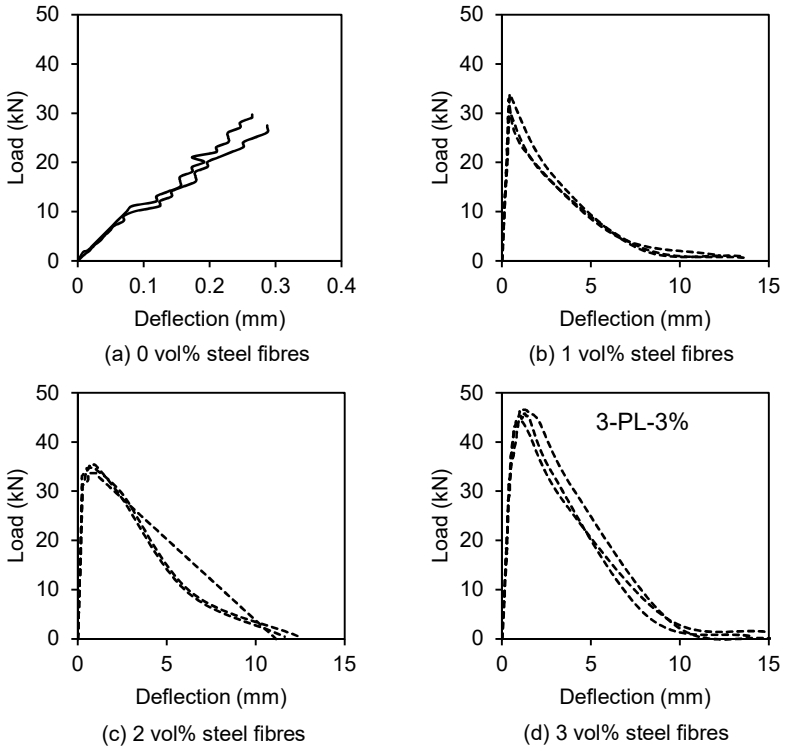

Figure 3: Load–deflection curves obtained from flexural tests.

The average flexural strengths of the specimens with different steel fibre volume fractions are listed in Table 3. The flexural strength is plotted against the volume fraction of steel fibres in

Fig. 4. Kang et al. [5] have reported that the flexural strength is linearly dependent on the volume fraction of steel fibres; the results plotted in Fig. 4 showed this same linear dependence with a high reliability (R^2 = 0.9034).

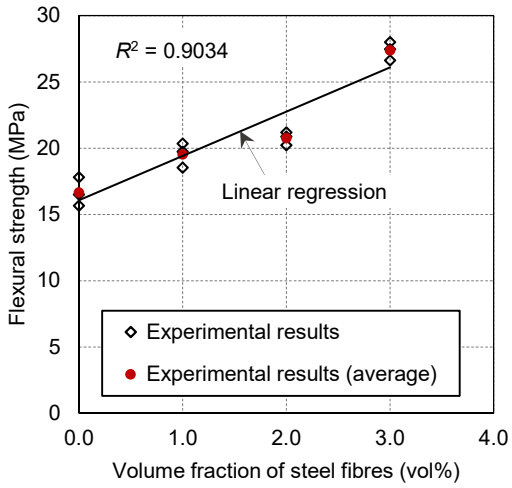

Figure 4: Flexural strength influenced by steel fibre contents.

Additionally, compression tests were conducted using cubic and cylindrical samples. It is known that the steel fibres enhance crack bridging and improve the strength of UHPC. According to Fehling et al. [30], the compressive and tensile strengths increased by approximately 15% and 50%, respectively, with the addition of fibres. The average compressive strengths of the samples with different steel fibre volume fractions are listed in Table 3. From Table 3, the results showed that, similar to the findings in the literature (Hoang and Fehling [31]; Alsalman et al. [32]), the compressive strength associated with the different volume fractions of steel fibres does not significantly increase in comparison to UHPC without steel fibres. Fig. 5 shows typical crack configurations obtained after compression tests. The UHPC without steel fibres demonstrated very brittle and explosive behaviour under compression. When the steel fibres were added, the UHPC showed some post-crack load-carrying capacity, as shown in Fig. 5.

Figure 5: Typical crack patterns obtained after UHPC compression tests.

2.3. Experiments on UHPC flexural members

2.3.1. Specimens and instrumentation

Details of the specimen arrangement and instrumentation for the experiments on the flexural members are depicted in Fig. 6. The experiments were conducted using simply supported UHPC specimens. Two specimens of 1600 mm in length, 300 mm in width, and 100 mm in height were prepared. The first, called NR-UHPC, was constructed only with UHPC through its entire length without longitudinal rebar, and the other, called R-UHPC, was reinforced with five high-tensile steel bars of 12 mm in diameter at the top and bottom as longitudinal rebar, as shown in Fig. 6. The yielding and ultimate strengths of the longitudinal rebar were obtained experimentally as f_y = 501.65 MPa and f_u = 564.68 MPa, respectively. UHPC-3 in Table 3 was used for the flexural members. Additionally, four 100-mm cubes and four cylinders of 100 mm in diameter and 200 mm in height were prepared for compressive strength measurements. The average compressive strengths of the cubes and cylinders were 169 and 153 MPa, respectively. The load cell device was used to record the load, and two linear variable differential transducers (LVDTs) were installed on each flexural member at midspan to measure the vertical deflection. The load–deflection curves were then plotted based on the average of the recordings from the two LVDTs.

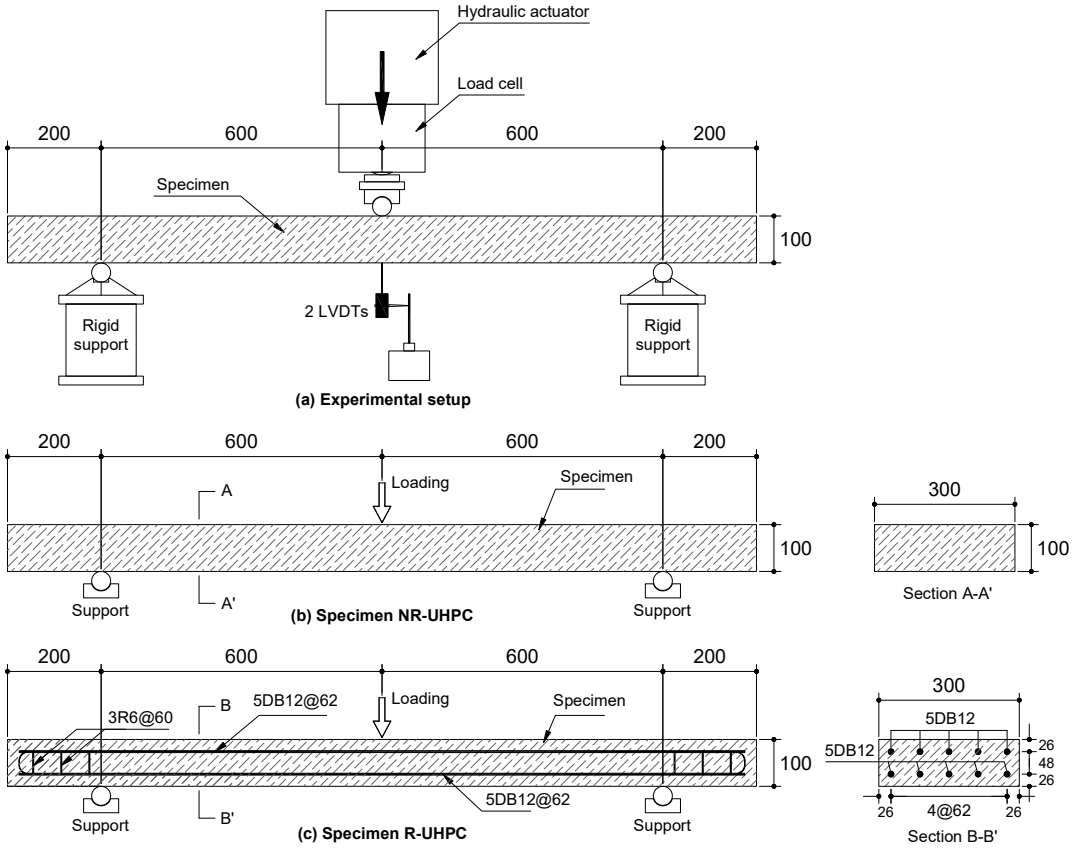

Note:
5DB12: 5 high tensile steel bars of 12 mm in diameter
3R6: 3 mild steel links of 6 mm in diameter installed to avoid anchorage failure at the end supports
[Units: mm]

Figure 6: Experimental setup, instrumentation, and detailed configurations of UHPC flexural members.

2.3.2. Experimental results of flexural members

The load–deflection curves for the flexural members are shown in Fig. 7. NR-UHPC and R-UHPC exhibited ductile behaviour. In addition, with longitudinal rebar, R-UHPC attained an ultimate load of 113 kN, which was 172% greater than that of NR-UHPC.

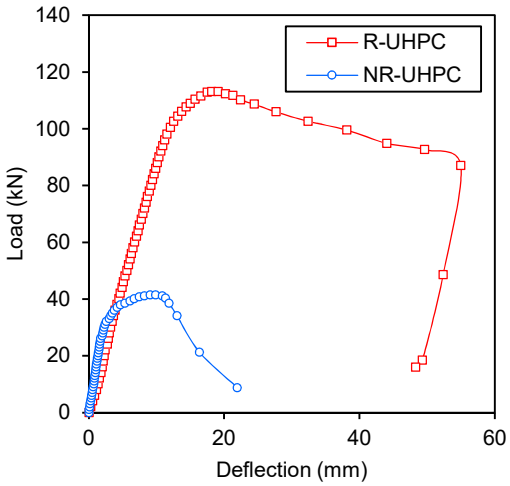

Figure 7: Experimentally obtained load–deflection curves for flexural members.

Fig. 8 illustrates the configurations of the mechanical failures of NR-UHPC and R-UHPC, which failed in rupture and flexural modes, respectively. In NR-UHPC, the UHPC experienced complete fracture, as shown in Fig. 8(a), because of the lack of longitudinal rebar, which resulted in the member being unable to support its own weight at the ultimate load. In contrast, R-UHPC featured a substantial flexural failure with only a single crack pattern at midspan, as shown in Fig. 8(b), as a result of the addition of longitudinal rebar.

(a) NR-UHPC (b) R-UHPC

Figure 8: Final crack patterns of flexural members.

3. Numerical simulation

3.1. FE modelling and conditions

In this study, LS-DYNA (version R8.0) [22] was used to simulate the overall behaviour of UHPC flexural specimens. UHPC was modelled using an eight-node constant-stress solid element. A 10-mm mesh was used unless otherwise indicated. For longitudinal rebar, a two-node beam element was used. A perfect bond was assumed between the longitudinal rebar and the UHPC. The implicit time integration algorithm, which is suitable for static analysis, was used to numerically solve the iterative equations. Default convergence tolerances such as displacement convergence tolerance (= 0.001), energy convergence tolerance (= 0.01), and absolute convergence tolerance (= 10^{-10}) were used in the numerical solutions. A geometric nonlinearity for large displacement range was considered. A loading rate of 2×10^{-5} m/s was adopted. A detailed discussion of the loading rate effect is presented in Section 4.3. Because the experiments used to validate the FE model were performed under static conditions, the dynamic increase factor (DIF) was not considered, except in the case discussed in Section 4.3.

Loading and support boundaries were modelled to represent the actual experimental conditions. Three node sets were created for the loading point and the two supports. The loading was applied directly to the node set, and displacement-controlled loading was used. For the left and right supports, the node sets were restricted in all translational directions and released in the horizontal direction with respect to the longitudinal axis of the specimen, respectively. All nodes for the supports were set to be free in each rotational direction.

3.2. Material model for UHPC

3.2.1. Concrete damage model

In this study, the concrete damage model MAT_72R3 in LS-DYNA was used in the FE analysis to simulate the UHPC behaviour. This concrete model, also known as the Karagozian & Case (K&C) concrete model, was first developed for DYNA3D [33] and is currently available in LS-DYNA as material type 72R3. The model uses three independent strength surfaces: an initial yield surface, a maximum failure surface, and a residual surface. The function of each of these strength surfaces can be expressed as [34]

$$F_i(p) = a_{0i} + \frac{p}{a_{1i} + a_{2i}p} \tag{2}$$

where p is the pressure; F_i is the ith failure surface; and a_{0i}, a_{1i}, and a_{2i} are parameters defining the three-parameter failure surfaces.

For strain hardening and softening, the plasticity surface was obtained as the interpolation between the initial yield and maximum failure surfaces and that between the maximum and residual surfaces, respectively. The plasticity surface interpolation was accomplished by internally scaling the softening and hardening of the variable η, called the yield scale factor, which is determined by a damage function λ. The value of η varies from 0 to 1 depending on the accumulated effective plastic strain measure λ, which is defined as [34]

$$\eta = \eta^L + \frac{\eta^U - \eta^L}{\lambda^U - \lambda^L}\left(\lambda - \lambda^L\right) \tag{3}$$

where $\lambda^L \le \lambda \le \lambda^U$; and η^U and η^L are points corresponding to λ^U and λ^L, respectively, in the (λ, η) input pairs. Here, λ is given as

$$\lambda = \begin{cases} \int_0^{\bar{\varepsilon}_p} \dfrac{d\bar{\varepsilon}_p}{\left(1 + p/rf_t\right)^{b_1}} & p \ge 0 \\ \int_0^{\bar{\varepsilon}_p} \dfrac{d\bar{\varepsilon}_p}{\left(1 + p/rf_t\right)^{b_2}} & p < 0 \end{cases} \tag{4}$$

where $\bar{\varepsilon}_p$ is the effective plastic strain; b_1 and b_2 are the damage parameters for the concrete hardening and softening behaviour, respectively; f_t is the quasi-static concrete tensile strength; and r is the scale factor of the strain rate effects. This scale factor is defined as

$$r = \frac{f'_{c,new}}{f'_{c,old}} \tag{5}$$

where $f'_{c,new}$ is the compressive strength to be modelled and $f'_{c,old}$ is the unconfined compressive strength. From this, the coefficients of the new material failure surfaces are given by $a_{0,new} = a_0 r$, $a_{1,new} = a_1$, and $a_{2,new} = a_2/r$. Further details of the model parameters can be found in the existing literature [23,33,34].

It should be noted that this concrete model in LS-DYNA was employed in two simulation methods. The first is a simple method using automatic parameter generation that requires only the concrete compressive strength f'_c as an input. The other parameters are calculated as functions of f'_c. The second method requires detailed input parameters describing the concrete properties. The second method may pose the difficulty of requiring a variety of data obtained from laboratory tests as model inputs. Thus, the first method has been used by many researchers to investigate the concrete performance [24–27,35]. In this study, a combination of the first and second methods was adopted. The first method was preliminarily conducted to obtain all of the parameters required in the second method. Then, the second method was used to modify the equation of state (EOS). A further description of the combined method is given in Section 4.4.

3.2.2. EOS

An EOS of the tabulated compaction (EOS_8) was employed in the concrete damage model in LS-DYNA. With this EOS, which can capture volumetric hardening, the concrete damage model becomes simple and flexible for use in calibrating the model for UHPC [21,34,36]. EOS_8 is given as a relationship between the pressure P and volumetric strain ε_v as [22]

$$P = C(\varepsilon_v) + \gamma T(\varepsilon_v) E \tag{6}$$

where ε_v is the volumetric strain given by the natural logarithm, C and T are coefficients that are functions ε_v, γ is the ratio of specific heats, and E is the internal energy. Fig. 9 shows the pressure–volumetric strain curve given by EOS_8. The bulk unloading modulus is a function of the volumetric strain. Uploading occurred along the uploading bulk modulus up to the cut-off pressure. Reloading followed the unloading path to the point where uploading began and continued on the loading path. The use of EOS_8 in this study is described in Section 4.4.

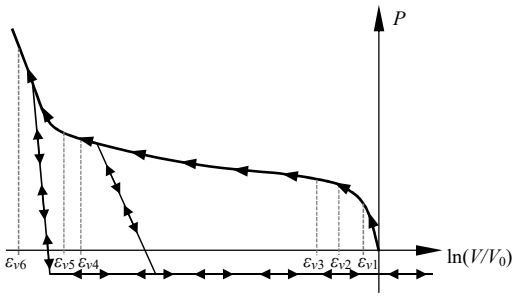

Figure 9: Pressure–volumetric strain curve given by EOS_8 [22].

3.3. Material model for longitudinal rebar

Material model type 3 (MAT_03) in LS-DYNA, which is an elastic–plastic model with kinematic and isotropic hardening, was used to model the longitudinal rebar in this study. A Young's modulus of 200 GPa was adopted for this material. The slope of the bilinear stress–strain curves (tangent modulus) was assumed to be zero, representing perfectly constant stress after yielding. The reliability of this model has been demonstrated in previous works [22,26].

4. Calibration of concrete damage model for UHPC

4.1. Overview

Section 4 focuses on a model calibration technique through the investigation of mesh size sensitivity and the concrete damage model. The use of an EOS and the determination of the concrete damage model parameters are described. Additionally, a study of the strain rate effect on a single mesh element is presented for reference.

4.2. Mesh size

The effect of the mesh size on the behaviour of a single concrete element has been investigated through explicit analysis in previous studies [26,37]. When an inappropriate mesh size is defined, problems with convergence in solving nonlinear equations may arise and cause the FE analysis to terminate prematurely. In this study, compressive and tensile simulations were conducted on an eight-node cubic element with a varying size using implicit analysis. Identical boundary conditions were applied to the model for all cases, and displacement-controlled static loading was applied. A compressive strength of f'_c = 153 MPa was used as an input, and other parameters, such as the tensile strength f_t, softening parameter b_2, and localised crack width w_c, and the EOS were automatically generated using automatic parameter generation with MAT_72R3 in LS-DYNA. The setup of a unit element model is depicted in Fig. 10. Four nodes of an element face were constrained as supports, and the other four nodes were used for the applied load. The results of the single element analysis are shown in Fig. 11, and the stress–strain curves with mesh sizes of 5, 10, and 20 mm size were very similar. With mesh size of 30 mm, the strain softening was accelerated to maintain constant fracture energy [26,34,37]. Therefore, the mesh size from 5 through 20 mm should be used in the numerical simulation.

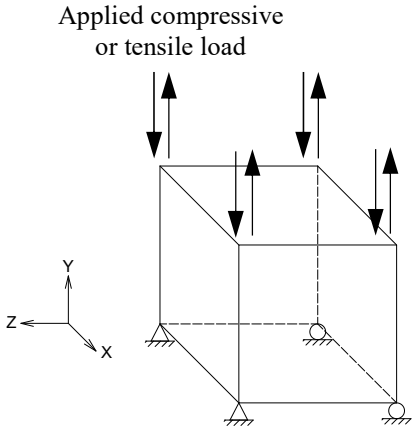

Figure 10: Single-element model setup for compression and tension.

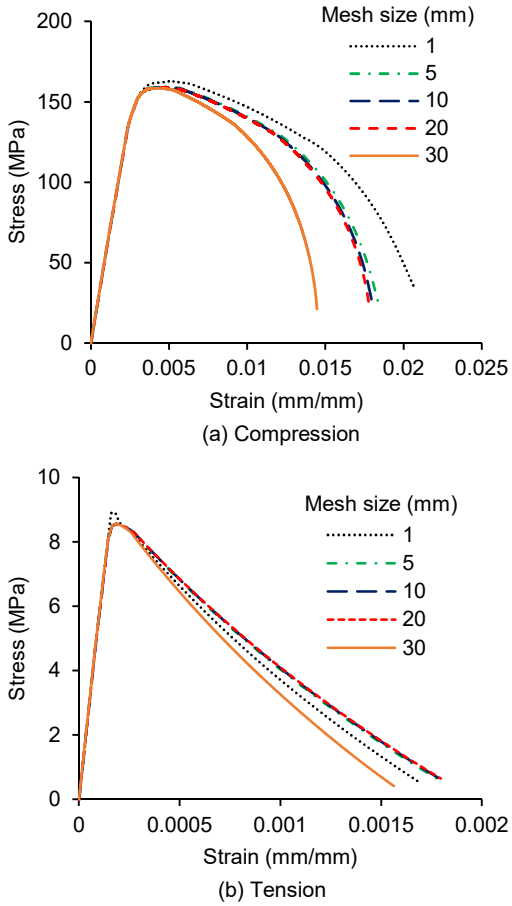

Figure 11: Stress–strain curves of single elements with various mesh sizes.

4.3. Strain rate effect

The DIF is commonly used to enhance the strength through the strain rate effect [38]. Even though no DIF was employed in this study because the experiments used to validate the FE model were performed under static conditions, the effect of the DIF on the single elements was investigated using implicit analysis for reference. The FE simulation model was the same as that described in Section 4.2 (mesh size of 10 mm).

Figs. 12 and 13 show the strain rate effect for the single-element model under various loading rates with and without the DIF taken into consideration, respectively. For comparison, a loading rate applied in the flexural tests (Section 2.2.3) was also used in the simulation. When the DIF was not considered (Fig. 13), the stress–strain response was independent of the load rate. When the DIF was considered (Fig. 12), the ultimate stress increased as the load rate increased. As shown in Fig. 12, the stress–strain curve using a loading rate of 2×10^{-5} m/s was in good agreement with the experimental loading rate of 3.7×10^{-6} m/s. Based on this element analysis, a simulated load rate of 2×10^{-5} m/s was used in this study.

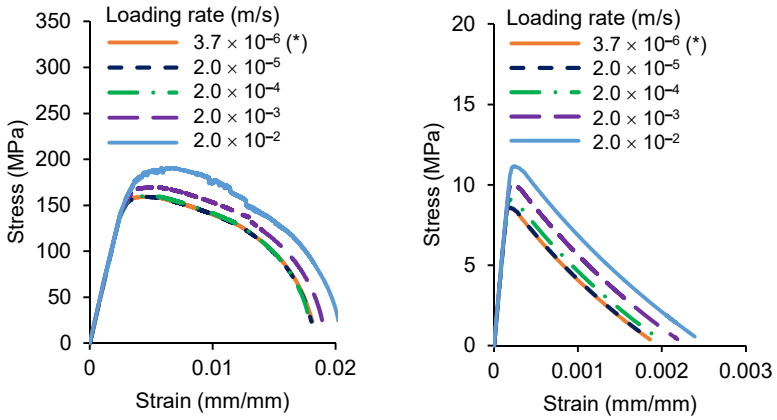

Note: (*): loading rate used in flexural tests (Section 2.2.3).

Figure 12: Stress–strain curves of single elements under various loading rates with DIF taken into consideration.

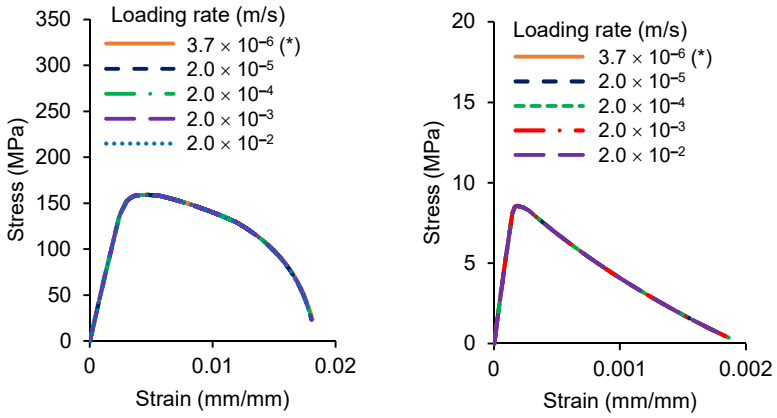

Note: (*): loading rate used in flexural tests (Section 2.2.3).

Figure 13: Stress–strain curves of single elements under various loading rates without DIF taken into consideration.

4.4. Stiffness correction by EOS

The Young's modulus E_c for the concrete damage model is calculated based on the properties of conventional concrete. According to Crawford et al. [23], the empirical equation $E_c = 4700{f'_c}^{0.5}$, where f'_c is the compressive strength in megapascals, is used to determine the Young's modulus for the model. For the Young's modulus E_u of UHPC, Graybeal [39] has proposed a similar equation relating E_u to f'_c as $E_u = 3800{f'_c}^{0.5}$. From these two equations, at a given f'_c value, E_c is greater than E_u. Therefore, to simulate UHPC using the concrete damage model, the Young's modulus should be modified appropriately to reflect its stiffness.

In this study, the initial stiffness of the UHPC was adjusted using the pressure and bulk modulus in the EOS to reflect the modification of Young's modulus E_u. The pressure p calculated from the EOS is given as

$$p = K\varepsilon_v^e \tag{7}$$

where K is the loading or unloading bulk modulus and ε_v^e is the elastic volumetric strain.

This modification was based on a preliminary analysis using automatic parameter generation to obtain the material properties of MAT_72R3 and the details of the EOS from a message output file generated by LS-DYNA. The generated outputs were then manually keyed in as the inputs for the detailed parameter method to apply the UHPC stiffness correction to the EOS. The FE simulation in this section was prepared using a mesh size of 10 mm, a concrete compressive strength of f'_c = 139 MPa, a tensile strength of f_t = 10 MPa, a softening parameter of b_2 = –2, and the localised crack width of w_c = 25.18 mm.

Fig. 14 shows the simulated load–deflection curves and the experimental curve for 3-PL-3% (Section 2.2.3). As shown in Fig. 14, the use of the modified EOS yielded a UHPC initial stiffness similar to that in the experimental results. However, the response from the modified EOS model did not reach the ultimate load achieved in the experiment. The final stage of model calibration was then carried out by further modifying the concrete model parameters, as presented in the following section.

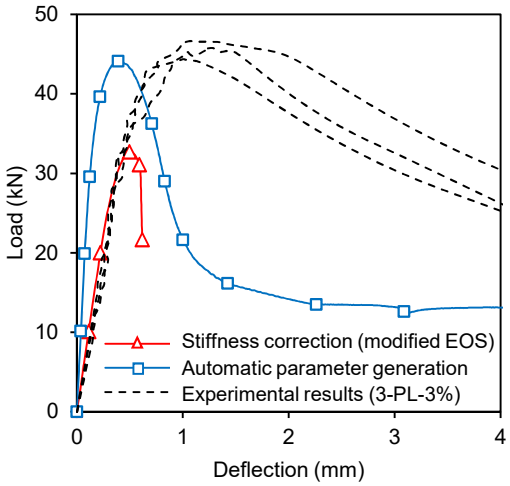

Figure 14: Simulated load–deflection curves obtained using automatic parameter generation and by applying stiffness correction to EOS in comparison to experimental results for 3-PL-3%.

4.5. Determination of model parameters for UHPC

4.5.1. Concrete softening parameter

As shown in Eq. (4), the parameters b_1 and b_2 are employed in the concrete damage model to control the concrete hardening and softening behaviour. Previous studies on specimens with various steel fibre contents [5,40] and different steel fibre lengths [2,3] have demonstrated that the effect of steel fibres is minor when the specimen is under compression but significant under tension. In the present investigation of the effects of b_1 and b_2 in the model developed in this study, changes in the compressive parameter b_1 did not significantly affect the flexural performance of the specimen model whereas changes in the tensile softening parameter b_2 demonstrated a clear effect.

Fig. 15(a) shows load–deflection curves for specimens with different values of b_2 obtained using the numerical FE model. The corresponding experimental curve for 3-PL-3% is plotted for comparison. The ultimate load is plotted against b_2 in Fig. 15(b). Except for the value of b_2,

the FE model parameters were the same as those used in the modified EOS discussed in Section 4.4. As shown in Fig. 15, the simulated curve for b_2 = –6 was initially similar to the experimental curve. However, the simulation did not perform well in the softening part of the curve. Other parameters were derived to model the softening behaviour, as described in the next section.

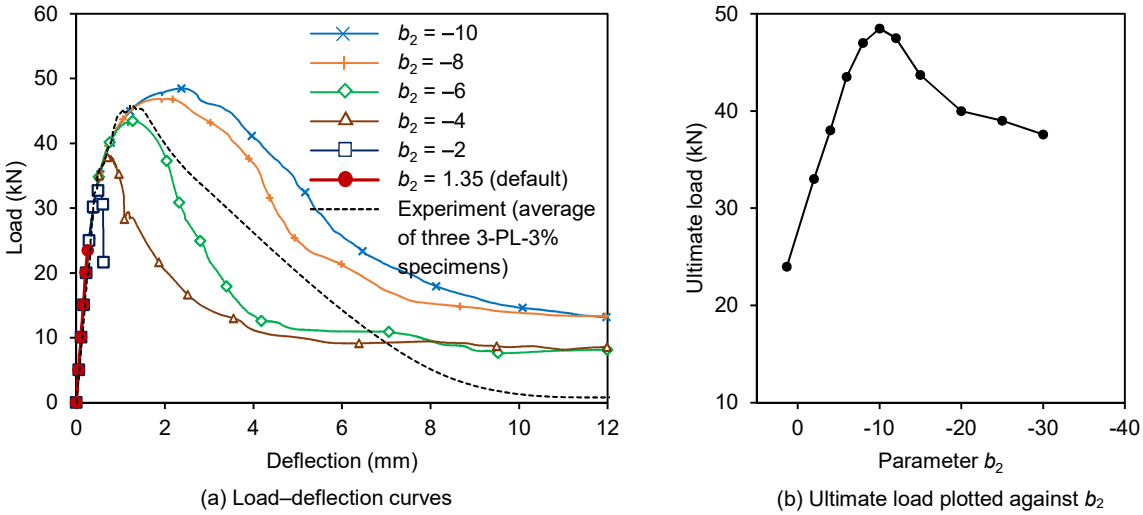

(a) Load–deflection curves

(b) Ultimate load plotted against b_2

Figure 15: Flexural behaviour of three-point bending specimens with different concrete softening parameters b_2.

4.5.2. Localised crack width parameter

The localised crack width w_c was used to eliminate the mesh size dependence in the concrete damage model. The tensile fracture energy under the stress–strain curve can be adjusted by varying w_c. The recommended value of w_c is three times the aggregate size for normal-strength concrete [22]. For UHPC, steel fibres play a more important role in defining the tensile fracture behaviour than do the other fine constituents of UHPC. However, the most appropriate value of w_c for the FE model of UHPC remains unclear. The effect of w_c on the three-point bending specimen 3-PL-3% was investigated, and the results are shown in Fig. 16. Except for the value of w_c, the FE model used in this investigation was the same as that described in Section 4.5.1 with b_2 = –6. As shown in Fig. 16, the flexural strength generally increased as w_c decreased. The load–deflection curve for the model with w_c = 15 mm showed the ultimate load and softening behaviour fairly agreed with the experimental curve.

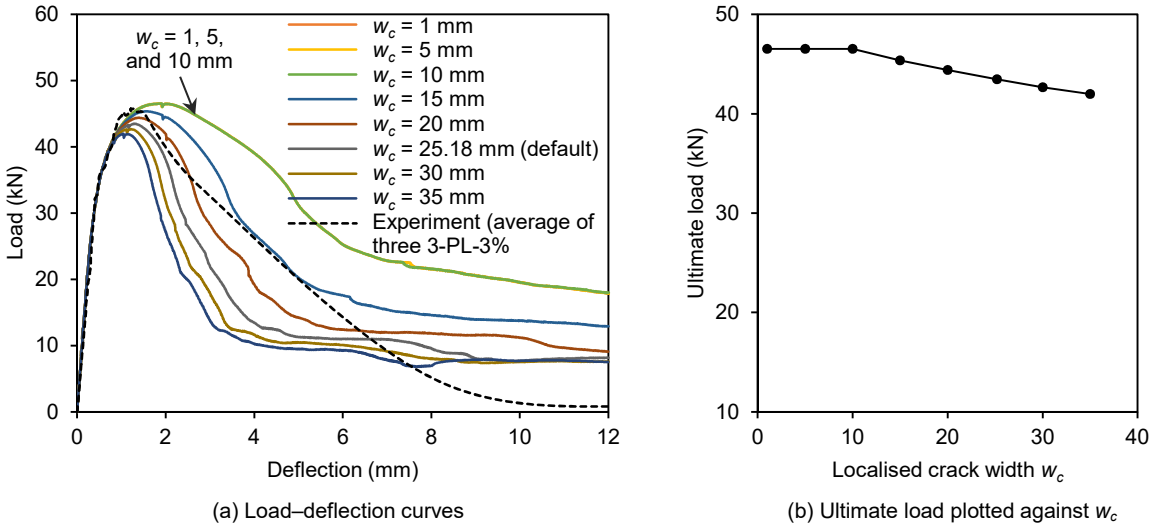

(a) Load–deflection curves (b) Ultimate load plotted against w_c

Figure 16: Flexural strength of three-point bending specimens with different localised crack widths w_c.

4.5.3. Concrete tensile strength

The effect of the tensile strength f_t of the UHPC on the flexural strength of three-point bending specimen 3-PL-3% was then investigated. The load–deflection curves shown in Fig. 17 were obtained using the model described in Section 4.5.2 with w_c = 15 mm and different tensile strengths f_t. Different f_t values can be used to model different steel fibre contents. As shown in Fig. 17, varying f_t significantly affected the flexural strength. Thus, an appropriate value of f_t should be used in the simulation.

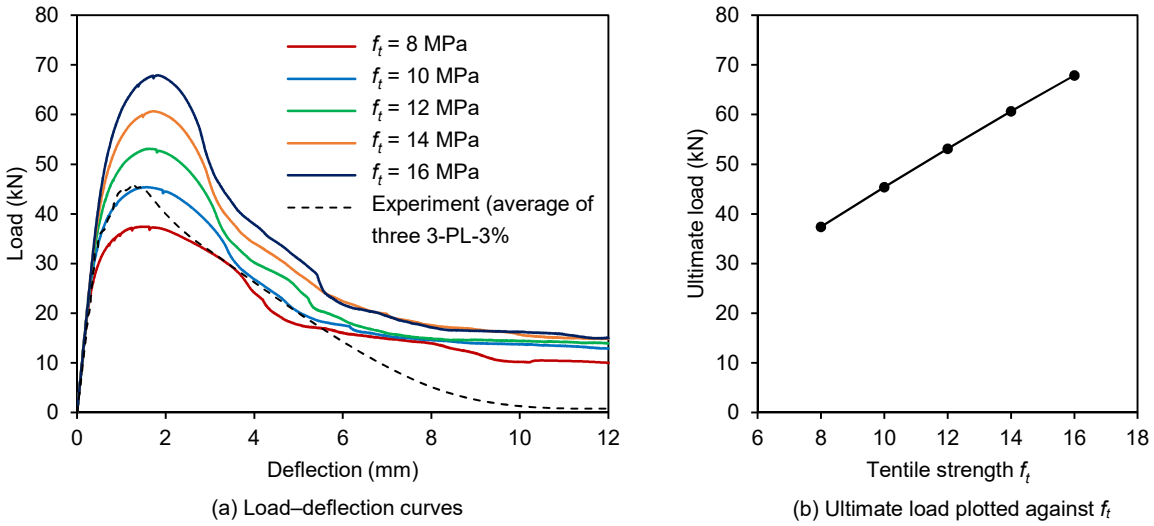

(a) Load–deflection curves (b) Ultimate load plotted against f_t

Figure 17: Flexural strength of three-point bending specimens with different tensile strengths f_t.

5. Validation of FE model

5.1. Database description

The FE model was validated by comparing the simulation results to experimental results obtained from a total of 21 specimens that were tested by the authors or selected from previously

published papers by other researchers. Details of the geometry and material properties of the specimens are summarised in Table 4. Of the 21 specimens, 12 are UHPC specimens without longitudinal rebar, and the remaining 9 are reinforced with longitudinal rebar. All specimens have rectangular cross sections with various dimensions ranging from model scales to full scale.

Table 4: Details of geometry and material properties of specimens.

Specimen	Geometry		UHPC	Steel fibres				Longitudinal rebar		
	$W \times H \times L$ (mm × mm × mm)	a/d	f'_c (MPa)	d_f (mm)	l_f (mm)	f_{yf} (MPa)	V_f (%)	A_s (mm^2)	f_y (MPa)	E_s (GPa)
3-PL-3%†	100 × 100 × 500	2.00	139	0.20	13.0	2300	3.0	-	-	-
NR-UHPC†	300 × 100 × 1600	6.00	153	0.20	13.0	2300	3.0	-	-	-
R-UHPC†	300 × 100 × 1600	8.11	153	0.20	13.0	2300	3.0	565.5	501.6	200
NR-2 [7]	180 × 270 × 2900	4.18	197	0.20	13.0	2500	2.0	-	-	-
R12-2 [7]	180 × 270 × 2900	4.81	191	0.20	13.0	2500	2.0	253.4	445.0	200
R13-2 [7]	180 × 270 × 2900	4.81	192	0.20	13.0	2500	2.0	380.1	445.0	200
R14-2 [7]	180 × 270 × 2900	4.81	196	0.20	13.0	2500	2.0	506.8	445.0	200
R22-1 [7]	180 × 270 × 2900	5.26	191	0.20	13.0	2500	2.0	506.8	445.0	200
R23-2 [7]	180 × 270 × 2900	5.26	196	0.20	13.0	2500	2.0	760.2	445.0	200
UH-N [11]	200 × 270 × 2900	3.89	197	0.20	13.0	2500	2.0	-	-	-
UH-0.35% [11]	200 × 270 × 2900	4.37	197	0.20	13.0	2500	2.0	265.4	522.7	200
UH-1.06% [11]	200 × 270 × 2900	4.37	197	0.20	13.0	2500	2.0	530.9	522.7	200
UH-1.71% [11]	200 × 270 × 2900	4.72	197	0.20	13.0	2500	2.0	796.4	522.7	200
3-PL [14]	145 × 50 × 600	4.56	130	0.20	10.0	2000	5.5	-	-	-
4-PL [14]	145 × 50 × 600	3.04	130	0.20	10.0	2000	5.5	-	-	-
SS20 [2]	100 × 100 × 400	1.00	200	0.20	13.0	2788	2.0	-	-	-
LS10SS00 [2]	100 × 100 × 400	1.00	200	0.30	30.0	2580	1.0	-	-	-
Mixture-1 [41]	150 × 150 × 700	1.33	180	0.15	9.0	2300	2.5	-	-	-
Mixture-2 [41]	150 × 150 × 700	1.33	175	0.15	17.0	2300	1.0	-	-	-
Method-A [42]	125 × 125 × 1000	2.00	217	0.30	20.0	1250	1.0	-	-	-
MF15 [43]	100 × 100 × 400	1.00	150	0.12	15.0	4295	2.5	-	-	-

†: Tested by present authors
Geometries: W, H, and L are specimen width, height, and length, respectively, and a/d is ratio of span-to-effective depth.
UHPC: f'_c is compressive strength.
Steel fibres: d_f, l_f, f_{yf}, and V_f are diameter, length, yield strength, and volume fraction, respectively.
Longitudinal rebar: A_s, f_y, and E_s are area, yield strength, and Young's modulus, respectively.

5.2. FE simulation results

FE simulations were conducted using the method described in Section 3 and with the stiffness correction applied to the EOS, as described in Section 4. A set of calibrated parameters was used for specimens fabricated with the same UHPC material regardless of their size and geometry following the suggestion by Magallanes et al. [21] that a reasonable set of model parameters should be used in a particular UHPC dataset.

The concrete model parameters for each UHPC specimen obtained from the model calibration using the proposed modelling technique are given in Table 5. The mesh size, number of elements, and number of steps employed in the FE model for the three specimen types considered in this study, 3-PL-3%, NR-UHPC, and R-UHPC, and for specimens in previous studies, are given in the corresponding load–deflection curves shown in Fig. 18(a)–(c), and Figs.

20–26, respectively. The following sections compare the results of the FE model against experimental results obtained by the authors and other researchers.

Table 5: Summary of FE model parameters and simulation results.

Authors	Specimen	UHPC model parameters				P_{exp} (kN)	P_{exp}/P_{FEM}	$\Delta_{u,exp}/\Delta_{u,FEM}$
		f'_c (MPa)	f_t (MPa)	b_2	w_c (mm)			
Present authors	3-PL-3%	139	10	–6	13	45.6**	0.99**	0.70**
	NR-UHPC	153	10	–6	13	41.5	1.00	0.97
	R-UHPC	153	10	–6	13	113.0	1.06	1.15
Yang et al. [7]	NR-2	197	14	–6	13	121.7	1.01	1.07
	R12-1	191	14	–6	13	154.0	0.92	1.09
	R13-2	192	14	–6	13	188.6	1.00	1.27
	R14-2	196	14	–6	13	206.8	0.99	1.22
	R22-2	191	14	–6	13	189.4	0.94	0.97
	R23-2	196	14	–6	13	233.0	0.98	1.16
Yoo et al. [11]	UH-N	197	11.4	–6	13	138.1	1.09	0.91
	UH-0.53%	197	11.4	–6	13	186.5	1.04	1.06
	UH-1.06%	197	11.4	–6	13	226.2	0.98	0.95
	UH-1.71%	197	11.4	–6	13	249.5	0.93	0.86
Habel and Gauvreau [14]	3-PL	130	9	–6	25.18*	12.70	0.97	1.07
	4-PL	130	9	–6	25.18*	18.86	1.07	1.15
Kim et al. [2]	SS20	200	15	–6	20	122.2	0.99	0.87
	LS10SS00	200	8	–10	15	73.36	0.98	0.86
Bornemann and Faber [41]	Mixture-1	180	9.5	–4	30	123.4	1.00	0.99
	Mixture-2	175	10	–30	13	127.9	0.97	0.79
Lappa et al. [42]	Method-A	217	17	–5	25.18*	97.4	0.98	1.27
Li et al. [43]	MF15	150	17	–12	35	143.8	1.04	1.12
	Mean						**1.00**	**1.02**

* Default value defined by LS-DYNA
** Average of three specimens

5.2.1. Specimens tested by the authors

Fig. 18 shows the simulated and experimental load–deflection curves for the three specimen types considered in this study: 3-PL-3%, NR-UHPC, and R-UHPC. A good agreement between the simulation and experimental results was observed. The FE model accurately predicted the load–deflection curves throughout the whole loading history for all the specimen types. The simulated peak loads (P_{FEM} = 46.1, 41.5, and 106.6 kN) were approximately equal to the experiments (P_{exp} = 45.6, 41.5, 113.0 kN for specimens 3-PL-3%, NR-UHPC, and R-UHPC, respectively). In addition, the predicted maximum loads occurred at approximately the same deflections as in the tests.

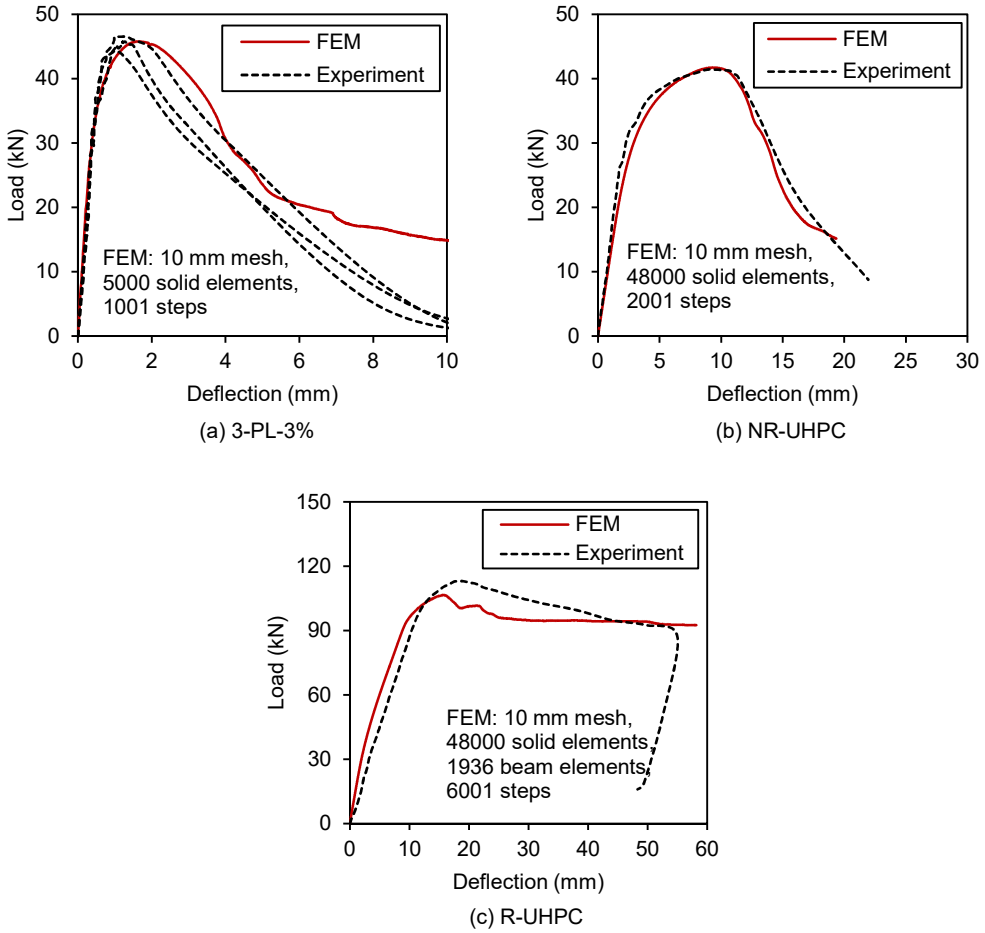

Figure 18: Experimental and simulated load–deflection curves of specimens tested in present study.

Fig. 19 shows a map of the effective plastic strain along the flexural specimen R-UHPC obtained from the FE simulation along with a photograph showing the experimental results of the final crack pattern of the same specimen. The numerical simulation showed a high effective plastic strain at midspan, which roughly agrees with the experimental observation.

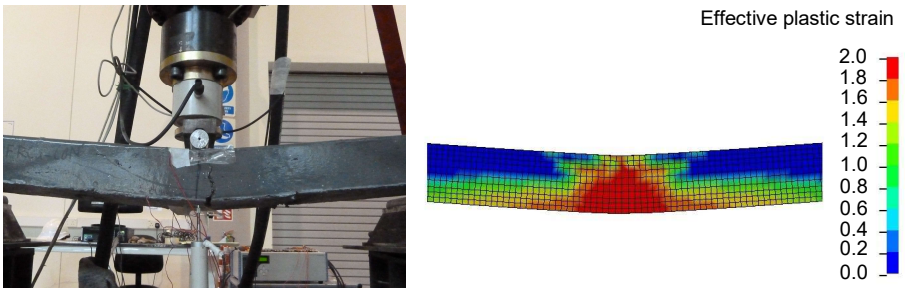

Figure 19: Cracking pattern and effective plastic stain of R-UHPC.

5.2.2. Specimens tested by other researchers

The UHPC flexural specimens tested by Yang et al. [7], Yoo et al. [11], Habel and Gauvreau [14], Kim et al. [2], Bornemann and Faber [41], Lappa et al. [42], and Li et al. [43] were used to validate the developed model. The details of specimens are summarised in Table 4.

Yang et al. [7] studied the effect of longitudinal rebar ratio on the flexural performance of their UHPC beams, in which 13-mm steel fibres were used. Because they did not report the yield strength of the longitudinal rebar, the previously reported strength of 445 MPa [44] was assumed and used in the FE simulation. These beams were considered using the same concrete model parameters b_2 and w_c as in the present study (Table 5). The experimental and numerical results for the load–deflection curves are shown in Fig. 20.

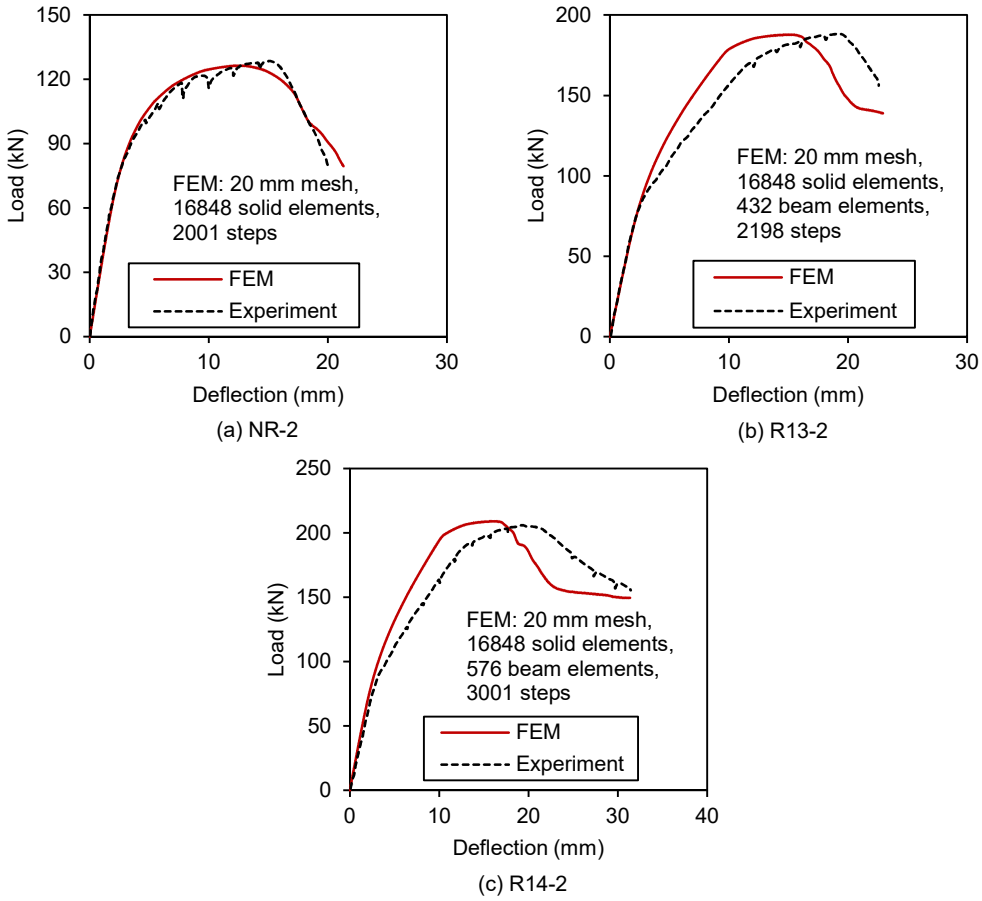

Figure 20: Experimental and simulated load–deflection curves of beams tested by Yang et al. [7].

The beam specimens tested by Yoo et al. [11] were similar those tested by Yang et al. [7]. Because the UHPC mixtures used in these works were almost identical, the set of concrete model parameters used to model the specimens tested by Yoo et al. [11] was chosen to be same as that for the specimens tested by Yang et al. [7]. The numerical results for the load–deflection curves are shown in Fig. 21. Habel and Gauvreau [14] tested UHPC panel specimens without rebar under three- and four-point loading conditions. The load–deflection curves obtained from the FE simulation and those obtained from their experiments are shown in Fig. 22.

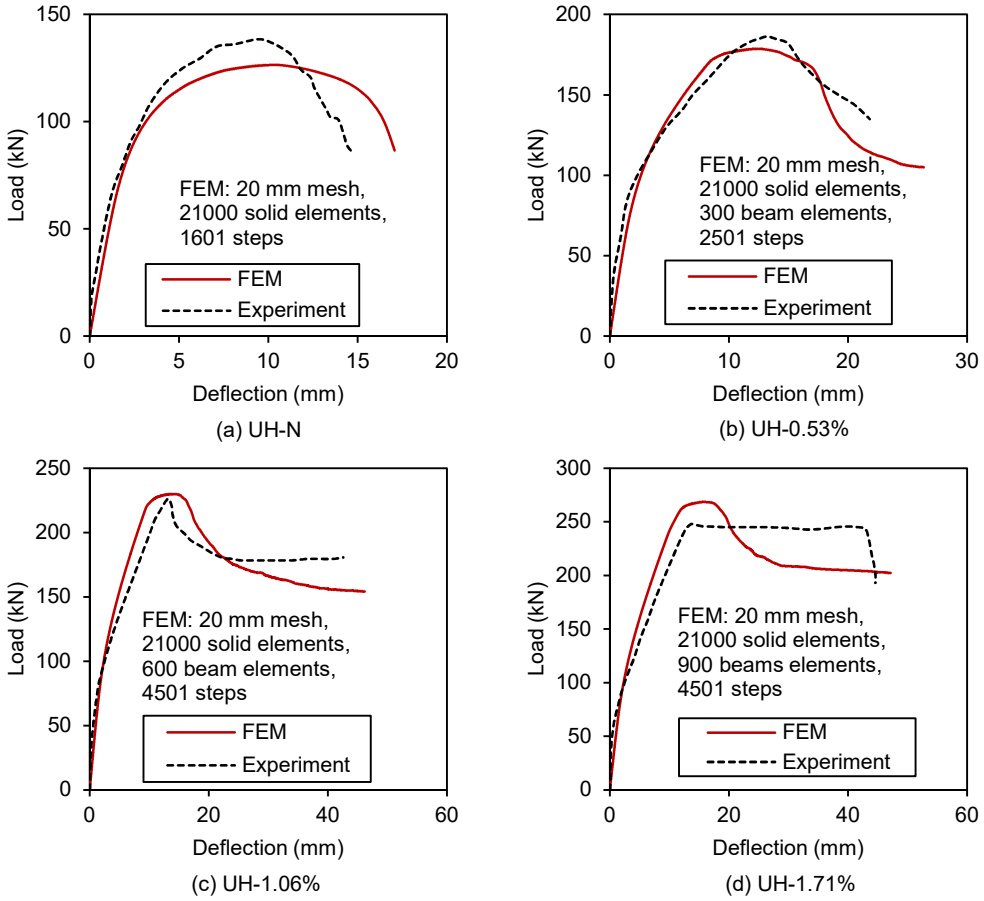

Figure 21: Experimental and simulated load–deflection curves of beams tested by Yoo et al. [11].

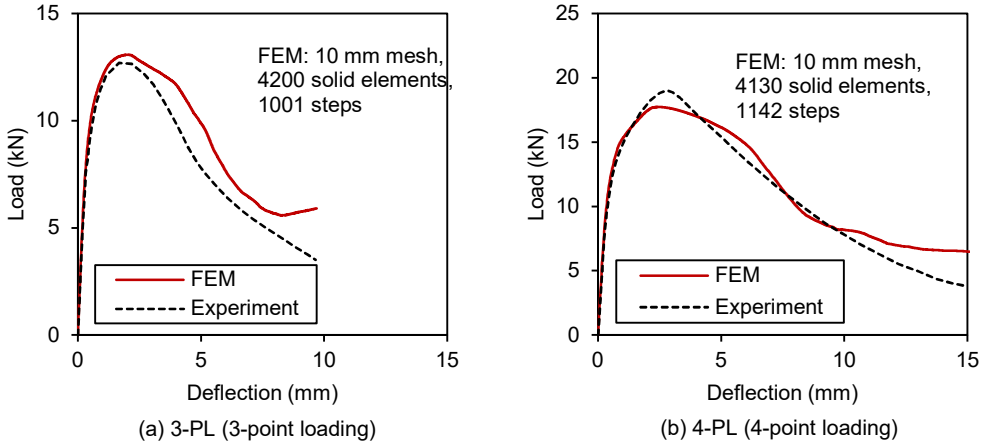

Figure 22: Experimental and simulated load–deflection curves of UHPC panels tested by Habel and Gauvreau [14].

Kim et al. [2], Bornemann and Faber [41], Lappa et al. [42], and Li et al. [43] investigated the flexural strength of standard prisms (Table 4). Kim et al. [2] used short (13 mm) and long (30 mm) steel fibres in two separate specimens (SS20 and LS10SS00). To model the influence of the short and long steel fibres on the UHPC, two sets of model parameters were used, as given in Table 5. Likewise, for the specimens tested by Bornemann and Faber [41], the experimental

results of Mixture-1 (9-mm steel fibres) and Mixture-2 (17-mm steel fibres) showed significantly different behaviours. Therefore, different sets of model parameters were adopted for each mixture. Figs. 23–26 show the experimental and simulated load–deflection curves for the specimens tested by Kim et al. [2], Bornemann and Faber [41], Lappa et al. [42], and Li et al. [43], respectively. As shown in Figs. 20–26, the load–deflection curves obtained using the FE model and modelling technique developed in this study conformed well to the experimental results.

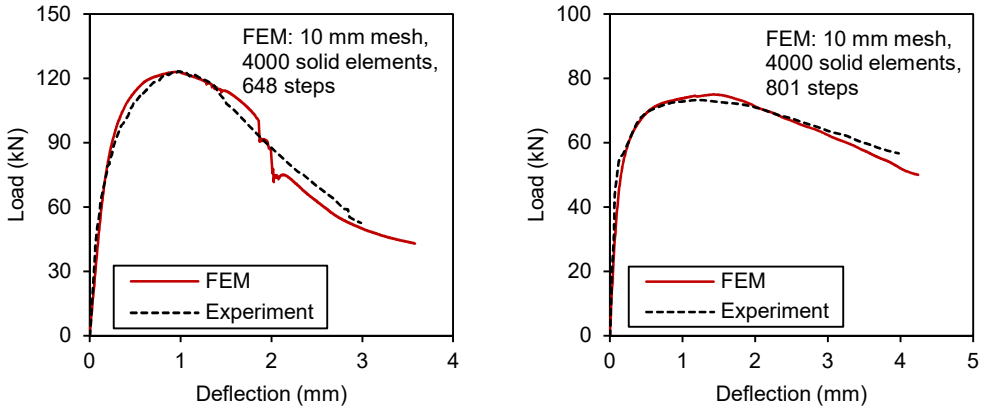

(a) SS20 (13-mm steel fibres) (b) LS10SS00 (30-mm steel fibres)

Figure 23: Experimental and simulated load–deflection curves of flexural specimens tested by Kim et al. [2].

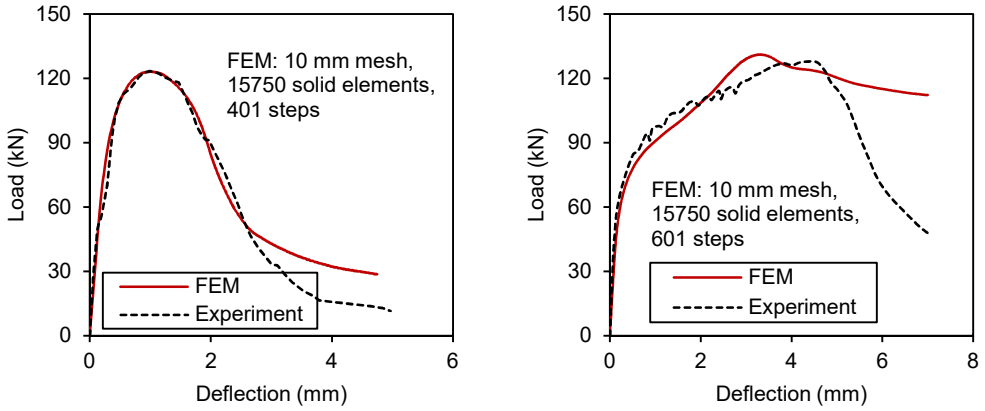

(a) Mixture-1 (9-mm steel fibres) (b) Mixture-2 (17-mm steel fibres)

Figure 24: Experimental and simulated load-deflection curves of flexural specimens tested by Bornemann and Faber [41].

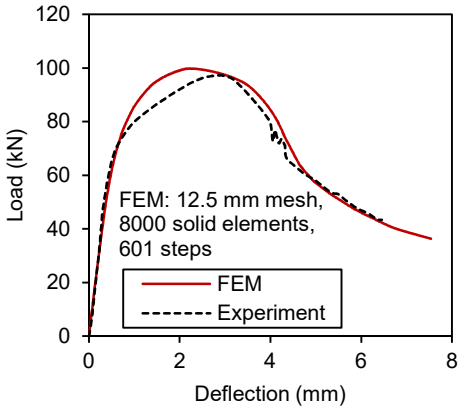

Figure 25: Experimental and simulated load–deflection curves of flexural specimen Method-A tested by Lappa et al. [42].

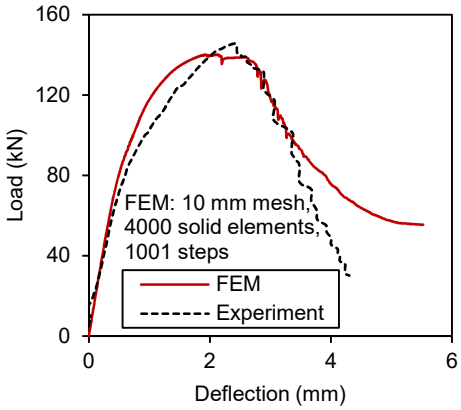

Figure 26: Experimental and simulated load–deflection curves of flexural specimen MF15 tested by Li et al. [43].

5.2.3. Peak load and deflection ratios

The experimental and numerical peak loads P_{exp} and P_{FEM} and the corresponding deflections at midspan $\Delta_{u,exp}$ and $\Delta_{u,FEM}$ were obtained and compared. The experimental-to-numerical peak load ratio P_{exp}/P_{FEM} and the corresponding peak load deflection ratio $\Delta_{u,exp}/\Delta_{u,FEM}$ were calculated, and the results are given in Table 5. From Table 5, for all of the specimens, P_{exp}/P_{FEM} and $\Delta_{u,exp}/\Delta_{u,FEM}$ ranged from 0.92 to 1.09 and from 0.70 to 1.27, respectively. Overall, good agreement was obtained between the numerical and experimental results, with mean P_{exp}/P_{FEM} and $\Delta_{u,exp}/\Delta_{u,FEM}$ values of 1.00 and 1.02, respectively. Fig. 27(a) and (b) show the numerical results plotted against the experimental results for the peak load and the corresponding midspan deflection, respectively. As shown in Fig. 27(a), the peak load results showed a very good distribution along the target line representing $P_{FEM} = P_{exp}$. For the midspan deflection at the peak load (Fig. 27(b)), although the results did not lie along the target line representing $\Delta_{u,FEM} = \Delta_{u,exp}$, almost all of the data points fell within the $\Delta_{u,FEM} = \Delta_{u,exp} \pm 20\%$ bounds, which indicates fair agreement.

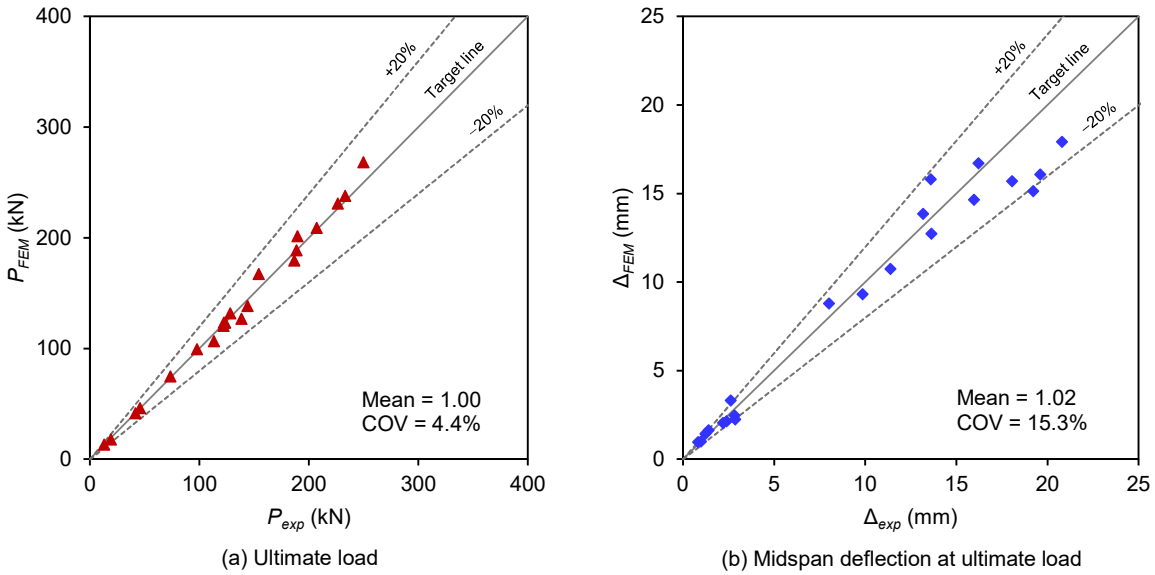

Figure 27: Simulation results obtained using proposed technique plotted against corresponding experimental results.

6. Conclusions

In this study, a finite element modelling for predicting the behaviour of UHPC flexural members was developed and validated. The concrete damage material model MAT_72R3, which is a plasticity-based concrete model, and an implicit solver in LS-DYNA were used in the numerical simulation. The present FE model and modelling technique were developed by calibrating the parameters to yield accurate predictions. This calibration included an initial stiffness correction through the modification of the EOS and the determination of the influential parameters of the concrete damage model; these parameters were found to be the tensile softening parameter b_2 and the localised crack width w_c.

The proposed FE model was validated by applying it to 21 UHPC specimens tested in this study and in previous works. Characteristics of the simulated load–deflection curves, including the ultimate strength, deflection at peak load, stiffness, and hardening and softening behaviours, were found to be in good agreement with those of the experimental curves. Furthermore, the influence of the length of the reinforcing steel fibres on the flexural behaviour of specimens was successfully predicted by adjusting b_2 and w_c. Regardless of the size and geometry of the specimen, a set of calibrated values of b_2 and w_c could be effectively employed for specimens made from the same UHPC mixture. In addition, the effective plastic strain patterns obtained using the numerical model were in good agreement with the cracking patterns observed in the experiments. These results demonstrate the effectiveness and adequacy of the developed FE model and modelling technique.

Acknowledgements

The authors would like to acknowledge financial support from Yayasan Universiti Teknologi PETRONAS Fundamental Research Grant (YUTP-FRG) Cycle 1/2013 (Malaysia), which was used to conduct experiments that contributed to this paper. Financial support was also provided by the Toda Scholarship Foundation 2017 Research Grant (Japan).

References

[1] Richard P, Cheyrezy M. Composition of reactive powder concretes. Cem Concr Res 1995;25(7):1501-11.

[2] Kim DJ, Park SH, Ryu GS, Koh KT. Comparative flexural behavior of hybrid ultra high performance fiber reinforced concrete with different macro fibers. Constr Build Mater 2011;25(11):4144-55.

[3] Park JJ, Yoo DY, Park GJ, Kim SW. Feasibility of reducing the fiber content in ultra-high-performance fiber-reinforced concrete under flexure. Mater 2017;10(2):118.

[4] Yoo DY, Kang ST, Yoon YS. Enhancing the flexural performance of ultra-high-performance concrete using long steel fibers. Compos Struct 2016;147:220-30.

[5] Kang ST, Lee Y, Park YD, Kim JK. Tensile fracture properties of an ultra high performance fiber reinforced concrete (UHPC) with steel fiber. Compos Struct 2010;92(1):61-71.

[6] Kang ST, Lee BY, Kim JK, Kim YY. The effect of fibre distribution characteristics on the flexural strength of steel fibre-reinforced ultra high strength concrete. Constr Build Mater 2011;25(5):2450-57.

[7] Yang IH, Joh C, Kim BS. Structural behavior of ultra high performance concrete beams subjected to bending. Eng Struct 2010;32(11):3478-87.

[8] Graybeal BA. Characterization of the behavior of ultra-high performance concrete. PhD thesis. University of Maryland, USA; 2005.

[9] Graybeal BA. Flexural behavior of an ultrahigh-performance concrete I-girder. J Bridge Eng 2008;13(6):602-10.

[10] Voo YL, Poon WK, Foster SJ. Shear strength of steel fiber-reinforced ultrahigh-performance concrete beams without stirrups. J Struct Eng 2010:136(11):1393-400.

[11] Yoo DY, Banthia N, Yoon YS. Experimental and numerical study on flexural behavior of ultra-high-performance fiber-reinforced concrete beams with low reinforcement ratios. Can J Civil Eng 2017:44(1):18-28.

[12] Yoo DY, Yoon YS. Structural performance of ultra-high-performance concrete beams with different steel fibers. Eng Struct 2015;102:409-23.

[13] Fujikake K, Senga T, Ueda N, Ohno T, Katagiri M. Study on impact response of reactive powder concrete beam and its analytical model. J Adv Concr Technol 2006;4(1):99-108.

[14] Habel K, Gauvreau P. Response of ultra-high performance fiber reinforced concrete (UHPFRC) to impact and static loading. Cem Concr Compos 2008;30(10):938-46.

[15] Yoo DY, Banthia N, Kim SW, Yoon YS. Response of ultra-high-performance fiber-reinforced concrete beams with continuous steel reinforcement subjected to low-velocity impact loading. Compos Struct 2015;126:233-45.

[16] Ngo T, Mendis P, Krauthammer T. Behavior of ultrahigh-strength prestressed concrete panels subjected to blast loading. J Struct Eng 2007;133(11):1582-90.

[17] Wu C, Oehlers D, Rebentrost M, Leach J, Whittaker A. Blast testing of ultra-high performance fibre and FRP-retrofitted concrete slabs. Eng Struct 2009;31(9):2060-69.

[18] Yi NH, Kim JHJ, Han TS, Cho YG, Lee JH. Blast-resistant characteristics of ultra-high strength concrete and reactive powder concrete. Constr Build Mater 2012;28(1):694-707.

[19] Li J, Wu C, Hao H. An experimental and numerical study of reinforced ultra-high performance concrete slabs under blast loads. Mater Des 2015;82:64-76.

[20] Singh M, Sheikh A, Ali MM, Visintin P, Griffith M. Experimental and numerical study of the flexural behaviour of ultra-high performance fibre reinforced concrete beams. Constr Build Mater 2017;138:12-25.

[21] Magallanes J, Wu Y, Crawford J, Morrill K. Feasibility studies of a plasticity-based constitutive model for ultra-high performance fiber-reinforced concrete. In: Int Symp: Military Aspects of Blast and Shock. Jerusalem, Israel; 2010.
[22] LS-DYNA Keyword User's Manual, Version R8.0, LSTC, Livermore, CA; 2015.
[23] Crawford J, Wu Y, Magallanes J, Choi H, Lan S. Use and validation of the release III K&C concrete material model in LS-DYNA. Karagozian & Case: Glendale; 2012.
[24] Adhikary SD, Li B, Fujikake K. Dynamic behavior of reinforced concrete beams under varying rates of concentrated loading. Int J Impact Eng 2012;47:24-38.
[25] Li J, Hao H. Numerical study of concrete spall damage to blast loads. Int J Impact Eng 2014;68:41-55.
[26] Lin X, Zhang YX, Hazell PJ. Modelling the response of reinforced concrete panels under blast loading. Mater Des 2014;56:620-28.
[27] Mao L, Barnett S, Begg D, Schleyer G, Wight G. Numerical simulation of ultra high performance fibre reinforced concrete panel subjected to blast loading. Int J Impact Eng 2014;64:91-100.
[28] Yin H, Teo W, Shirai K. Experimental investigation on the behaviour of reinforced concrete slabs strengthened with ultra-high performance concrete. Constr Build Mater 2017;155:463-74.
[29] BS EN 12390-5. Testing hardened concrete. Part 5: Flexural strength of test specimens. British Standards Institution; 2009.
[30] Fehling E, Leutbecher T, Bunje K. Design relevant properties of hardened ultra high performance concrete. In: Int Symp Ultra High Performance Concrete 2004. p. 327-38.
[31] Hoang AL, Fehling E. Influence of steel fiber content and aspect ratio on the uniaxial tensile and compressive behavior of ultra high performance concrete. Constr Build Mater 2017;153:790-806.
[32] Alsalman A, Dang CN, Prinz GS, Hale WM. Evaluation of modulus of elasticity of ultra-high performance concrete. Constr Build Mater 2017;153:918-28.
[33] Malvar LJ, Crawford JE, Wesevich JW, Simons D. A plasticity concrete material model for DYNA3D. Int J Impact Eng 1997;19:847-73.
[34] Magallanes JM, Wu Y, Malvar LJ, Crawford JE. Recent improvements to release III of the K&C concrete model. In: 11th International LS-DYNA Users Conference 2010;1(3). p. 37-48. LSTC, Livermore, CA.
[35] Chen W, Hao H, Chen S. Numerical analysis of prestressed reinforced concrete beam subjected to blast loading. Mater Des 2015;65:662-74.
[36] Markovich N, Kochavi E, Ben-Dor G. An improved calibration of the concrete damage model. Finite Elem Anal Des 2011;47(11):1280-90.
[37] Li J, Zhang YX. Evolution and calibration of a numerical model for modelling of hybrid-fibre ECC panels under high-velocity impact. Compos Struct 2011;93(11):2714-22.
[38] Malvar LJ, Ross CA. Review of strain rate effects for concrete in tension. ACI Mater J 1998;95(6):735-39.
[39] Graybeal BA. Material property characterization of ultra-high performance concrete. Federal Highway Administration; 2006.
[40] Hassan A, Jones S, Mahmud G. Experimental test methods to determine the uniaxial tensile and compressive behaviour of ultra high performance fibre reinforced concrete (UHPFRC). Constr Build Mater 2012;37:874-82.
[41] Bornemann R, Faber S. UHPC with steel-and non-corroding high-strength polymer fibres under static and cyclic loading. In: Int Symp Ultra High Performance Concrete 2004. p. 673-81.
[42] Lappa ES, Braam CR, Walraven JC. Static and fatigue bending tests of UHPC. In: Int Symp Ultra High Performance Concrete 2004. p. 449-59.

[43] Li J, Wu C, Hao H, Su Y. Investigation of ultra-high performance concrete under static and blast loads. Int J Protect Struct 2015;6:217-35.
[44] Yang IH, Joh C, Lee JW, Kim BS. Torsional behavior of ultra-high performance concrete squared beams. Eng Struct 2013;56:372-83.

Chapter IV

Paper III

Numerical model for predicting the structural response of composite UHPC–concrete members considering the bond strength at the interface

The content of this Chapter IV has been submitted for consideration for publication as follows.

Hor Yin, Kazutaka Shirai, Wee Teo, "Numerical model for predicting the structural response of composite UHPC–concrete members considering the bond strength at the interface," Composite Structures, (submitted date: 25 April 2018, submitted).

Numerical model for predicting the structural response of composite UHPC–concrete members considering the bond strength at the interface

Abstract

In this study, an improved finite element (FE) model was developed for the prediction of the structural behaviour of reinforced concrete members strengthened with ultrahigh-performance concrete (UHPC). A concrete damage model and an implicit solver in LS-DYNA were adopted in the numerical simulation. The model was calibrated and validated using experimental data. Accurately representing the interfacial bond characteristics of composite UHPC–concrete members was the primary challenge in developing the modelling technique. A novel technique using equivalent beam elements at the interface between UHPC and normal strength concrete (NSC) substrate was proposed for this purpose. The material properties of the equivalent beam elements were defined to represent the equivalent bond characteristics of NSC. The developed FE model was found to be able to effectively and efficiently predict the structural response of composite UHPC–concrete members with good accuracy.

Keywords: Ultrahigh-performance concrete (UHPC); UHPC strengthening; Interfacial bond strength; Finite element modelling; LS-DYNA

1. Introduction

Strengthening reinforced concrete (RC) structures with ultrahigh-performance concrete (UHPC) is an emerging technique for the design and protection of new or existing structures because of the superior mechanical properties of UHPC, including its high strength, low permeability, and energy absorption [1]. In addition, UHPC has shown high bond strength and good adherence to normal-strength concrete (NSC) substrates [2–4]. Over the past decade, several experimental studies on the behaviour of members strengthened with UHPC have been conducted. UHPC has been applied to existing RC members through either in-situ casting or the use of epoxy adhesive (in the case of prefabricated UHPC layers); after they have been strengthened, the members have been shown to achieve enhanced structural performance as composite members [4–11].

The interfacial bonding behaviour of composite UHPC–concrete members has been reported through experimental investigation [6–8,11]. Local failures such as the de-bonding and/or fracture of UHPC in the interface zone can cause the premature failure of composite members [7,8]. According to Habel et al. [11], the bond between NSC and UHPC is stronger than the tensile strength of NSC at the level of the longitudinal rebar of the RC members. Noshiravani and Brühwiler [7] have reported that the structural resistance of composite UHPC–concrete members depends on the bonding conditions in the interaction between the three materials in tension (longitudinal rebar, UHPC, and NSC). Denarié et al. [6] have shown that the bonding mechanism between NSC and UHPC is more efficient in terms of energy dissipation than the mechanism in the cracking of RC members. Al-Osta et al. [4] conducted tests and reported that no de-bonding was observed but horizontally fine cracks appeared near the interface. Yin et al. [8] used UHPC as patch material for repairing deteriorated concrete members. The strengthened specimens failed in flexure, and no de-bonding occurred. When they used UHPC overlaid onto soffits of RC members, all the specimens failed in shear, and de-bonding was observed after the tests. The investigations in these previous studies [4,6–8,11] demonstrate that the strength of the bond between NSC and UHPC is a crucial factor in the performance of the composite.

Studies on the behaviour of composite UHPC–concrete members using the finite element (FE) method, which is an effective tool for numerical simulations, have been very limited in the past [4,10,12,13]. Sadouki et al. [12] conducted the two-dimensional (2D) FE modelling of the response of the composite UHPC–concrete beams tested by Noshiravani and Brühwiler [7]. The simulation results showed good agreement with the experimental results. Lampropoulos et al. [13], Al-Osta et al. [4], and Safdar et al. [10] predicted the behaviour of composite UHPC–concrete members using three-dimensional (3D) FE analysis. In the study by Lampropoulos et al. [13], the bond interface was modelled by adopting a friction coefficient of 1.5 and a cohesion of 1.9 MPa for a well-roughened substrate, but no experimental data for UHPC–concrete members were used to validate their model. The simulation of UHPC–concrete members was conducted and compared only to the results for beams strengthened with conventional RC layers. Al-Osta et al. [4] and Safdar et al. [10] conducted FE simulations of the behaviour of the composite members under the assumption of a perfect bond at the NSC–UHPC interface. This simplification might result in the overestimation of the ultimate capacity of the composite members. However, none of the above-mentioned studies on the FE method addressed the interfacial bond characteristics between NSC and UHPC in FE model or validated the model with test data for composite UHPC–concrete members.

The main objective of the present study was to develop a 3D FE model with the bond strength between UHPC and NSC taken into account for the prediction of the behaviour of composite UHPC–concrete members using the non-linear FE software LS-DYNA [14]. The remainder of this paper is organized as follows. First, the experimental data used to validate the FE model, which were previously obtained by the present authors [8] and other researchers, are described. Second, the FE model and the material models adopted for the non-composite RC and UHPC members are presented. Next, the model development process is presented. A concrete damage model in LS-DYNA was used for both NSC and UHPC. The non-composite analysis was developed in preparation for the analysis of composite members. To model composite UHPC–concrete members, three analysis cases were simulated and compared. In two of these cases, the bond strength was neglected by assuming a perfectly bonded or unbonded interface between the NSC and UHPC. The third case is the proposed method, and it employs a novel modelling technique using equivalent beam elements at the NSC–UHPC interface to consider the bonding characteristics for composite UHPC–concrete members. Finally, the simulation results are validated and discussed.

2. Description of specimens

This section briefly describes the experimental specimens used to validate the FE model developed in the present study. A total of 17 specimens consisting of non-composite members and composite UHPC–concrete members were used.

Nine slab specimens with various composite UHPC–concrete configurations were tested by Yin et al. [8] under the three-point loading system shown in Fig. 1(a). Two of them were non-composite members (Fig. 1(b)); specifically, slabs RE-0 and RE-100 were composed solely of NSC and UHPC, respectively. Details of the geometry and material properties of the non-composite specimens are given in Table 1. The remaining seven specimens were composite UHPC–concrete slabs designed to investigate the application of UHPC in the tension zone as additional UHPC overlays or as a patch material for rehabilitation of concrete structures (Fig. 1(c)). At the time the composite specimens were constructed, the NSC surface was roughened using a chisel and hammer before the UHPC was cast to create a good bond interface. Details of the geometry and material properties of the composite UHPC–concrete specimens are

summarised in Table 2. Each slab was 1600 mm long with a clear span of 1200 mm. All slabs had five 12-mm-diameter high tensile steel bars at the top and bottom, except for two UHPC-overlay-strengthened slabs with five additional 10-mm diameter high-tensile-strength steel bars in the UHPC layer (slabs OV-25a and OV-50a). No transverse shear reinforcement was provided; however, to avoid anchorage failure at the end supports, three 6-mm-diameter mild steel links were installed.

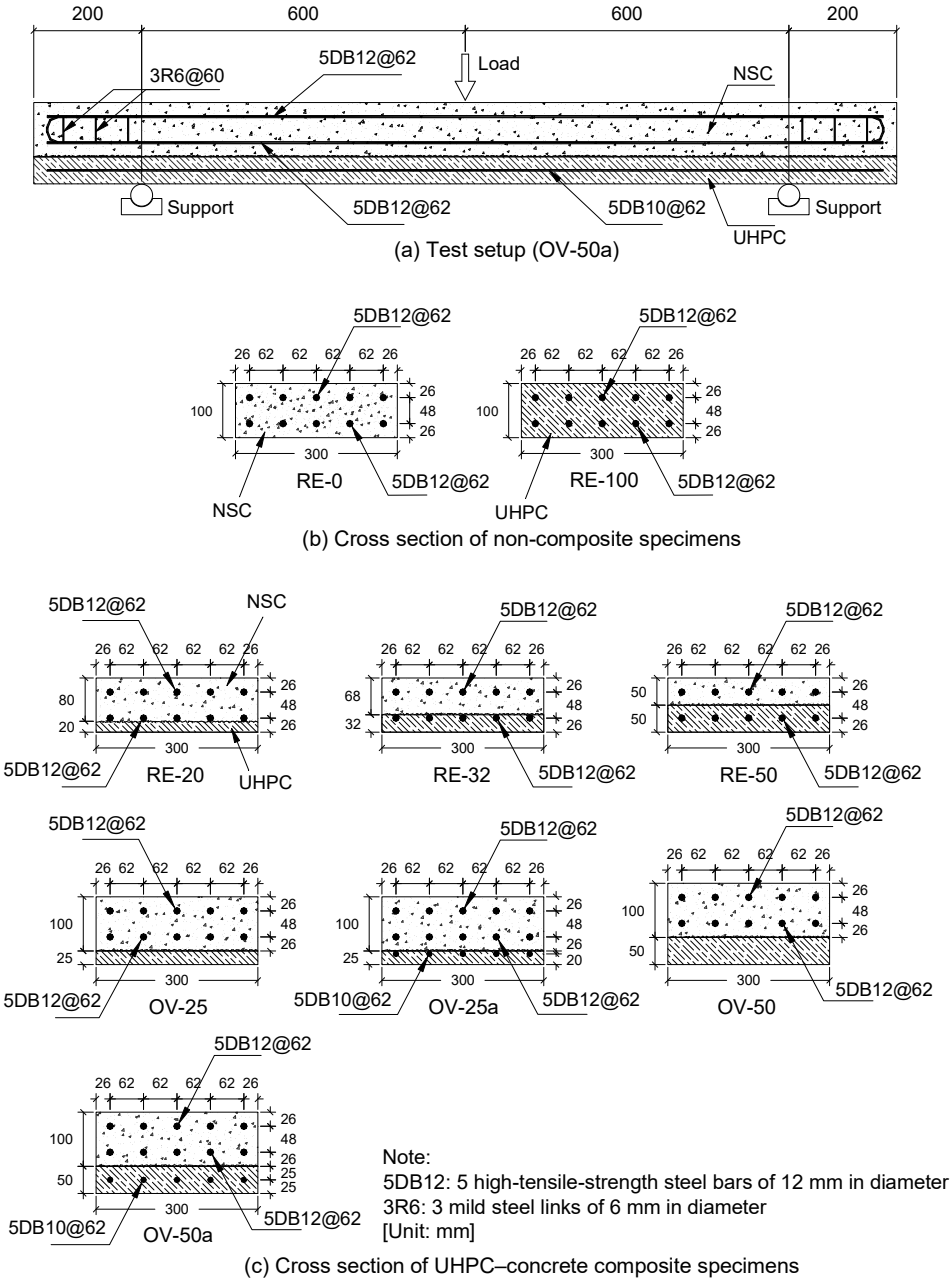

Figure 1: Detailed geometry of UHPC–concrete specimens [8].

In addition, for the non-composite members, eight additional numerical models of UHPC beams tested by Yang et al. [15] and Yoo et al. [16] were used, as listed in Table 1. It should be noted that Yang et al. [15] did not report the yield strength of the longitudinal rebar; therefore, the previously reported strength of 445 MPa [17] was assumed in the FE simulation.

Table 1: Geometric and material details of the non-composite specimens.

Authors	Specimen	Geometry			NSC	UHPC	Longitudinal rebar	
		b (mm)	h (mm)	a/d	f'_c (MPa)	f'_c (MPa)	A_s (mm^2)	f_y (MPa)
Yin et al. [8]	RE-0	300	100	8.11	23	–	565.5	501.6
	RE-100	300	100	8.11	–	153	565.5	501.6
Yang et al. [15]	R12-1	180	270	4.81	–	191	253.4	445.0
	R13C-1	180	270	4.81	–	192	380.1	445.0
	R14-2	180	270	4.81	–	196	506.8	445.0
	R22-2	180	270	5.26	–	191	506.8	445.0
	R23-2	180	270	5.26	–	196	760.2	445.0
Yoo et al. [16]	UH-0.53%	200	270	4.37	–	197	265.4	522.7
	UH-1.06%	200	270	4.37	–	197	530.9	522.7
	UH-1.71%	200	270	4.72	–	197	796.4	522.7

b: Width of specimens
h: Total height of specimens
a/d: Span-to-effective depth ratio
f'_c: Compressive strength of NSC or UHPC
A_s: Area of longitudinal rebar
f_y: Yield strength of longitudinal rebar

Table 2: Geometric and material details of the composite UHPC–concrete specimens.

Authors	Specimen	Geometry				NSC	UHPC	Longitudinal rebar			
		b (mm)	h (mm)	h_U (mm)	a (mm)	f'_c (MPa)	f'_c (MPa)	A_s (mm^2)	$f_{y,s}$ (MPa)	A_{sU} (mm^2)	$f_{y,sU}$ (MPa)
Yin et al. [8]	RE-20	300	100	20	600	23	153	565.5	501.6	–	–
	RE-32	300	100	32	600	23	153	–	–	565.5	501.6
	RE-50	300	100	50	600	23	153	–	–	565.5	501.6
	OV-25	300	125	25	600	23	153	565.5	501.6	–	–
	OV-25a	300	125	25	600	23	153	565.5	501.6	392.7	474.9
	OV-50	300	150	50	600	23	153	565.5	501.6	–	–
	OV-50a	300	150	50	600	23	153	565.5	501.6	392.7	474.9

b: Width of specimens
h: Total height of specimens
h_U: UHPC thickness
a: Distance from support to loading point
f'_c: Compressive strength of NSC or UHPC
A_s: Area of longitudinal rebar in NSC
$f_{y,s}$: Yield strength of longitudinal rebar in NSC
A_{sU}: Area of longitudinal rebar in UHPC
$f_{y,sU}$: Yield strength of longitudinal rebar in UHPC

3. Finite element modelling of non-composite members

3.1. Modelling and conditions

Section 3 describes the modelling method for the non-composite specimens shown in Table 1. In the present study, LS-DYNA [14] (version R8.0) was used to simulate the overall response of composite UHPC–concrete specimens. A full-scale 3D model was prepared for each specimen. NSC and UHPC were modelled using eight-node solid elements. For the longitudinal rebar in the specimens, two-node beam elements were used. A perfect bond was assumed between the longitudinal rebar and the concrete. A mesh size of 10 mm was used for the slab specimens previously tested by the present authors [8], and a mesh size of 20 mm was used for the beam specimens tested by Yang et al. [15] and Yoo et al. [16]. These mesh sizes were

determined through convergence investigation to ensure the model can yield good predictions. The overall configuration of the FE model is shown in Fig. 2.

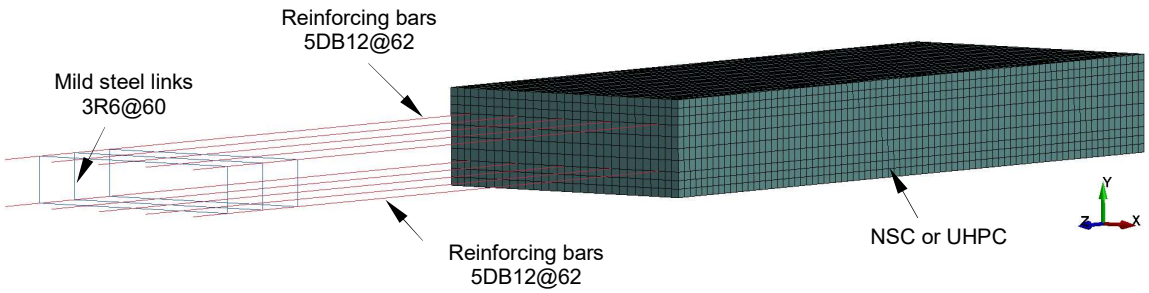

Figure 2: Overall FE model (RE-0 or RE-100).

Support boundaries were modelled using simply supported conditions, as in the experiments. The nodes of the left support of each specimen were restricted in all translational directions, and those of the right support were allowed to move freely in the horizontal direction with respect to the longitudinal axis of the specimen. All nodes were free in the rotational directions.

Implicit analysis, which is suitable for static loading conditions, was used to numerically solve the iterative equation. A loading rate of 2×10^{-5} m/s was adopted for quasi-static loading. The load was applied directly to the nodes, and displacement-controlled loading was used. Because the experiments used to validate the FE model were performed under static conditions, the strain rate effect was not considered.

3.2. Concrete material model

The concrete damage model Mat-72r3 in LS-DYNA was used in the FE analysis to simulate the behaviour of both NSC and UHPC in the present study. The reliability of the concrete model Mat-72r3 has been previously reported [18,19]. This concrete model, also known as the Karagozian & Case (K&C) concrete model, was first developed for DYNA3D [20]. In Release III of the K&C model, an automatic input capability was added, and this model is currently available in LS-DYNA as material type 72r3. The major advantage of the model is that it requires a single parameter, the unconfined compressive concrete strength f'_c, as an input. The remaining parameters are automatically generated using a built-in algorithm and can also be modified by the user. A brief overview of the concrete damage model is presented in the following sections.

3.2.1. Strength surfaces

The concrete damage model is a plasticity-based constitutive model for concrete using three independent strength surfaces: an initial yield surface, a maximum failure surface, and a residual surface. The function of each of these strength surfaces can be expressed as [20]

$$\Delta\sigma_y = a_{0y} + \frac{p}{a_{1y} + a_{2y}p} \tag{1}$$

$$\Delta\sigma_m = a_{0m} + \frac{p}{a_{1m} + a_{2m}p} \tag{2}$$

$$\Delta\sigma_r = \frac{p}{a_{1r} + a_{2r} p} \tag{3}$$

where p is the pressure; and $\Delta\sigma_y$, $\Delta\sigma_m$, and $\Delta\sigma_r$ are the initial yield, maximum failure, and residual surfaces, respectively. The eight parameters (a_{0i}, a_{1i}, a_{2i}) define the three-parameter failure surfaces.

The failure surface $\Delta\sigma$ for the deviatoric stresses, which is based on the second invariant of the deviatoric stress, is defined as

$$\Delta\sigma = \sqrt{3J_2} \tag{4}$$

where $J_2 = (s_1^2 + s_2^2 + s_3^2)/2$ is the second invariant of the deviatoric stress; and s_1, s_2, and s_3 are the principal deviatoric stresses.

The plasticity surface representing the strain hardening after it reaches the yield surface is obtained as the interpolation between the initial yield and maximum failure surfaces, which is given by

$$\Delta\sigma = \eta\left(\Delta\sigma_m - \Delta\sigma_y\right) + \Delta\sigma_y \tag{5}$$

Similarly, the post-failure surface for strain softening is defined as the interpolation between the maximum failure and residual surfaces as

$$\Delta\sigma = \eta\left(\Delta\sigma_m - \Delta\sigma_r\right) + \Delta\sigma_r \tag{6}$$

The surface interpolation is accomplished by internally scaling the softening and hardening of the variable η, called the yield scale factor, which is determined from the damage function λ as

$$\lambda = \begin{cases} \displaystyle\int_0^{\overline{\varepsilon_p}} \frac{d\overline{\varepsilon_p}}{\left(1 + p/f_t\right)^{b_1}} & p \geq 0 \\ \displaystyle\int_0^{\overline{\varepsilon_p}} \frac{d\overline{\varepsilon_p}}{\left(1 + p/f_t\right)^{b_2}} & p < 0 \end{cases} \tag{7}$$

where $\overline{\varepsilon_p}$ is the effective plastic strain, b_1 and b_2 are the damage parameters for the concrete hardening and softening behaviour, respectively, and f_t is the quasi-static concrete tensile strength.

The value of η varies from 0 to 1 depending on the accumulated effective plastic strain parameter λ. A series of (η, λ) pairs was used as inputs in LS-DYNA. As shown in Fig. 3, η begins at 0 at $\lambda = 0$, increases to 1 at some damage function value $\lambda = \lambda_m$ (maximum), and then decreases to 0 at some larger value of λ. When $\lambda \leq \lambda_m$, the current surface is obtained as the interpolation between the initial yield and maximum failure surfaces. For $\lambda > \lambda_m$, the surface is obtained as the interpolation between the maximum and residual surfaces.

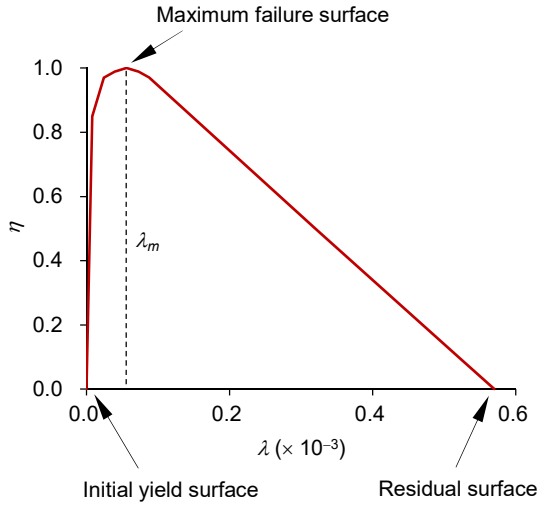

Figure 3: Plot of λ–η relationship.

3.2.2. Equation of state

An equation of state (EOS) of the tabulated compaction was employed in the concrete damage model. With this EOS, which can capture volumetric hardening, the concrete damage model becomes simple and flexible for use in calibrating the model for UHPC [20]. The EOS is given as the relationship between the pressure P and volumetric strain ε_v as [14]

$$P = C(\varepsilon_v) + \gamma T(\varepsilon_v) E \tag{8}$$

where ε_v is the volumetric strain given by the natural logarithm, C and T are coefficients that are functions of ε_v, γ is the specific heat ratio, and E is the internal energy.

3.2.3. Determination of model parameters

As described in Section 3.2.1, the concrete damage model contains a number of parameters to express the concrete behaviour. According to Eqs. (1)–(3), the eight parameters (a_{0i}, a_{1i}, a_{2i}) should be determined through unconfined and triaxial compression tests over a range of confining pressures [20].

However, in the present study, the model parameters were not defined using the properties of actual concrete because of insufficient test data. In Release III of the concrete damage model (Mat-72r3 in LS-DYNA), two simulation methods are available. The first is a simple method using automatic parameter generation that requires only the concrete compressive strength f'_c as an input and calculates the other parameters as functions of f'_c. The second method requires detailed input parameters describing the concrete properties, posing the difficulty of requiring a variety of data obtained from laboratory tests as model inputs. In the present study, a combination of the first and second methods was adopted. The first method was preliminarily conducted by inputting f'_c to obtain all of the other parameters required in the second method. Then, the second method was carried out to modify the EOS. The initial stiffness of the members was adjusted based on the pressure and bulk modulus in the EOS to reflect the modification of Young's modulus of concrete. The pressure p calculated from the EOS is given as

$$p = K\varepsilon_v \tag{9}$$

where K is the loading or unloading bulk modulus and ε_v is the elastic volumetric strain.

The parameters b_1 and b_2 in Eq. (7) are employed in the concrete damage model to control the concrete hardening and softening behaviour. Although the details are omitted here, from an investigation of the effects of b_1 and b_2 in the model developed in the present study, similar to findings in [21], changes in the compressive softening parameter b_1 did not significantly affect the flexural performance of the specimen model, whereas changes in the tensile softening parameter b_2 demonstrated a clear effect. Based on this, the default value of b_1 (= 1.6) was used, and b_2 was modified from its default value (b_2 = 1.35) and set to −10 and −25 to reflect the actual behaviour of NSC and UHPC, respectively.

Table 3: Material properties used in the FE model for specimens tested by Yin et al. [8].

Component (element)	Description	Value of model parameters
NSC (solid)	Material type 72r3 (MAT_CONCRETE_DAMAGE_REL3)	–
	Density (kg/m^3)	2200
	Poisson's ratio	0.19
	Compressive strength (MPa)	23
	Tensile strength (MPa)	3
	Tensile softening parameter b_2	−10
	Localised crack width w_c (mm)	25.18†
UHPC (solid)	Material type 72r3 (MAT_CONCRETE_DAMAGE_REL3)	–
	Density (kg/m^3)	2200
	Poisson's ratio	0.19
	Compressive strength (MPa)	153
	Tensile strength (MPa)	10.5
	Tensile softening parameter b_2	−25
	Localised crack width w_c (mm)	13
Longitudinal rebar (beam)	Material type 03 (MAT_PLASTIC_KINEMATIC)	–
	Density (kg/m^3)	7830
	Poisson's ratio	0.3
	Young's modulus (GPa)	200
	Yield strength (MPa)	501.6 for DB12 475.0 for DB10
Equivalent beam elements for bond interface (beam)	Material type 03 (MAT_PLASTIC_KINEMATIC)	–
	Density (kg/m^3)	2200
	Poisson's ratio	0.19
	Young's modulus (GPa)	Equivalent Young's modulus of NSC
	Yield strength (MPa)	Equivalent maximum bond strength (τ_{max} = 0.55 MPa [22])
Note: †: Default value in LS-DYNA		

The localised crack width parameter w_c is used to eliminate the mesh size dependence in the concrete damage model. The tensile fracture energy under the stress–strain curve can be adjusted by varying w_c. The recommended value of w_c is three times the aggregate size for NSC [14]. For UHPC, steel fibres play a more important role in defining the tensile fracture behaviour than do the other fine constituents of UHPC. However, the optimal value of w_c for the FE model of UHPC remains unclear. In the present study, values of w_c = 25.18 mm (default) and 13 mm were adopted in the NSC and UHPC models, respectively. The parameters of the concrete damage model used for the specimens tested by the present authors are listed in Table 3.

3.3. Material model for longitudinal rebar

Material model type 3 (Mat-03) in LS-DYNA, which is an elastic–plastic model with kinematic and isotropic hardening, was used to model the longitudinal rebar in the present study. A Young's modulus of 200 GPa was adopted for this material. The slope of the bilinear stress–strain curves (tangent modulus) was assumed to be zero, representing perfectly constant stress after yielding. The properties used to model the longitudinal rebar were the same as those used in the authors' previous study [8] and are given in Table 3.

4. Modelling of composite UHPC–concrete members

4.1. Numerical model of perfectly bonded interface

Section 4 describes the modelling method for the composite UHPC–concrete specimens listed in Table 2. As previously mentioned, three analytical cases for the bond interface between NSC and UHPC were considered. Case 1 is the case of a perfectly bonded interface, which was considered to investigate the response of the specimens when UHPC is ideally bonded to the NSC substrate. Case 2 is the case of a perfectly unbonded interface, which was used for reference. Case 3 demonstrates the application of the newly proposed model using equivalent beam elements to consider the bond strength at the interface. The same parameters used for the non-composite members described in Section 3 were adopted for all three analytical cases.

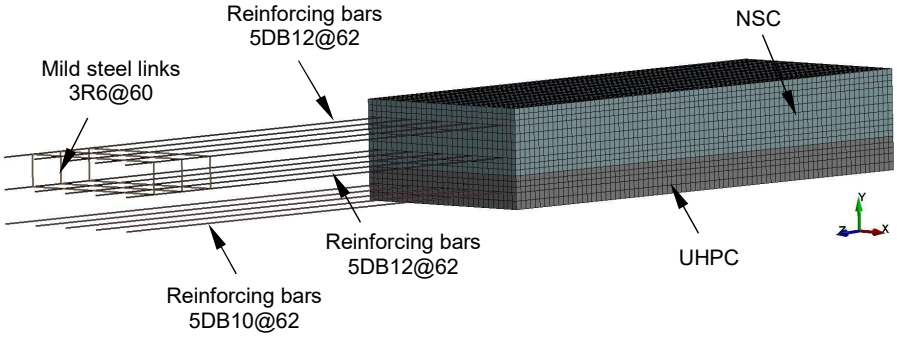

Figure 4: Layout of FE model, Case 1 (OV-50a).

In Case 1, a perfectly bonded interface between the NSC and UHCP of the composite UHPC–concrete specimens was assumed, and shared nodes were adopted at the interface. Except for the interface, the FE models used in Case 1 were the same as those described in Section 3. Fig. 4 illustrates the configuration of the FE model for Case 1. Details of the perfect bonding assumption are shown in Fig. 5(a) and (b).

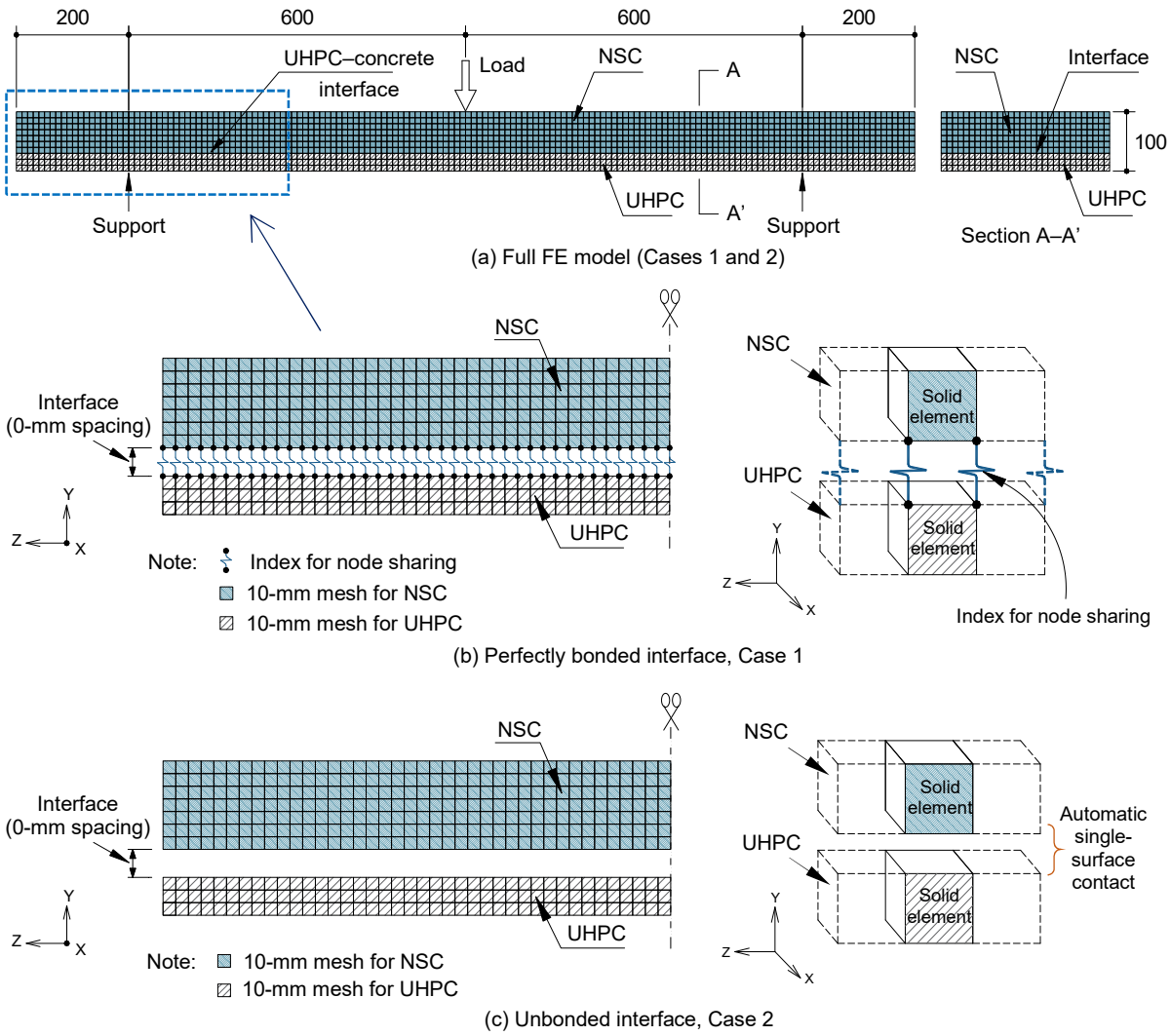

Figure 5: Details of perfectly bonded and unbonded interface models.

4.2. Numerical model of unbonded interface

In Case 2, a perfectly unbonded interface between the NSC and UHPC of the composite UHPC–concrete specimens was adopted, and the nodes at the interface were not shared. Except for the interface, the FE models used in Case 2 were the same as those described in Section 3. To avoid element penetration between NSC and UHPC, the penalty-based automatic single-surface contact algorithm in LS-DYNA was employed at the interface. The modelling details of the unbonded interface are shown in Fig. 5(a) and (c).

4.3. Numerical model considering the bond strength at the interface

4.3.1. Modelling the bond interface

In Case 3, a modelling technique using equivalent beam elements at the NSC–UHPC interface was proposed to assess the interfacial bond strength for composite UHPC–concrete members. Instead of a friction or cohesive element at the interface [13], equivalent beam elements were adopted for stability in the FE simulation. The application of this modelling technique is simple. Equivalent beam elements were created along the longitudinal direction of the specimens

through each node at the interface, and no transverse equivalent beam elements were provided. As in Case 2, Case 3 also used the automatic single-surface contact algorithm to prevent element penetration at the interface. The overall FE configuration with the proposed equivalent beam elements is shown in Fig. 6, and the modelling details are shown in Fig. 7. The FE model described in Section 3 was implemented to model the UHPC and NSC members. The equivalent beam elements were modelled using Mat-03 (Section 3.3) to provide elastic–plastic characteristics.

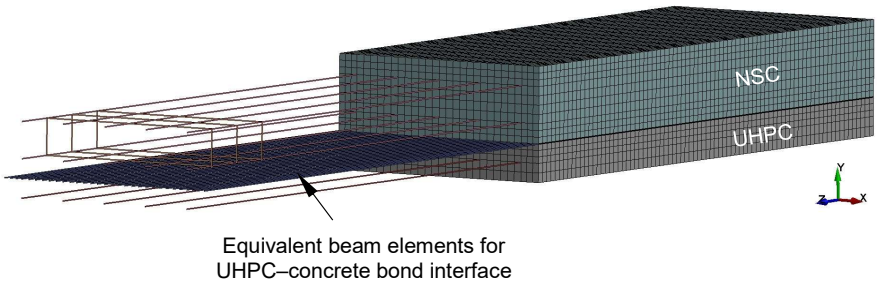

Figure 6: Illustration of equivalent beam elements for modelling bond strength, Case 3 (OV-50a).

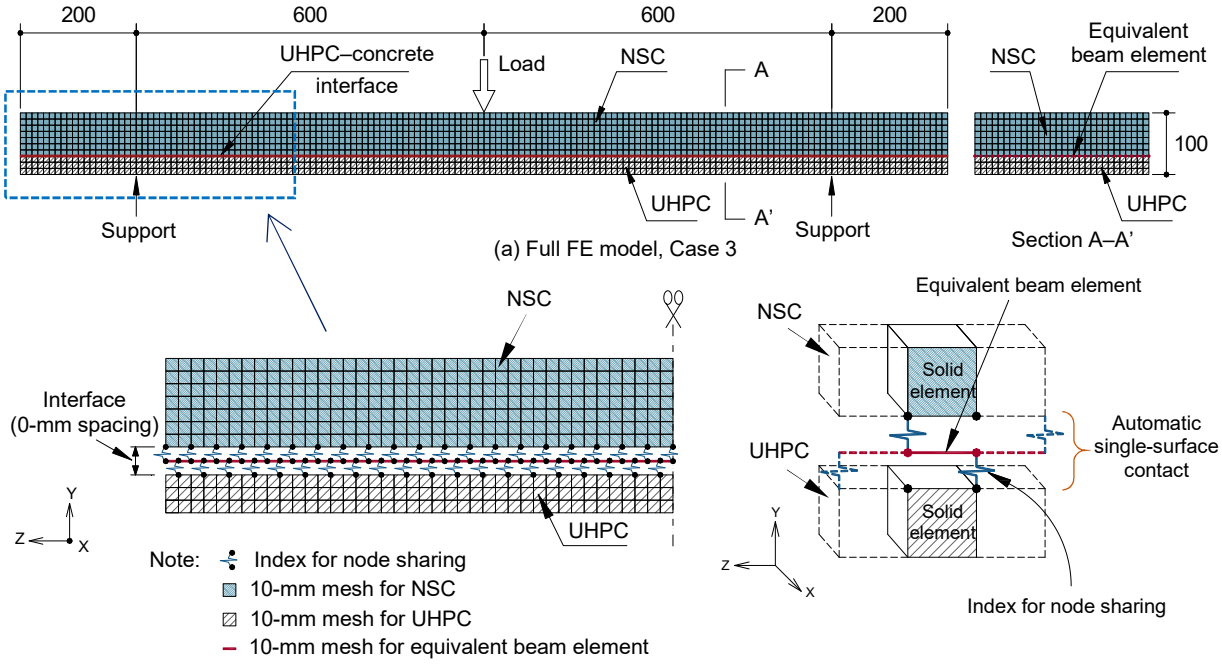

Figure 7: Details of proposed bond interface model using equivalent beam elements at the interface.

The interfacial bond between the NSC substrate and the UHPC can be expressed using the equivalent beam elements with an appropriate modelling technique for the bond behaviour at the interface. The nodes of the equivalent beam elements for the bond interface and those of the solid elements for the NSC and UHPC were intentionally created to coincide in order to enable

node sharing at the interface. To avoid perfect bonding and consider a finite bond strength, the equivalent beam elements alternately shared nodes with the solid elements of the two types of concrete, as seen in Fig. 7(b). That is, when the *i*th node of the equivalent beam elements is shared with a node of the NSC solid elements, the (*i*+1)th node of the equivalent beam elements is shared with a node of the UHPC solid elements. The following sections focus on the characteristics of the interfacial bond between the NSC and UHPC used in the FE model.

4.3.2. Interfacial bond for composite UHPC–concrete members

Because the equivalent beam elements were used to define the bond characteristics at the NSC–UHPC interface in the present study, the Young's modulus (stiffness) and yield strength (bond strength) of the equivalent beam elements were defined as inputs for Mat-03 in LS-DYNA. These properties were assumed to correspond to those of the weak concrete NSC. The Young's modulus and yield strength were obtained using the following equations.

The stiffness K_c of NSC is defined as

$$K_c = \frac{G_c A_c}{t_{c,bond}} \tag{10}$$

where G_c is the shear modulus of NSC, A_c is the area of the concrete surface at the interface, and $t_{c,bond}$ is the thickness of the bonded surface. The thickness $t_{c,bond}$ was assumed to be 1 mm.

The shear modulus G_c is given by

$$G_c = \frac{E_c}{2(1+\nu_c)} \tag{11}$$

where E_c is the Young's modulus of NSC and ν_c is the Poison's ratio of NSC.

The stiffness K_{eb} of each equivalent beam element is defined as

$$K_{eb} = \frac{E_{eb} A_{eb}}{L_{eb}} \tag{12}$$

where E_{eb}, A_{eb}, and L_{eb} are the Young's modulus, area, and length of the equivalent beam element, respectively.

At the equivalent state ($K_c = K_{eb}$), E_{eb} is expressed as

$$E_{eb} = \frac{E_c}{2(1+\nu_c)} \frac{A_c}{A_{eb}} \frac{L_{eb}}{t_{c,bond}} \tag{13}$$

The yield strength of the equivalent beam elements was defined based on the equivalent bond strength of UHPC to NSC substrates. Because previous investigations on the bond strength of NSC to UHPC have been very limited in previous studies [2,3], a maximum bond strength of 0.55 MPa, as suggested by ACI 318 [22] for intentionally roughened surfaces, was adopted. The yield strength $f_{y,eb}$ was then defined as

$$f_{y,eb} = \frac{\tau_{\max} A_c}{A_{eb}} \tag{14}$$

where $\tau_{\max}$ is the maximum bond strength ($\tau_{\max}$ = 0.55 MPa [22]). The simplified elastic–plastic characteristic curve shown in Fig. 8 was adopted for the equivalent beam elements. The overall features of the bond can be found in [23,24].

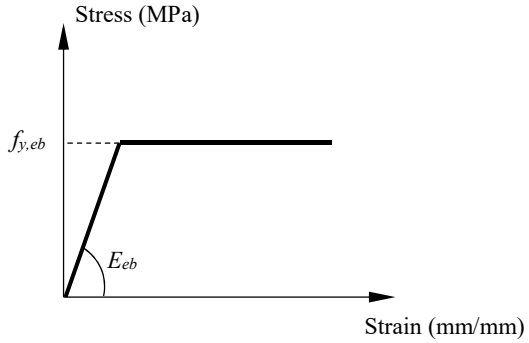

Figure 8: Adopted interfacial bond characteristics of equivalent beam elements for composite UHPC–concrete members.

5. Simulation results and verification

5.1. Results for non-composite specimens

Fig. 9 shows the simulated and experimental load–deflection curves for the two non-composite specimens RE-0 and RE-100 [8]. Good agreement was observed between the simulation and experimental results. For the NSC slab (RE-0), both the experimental and numerical curves showed a sudden drop in the force just after the peak load, as shown in Fig. 9(a). For the UHPC slab (RE-100), the FE simulation yielded a load–deflection curve with ductile behaviour that was very similar to the experimental results, as shown in Fig. 9(b). In addition, for both specimens, the simulated peak loads were approximately equal to the loads obtained experimentally, and the predicted maximum loads occurred at approximately the same deflections as in the experiment. Fig. 10 shows the damage pattern of the effective plastic strain distribution obtained from the numerical model along with the experimental final cracking pattern of the specimen RE-100. The numerical simulation showed a high effective plastic strain at the midspan, which agreed well with the experimental observation.

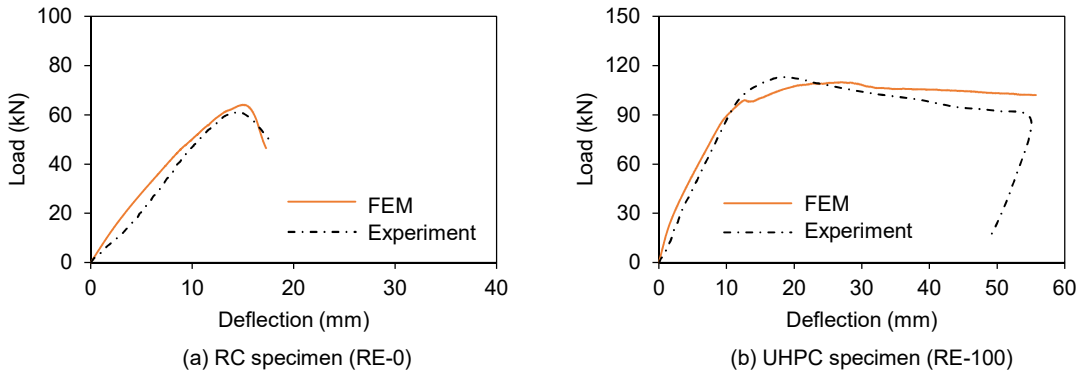

Figure 9: Load–deflection curves for non-composite NSC and UHPC specimens tested by the present authors [8].

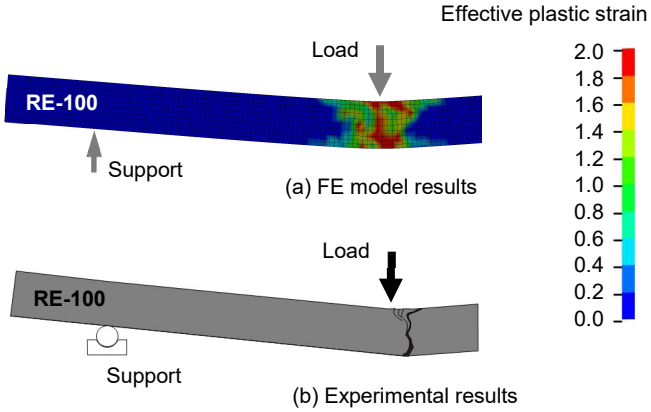

Figure 10: Simulated and experimental damage patterns for the non-composite UHPC specimen (RE-100).

Figs. 11 and 12 show the experimental and simulated load–deflection curves for the non-composite specimens tested by Yang et al. [15] and Yoo et al. [16], respectively. It should be noted that only the key points of load–deflection curves, such as the first cracking load, yield load, peak load, and the corresponding midspan deflections, were reported by Yang et al. [15] for specimens R12-1, R22-2, and R23-2. These points were used for comparison and are depicted in Fig. 11. As shown in Figs. 11 and 12, the overall response of the load–deflection curves for the UHPC beams obtained from the FE simulation agreed well with the corresponding experimental curves.

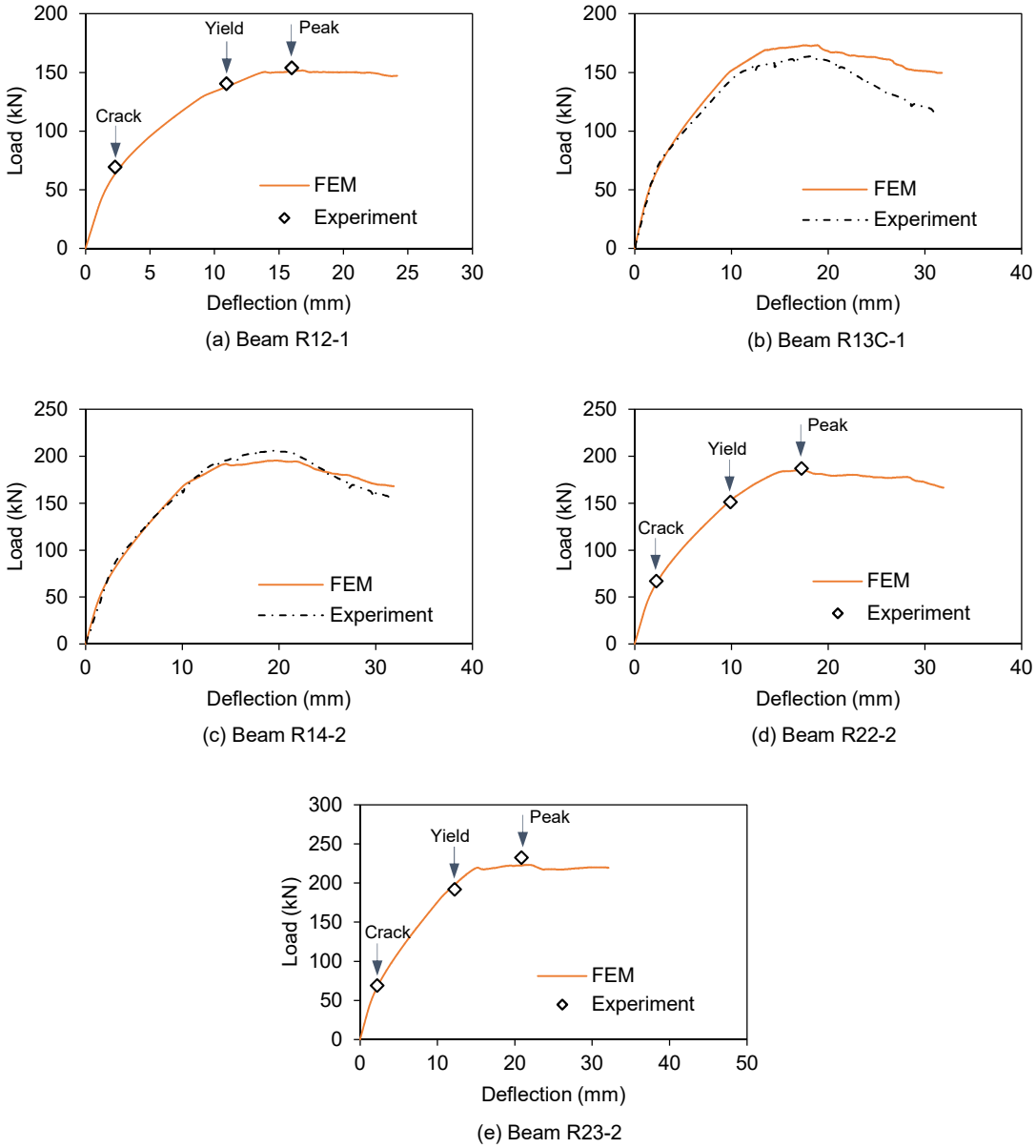

Figure 11: Simulated and experimental load–deflection curves for non-composite UHPC beams tested by Yang et al. [15].

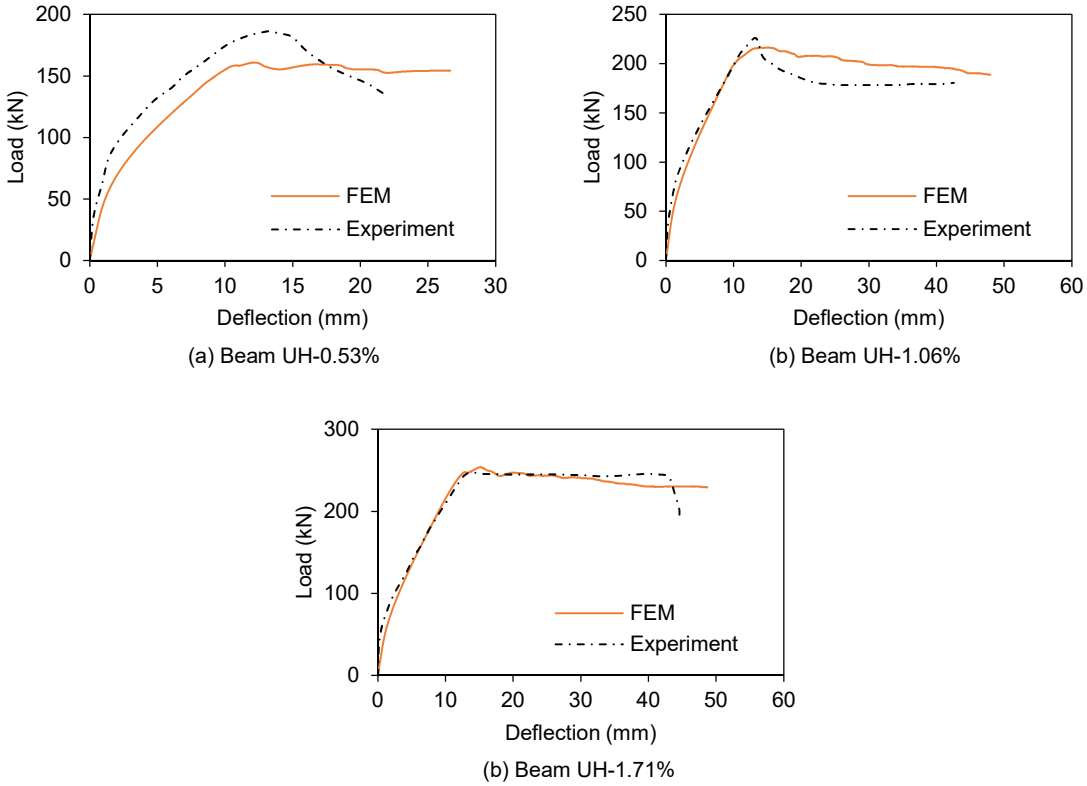

Figure 12: Simulated and experimental load–deflection curves for non-composite UHPC beams tested by Yoo et al. [16].

5.2. Results for composite UHPC–concrete specimens

5.2.1. Results obtained from analysis of perfectly bonded interface

The load–deflection curves for the composite UHPC–concrete specimens obtained from the FE model under the assumption of perfect bonding at the NSC–UHPC interface (Case 1, Section 4.1) are illustrated in Fig. 13. From Fig. 13, when the interface between NSC and UHPC was perfectly bonded, the ultimate loads obtained from the numerical simulation were significantly higher than those obtained experimentally for all specimens except OV-25 and OV-50. It should be noted that specimens OV-25 and OV-50 had no longitudinal rebar in the UHPC overlay.

5.2.2. Results obtained from analysis of unbonded interface

With the assumption of a perfectly unbonded NSC–UHPC interface (Case 2, Section 4.2), the numerical estimates were below the experimental curves for all the specimens except RE-20, as shown in Fig. 13. From the results of Cases 1 and 2 in Fig. 13, when the effect of the bond strength is not taken into account in the FE model for the composite UHPC–concrete specimens, the analysis yields poor results, i.e., the simulation estimates curves that are significantly higher or lower than the experimental curves for perfectly bonded or unbonded interfaces, respectively.

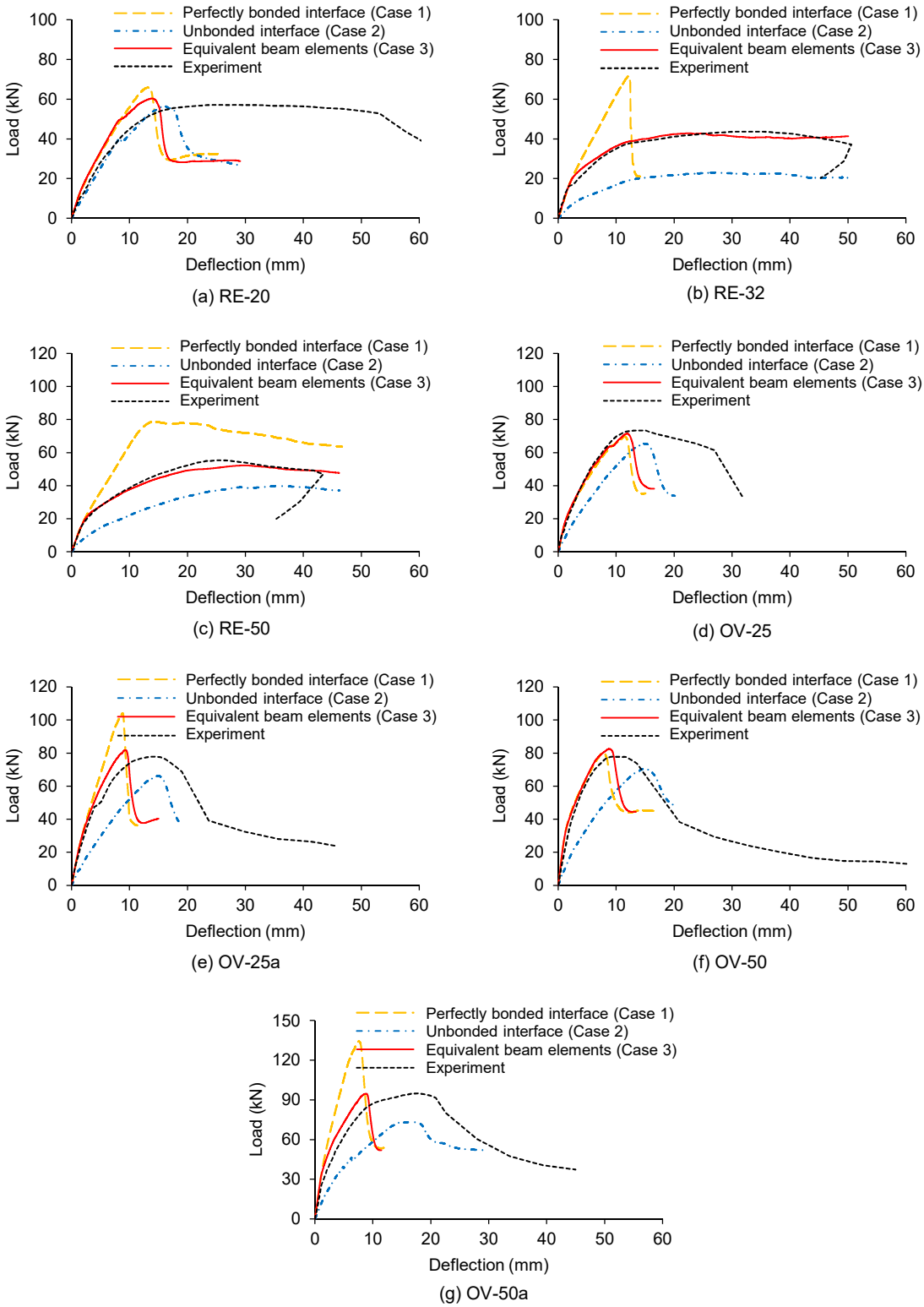

Figure 13: Simulated and experimental load–deflection curves for composite UHPC–concrete specimens [8].

5.2.3. Results obtained from proposed equivalent beam elements at the interface

The simulated load–deflection curves obtained from the FE model considering the bond strength effect using the proposed equivalent beam elements at the NSC–UHPC interface (Case 3, Section 4.3) were compared with the experimental results and those from analysis in Cases 1 and 2 (Fig. 13). As shown in Fig. 13, the curves obtained in Case 3 were between those obtained in Cases 1 and 2 and agreed well with the experimentally obtained curves. The FE model in Case 3 accurately predicted the initial stiffness and ultimate load for all of the composite specimens. For composite slabs RE-32 and RE-50, the simulated load–deflection curves of Case 3 were in good agreement with the experimental curves throughout the loading history, as shown in Fig. 13(b) and (c), respectively. For the other composite specimens, although the experimental results indicated that the specimens underwent ductile behaviour, the simulated curves showed a sudden drop after the peak load. These results may have been caused by the effect of the bond strength between the longitudinal rebar and concrete [8,25,26], as the proposed model does not consider the effect of the strength of this bond and instead assumes a perfect bond at this interface. However, the analysis in Case 3 demonstrated the effectiveness of the proposed method in the prediction of the initial stiffness and peak load and achieved fair agreement with the experimental results for the ultimate midspan deflections.

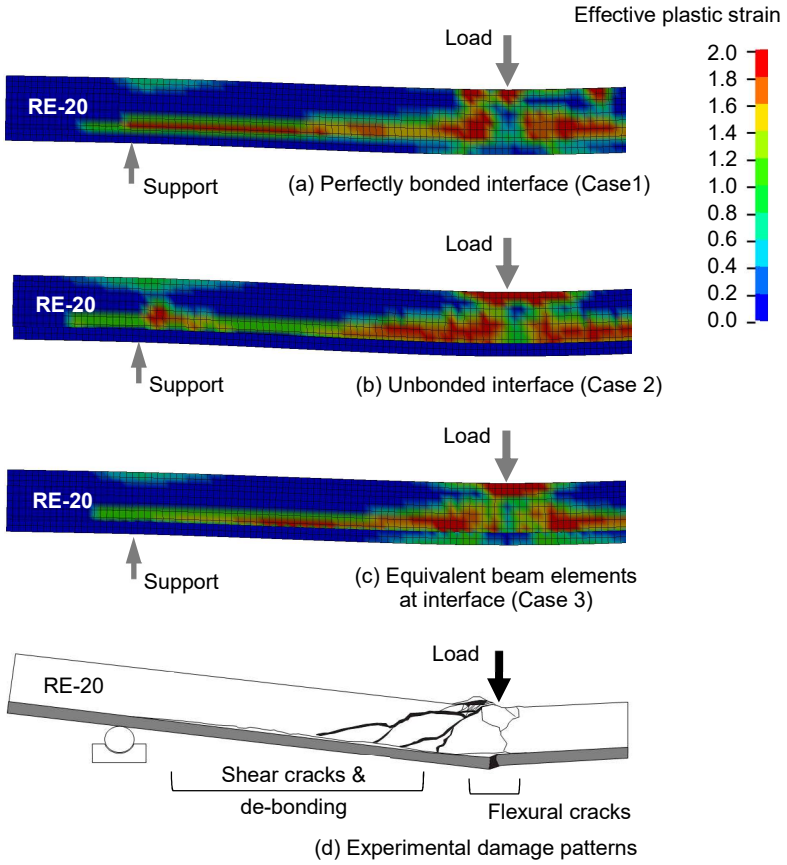

Figure 14: Damage patterns for composite slab RE-20 obtained from FEM simulations with different interface conditions.

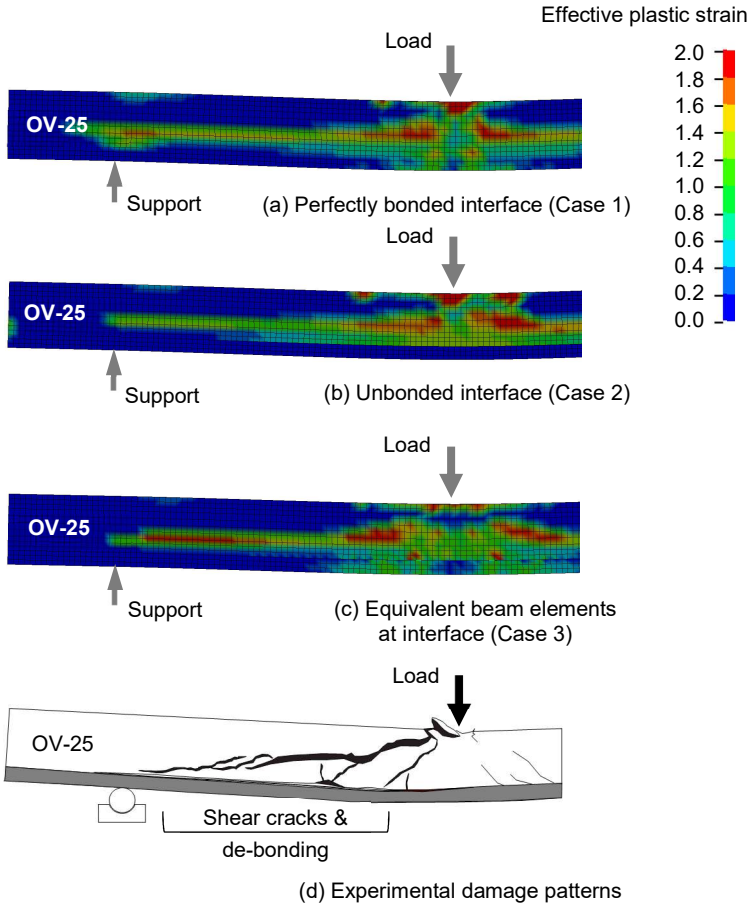

Figure 15: Damage patterns for composite slab OV-25 obtained from FEM simulations with different interface conditions.

Figs. 14 and 15 show damage maps of the effective plastic strain obtained from the FE simulations along with sketches obtained from the experimental results of the final crack patterns for the composite slabs RE-20 and OV-25, respectively. These sketches show that the features of the effective plastic strain results from the analysis of Cases 1 and 3 were roughly similar to each other but quite different from the Case 2 analysis. This is because the shared nodes in Case 1 and the equivalent beam elements in Case 3 transferred the effective plastic strain to the UHPC layer, whereas the unbonded interface in Case 2 did not allow the transmission of any high effective plastic strain to the UHPC layer. The regions of high effective plastic strain in Figs. 14(c) and 15(c) for Case 3 were found to be fair agreement with the corresponding experimental cracking patterns in Figs. 14(d) and 15(d).

Fig. 16 shows the experimental-to-numerical peak load ratio P_{exp}/P_{FEM} obtained from the FE simulations in the cases of a perfectly bonded interface (Case 1), an unbonded interface (Case 2), and equivalent beam elements at the interface (Case 3) for the composite UHPC–concrete specimens. It was clearly demonstrated that the results in Case 3, which considers the bond strength at the NSC–UHPC interface, showed good accuracy in terms of the P_{exp}/P_{FEM} ratios, with the ratios in all cases approximately at the target line of $P_{exp}/P_{FEM} = 1.0$. In contrast, Cases 1 and 2 greatly deviated from the target line (i.e., yielded erroneous results).

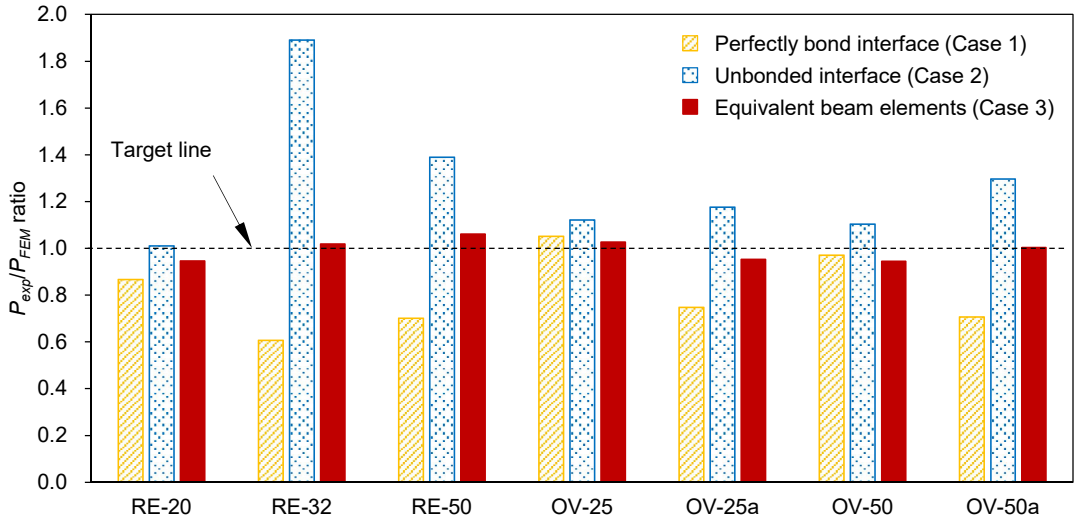

Figure 16: Experimental-to-numerical peak load ratios for composite UHPC–concrete specimens simulated with different interface conditions.

5.3. Peak load and corresponding midspan deflection

The experimental and numerical peak loads P_{exp} and P_{FEM} and the corresponding midspan deflections Δ_{exp} and Δ_{FEM} were compared for all non-composite and composite specimens, where the P_{FEM} and Δ_{FEM} values were those obtained using the proposed equivalent beam element method (Case 3). The experimental-to-numerical peak load ratios P_{exp}/P_{FEM} and the corresponding peak load deflection ratios $\Delta_{exp}/\Delta_{FEM}$ were calculated for the Case 3 analysis, and the results are given in Table 4. From Table 4, the numerical peak loads showed good accuracy, achieving an average P_{exp}/P_{FEM} ratio of 1.01 and a coefficient of variation (COV) of 5.5%. The predicted corresponding midspan deflections also showed fair correlations, yielding an average $\Delta_{exp}/\Delta_{FEM}$ ratio of 1.13 and a COV of 31.2%.

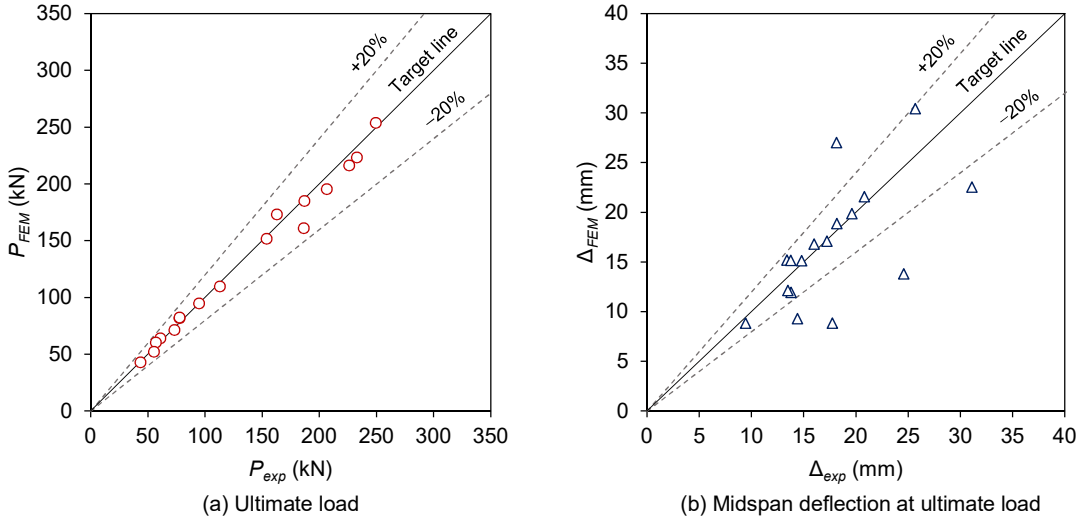

Figure 17: Simulation results for non-composite and composite (Case 3) members plotted against experimental results.

Fig. 17(a) and (b) shows the numerical results of the non-composite and composite (Case 3) specimens plotted against the experimental results for the peak load and the corresponding midspan deflection, respectively. As shown in Fig. 17(a), the peak load results showed a very good distribution along the target line representing $P_{FEM} = P_{exp}$. For the midspan deflection at the peak load shown in Fig. 17(b), although the results did not lie along the target line representing $\Delta_{exp} = \Delta_{FEM}$, most of the data points fell within the $\Delta_{exp} = \Delta_{FEM} \pm 20\%$ bounds, which indicates fair agreement.

Table 4: Summary of the FE model and experimental results.

Type	Authors	Specimen	P_{exp} (kN)	P_{FEM} (kN)	Δ_{exp} (mm)	Δ_{FEM} (mm)	P_{exp}/P_{FEM}	$\Delta_{exp}/\Delta_{FEM}$
Non-composite	Yin et al. [8]	RE-0	61.08	64.03	14.79	15.15	0.95	0.98
		RE-100	113.05	109.88	18.14	27.05	1.03	0.67
	Yang et al. [15]	R12-1	154.00	151.64	15.99	16.84	1.02	0.95
		R13C-1	163.10	173.22	18.18	18.88	0.94	0.96
		R14-2	206.80	195.41	19.62	19.89	1.06	0.99
		R22-2	187.10	185.06	17.23	17.13	1.01	1.01
		R23-2	233.00	223.34	20.82	21.61	1.04	0.96
	Yoo et al. [16]	UH-0.53%	186.5	160.96	13.49	12.17	1.16	1.11
		UH-1.06%	226.2	216.36	13.41	15.23	1.05	0.88
		UH-1.71%	249.5	253.98	13.77	15.18	0.98	0.91
Composite	Yin et al. [8]	RE-20	57.18	60.38	24.59	13.82	0.95	1.78
		RE-32	43.68	42.85	31.12	22.55	1.02	1.38
		RE-50	55.38	52.19	25.68	30.47	1.06	0.84
		OV-25	73.47	71.52	13.78	11.97	1.03	1.15
		OV-25a	77.97	81.77	14.42	9.32	0.95	1.55
		OV-50	77.97	82.52	9.43	8.86	0.94	1.06
		OV-50a	95.06	94.68	17.75	8.85	1.00	2.00
		Average					**1.01**	**1.13**
		Coefficient of variation (COV)					**5.5%**	**31.2%**

P_{exp}: Experimental peak load
P_{FEM}: Numerical peak load (Case 3 for composite specimens)
Δ_{exp}: Midspan deflection corresponding to the experimental peak load
Δ_{FEM}: Midspan deflection corresponding to the numerical peak load (Case 3 for composite specimens)

6. Conclusions

The structural response of composite UHPC–concrete members was simulated using the developed FE model with LS-DYNA software. The model was based on the calibrated parameters of the concrete damage model obtained for non-composite members (NSC or UHPC specimens). For composite members, the proposed modelling technique using equivalent beam elements was adopted to represent the bond behaviour at the interface between the NSC and UHPC slabs. For comparison, FE analysis was also conducted assuming a perfectly bonded or unbonded interface. From the present study, the following conclusions could be drawn.

(1) The developed FE model yielded good predictions for the overall response of both the non-composite and composite UHPC–concrete members.

(2) The proposed technique using the equivalent beam element at the interface between the NSC and UHPC was effective and efficient for simulating the behaviour of

composite UHPC–concrete members. These equivalent beam elements characterised by appropriate concrete properties were able to adequately capture the bond performance.

(3) The proposed FE model for the composite UHPC–concrete members accurately predicted the load–deflection curves, whereas the curves from the analysis cases in which a perfectly bonded or unbonded interface were considered showed relatively poor correlation. In addition, the overall configuration of the effective plastic strain obtained from the proposed FE model roughly agreed with the crack damage patterns observed in the experiments.

(4) The experimental-to-numerical peak load ratio P_{exp}/P_{FEM} obtained using the equivalent beam elements showed good accuracy, with the ratio approaching the target line ($P_{exp}/P_{FEM} = 1.0$). In contrast, the perfectly bonded or unbonded interface analysis cases yielded a large deviation. However, the corresponding midspan deflection obtained from the proposed FE model showed only fair agreement with the experimental results.

The numerical investigation in the present study revealed that the bond strength between NSC and UHPC should be taken into account when conducting the FE analysis of composite UHPC–concrete members. The results of this investigation demonstrate that although UHPC exhibits a good bond quality with RC members, it would not form a perfectly bonded interface. However, in future work, the effect of the mechanical concrete zone covering the longitudinal rebar on the overall numerical response should also be considered, and the post-peak ductile behaviour of the model should be improved.

Acknowledgments

We gratefully acknowledge the financial support from the Toda Scholarship Foundation 2017 Research Grant.

References

[1] Brühwiler E, Denarie E. Rehabilitation of concrete structures using ultra-high performance fibre reinforced concrete. In: The Second International Symposium on Ultra High Performance Concrete, 2008. p. 05-07.

[2] Tayeh BA, Bakar BA, Johari MM, Voo YL. Mechanical and permeability properties of the interface between normal concrete substrate and ultra high performance fiber concrete overlay. Constr Build Mater 2012;36:538-48.

[3] Harris DK, Muñoz MAC, Gheitasi A, Ahlborn TM, Rush SV. The challenges related to interface bond characterization of ultra-high-performance concrete with implications for bridge rehabilitation practices. Adv Civil Eng Mater 2014;4(2):75-101.

[4] Al-Osta M, Isa M, Baluch M, Rahman M. Flexural behavior of reinforced concrete beams strengthened with ultra-high performance fiber reinforced concrete. Constr Build Mater 2017;134:279-96.

[5] Habel K. Structural behaviour of elements combining UHPFRC and reinforced concrete. Doctoral thesis, Ecole Polytechnique Fédérale de Lausanne (EPFL), 2004.

[6] Denarié E, Habel K, Briihwiler E. Structural behavior of hybrid elements with Advanced Cementitious Materials (HPFRCC). In: 4th International RILEM Workshop on High Performance Fiber Reinforced Cement Composites (HPFRCC 4), 2003. p. 301.

[7] Noshiravani T, Brühwiler E. Experimental investigation on reinforced ultra-high-performance fiber-reinforced concrete composite beams subjected to combined bending and shear. ACI Struct J 2013;110(2):251-62.
[8] Yin H, Teo W, Shirai K. Experimental investigation on the behaviour of reinforced concrete slabs strengthened with ultra-high performance concrete. Constr Build Mater 2017;155:463-74.
[9] Oesterlee C. Structural response of reinforced UHPFRC and RC composite members. Doctoral thesis. Ecole Polytechnique Fédérale de Lausanne (EPFL), 2010.
[10] Safdar M, Matsumoto T, Kakuma K. Flexural behavior of reinforced concrete beams repaired with UHPFRC. Compos Struct 2016;157:448-60.
[11] Habel K, Denarié E, Brühwiler E. Experimental investigation of composite ultra-high-performance fiber-reinforced concrete and conventional concrete members. ACI Struct J 2007;104(1):93-104.
[12] Sadouki H, Denarié E, Brühwiler E. Validation of a FEA model of structural response of RC-cantilever beams strengthened with a (R-) UHPFRC layer. Constr Build Mater 2017;140:100-8.
[13] Lampropoulos A, Paschalis SA, Tsioulou O, Dritsos SE. Strengthening of reinforced concrete beams using ultra high performance fibre reinforced concrete (UHPFRC). Eng Struct 2016;106:370-84.
[14] LS-DYNA Keyword User's Manual, Version R8.0, LSTC, Livermore, CA, 2015.
[15] Yang IH, Joh C, Kim BS. Structural behavior of ultra high performance concrete beams subjected to bending. Eng Struct 2010;32(11):3478-87.
[16] Yoo DY, Banthia N, Yoon YS. Experimental and numerical study on flexural behavior of ultra-high-performance fiber-reinforced concrete beams with low reinforcement ratios. Can J Civil Eng 2017;44(1):18-28.
[17] Yang IH, Joh C, Lee JW, Kim BS. Torsional behavior of ultra-high performance concrete squared beams. Eng Struct 2013;56:372-83.
[18] Li J, Hao H. Numerical study of concrete spall damage to blast loads. Int J Impact Eng 2014;68:41-55.
[19] Li J, Zhang Y. Evolution and calibration of a numerical model for modelling of hybrid-fibre ECC panels under high-velocity impact. Compos Struct 2011;93(11):2714-22.
[20] Malvar LJ, Crawford JE, Wesevich JW, Simons D. A plasticity concrete material model for DYNA3D. Int J Impact Eng 1997;19(9)-(10):847-73.
[21] Mao L, Barnett S, Begg D, Schleyer G, Wight G. Numerical simulation of ultra high performance fibre reinforced concrete panel subjected to blast loading. Int J Impact Eng 2014;64:91-100.
[22] ACI Committee. Building code requirements for structural concrete (ACI 318-08) and commentary. American Concrete Institute; 2008.
[23] Loov R, Patnaik A. Horizontal shear strength of composite concrete beams with a rough interface. PCI J 1994;39(1):48-69.
[24] Dai J, Ueda T, Sato Y. Development of the nonlinear bond stress–slip model of fiber reinforced plastics sheet-concrete interfaces with a simple method. J Compos Constr 2005;9(1):52-62.
[25] An X, Maekawa K, Okamura H. Numerical simulation of size effect in shear strength of RC beams. JSCE J Mater Conc Struct Pavements 1997;35(564):297–316.
[26] Saito S, Hikosaka H. Numerical analyses of reinforced concrete structures using spring network models. JSCE J Mater Conc Struct Pavements 1999;44(627):289-303.

Chapter V

Paper IV

Behaviour of UHPC-concrete composite members subjected to static and dynamic loading: Numerical study

Behaviour of UHPC-concrete composite members subjected to static and dynamic loading: Numerical study

Abstract

This paper addresses the static and dynamic behaviour of composite reinforced concrete (RC) strengthened with ultra-high performance concrete (UHPC) obtained using the developed finite element (FE) modelling. In the static analysis, both implicit and explicit solvers in LS-DYNA were individually used for both monotonic and cyclic loading. The numerical results for monotonic loading were verified with previous experimental results. The numerical response under cyclic loading was conducted by comparing the implicit and explicit methods. For dynamic behaviour, blast simulation was performed using explicit method developed in static analysis. The blast model was validated with test data of non-composite RC or UHPC members available in the literature. Although there were no test data on UHPC-concrete composite members in open documents, the blast simulations were carried out to investigate the influence of UHPC strengthening layer on the blast resistance capacity of UHPC-concrete composite members. The structural responses including the midspan deflection, residual deflection, and damage cracking patterns were extracted from the numerical results. The effectiveness of UHPC layer of UHPC-concrete composite members was demonstrated through comparing the results with reference non-composite RC and UHPC members under same blast loading.

Keywords: Blast simulation, finite element modelling, structural response, RC members, UHPC strengthening, bond interface

1. Introduction

Concrete is one of the most commonly used materials in buildings. During service life of reinforced concrete (RC) structures, the repair or retrofitting of the structures may be required due to the deterioration of concrete or excessive deformation of the structural elements. Therefore, repair materials with high strength and high stiffness are desirable to use. The recent development of ultra-high performance concrete (UHPC), a cementitious concrete material containing small amount of steel fibres in the mix matrix, has been proven to be suitable in strengthening RC structures [1-3]. Due to the excellent properties of UHPC such as high strength, high stiffness, strain hardening, and energy absorption, the RC members after being strengthened with UHPC exhibits enhancement of structural performance [4-7]. Moreover, UHPC has shown good adherence to normal strength concrete (NSC) substrates [8, 9]. However, the studies on composite RC members strengthened with UHPC are very limited in the literature.

In addition, dynamic behaviour of structural members particularly under explosions is relatively more complex than static behaviour. Although accidental or intentional explosions rarely occur, blast damages of RC structures would become disastrous consequence. Blast loads with short duration can produce extremely large amount of energy to the structures and excite global or local responses. The excitement of the blast effect can cause immediate failure of structural members or executes the risk of structural progressive collapse. To mitigate the blast effect, use of UHPC layer onto RC members could be essential because the ductile behaviour of UHPC can help absorb large amount of blast energy. According to the past experimental studies [10-14], it demonstrated that UHPC structural members under blast loading significantly enhances the blast resistance capacity than the conventional RC members made of NSC. However, the dynamic behaviour of composite RC members strengthened with UHPC under blast loading has not yet been investigated.

In the present study, the numerical simulations were conducted to figure out the static and dynamic response of composite RC members strengthened with UHPC. The numerical model developed for the composite members under static loading was validated with the previously reported experimental results. The dynamic behaviour of composite UHPC-concrete members subjected to blast loading was numerically investigated. The reliability of the numerical model was based on the results calibrated with the some test results available in the literature. The numerical simulations of composite RC members strengthened with different UHPC configurations were carried out by varying the blast charge weight. The numerical results of non-composite and composite members are compared. The effect of UHPC layer on the blast resistance of UHPC-concrete composite members observed from the numerical model is presented.

2. Overall FE model

2.1. Modelling and conditions

In this paper, the behaviour of non-composite RC or UHPC members, and UHPC-concrete composite members was numerically studied. Commercial FE software LS-DYNA [15] was used for the numerical simulation. Both NSC and UHPC were modelled using an eight-node constant-stress solid element. For longitudinal rebar, a two-node beam element was used. A perfect bond was assumed between the longitudinal rebar and the NSC or UHPC.

Loading and support boundaries were modelled to represent the actual experimental conditions available in the literature by appropriate constraint. Static and blast loads were used. For static loading, the behaviour of the members were simulated using both implicit and explicit solvers in LS-DYNA, and displacement-controlled loading was used. For blast loading, only explicit analysis was used. Details of loading condition are described in Section 3.

2.2. Material model for concrete

Several material models in LS-DYNA such as Mat Johnson Holmquist Concrete (Mat-111); Mat Pseudo Tensor (Mat-16); Mat CSCM Concrete (Mat-159); Mat Concrete Damage (Mat-72r3) can be employed to model the behaviour of concrete material. In the present study, the concrete damage model (Mat-72r3), a plasticity-based constitutive model [16], was used for both the NSC and UHPC; and its reliability has been shown in [17-19].

The major advantage of the concrete model Mat-72r3 is that a single parameter, the unconfined compressive concrete strength f'_c, is required as an input. The remaining parameters are automatically generated using a built-in algorithm and can also be modified by the user. A brief description of the concrete damage model is presented in the following sections.

2.2.1. Strength surfaces

The concrete damage model is defined by three independent strength surfaces: an initial yield surface, a maximum failure surface, and a residual surface. The function of each of these strength surfaces can be expressed as [20]

$$F_i(p) = a_{0i} + \frac{p}{a_{1i} + a_{2i}p} \tag{1}$$

where p is the pressure; F_i is the ith failure surface; and a_{0i}, a_{1i}, and a_{2i} are parameters defining the three-parameter failure surfaces.

2.2.2. Strain rate effect

As commonly known, the concrete material is a strain rate dependent material. The behaviour of concrete material under dynamic loading such impact or blast (strain rate of $10^{-1} – 10^{3}$ s^{-1}) performs differently in comparison to the quasi-static event (strain rate of $10^{-6} – 10^{-4}$ s^{-1}). The effect of strain rate is defined by dynamic increase factor (DIF).

For NSC material, DIFs in compression and tension can be obtained using existing empirical models in [21]. For UHPC material, the strain rate effect found in literature is very limited. According to the work done by Ngo et al. [22], the DIF was derived from proposed model with high concrete strength of 160 MPa; and at given strain rate of 300 s^{-1}, the DIF was obtained as 1.5. Teng et al. [23] carried out the numerical simulation on impact response of reinforced fibre concrete, and the constant DIF value of 1.5 was used. Wang et al. [24] conducted the simulation of penetration of steel fibre reinforced concrete and no strain rate effect was considered in their model; but the numerical results yielded good performance.

Similar to the work done by Wang et al. [24], no strain rate effect was considered in the FE model developed in the present study.

2.2.3. Equation of state

An equation of state (EOS), the tabulated compaction, was employed in the concrete damage model Mat-72r3. This EOS is given as the relationship between the pressure P and volumetric strain ε_v as [15]

$$P = C(\varepsilon_v) + \gamma T(\varepsilon_v)E \tag{2}$$

where ε_v is the volumetric strain given by the natural logarithm, C and T are coefficients that are functions of ε_v, γ is the specific heat ratio, and E is the internal energy.

2.2.4. Determination of concrete model parameters

In the concrete damage model Mat-72r3, two simulation methods are available. The first is a simple method using automatic parameter generation that requires only the concrete compressive strength f'_c as an input. The second method requires detailed input parameters describing the concrete properties, and this method usually poses the difficulty of requiring a variety of data obtained from laboratory tests. In the present study, a combination of the first and second methods was adopted. The first method was preliminarily conducted by inputting f'_c to obtain all of the other parameters required in the second method. Then, the second method was carried out to modify the EOS. The detailed procedure for determining the concrete model parameters could be found in [17].

2.3. Material model for longitudinal rebar

For the longitudinal reinforcement, a material model (Mat-03) in LS-DYNA, which is an elastic–plastic model with kinematic and isotropic hardening, was used in the present study. The reliability of this model has been demonstrated in previous works [25, 26].

3. Loading conditions

3.1. Static loading

3.1.1. Monotonic loading

A monotonic loading rate of 2×10^{-5} m/s was used for both implicit and explicit methods. The implicit method is used to solve iterative equations and effectively applied to static problems. The implicit analysis is unconditionally stable for large time steps. However, it is often inaccurate in the numerical solution when the convergence of the equilibrium iterations is difficult to achieve. Several iterative solver schemes are available in LS-DYNA. In the present study, quasi-Newton methods, which is the most robust solver among the options, was employed.

The explicit method directly solves the problem and does not require iterations. However, this method is conditionally stable and it requires small time increment for accurate procedure. The explicit solution under monotonic loading for the static problems leads to an inevitably large number of time steps. To shorten the simulation time, it can be done either by reducing the total time steps or by increasing the time increment, and the results can be acceptable when the kinetic energy was negligible compared to the internal energy in the model. In the present study, an increased loading rate of 2×10^{-3} m/s was adopted to reduce the total time steps.

3.1.2. Cyclic loading

Similar to the monotonic loading (Section 3.1.1), reversed cyclic loading in this study was adopted for both implicit and explicit analysis. Fig. 1 shows the cyclic loading history used in the FE model with displacement increments. Two loading cycles were composed at each displacement increment. Each displacement increment of 2 mm was set.

For implicit analysis, as shown in Fig. 1(a), the loading rate used in reversed cycles was same as that described in monotonic loading. For explicit analysis, the simulation time under cyclic loading is significantly longer than monotonic loading at same loading rate. To shorten the simulation time, both reducing the total time steps and increasing the time increment were adopted. In the present study, the loading rate of 2×10^{-3} m/s was used to reduce the total time steps (Fig. 1(b)), and the constant time step of dt = 1.5×10^{-5} s was set using mass scaling to increase the time increment.

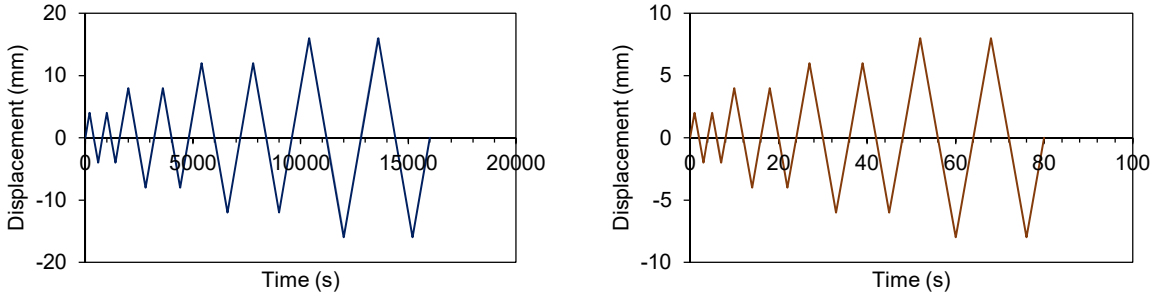

(a) Time-displacement history for implicit analysis

(a) Time-displacement history for explicit analysis

Figure 1: Cyclic loading history.

The cyclic loading was applied to rigid rollers as shown in Fig. 2. The rigid rollers and supports were modelled using solid element and rigid material (Mat-20 in LS-DYNA) was employed.

An automatic single contact surface was used to prevent element penetration. It should be noticed that the cyclic simulation is implemented only in Section 5 for assessment study of blast simulation.

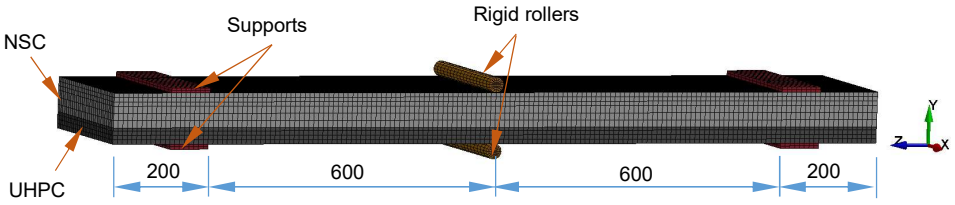

Figure 2: Overview of FE model (RE-32) for cyclic loading (all dimensions in mm).

3.2. Blast loading
3.2.1. Overview

The high explosive creates shock waves, burst or shatter materials, penetrate materials, produce lift and heave of materials. When this high explosive detonated in air, it produces air blast [27]. The high-pressure causes a violent expansion of the gaseous products and the surrounding air is forced out of the volume it occupies. The layer of this air contains most of the explosive energy and is known as the blast wave. Since a disequilibrium is set up between the highly compressed air in the blast wave and the undisturbed air in front of it, the blast wave travels outwards from the centre of the explosion. The total energy in the system is now constant because the explosive has now fully detonated. The pressure at the blast wave front decreases as the wave front travels further from the explosion. The momentum of the gas causes it to over-expand and results in the pressure at the tail of the blast wave falling below the air pressure of the atmosphere. This creates a negative pressure phase due to the air removed from atmosphere, resulting in reversal of flow back towards the explosion centre. Eventually equilibrium is restored to ambient air.

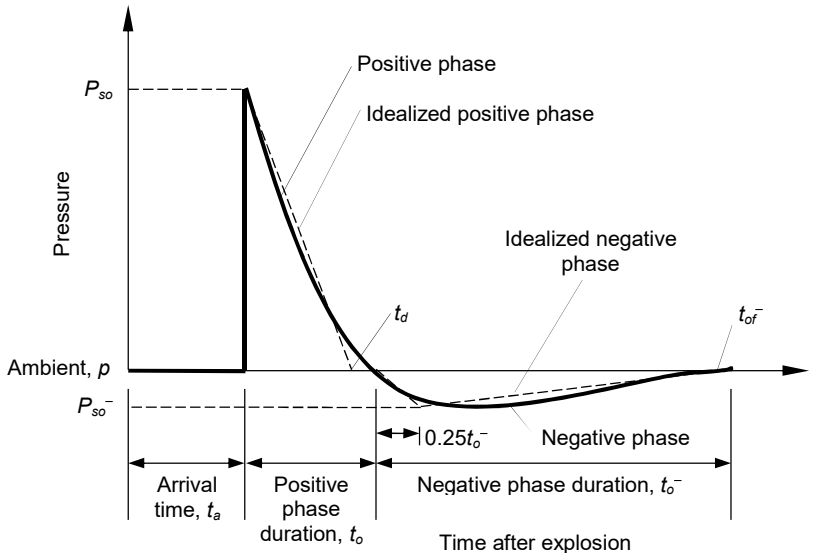

Figure 3: Idealization of pressure-time history [28].

Fig. 3 shows an idealization of pressure time history curve for a blast wave in free air. The peak pressure in the negative phase is typically small relative to the peak pressure in the positive

phase. The pressure time history of a blast wave can be described by exponential function, i.e. the Friedlander Equation given as:

$$p(t) = p_{so}\left(1-\frac{t}{t_a}\right)\exp\left\{-\frac{\alpha t}{t_d}\right\} \tag{3}$$

where t is the wave duration time; t_a is the arrival time; t_d is the duration time of the positive phase; p_{so} is the peak overpressure; and α is the waveform parameter. The impulse, i_{so}, the area beneath the pressure time curve of positive pressure phase. The peak overpressure produced by the spherical blast wave is given as a function of the scaled distance $Z = R/W^{1/3}$, where R is the actual effective distance from explosion, and W is the blast charge weight. The summary of blast effects on structures could be found in [29].

3.2.2. Blast load modelling

In the present numerical simulation, the blast loading is modelled using built-in algorithm load-blast-enhanced function. In LS-DYNA, this function was based on the empirical model described in TM5-855 US army handbook (CONWEP) [28]. The load-blast-enhanced function was commonly used by many researchers and it yields highly reliability [13, 19, 25, 26].

The major advantage of the blast-enhanced function is that it can avoid the detailed modelling of the explosive charge and shock wave in air. The function requires only the equivalent mass of TNT (trinitrotoluene), location of detonation charge, and type of blast. The blast type used in the present simulation was the spherical free-air burst (default).

3.2.3. Blast pressure response

The incident pressures obtained using blast load modelling as described in Section 3.2.2 was compared with those from the experiment measured at a distance of 5 m and performed by Yi et al. [10]. As shown in Fig. 4, similar to the numerical results conducted by Yi et al. [10], the present numerical simulations agreed well with the first peak pressure of the experimental results. In the present study, the reflected pressures, which is almost identical to the incident pressures, was also computed from the Unified Facilities Criteria (UFC 3-340-02) [30] and depicted in Fig. 4 for comparison.

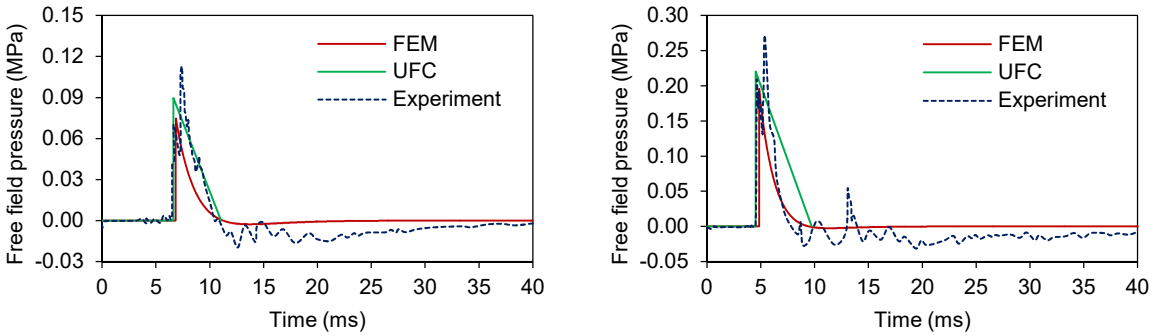

Figure 4: Comparison of free field pressures obtained from FEM, UFC, and experiment performed by Yi et al. [10].

4. Validation of FE simulation

4.1. General description

To validate the present FE model, specimens tested by Li et al. [31] and Yi et al. [10] were used. Geometric and material properties of the specimens by Li et al. [31], and Yi et al. [10] are described in Sections 4.2 and 4.3, respectively.

For the blast response, global damping system (mass-proportional damping) in LS-DYNA was used to consider damping effect in the present numerical simulation to reduce the vibration. Through several trials, it was found that the most appropriate damping ratio was 5%, and it was then applied to all blast simulations in this study.

4.2. Specimens tested by Li et al. [31]

Two specimens tested by Li et al. [31] were modelled using the present FE model. One was under static loading (monotonic) and the other was under blast loading. A four-point bending system was used for static test on 100 mm × 100 mm × 400 mm UHPC specimen, which was named MF15, with no reinforcement rebar. The blast test was conducted on 200 mm × 200 mm × 2500 mm UHPC specimen; namely U1B1. The specimen U1B1 was reinforced with six longitudinal rebar of 16 mm in diameter (6ϕ16) across the section, and transverse steels of 8 mm in diameter were also installed. The blast charge of 1 kg TNT was hung over the centre of the specimen at a height of 1500 mm. Table 1 shows further details of geometry and material properties of the specimens. For full details, it could be found in [31].

Table 1: Geometry and material properties of specimens [31].

Specimen	Geometry			UHPC	Longitudinal steel			Transverse steel		Load
	W (mm)	H (mm)	L (mm)	f'_c (MPa)	ϕ (mm)	f_y (MPa)	$f_{y,\max}$ (MPa)	ϕ (mm)	f_y (MPa)	
MF15	100	100	400	150	-	-	-	-	-	Static
U1B1	200	200	2500	150	16	1350	1600	8	300	Blast

Note:
W: Width
H: Total height
L: Total longitudinal length
f'_c: Compressive strength of UHPC
ϕ: Diameter of reinforcement
f_y: Yield strength of reinforcement
$f_{y,\max}$: Ultimate strength of reinforcement

4.2.1. Simulation results for the flexural specimen under static loading

The static specimen MF15 tested by Li et al. [31] were modelled using 10-mm mesh size. The material models described in Section 3 were implemented. The static loading and supports was applied directly to nod sets. The nod sets for supports were constrained as simply supported test specimen. The concrete model parameters used in the FE model are listed in Table 2.

Fig. 5 illustrates the comparison of static load-deflection curves obtained from numerical simulations and the experiment. When the FE model used equal parameters, that yielded good results for implicit analysis, for explicit analysis, the numerical peak load in explicit analysis showed significant decrease than in implicit analysis as shown in Fig. 5(a). A new set of concrete model parameters was then recalibrated in explicit analysis using the procedure described in Section 2.2.4. By adopting the newly set parameters (Table 2), the load-deflection

curve using explicit solver agreed well with the experimental curve as shown in Fig. 5(b). These parameters were then used for the blast simulation, for which the explicit solver was also used.

Table 2: Concrete model parameters employed in the numerical simulation for specimens tested by Li et al. [31].

Experiment		Model parameter for implicit analysis			Model parameter for explicit analysis		
Specimen	f'_c (MPa)	b_2	w_c (mm)	f_t (MPa)	b_2	w_c (mm)	f_t (MPa)
MF15	150	–12	35	17	–38	15	23
U1B1	150	-	-	-	–38	15	23

Note:
f'_c: Compressive strength of UHPC
f_t: Tensile strength of UHPC
b_2: Tension softening concrete parameter of concrete damage model
w_c: Localised crack width of concrete damage model

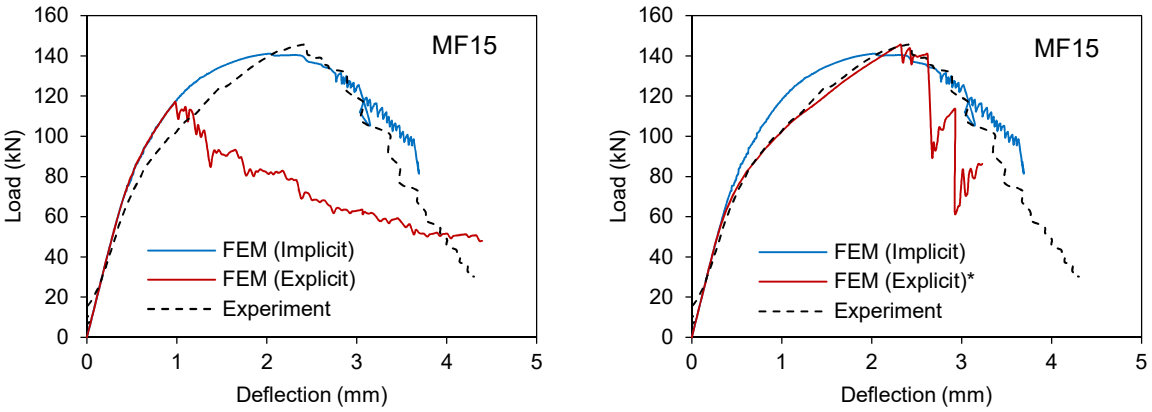

(a) Application of equal parameters to both implicit and explicit analysis

(b) Application of modified parameters to explicit analysis

Note:
*: Newly calibrated parameters of concrete damage model

Figure 5: Comparison of load-deflection curves obtained from FE model and experiment tested by Li et al. [31].

4.2.2. Simulation results for the specimen under blast loading

Full-scale blast specimen U1B1 tested by Li et al. [31] were modelled using 20-mm mesh size. The material models described in Section 3 were implemented. The supports was modelled using solid rigid panels and constrained in all directions. The overall configuration of model setup is shown in Fig. 6.

As earlier mentioned, the global damping system was used. This could be done by conducting the preliminary analysis without damping effect. The natural period T was determined as the second loop (see Fig. 7(a)), and it was used to compute damping constant as an input in LS-DYNA.

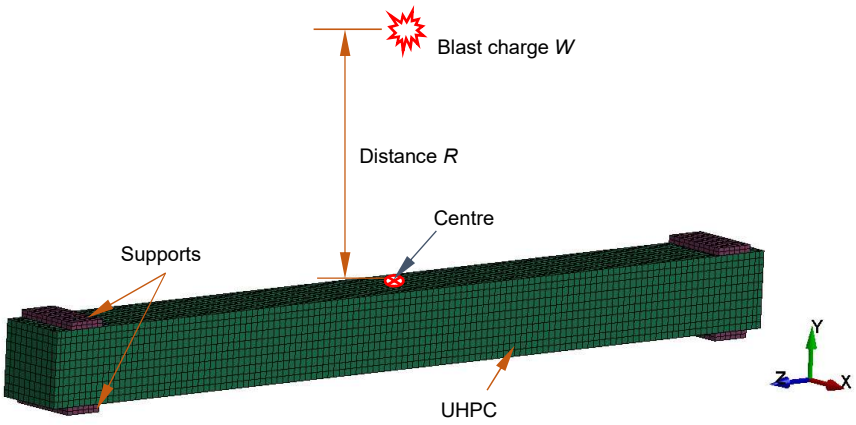

Figure 6: Overview of configuration of FE model for blast simulation on specimen tested by Li et al. [31].

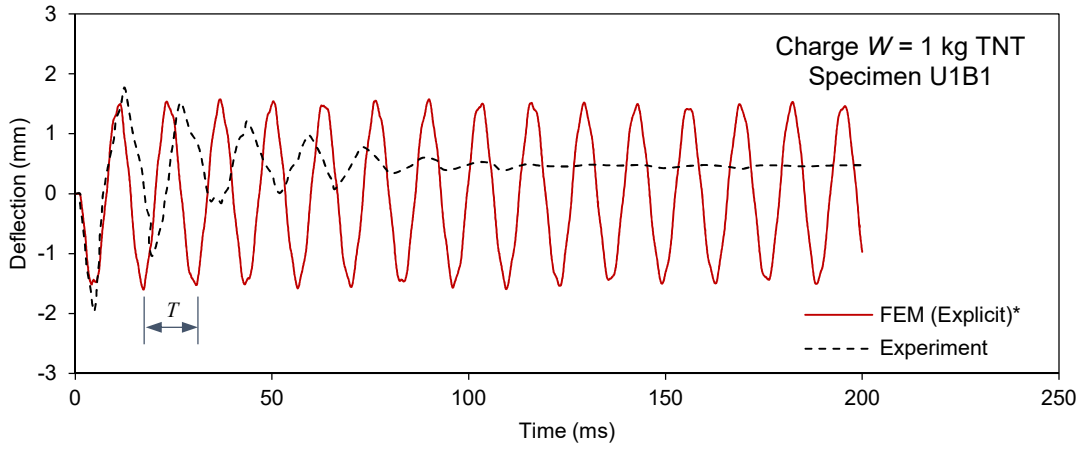

(a) No damping effect taken into account

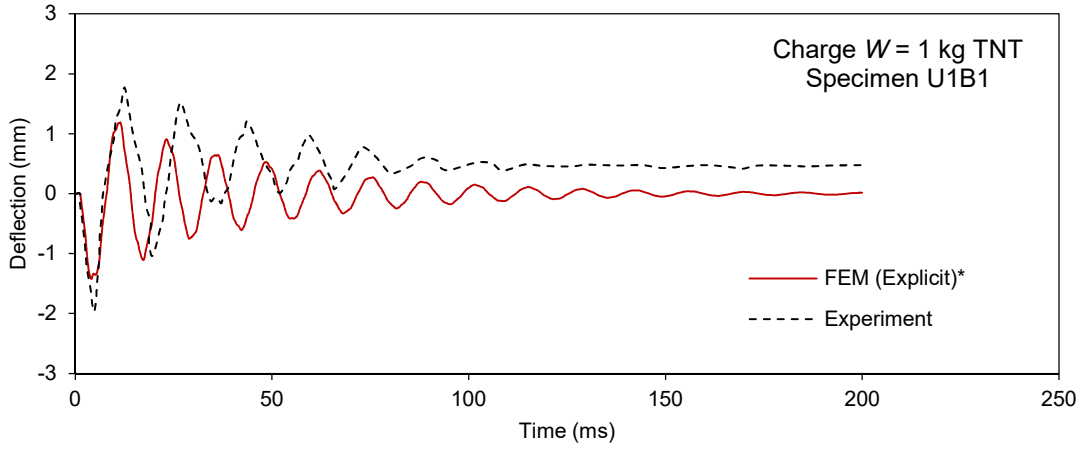

(b) Consideration of damping ratio of 5% in the FE model

Note:
*: Newly calibrated parameters of concrete damage model
T: Adopted natural period for computing damping constant in LS-DYNA

Figure 7: Comparisons of deflection-time histories for specimen U1B1.

Fig. 7(a) and (b) show the comparisons between experimental results and numerical responses without damping effect and the consideration of damping ratio of 5%, respectively. As shown in Fig. 7(a), it was clearly shown that the numerical simulation result indicated likely free vibration. When the damping ratio of 5% was used in the FE model, the numerical response fairly agreed with the experimental result as shown in Fig. 7(b).

4.3. Specimens tested by Yi et al. [10]

Two NSC and two UHPC specimens tested by Yi et al. [10] were modelled using the present FE model. All specimens were reinforced with two layers of mesh reinforcements of 10 mm in diameter in both directions. Table 3 shows the geometry and material properties of the specimens. The blast charge was installed at a height of 1500 mm above the centre of the specimens. The NSC specimens, named as NSC1 and NSC2, were tested under the blast charge of 15.88 kg TNT and 15.88 kg ANFO (= 13.02 kg TNT), respectively. The UHPC specimens, named RPC1 and RPC1, were tested under same blast weight of 15.88 kg ANFO. For full details, it could be found in [10].

Table 3: Geometry and material properties of blast specimens tested by Yi et al. [10].

Specimen	Geometry			NSC/UHPC	Longitudinal steel		
	W (mm)	H (mm)	L (mm)	f'_c (MPa)	ϕ (mm)	f_y (MPa)	$f_{y,max}$ (MPa)
NSC1,2	1000	150	1000	25.6	10	400	600
RPC1,2	1000	150	1000	202.9	10	400	600

Note:
W: Width
H: Total height
L: Total longitudinal length
f'_c: Compressive strength of UHPC
ϕ: Diameter of reinforcement
f_y: Yield strength of reinforcement
$f_{y,max}$: Ultimate strength of reinforcement

4.3.1. Simulation results for the NSC specimens under blast loading

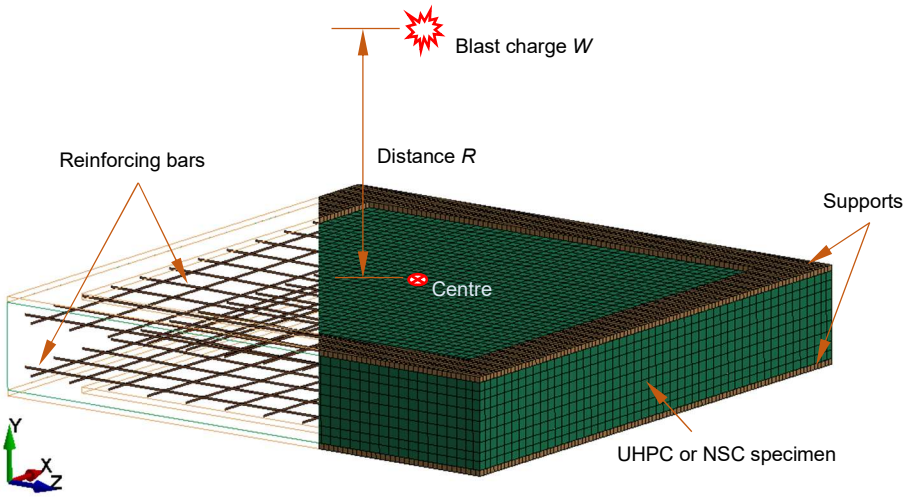

Figure 8: Overview of configuration of FE model for blast simulation on specimen tested by Yi et al. [10].

Similar to the modelling of the specimen tested by Li et al. [10], the specimens tested by Yi et al. [10] were modelled using 20-mm mesh size. The material models for concrete and longitudinal rebar described in Section 3 were implemented. The supports was modelled using solid rigid panels and constrained in all directions. The overall configuration of FE model is shown in Fig. 8. Table 4 listed the concrete damage model parameters used for the NSC and UHPC specimens.

Table 4: Concrete model parameters employed in the numerical simulation for specimens tested by Yi et al. [10].

Experiment		Concrete model parameter		
Specimen	f'_c (MPa)	b_2	w_c (mm)	f_t (MPa)
NSC1,2	25.6	−1	15	3
RPC1,2	202.9	25.18[§]	15	12

Note:
[§]: Default defined by LS-DYNA
f'_c: Compressive strength of UHPC
f_t: Tensile strength of UHPC
b_2: Tension softening concrete parameter of concrete damage model
w_c: Localised crack width of concrete damage model

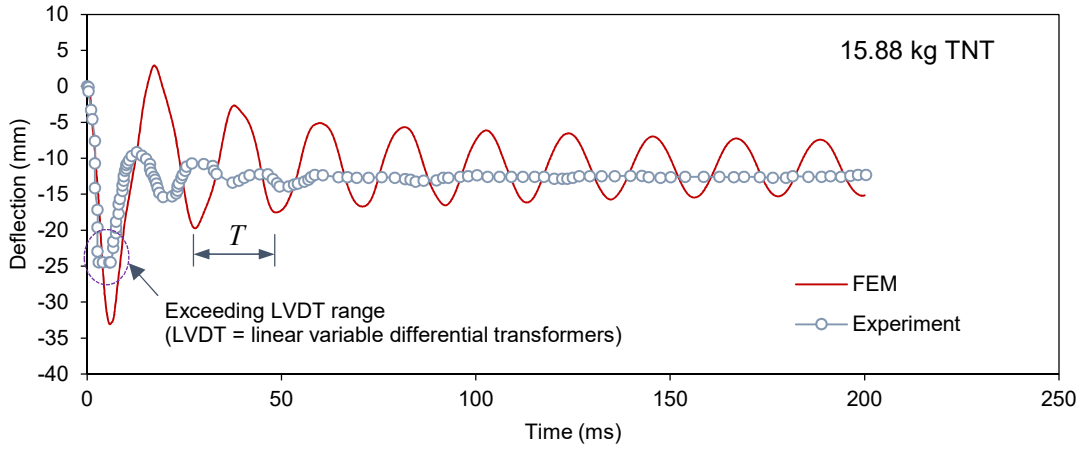

(a) No damping effect taken into account

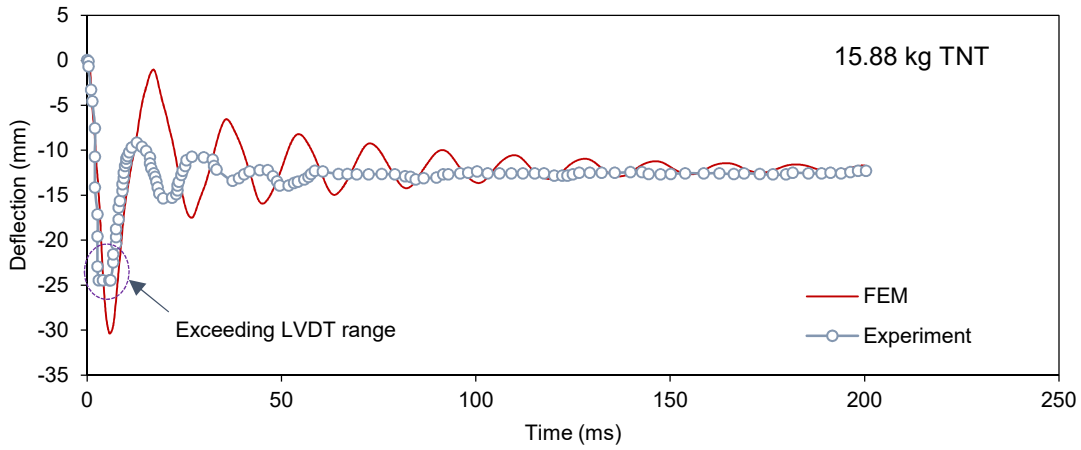

(b) Consideration of damping ratio of 5% in the FE model

Figure 9: Comparisons of deflection-time histories for specimen NSC1.

Fig. 9(a) and (b) show the comparisons between experimental results and numerical responses without damping effect and the consideration of damping ratio of 5% for specimen NSC1, respectively. As shown in Fig. 9(a), it showed that from the numerical simulation result free vibration after the first cycle of deflection-time history occurred. When the damping ratio of 5% was used in the FE model, the permanent deflection obtained from the numerical simulation agreed well with the experimental result as shown in Fig. 9(b). It could be noticed that the maximum deflection obtained from the numerical simulation was higher than that measured from the experiment because the maximum deflection measured from the experiment exceeded the measurement device for the specimen NSC1 under 15.88 kg TNT reported by Yi et al. [10].

Fig. 10(a) and (b) show the comparison of simulated and experimental results for specimen NSC2 subjected to the blast charge of 15.88 kg ANFO (ammonium nitrate/fuel oil). As shown in Fig. 10(b), the numerical result using the damping ratio of 5% showed good agreement with the experimental results. The simulated damage crack pattern of specimen NSC2 is shown in Fig. 11.

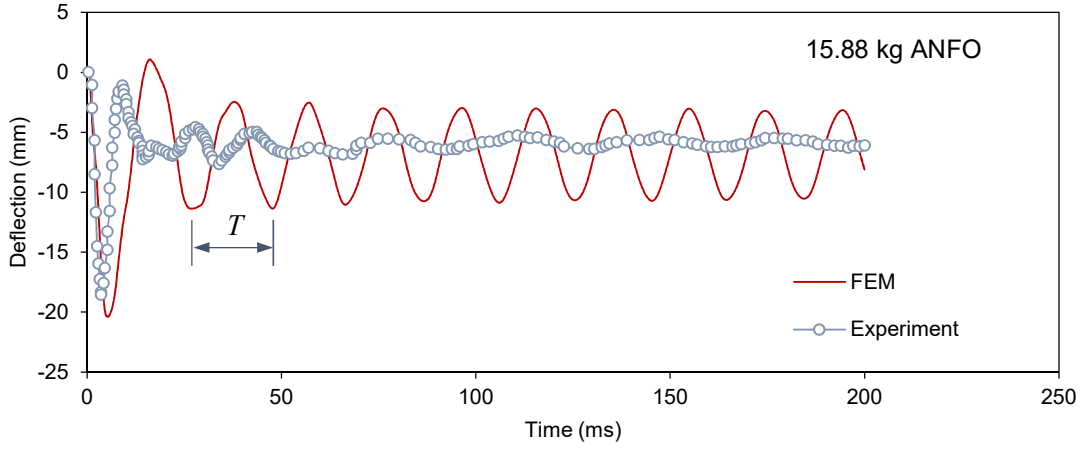

(a) No damping effect taken into account

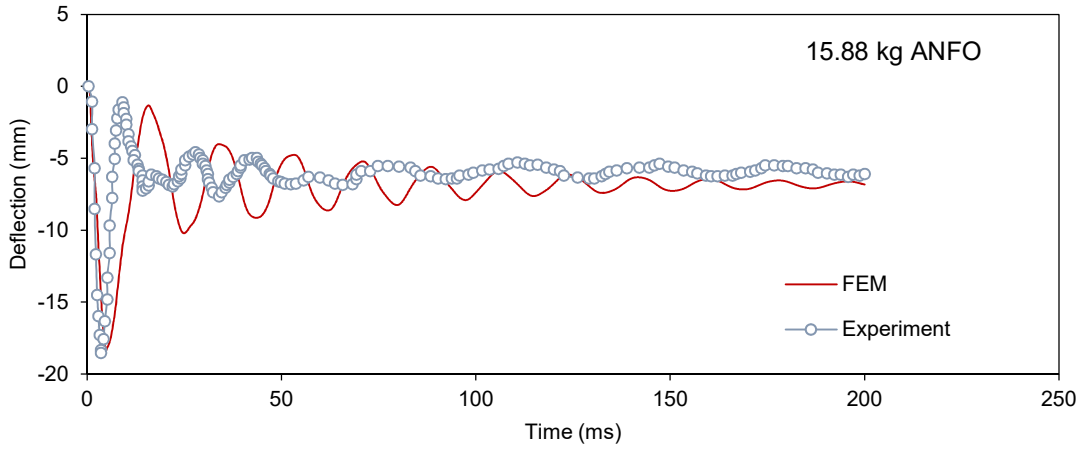

(b) Consideration of damping ratio of 5% in the FE model

Figure 10: Comparisons of deflection-time histories for specimen NSC2.

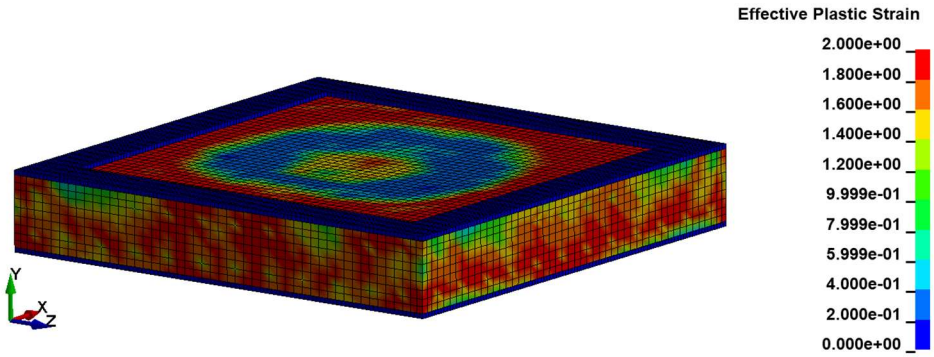

Figure 11: Numerical damage pattern of specimen NSC2.

4.3.2. Simulation results for the UHPC specimens under blast loading

Fig. 12(a) and (b) show the comparisons between experimental results and numerical responses without damping effect and the consideration of damping ratio of 5% for UHPC specimens, respectively. As shown in Fig. 12(a), once again, it was clearly shown that the numerical simulation result demonstrated free vibration after the first cycle of deflection-time history. When the damping ratio of 5% was used in the FE model, the permanent deflection obtained from the numerical simulation agreed well with the experimental results as shown in Fig. 12(b).

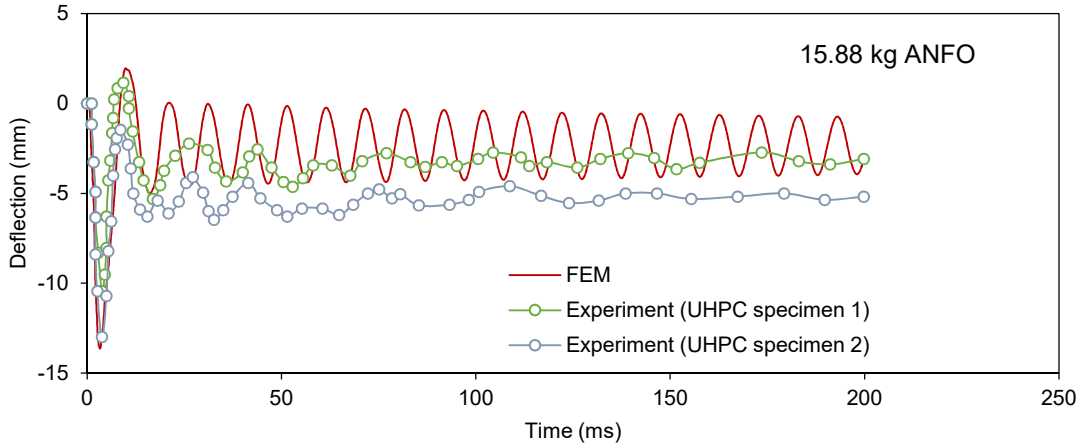

(a) No damping effect taken into account

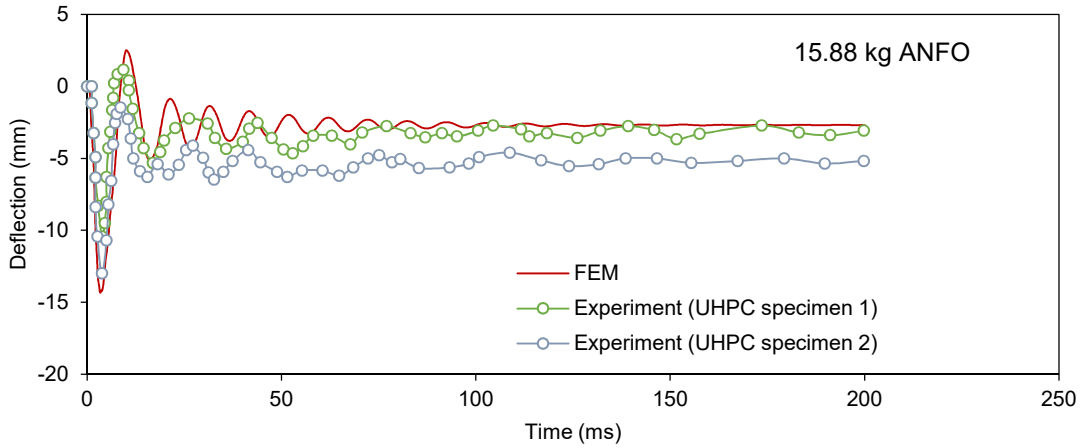

(b) Consideration of damping ratio of 5% in the FE model

Figure 12: Comparisons of deflection-time histories for specimen RPC1,2.

Fig. 13 shows the configuration of effective plastic stain for the numerical damage pattern of specimen RPC1,2. Owing to the high performance of UHPC including highly compressive and tensile strength, an improvement of damage crack pattern obtained from the simulation was observed as compared to that of the NSC specimen (Fig. 11).

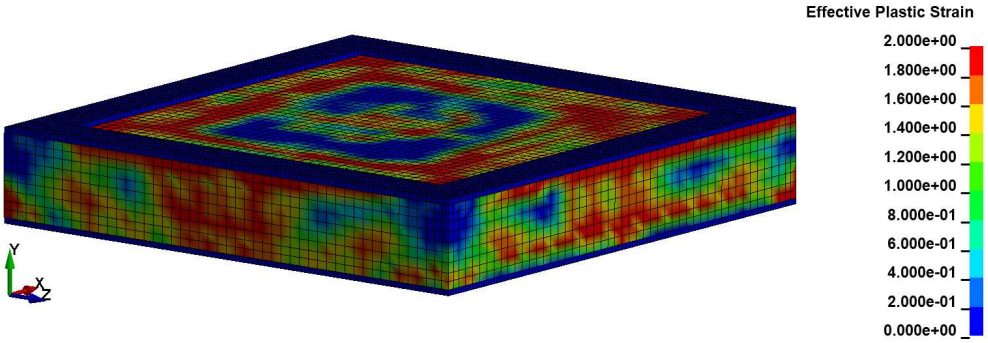

Figure 13: Numerical damage pattern of specimen RPC1,2.

5. Numerical assessment for UHPC-concrete composite members

5.1. Description details

This section describes the numerical assessment for UHPC-concrete composite members in details. The description includes the details of specimens, FE modelling, loading conditions, and parameter study for blast simulation. The following sections detail the descriptions.

5.1.1. Description of specimens

Four specimens with different cross-sectional configurations performed by Yin et al. [7] were modelled. The specimens had five high-tensile-strength steels of 12 mm in diameter (5DB12) installed both the bottom and top as longitudinal reinforcement. Of four specimens, two were non-composite members made of NSC and UHPC; namely RE-0 and RE-100, respectively. Others were UHPC-concrete composite members named as RE-32 and OV-50. The details of the geometry and material properties of the specimens are shown in Fig. 14 and Table 5.

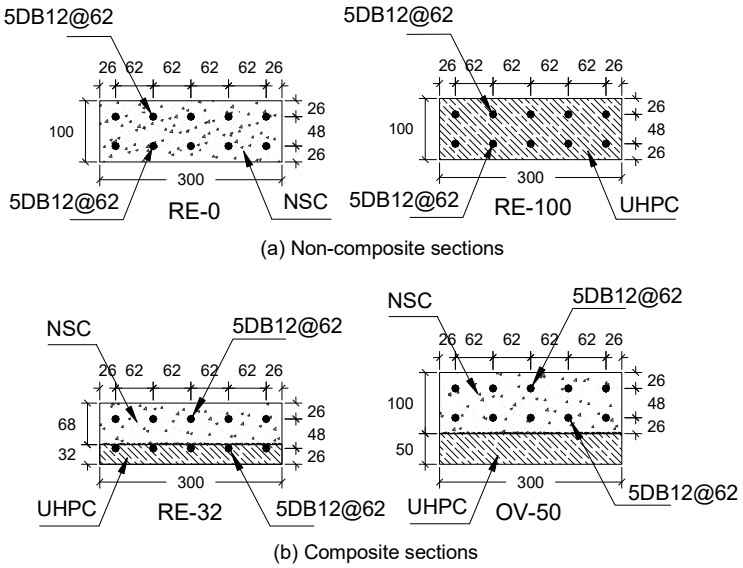

Figure 14: Details of non-composite and UHPC-concrete composite sections (all dimensions in mm) [7].

Table 5: Geometry and material properties details of the specimens [7].

Description	Specimen	Geometry				NSC	UHPC	Longitudinal steel	
		W (mm)	H (mm)	L (mm)	h_U (mm)	f'_c (MPa)	f'_c (MPa)	f_y (MPa)	$f_{y,\max}$ (MPa)
Non-composite NSC	RE-0	300	100	1600	-	23	-	502	565
Non-composite UHPC	RE-100	300	100	1600	100	-	153	502	565
UHPC-concrete composite	RE-32	300	100	1600	32	23	153	502	565
	OV-50	300	150	1600	50	23	153	502	565

Note:
W: Width
H: Total height
L: Total longitudinal length
h_U: UHPC layer thickness
f'_c: Compressive strength of NSC or UHPC
f_y: Yield strength of reinforcement
$f_{y,\max}$: Ultimate strength of reinforcement

5.1.2. Description of FE modelling

Specimens described in Section 5.1.1 were modelled using 10-mm mesh size. The material models described in Section 3 were implemented. The modelling details could be found in [17, 32, 33]. The effect of bond strength at the interface between UHPC and NSC substrate was considered for UHPC-concrete composite members [32, 33]. The bond interface modelling could be sumarised as follows.

The bond between UHPC and NSC was modelled using equivalent beam elements at the interface. The equivalent beam elements were created from all nodes of the cross-sectional interface with the respect of the longitudinal specimen axis. The maximum bond strength of 0.55 MPa suggested by ACI 318 [34] was adopted for the equivalent beam elements. Detailled configuration of the FE model with the equivalent beam elements is illustrated in Fig. 15.

For the equivalent beam elements, an elastic-plastic characteristic was adopted as shown in Fig. 15(d), and Mat-03 described in Section 2.3 was used. The equivalent bond strength $f_{y,eb}$ was derived from the maximum bond (0.55 MPa [34]), and the Young's modulus E_{eb} at the equivalent state was given as:

$$E_{eb} = \frac{E_c}{2(1+v_c)} \frac{A_c}{A_{eb}} \frac{L_{eb}}{t_{c,bond}} \tag{4}$$

where E_c, v_c, and A_c are the Young's modulus, poison ratio, and concrete area of the NSC, respectively; A_{eb} and L_{eb} are the area and length of the equivalent beam element, respectively; and $t_{c,bond}$ is the bond thickness assumed to be 1 mm.

The yield strength of the equivalent beam elements was defined based on the equivalent bond strength of UHPC to NSC substrate. Because previous investigations on the bond strength of NSC to UHPC have been very limited in previous studies [9], a maximum bond strength of 0.55 MPa, as suggested by ACI 318 [34] for intentionally roughened surfaces, was adopted. The yield strength $f_{y,eb}$ was then given as

$$f_{y,eb} = \frac{\tau_{\max} A_c}{A_{eb}} \tag{5}$$

where τ_{max} is the maximum bond strength (τ_{max} = 0.55 MPa [34]).

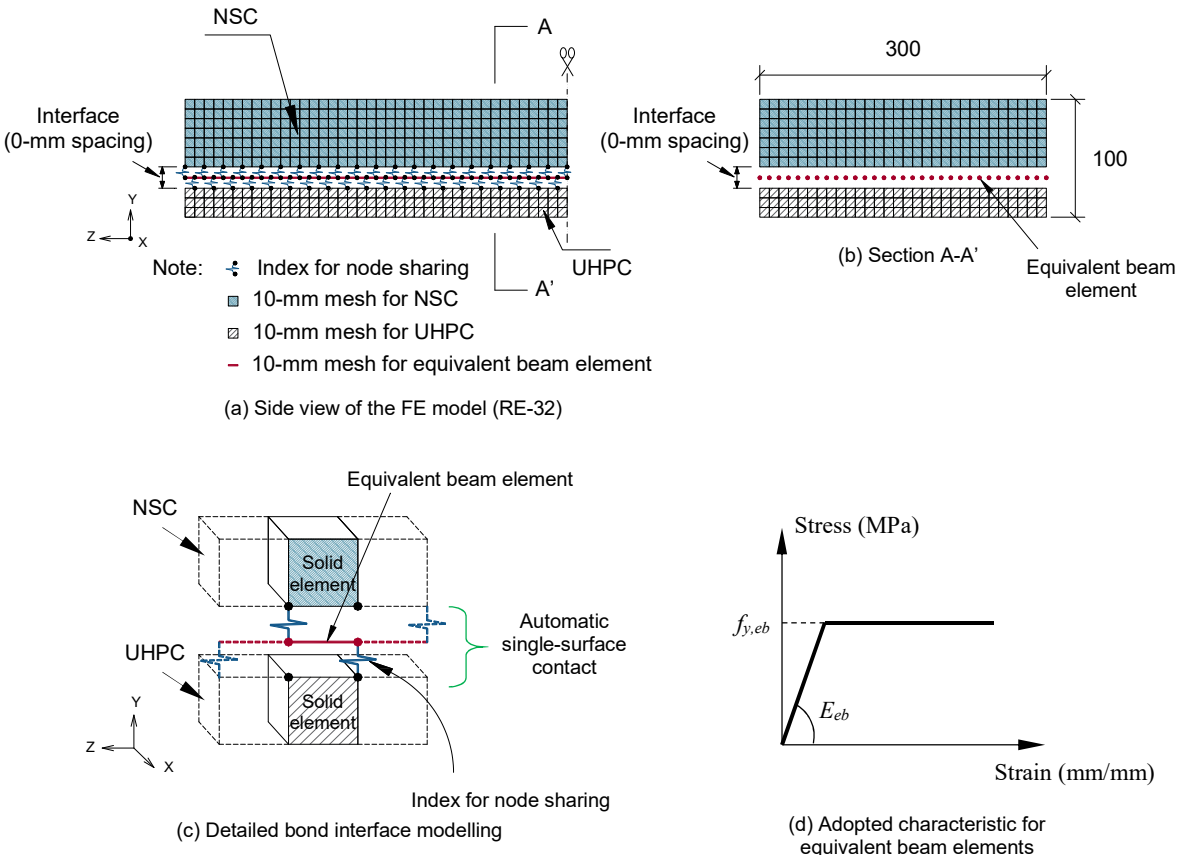

Figure 15: Details of FE modelling for UHPC-concrete composite members [34].

Tables 6 and 7 list the model parameters used in the numerical simulation for all specimens described in Section 5.1.1. In the tables, it should be noticed that equal parameters were applied to all material models for both implicit and explicit analyses, except UHPC material. Two different sets of concrete model parameters were used as shown in Table 6.

Table 6: Concrete model parameters used in the numerical simulation for NSC/UHPC materials of non-composite and composite specimens.

NSC				UHPC							
Implicit/explicit				Implicit				Explicit			
b_2	w_c (mm)	f_t (MPa)	f'_c (MPa)	b_2	w_c (mm)	f_t (MPa)	f'_c (MPa)	b_2	w_c (mm)	f_t (MPa)	f'_c (MPa)
–10	25.18	3	23	–25	13	10.5	153	–8	10	10.5	153

Note:
f'_c: Compressive strength of NSC/UHPC
f_t: Tensile strength of NSC/UHPC
b_2: Tension softening concrete parameter of concrete damage model
w_c: Localised crack width of concrete damage model

Table 7: Material properties used in the numerical simulation for longitudinal steel and equivalent beam element.

Longitudinal steel		Equivalent beam element	
Implicit/explicit		Implicit/explicit	
f_y (MPa)	E_s (GPa)	$f_{y,eb}$ (MPa)	E_{eb} (GPa)
502	200	Equivalent maximum bond strength (τ_{max} = 0.55 MPa [34])	Equivalent Young's modulus of NSC

Note:
f_y: Yield strength of longitudinal steel
E_s: Young's modulus of longitudinal steel
$f_{y,eb}$: Yield strength of equivalent beam element
E_{eb}: Young's modulus of equivalent beam element

For the numerical simulation under static loading, the detailed FE model could be found in [17, 32, 33]. For the numerical simulation under cyclic loading, the rigid rollers and plates were used for loading application and supports (see Fig. 2), respectively. For blast simulation, similar to the cyclic simulation, rigid support plates were created and fixed in all directions. The general overview of FE model for blast response is shown in Fig. 16. In the blast simulation (explicit analysis), the damping effect was also considered with an assumed damping ratio of 5% same as described in Section 4.

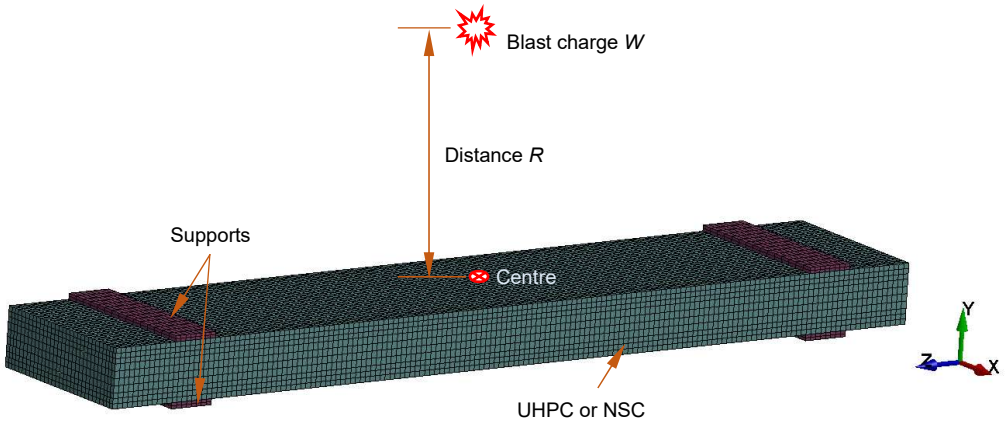

Figure 16: Configuration of FE model for blast simulation.

5.1.3. Description of loading conditions

In static analysis, as described in Section 3.1.1, two different loading rates of 2×10^{-5} and 2×10^{-3} m/s were adopted for monotonic loading for implicit and explicit analyses, respectively. A three-point loading test setup was used for the specimens shown in Section 5.1.1. The monotonic loading was applied directly to the nodes at the mid-span of the specimens. The displacement-controlled loading was used. For cyclic loading, as described in Section 3.1.2, the loading rate of 2×10^{-5} m/s was used for implicit analysis. For explicit analysis, the cyclic loading rate of 2×10^{-3} m/s and the constant time step of dt = 1.5×10^{-5} s were adopted. Two rigid rollers (see Fig. 2) were modelled and used for loading application. The boundary-prescribed-motion-rigid with displacement-controlled loading was used.

For blast loading, as described in Section 3.2, the load-blast-enhanced function was employed. The blast charge W was positioned at the distance R from the centre of the top surface of the specimens (see Fig. 16).

5.1.4. Description of parameter study for blast simulation

In the present study, three different blast charge weights (W) of 1, 5, and 10 kg TNT were used for each specimen, and installed at a constant distance (R) of 1.5 m from the centre of the specimens. The blast simulation program is shown in Table 8. It should be noted that two additional simulations on reversed UHPC-concrete composite specimens, $(\text{RE-32})_{REV}$ and $(\text{OV-50})_{REV}$, were conducted. These investigations could reflect the effect of UHPC strengthening layer subjected to blast in comparison to the responses of the blasting on the NSC part of the composites.

Table 8: Parameter study program for blast simulation on UHPC-concrete composite members.

Description	Specimen	h_U (mm)	R (m)	W (kg)	Z (m/kg$^{1/3}$)
Non-composite NSC	RE-0	-	1.5	1	1.50
		-	1.5	5	0.88
		-	1.5	10	1.69
Non-composite UHPC	RE-100	100	1.5	1	1.50
		100	1.5	5	0.88
		100	1.5	10	1.69
UHPC-concrete composite (NSC faced to detonation)	RE-32	32	1.5	1	1.50
		32	1.5	5	0.88
		32	1.5	10	1.69
	OV-50	50	1.5	1	1.50
		50	1.5	5	0.88
		50	1.5	10	1.69
UHPC-concrete composite (UHPC faced to detonation)	$(\text{RE-32})_{\text{REV}}$	32	1.5	1	1.50
		32	1.5	5	0.88
		32	1.5	10	1.69
	$(\text{OV-50})_{\text{REV}}$	50	1.5	1	1.50
		50	1.5	5	0.88
		50	1.5	10	1.69

Note:
h_U: UHPC thickness
R: Charge distance
W: TNT equivalent charge
Z: Scaled distance, $Z = R/(W)^{1/3}$
$(\text{specimen})_{\text{REV}}$: Composite specimens were turned upsidedown in order to investigate the effect of UHPC layer directly subjected to blast loading in comparison to the respective original layouts where NSC was subjected to blast.

5.2. Simulation results under static loading

5.2.1. Numerical results of monotonic loading

Fig. 17 shows the comparisons of load-deflection curves obtained from static simulations and the experiments. It should be mentioned that the numerical results using implicit solver were conducted in the previous study [32]. However, the present study added new simulation results using explicit solver on all specimens presented in Section 5.1.1, except RE-32, which was previously reported in [33]. As seen from Fig. 17, the implicit and explicit load-deflection curves revealed the similar performance, and agreed well with the experimental results. Based

on this agreement, the implicit and explicit analyses are further conducted on cyclic response of the specimens in Section 5.2.2.

As earlier discussed in Section 4.2, the numerical model developed using explicit method for the static behaviour of the structural members used for the blast response showed reasonable results. The numerical model using explicit method in this section, similar to the case in Section 4.2, was adopted for the blast simulation of UHPC-concrete composite members. Simulated blast results are shown in Section 5.3.

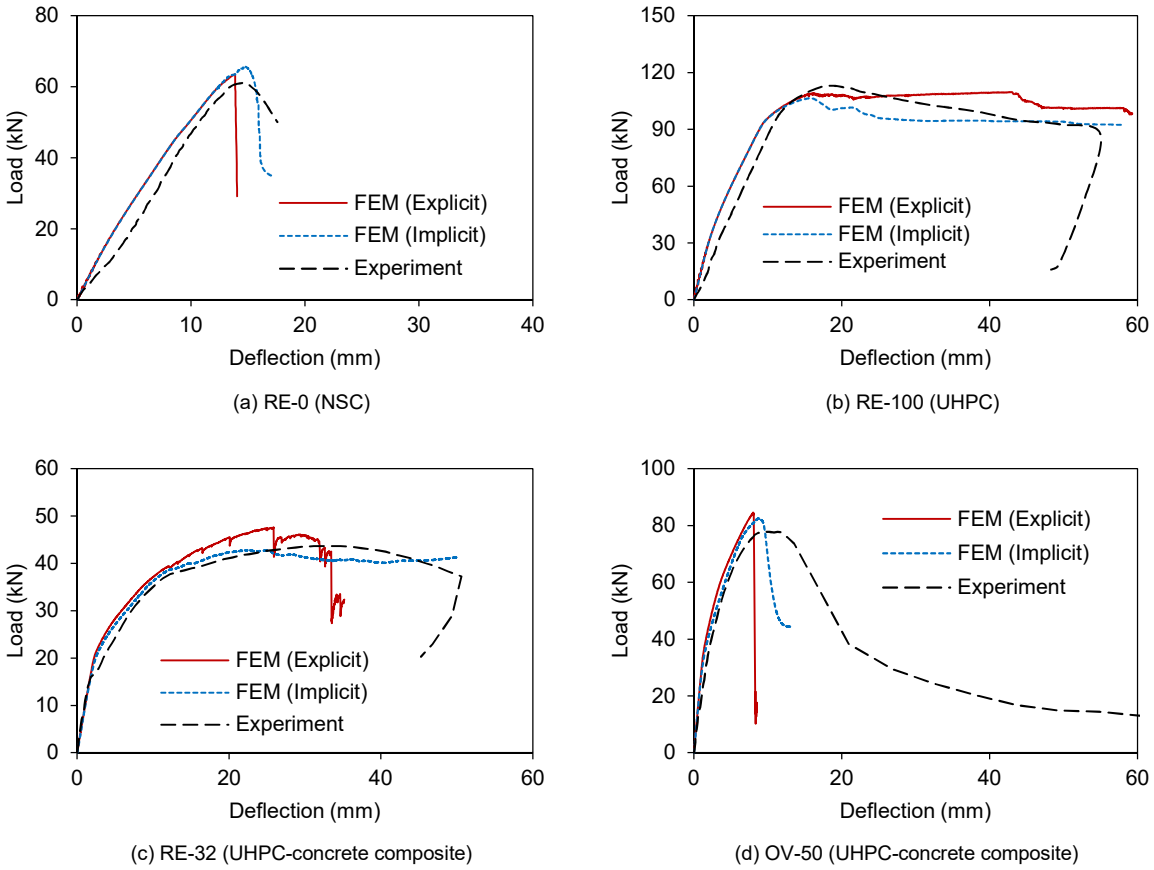

Figure 17: Comparisons of load-deflection curves obtained from numerical simulation under static loading.

5.2.2. Numerical results of cyclic loading

Fig. 18 compares the cyclic responses extracted from the implicit and explicit methods. It was observed that at given small range of cyclic displacements, the peak loads for both implicit and explicit methods agreed well, while at given large cyclic displacements, the cyclic peak loads obtained from implicit solver gave higher than those from explicit solver did. Although no experimental results were conducted to validate the numerical models, the cyclic simulations showed very promising results. The numerical model could be able to use for the improvement of the cyclic analysis.

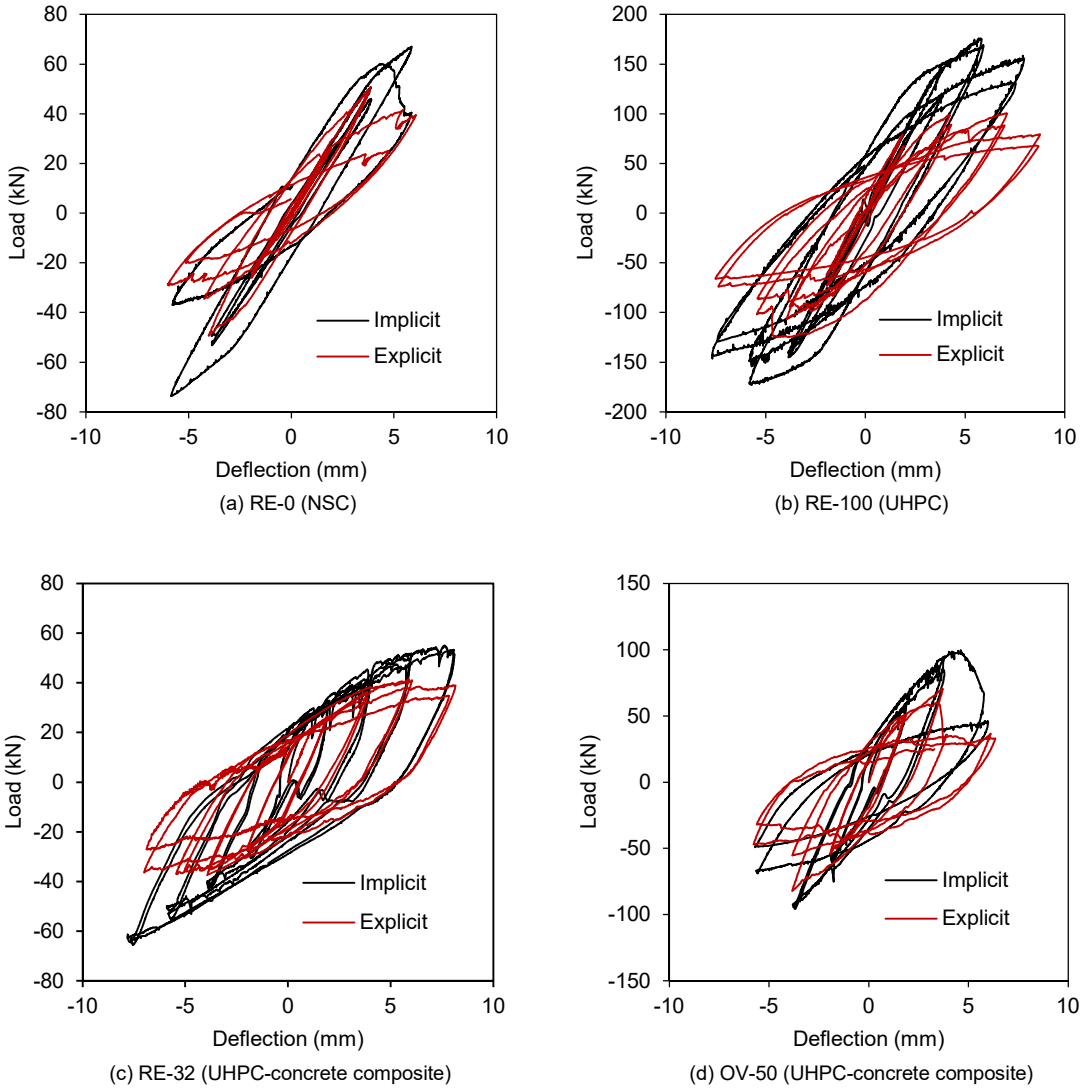

Figure 18: Comparisons of load-deflection responses obtained for numerical simulation under cyclic loading.

5.3. Simulation results under blast loading

5.3.1. Blast response for non-composite NSC and UHPC specimens

Fig. 19 shows the comparisons of the simulated blast responses of non-composite NSC specimen RE-0 and UHPC specimen RE-100 under three blast loading weights 1, 5, and 10 kg TNT. It can be clearly seen that UHPC significantly enhances blast resistance by reducing the maximum and residual deflection at the midspan of specimen RE-100 compared to those of the specimen RE-0.

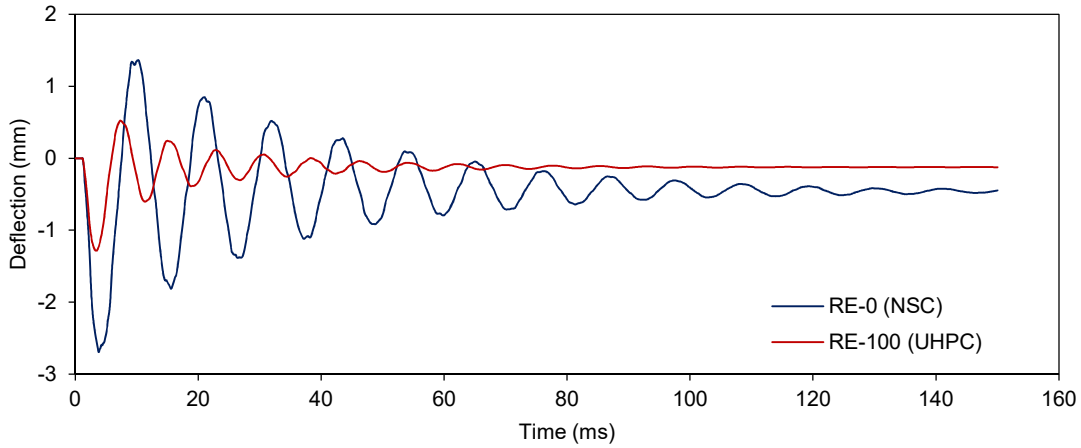

(a) Blast charge weight of 1 kg TNT

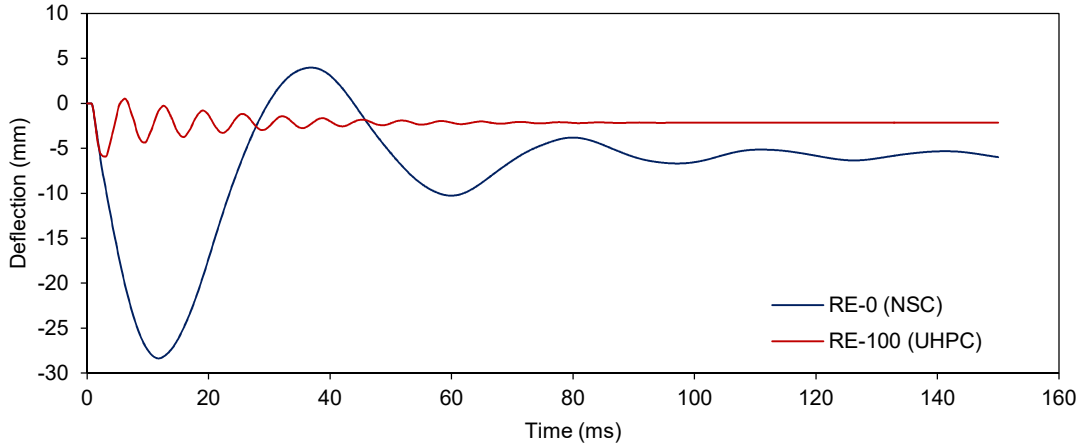

(b) Blast charge weight of 5 kg TNT

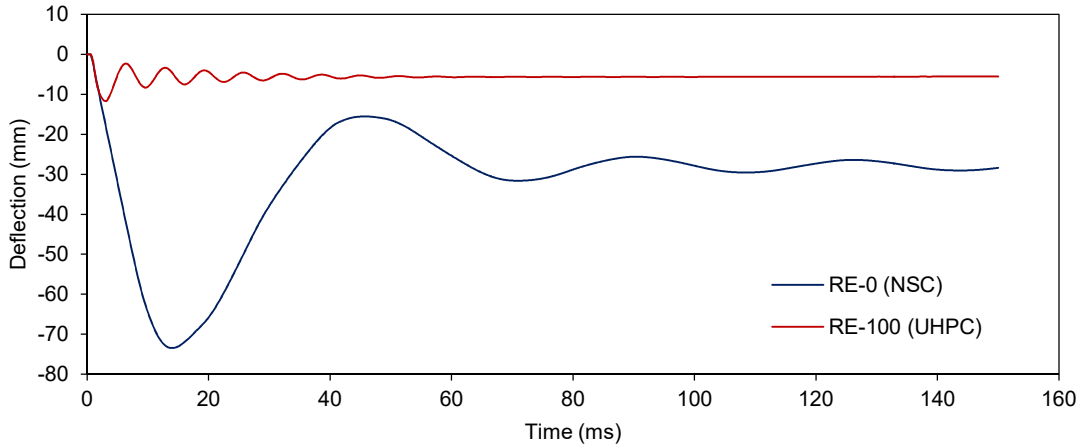

(c) Blast charge weight of 10 kg TNT

Figure 19: Comparisons of simulated deflection-time histories for non-composite RE-0 (NSC) and RE-100 (UHPC).

5.3.2. Blast response for UHPC-concrete composite specimens

Fig. 20 compares the simulated deflection-time curves of composite specimen RE-32 with those of non-composite NSC specimen RE-0 and UHPC specimen RE-100. It should be mentioned

that the specimen RE-32, which was strengthened with 32-mm UHPC thickness, had same total height of 100 mm as RE-0 or RE-100 (see Fig. 14). The simulation response under low blast weight of 1 kg TNT showed the maximum deflection of RE-32 similar to that of RE-0 as shown in Fig. 20(a). It was, however, clearly seen from Fig. 20(b) and (c) that UHPC strengthening layer significantly improves the blast resistance compared to the conventional NSC specimen RE-0 under blast weights of 5 and 10 kg TNT.

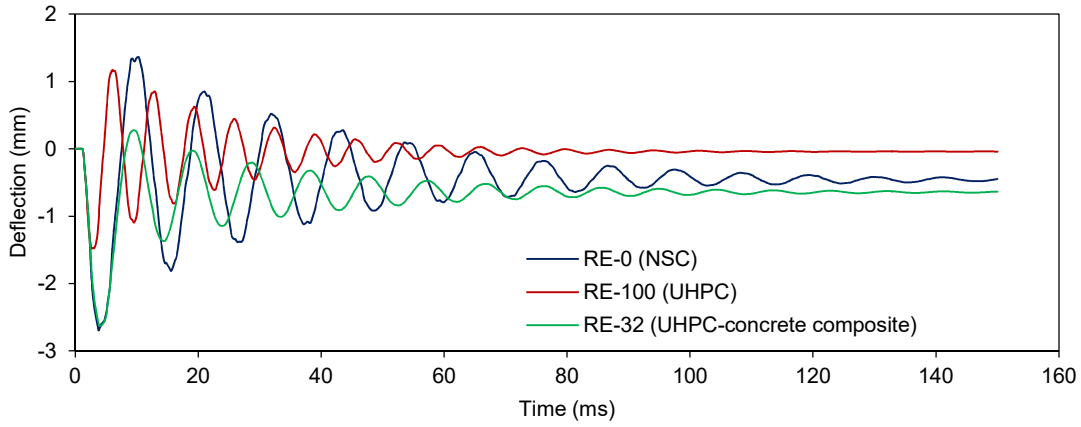

(a) Blast charge weight of 1 kg TNT

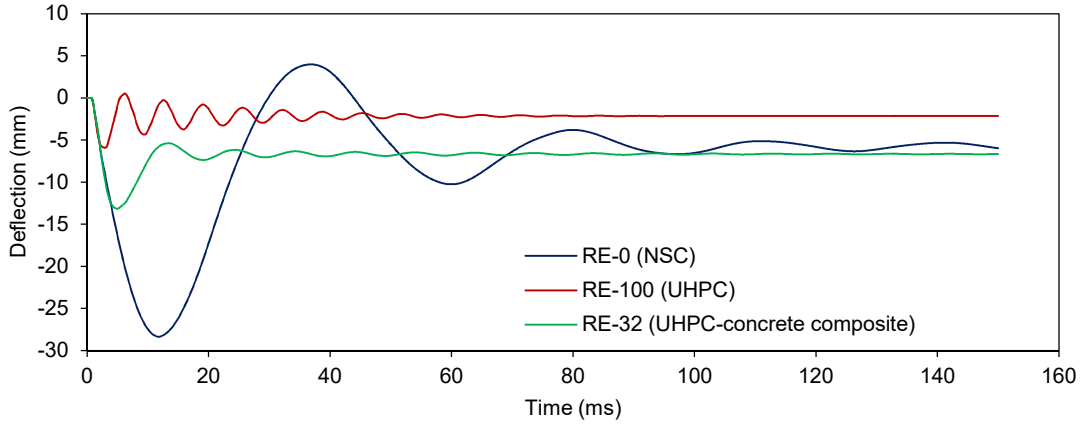

(b) Blast charge weight of 5 kg TNT

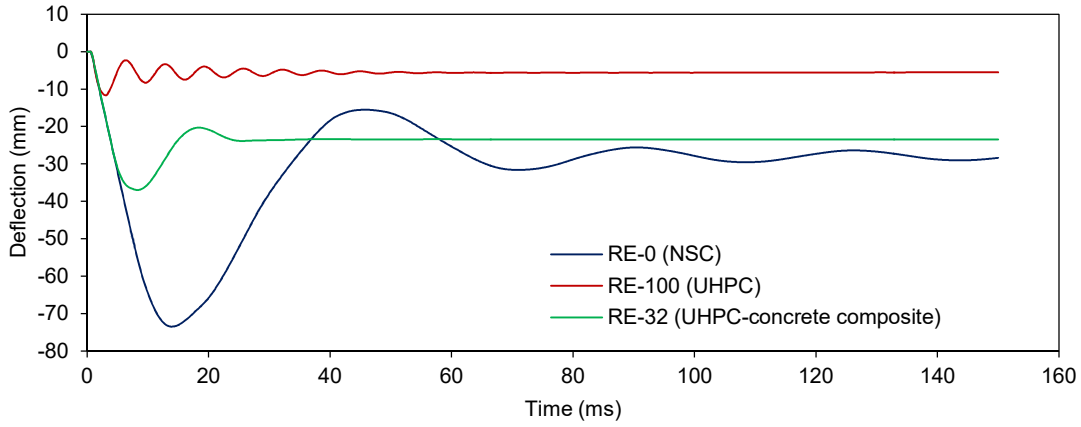

(c) Blast charge weight of 10 kg TNT

Figure 20: Comparisons of simulated deflection-time histories for UHPC-concrete composite specimen RE-32, and non-composite specimens RE-0 (NSC) and RE-100 (UHPC).

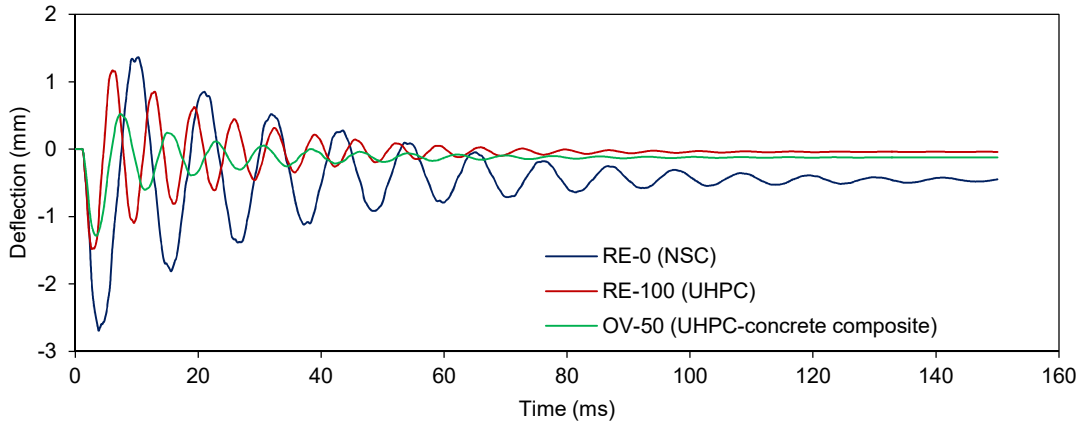

(a) Blast charge weight of 1 kg TNT

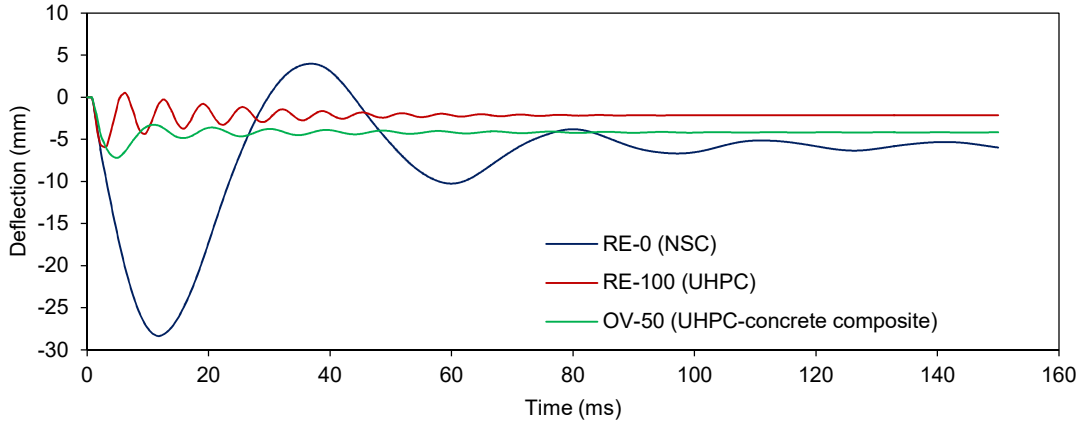

(b) Blast charge weight of 5 kg TNT

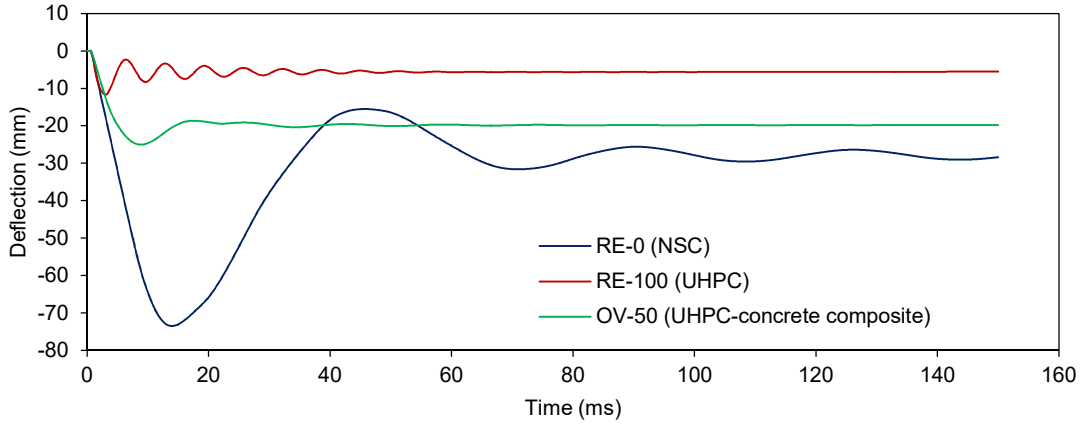

(c) Blast charge weight of 10 kg TNT

Figure 21: Comparisons of simulated deflection-time histories for UHPC-concrete composite specimen OV-50, and non-composite specimens RE-0 (NSC) and RE-100 (UHPC).

Fig. 21 compares the simulated deflection-time curves of composite specimen OV-50 with those of RE-0 and RE-100. Once again, the simulated results of OV-50 showed that UHPC layer significantly improves the blast resistance compared to those of RE-0. It can be noted that the blast responses of UHPC specimen RE-100 showed high reduction maximum deflection compared to those of composite specimens RE-32 and OV-50. The improvement of blast resistance of RE-100 might be because of the UHPC facing directly to the detonation. It is,

therefore, of interest to investigate the effect of different positions of UHPC layer on the blast response. Results of this effect are described in the following section.

5.3.3. Effect of position of UHPC strengthening layer

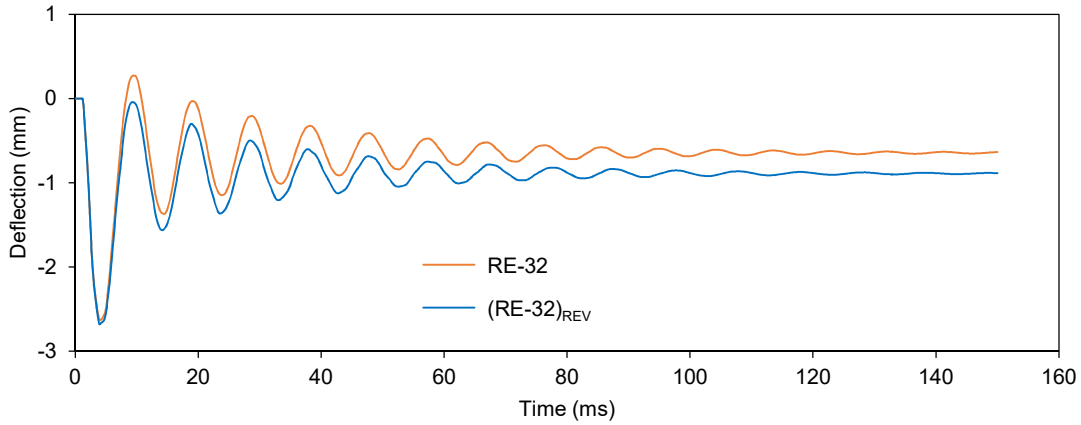

(a) Blast charge weight of 1 kg TNT

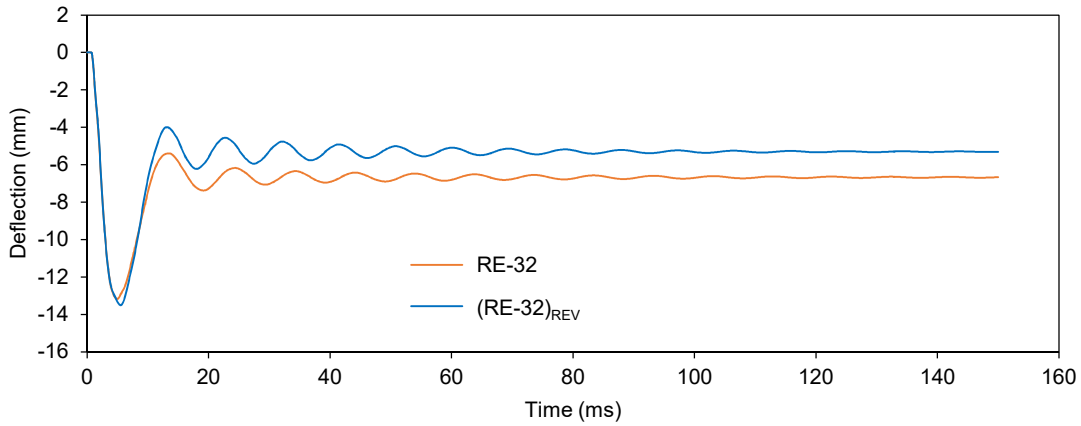

(b) Blast charge weight of 5 kg TNT

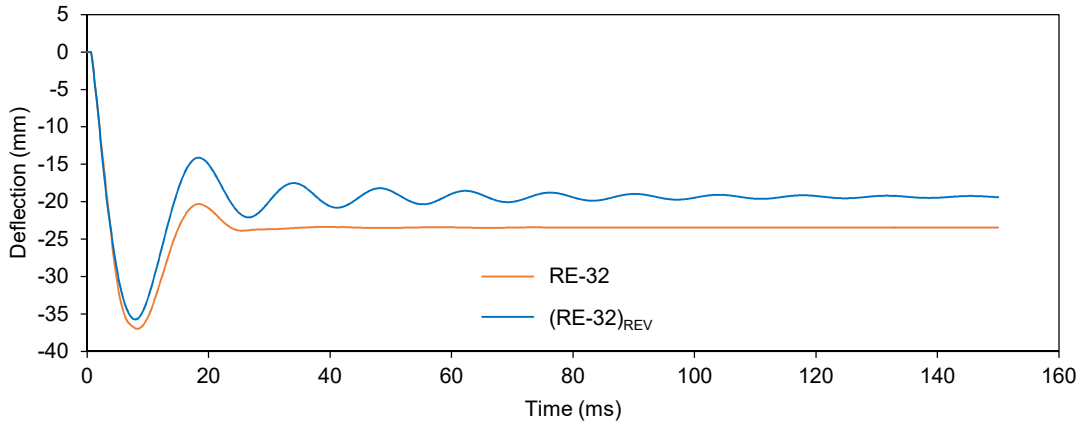

(c) Blast charge weight of 10 kg TNT

Figure 22: Comparisons of simulated deflection-time histories of RE-32 and $(RE\text{-}32)_{REV}$.

This section is to figure out the effect of position of UHPC layer on the blast response of composite UHPC-concrete members. For this purpose, blast simulations were conducted on

reversed composite UHPC-concrete specimens, which were named as (RE-32)$_{REV}$ and (OV-50)$_{REV}$. This was done to allow the position of UHPC layer to face directly towards the blast wave. The numerical results of (RE-32)$_{REV}$ and (OV-50)$_{REV}$ were obtained and compared to the respective original specimens RE-32 and OV-50 as shown in Figs. 22 and 23. The simulated deflection-time curves showed that the direct blast on UHPC layer for the reversion could serve a better improvement of the blast response. As seen in Figs. 22(c) or 23(c), the peak deflections of (RE-32)$_{REV}$ and (OV-50)$_{REV}$ were reduced compared to those of RE-32 and OV-50.

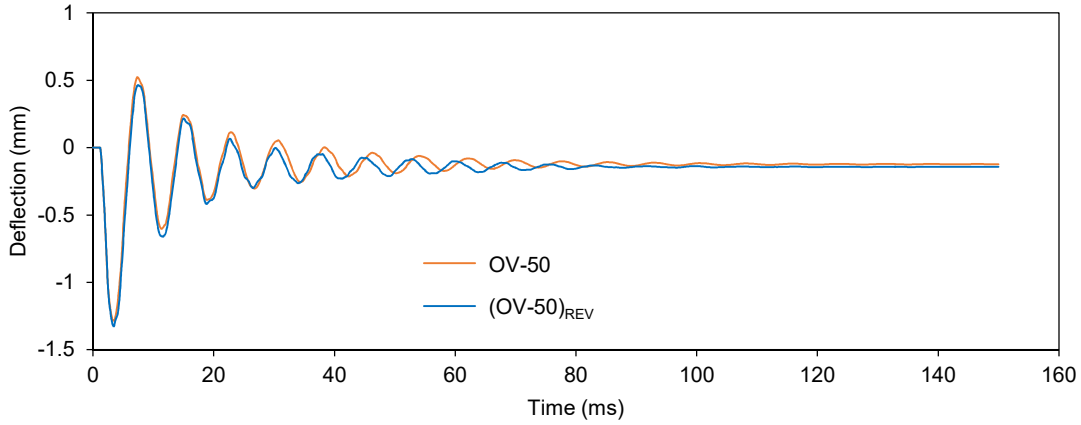

(a) Blast charge weight of 1 kg TNT

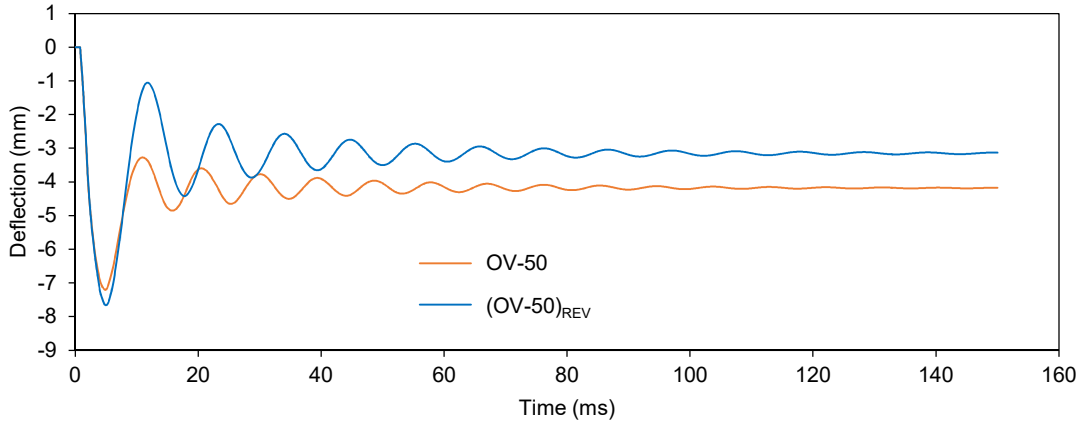

(b) Blast charge weight of 5 kg TNT

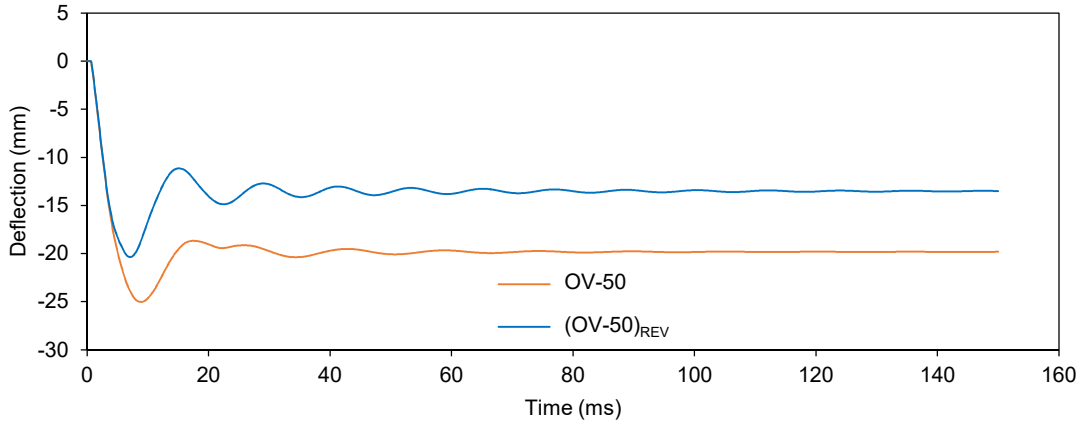

(c) Blast charge weight of 10 kg TNT

Figure 23: Comparisons of simulated deflection-time histories of OV-50 and (OV-50)$_{REV}$.

6. Conclusions

The static and dynamic behaviour of composite RC members strengthened with UHPC using the FE modelling was presented. In the numerical simulation for static behaviour, both implicit and explicit methods in LS-DYNA were used. The numerical results were compared with the experimental results. For dynamic behaviour of composite UHPC-concrete members, blast simulations were conducted using explicit method developed in static FE model. The blast responses were carried out with parameter study including different blast charge weights. From this study, the conclusions could be drawn as follows.

(1) The implicit and explicit methods could be used in the numerical simulation for static behaviour of composite UHPC-concrete members. Both methods could produce similar load-deflection curves by using individually different set of concrete damage model parameters. It showed that the simulation results agreed well with experimental results.

(2) The dynamic behaviour of non-composite RC or UHPC members under blast loading was well predicted using the developed FE model. Using equal static model parameters of explicit method in the blast simulation, the simulated deflection-time histories fairly agreed with the blast test results in the literature.

(3) The blast resistance response of composite UHPC-concrete members showed that UHPC strengthening layer significantly improves the blast resistance of the members. UHPC layer could reduce the maximum deflection as compared to the conventional RC members.

(4) The comparison of the response of the UHPC layer positioned towards the detonation with that of the blast on NSC part was presented. It showed that the UHPC layer positioned with the face towards the detonation could result in a better control of the peak deflection at the same blast loads.

(5) An adopted damping ration of 5% used throughout the blast simulations could yield a reasonable accuracy of the FE model.

Acknowledgments

The authors are grateful to the Toda Scholarship Foundation 2017 Research Grant for financial support for this work.

References

[1] Richard P, Cheyrezy M. Composition of reactive powder concretes. Cem Concr Res 1995;25:1501-11.
[2] Brühwiler E, Denarie E. Rehabilitation of concrete structures using ultra-high performance fibre reinforced concrete. In: proc. UHPC-2008: The Second International Symposium on Ultra High Performance Concrete; 2008:05-07.
[3] Tayeh BA, Bakar BA, Johari MM, Voo YL. Utilization of ultra-high performance fibre concrete (UHPFC) for rehabilitation–a review. Procedia Eng 2013;54:525-38.
[4] Alaee FJ, Karihaloo BL. Retrofitting of reinforced concrete beams with CARDIFRC. J Compos Constr 2003;7:174-86.

[5] Noshiravani T, Brühwiler E. Experimental investigation on reinforced ultra-high-performance fiber-reinforced concrete composite beams subjected to combined bending and shear. ACI Struct J 2013;110(2):251-62.
[6] Safdar M, Matsumoto T, Kakuma K. Flexural behavior of reinforced concrete beams repaired with UHPFRC. Compos Struct 2016;157:448-60.
[7] Yin H, Teo W, Shirai K. Experimental investigation on the behaviour of reinforced concrete slabs strengthened with ultra-high performance concrete. Constr Build Mater 2017;155:463-74.
[8] Tayeh BA, Bakar BA, Johari MM, Voo YL. Mechanical and permeability properties of the interface between normal concrete substrate and ultra high performance fiber concrete overlay. Constr Build Mater 2012;36:538-48.
[9] Harris DK, Muñoz MAC, Gheitasi A, Ahlborn TM, Rush SV. The challenges related to interface bond characterization of ultra-high-performance concrete with implications for bridge rehabilitation practices. Adv Civil Eng Mater 2014;4(2):75-101.
[10] Yi NH, Kim JHJ, Han TS, Cho YG, Lee JH. Blast-resistant characteristics of ultra-high strength concrete and reactive powder concrete. Constr Build Mater 2012;28:694-707.
[11] Li J, Wu C, Hao H, Wang Z, Su Y. Experimental investigation of ultra-high performance concrete slabs under contact explosions. Inter J Impact Eng 2016;93:62-75.
[12] Li J, Wu C, Hao H, Su Y. Experimental and numerical study on steel wire mesh reinforced concrete slab under contact explosion. Mater Des 2017;116:77-91.
[13] Mao L, Barnett S, Begg D, Schleyer G, Wight G. Numerical simulation of ultra high performance fibre reinforced concrete panel subjected to blast loading. Int J Impact Eng 2014;64:91-100.
[14] Mao L, Barnett SJ, Tyas A, Warren J, Schleyer G, Zaini S. Response of small scale ultra high performance fibre reinforced concrete slabs to blast loading. Constr Build Mater 2015;93:822-30.
[15] LS-DYNA Keyword User's Manual, Livermore, CA; 2015.
[16] Malvar LJ, Crawford JE, Wesevich JW, Simons D. A plasticity concrete material model for DYNA3D. Int J Impact Eng 1997;19(9)-(10):847-73.
[17] Yin H, Shirai K, Teo W. Finite element modelling to predict the flexural behaviour of ultra-high performance concrete members. Eng Struct (under review); 2018.
[18] Li J, Zhang Y. Evolution and calibration of a numerical model for modelling of hybrid-fibre ECC panels under high-velocity impact. Compos Struct 2011;93(11):2714-22.
[19] J Li J, Hao H. Numerical study of concrete spall damage to blast loads. Int J Impact Eng 2014;68:41-55.
[20] Magallanes JM, Wu Y, Malvar LJ, Crawford JE. Recent improvements to release III of the K&C concrete model. In: 11th international LS-DYNA Users conference; 2010:6-8.
[21] CEB-FIP MC 90. Design of concrete structures. CEB-FIP-Model Code 1990. Thomas Telford; 1993.
[22] Ngo T, Mendis P, Krauthammer T. Behavior of ultrahigh-strength prestressed concrete panels subjected to blast loading. J Struct Eng 2007;133:1582-90.
[23] Teng TL, Chu YA, Chang FA, Shen BC, Cheng DS. Development and validation of numerical model of steel fiber reinforced concrete for high-velocity impact. Comput Mater Sci 2008;42:90-9.
[24] Wang Z, Wu J, Wang J. Experimental and numerical analysis on effect of fibre aspect ratio on mechanical properties of SRFC. Constr Build Mater 2010;24:559-65.
[25] Lin X, Zhang Y, Hazell PJ. Modelling the response of reinforced concrete panels under blast loading. Mater Des 2014;56:620-28.
[26] Chen W, Hao H, Chen S. Numerical analysis of prestressed reinforced concrete beam subjected to blast loading. Mater Des 2015;65:662-74.

[27] Mays G, Smith PD. Blast effects on buildings: Design of buildings to optimize resistance to blast loading. London: Thomas Telford; 1995.
[28] US Army, US Navy, US Air Force. Structures to resist the effects of accidental explosions. TM5-1300, NAVFAC P-397, AFR 88-22; 1990.
[29] Ngo T, Mendis P, Gupta A, Ramsay J. Blast loading and blast effects on structures—an overview. Electron J Struct Eng 2007;7:76-91.
[30] UFC 3-340-02. Design and analysis of hardened structures to conventional weapons effects. Washington, DC, USA; 2008.
[31] Li J, Wu C, Hao H, Su Y. Investigation of ultra-high performance concrete under static and blast loads. Inter J Protect Struct 2015;6:217-35.
[32] Yin H, Shirai K, Teo W. Numerical model for predicting the structural response of composite UHPC–concrete members considering the bond strength at the interface. Compos Struct (under review); 2018.
[33] Yin H, Shirai K, Teo W. Response of UHPC-concrete composite structural members using implicit and explicit finite element method. The 3rd International Conference on Advanced Functional Materials (ICAFM 2018), San Francisco, United States, August 3–5; 2018 (accepted).
[34] ACI 318 Committee. Building code requirements for structural concrete and commentary. American Concrete Institute; 2008.

Chapter VI

Paper V

Prediction of shear capacity of UHPC–concrete composite structural members based on existing codes

The content of this Chapter VI has been submitted for consideration for publication as follows.

Hor Yin, Kazutaka Shirai, Wee Teo, "Prediction of shear capacity of UHPC–concrete composite structural members based on existing codes," Journal of Civil Engineering and Management, (submitted date: 25 May 2018, under review).

Prediction of shear capacity of UHPC–concrete composite structural members based on existing codes

Abstract

Reinforced concrete (RC) structural members strengthened with ultrahigh-performance concrete (UHPC) have shown excellent performance in past experimental investigations. However, methods of predicting their capacity are currently very limited. This paper presents six independent methods of predicting the shear capacity of UHPC–concrete composite members based on the application of existing design codes. Three of these methods are based on the conversion of the volume fraction of steel fibres in the UHPC in an equivalent longitudinal steel ratio. The other three methods involve the computation of the shear strength as a sum of the contributions to the shear strength by the RC member and the UHPC layer, each of which is independently calculated. It was demonstrated that the proposed methods based on existing design codes are able to predict the strength of UHPC–concrete composite members with reasonable accuracy.

Keywords: Ultrahigh-performance concrete; reinforced concrete; composite members; code prediction; shear strength; UHPC layer

Introduction

Recently, ultrahigh-performance concrete (UHPC) has been increasingly considered as a potential tool in strengthening reinforced concrete (RC) structural elements. Methods of using UHPC to strengthen parts of structures that fully exploit the outstanding properties of UHPC have been proposed by Brühwiler and Denarie (2008). They validated these methods using four full-scale applications. Their study has demonstrated that UHPC is excellently suited for use in either cast-in-situ or precast applications.

Over the last two decades, many experimental studies have been conducted on UHPC–concrete composite members (Brühwiler, Denarie 2008; Alaee, Karihaloo 2003; Habel et al. 2007; Noshiravani, Brühwiler 2013; Yin et al. 2017). The excellent properties of UHPC in terms of strain hardening and energy absorption (Graybeal, Baby 2013; Habel 2004; Yoo, Banthia 2016; Graybeal 2005; Yoo, Yoon 2016; Wille et al. 2014) lead to members showing significantly improved structural performance after being strengthened with a UHPC layer. In addition, UHPC has been applied to the strengthening of RC members in the form of precast plates (Alaee, Karihaloo 2003), overlays (Habel et al. 2007; Noshiravani, Brühwiler 2013; Oesterlee 2010), and patch material for rehabilitation (Yin et al. 2017). UHPC has been shown to greatly influence the overall response of structural members, including their cracking development patterns, ultimate strength, and ductility.

However, studies on analytical methods for the shear strength prediction of composite structural members have been very limited. Noshiravani and Brühwiler (2013) have reported an analytical model for the flexural–shear resistance of composite beams. They adopted an elastic–plastic fictitious composite hinge model for the cracking in RC members and considered the interaction between the two elements of the composite members; however, this method requires several analytical steps.

For non-composite members, the structural capacity can be obtained using existing design codes. Several current design codes for RC structural members, such as ACI 318 (ACI

Committee 318 2008), or for fibre-reinforced concrete (FRC) members, such as ACI 544 (ACI Committee 544 1988), involve the calculation of the shear strength as the sum of the shear force resisted by normal-strength concrete (NSC) or UHPC and by shear reinforcement.

To date, no design provisions have been made available for the prediction of the shear capacity of UHPC–concrete composite members. Methods that can be used to predict the shear capacity are therefore needed. Applications based on the modification of existing design models of RC or FRC structures could be useful because they are simple and easy to use.

For this purpose, this paper introduces six methods of predicting the shear capacity of UHPC–concrete composite members based on modifications to existing design models. Nine UHPC–concrete composite slabs tested by Yin et al. (2017) were used to verify the proposed methods. The remainder of this paper is organized as follows. A brief description of the current design models for non-composite members is provided. The six methods are then described in detail, and the predicted shear capacities are verified against test results. Moreover, the predicted failure mode derived from the calculated flexural moment reported by Shirai et al. (2018) is discussed. In addition, the present paper expands on a previous study (Yin et al. 2018) by adding new methods, results, and findings.

1. Description of specimens and test results

1.1. Geometric details of specimens

This section gives the parameters of RC slabs strengthened with various UHPC configurations that were previously tested by Yin et al. (2017) and summarises the test results, which were used to validate the analytical methods in the present study. The full details of the previous experiment can be found in the original document (Yin et al. 2017).

Nine slabs were tested in the previous study. Five were classified into the RE series, which had UHPC patches of different thicknesses applied in the tension zone for the repair and rehabilitation of the structural members. All slabs in the RE series had five high-tensile-strength rebars of 12 mm in diameter at the top and bottom, as shown in Fig. 1. The other four slabs were classified as the OV series and had similar cross-sectional dimensions as RE series but with two additional UHPC overlay patches strengthening the tension zone. There were two slab specimens for each considered overlay thickness: one was not reinforced, whereas the other had five high-tensile-strength rebars of 10 mm in diameter as longitudinal reinforcement. The geometric and reinforcement details of the experimental specimens are summarised in Table 1.

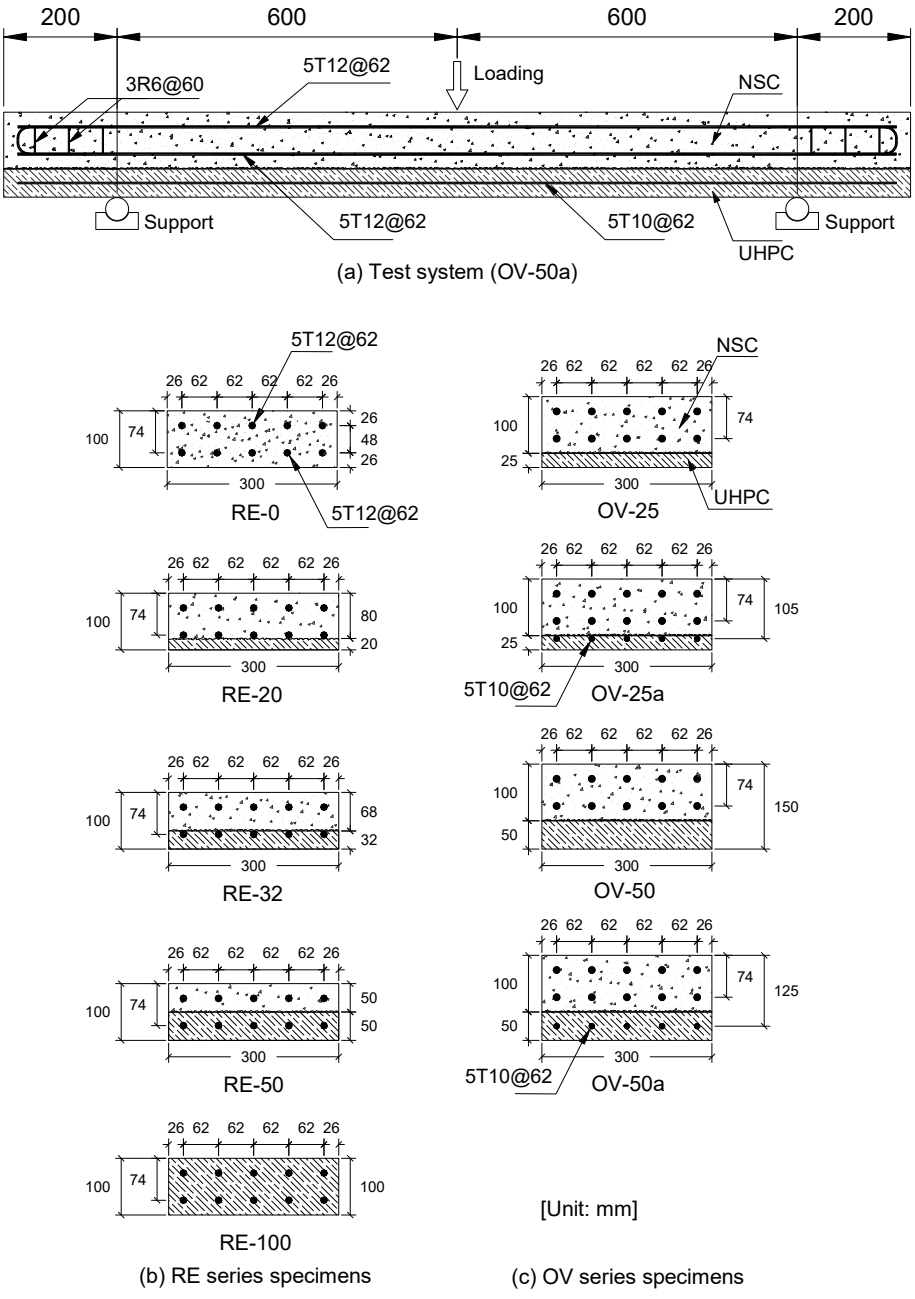

Fig. 1. Test system and specimen details (Yin et al. 2017).

Table 1. Details of the specimens (Yin et al. 2017).

Specimen	Geometric			Longitudinal reinforcement						
							T12		T10	
	b (mm)	h (mm)	h_U (mm)	A'_s (mm^2)	A_s (mm^2)	A_{sU} (mm^2)	f_y (MPa)	f_{max} (MPa)	f_y (MPa)	f_{max} (MPa)
RE-0	300	100	–	565	565	–	501.6	564.7	–	–
RE-20	300	100	20	565	565	–	501.6	564.7	–	–
RE-32	300	100	32	565	–	565	501.6	564.7	–	–
RE-50	300	100	50	565	–	565	501.6	564.7	–	–
RE-100	300	100	100	565	–	565	501.6	564.7	–	–
OV-25	300	125	25	565	565	–	501.6	564.7	–	–
OV-25a	300	125	25	565	565	393	501.6	564.7	474.9	506.6
OV-50	300	150	50	565	565	–	501.6	564.7	–	–
OV-50a	300	150	50	565	565	393	501.6	564.7	474.9	506.6

Note:
b width of the specimen
h height of the specimen
h_U thickness of the UHPC layer
A'_s area of the top longitudinal reinforcement
A_s area of the bottom longitudinal reinforcement
A_{sU} area of the longitudinal reinforcement provided in the UHPC layer
f_y yield strength of the longitudinal reinforcement
f_{max} maximum strength of the longitudinal reinforcement

1.2. Material properties

The average mechanical properties of the NSC and UHPC tested at day 28 are listed in Table 2. UHPC with a steel fibre volume fraction of 3% was adopted. Straight steel fibres of 13 mm in length and 0.2 mm in diameter were used. The detailed UHPC mix design and the procedures for the preparation of the slabs can be found in the original document (Yin et al. 2017). The longitudinal reinforcement properties are given in Table 1.

Table 2. Average mechanical properties of concrete (Yin et al. 2017).

Material	Compressive strength (MPa)	Flexural strength (MPa)	Young's modulus (GPa)
NSC	23	–	22.5[§]
UHPC	153	27.4	58.1[§]

[§] Calculated using $E_c = 4700(f'_c)^{0.5}$ where f'_c is the compressive strength in megapascals (ACI Committee 318 2008).

1.3. Summary of test results

Fig. 2 shows typical crack patterns of the RE and OV series after testing. The specimens in the RE and OV series mainly failed in flexure and shear, respectively. The debonding of the UHPC from the RC members induced by shear cracks was also observed in the OV series.

Fig. 3(a) and (b) illustrates the load–deflection curves of the specimens of the RE and OV series, respectively. As shown in Fig. 3(a), all rehabilitated slabs (RE-20, RE-32, and RE-50) experienced extensive deflection hardening and ductility during the post-cracking stage. Although no improvement to the ultimate load was found in any of the rehabilitated slabs in

comparison with RE-0 (Fig. 3(a)), it was reached at a larger displacement as a result of the excellent energy absorption capabilities of the rehabilitated slabs (Yin et al. 2017).

For the OV series (Fig. 3(b)), because of the strengthening effect, including the increase in the total specimen height, the RC members with a UHPC layer in the tension zone showed an enhanced overall response, including improved stiffness and load carrying capacity, in comparison with RE-0. Although the initial stiffness of the specimens containing reinforcing bars in the UHPC did not seem to differ from that of the specimens without rebar, as demonstrated by the similarity in the behaviour of OV-50 and OV-50a, the reinforcing bars in the UHPC increased the ultimate load of the members relative to their non-reinforced counterparts (Yin et al. 2017).

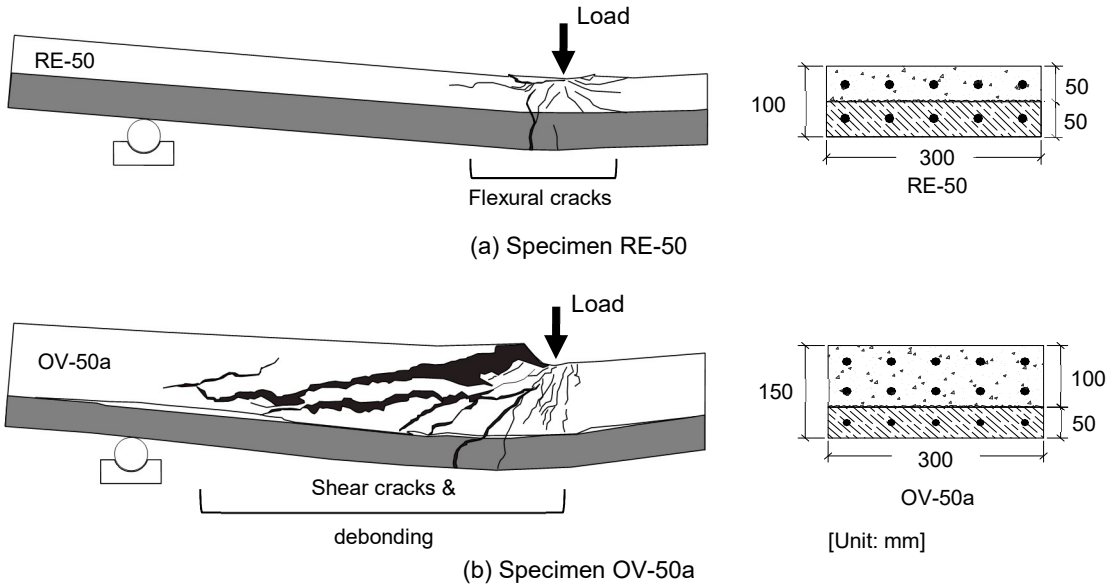

Fig. 2. Typical crack patterns observed for the specimens in the RE and OV series (Yin et al. 2017).

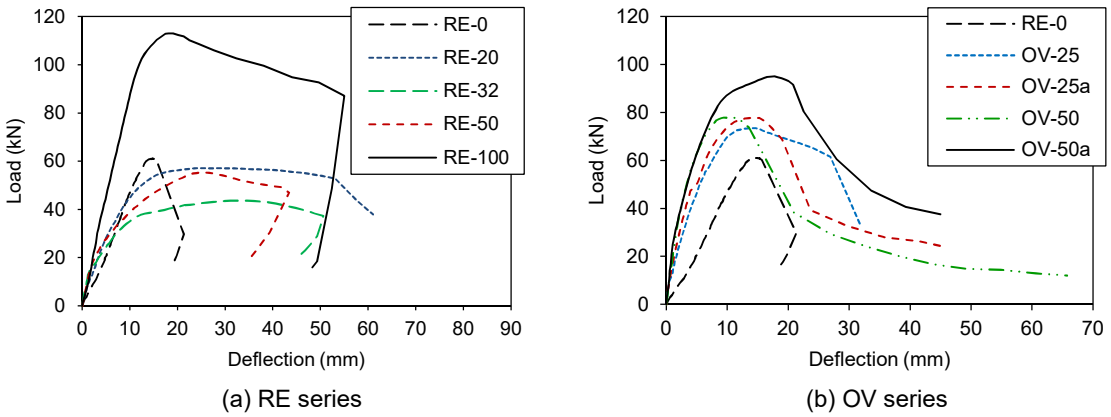

Fig. 3. Load–deflection curves of the test specimens (Yin et al. 2017).

2. Review of existing design codes

2.1. Design shear strength models for RC members

Current design provisions for non-composite RC members, including ACI 318 (ACI Committee 318 2008), EC2 (Eurocode 2: EN 1992-1-1 2004), and JSCE-2007 (JSCE Concrete Committee 2010), adopt similar approaches for calculating the nominal shear capacity V_n as a sum of the contributions of the transverse reinforcement, V_s, and the concrete, V_c, as follows

$$V_n = V_s + V_c. \tag{1}$$

For shear reinforcement (stirrups), V_s is given as $V_s = A_{sw}f_{yt}d/s$, where A_{sw} is the area of shear reinforcement, f_{yt} is the yield strength of stirrups, d is the effective depth, and s is the spacing of the stirrups. For concrete, V_c can be expressed as follows for the considered design codes.

– Design code ACI 318

$$V_c = \left(0.16\lambda\sqrt{f_c^{'}} + 17\rho_s \frac{V_u d}{M_u} \right) b_w d \,, \tag{2}$$

where λ is the reduction factor, f'_c [MPa] is the compressive strength of concrete, ρ_s is the longitudinal ratio, V_u is the shear force, M_u is the ultimate moment, d is the effective depth, and b_w is the web width.

– Design code EC2

$$V_c = \left\{ \frac{0.18}{\gamma_c} k \left[100\rho_s f_{ck} \right]^{\frac{1}{3}} \right\} b_w d \,, \tag{3}$$

where γ_c is the concrete safety factor, ρ_s is the longitudinal ratio, f_{ck} [MPa] is the concrete strength, d is the effective depth, b_w is the web width, and k is the size effect factor. Here, k is given by

$$k = 1 + \sqrt{\frac{200}{d}} \le 2.0 \qquad (d \text{ in mm}). \tag{4}$$

– Design guideline JSCE-2007

$$V_c = \frac{\beta_d \beta_p \beta_n f_{vcd} b_w d}{\gamma_b}. \tag{5}$$

Here,

$f_{vcd} = 0.2\sqrt[3]{f_{cd}^{'}}$ (f'_{cd} in MPa), where $f_{vcd} \le 0.72$ MPa;

$\beta_d = \sqrt[4]{\frac{1000}{d}}$ (d in mm), where $\beta_d \le 1.5$;

$\beta_p = \sqrt[3]{100 p_v}$, where $\beta_p \le 1.5$;

$\beta_n = 1 + \frac{2M_0}{M_{ud}} \quad (N_d^{'} \ge 0)$, where $\beta_n \le 2$;

$$\beta_n = 1 + \frac{4M_0}{M_{ud}} \quad (N'_d < 0), \qquad \text{where } \beta_n \geq 0.$$

In these formulae, N'_d is the design axial compressive force, M_{ud} is the flexural capacity without consideration of the axial force, M_0 is the flexural moment necessary to cancel the stress due to the axial force at the extreme tension fibre, b_w is the web width, d is the effective depth, p_v is the reinforcing bar ratio ($p_v = A_s/(b_w d)$), A_s is the area of tension reinforcement, f'_{cd} is the design compressive strength of concrete, and γ_b (= 1.3) is the member factor.

2.2. Design shear strength models for FRC members

The current design guidelines for FRC members ACI 544 (ACI Committee 544 1988), MC 2010 (CEB-FIB Model Code 2010), and JSCE (2006) (JSCE Concrete Committee 2006) can be summarised as follows.

– Design guideline ACI 544

This design code gives the nominal shear strength V_n for FRC members as

$$V_n = \frac{2}{3} f_{ct} \left(\frac{d}{a} \right)^{0.25} b_w d \,, \tag{6}$$

where f_{ct} is the tensile strength of FRC, a is the distance from the loading point to the support, d is the effective depth, and b_w is the web width. It is important to note that the empirical formula does not account for factors widely recognised as significantly influencing the shear strength, including the fibre length, fibre type, and the longitudinal rebar ratio.

– Design guideline MC 2010

This code provides the shear strength for FRC members with or without shear reinforcement (stirrups). The nominal shear strength V_n can be expressed as

$$V_n = V_{c,F} + V_s, \tag{7}$$

where $V_{c,F}$ is the FRC contribution to the shear strength and V_s is the shear strength provided by the stirrups.

In this code, the contribution of fibres to the shear capacity may be taken into account; however, it is recommended to use this code only when the FRC exhibits hardening tensile behaviour. Instead of separately predicting the fibrous contribution, the FRC shear contribution $V_{c,F}$ is estimated solely by modifying the formula for RC members (Eq. (3)) by adding an extra term, as

$$V_{c,F} = \left\{ \frac{0.18}{\gamma_c} k \left[100 \rho_s \left(1 + 7.5 \frac{f_{Ftuk}}{f_{ctk}} \right) f_{ck} \right]^{\frac{1}{3}} \right\} b_w d \,, \tag{8}$$

where γ_c is the safety factor, ρ_s is the longitudinal ratio, f_{Ftuk} is the characteristic value of the ultimate residual tensile strength for the FRC, f_{ctk} is the characteristic value of the FRC tensile strength, f_{ck} [MPa] is the concrete strength, d is the effective depth, b_w is the web width, and k is the size effect factor. Here, k is given by

$$k = 1 + \sqrt{\frac{200}{d}} \le 2.0 \qquad (d \text{ in mm}), \tag{9}$$

and V_s is given as

$$V_s = \frac{A_w}{s} z f_{ywd} (\cot\phi + \cot\theta) \sin\phi . \tag{10}$$

In these formulae, A_w is the cross-sectional area of the stirrups, s is the spacing of stirrups, f_{ywd} is the design yield strength of the stirrups, θ (= 45°) is the angle between the concrete compression strut and the beam axis perpendicular to the shear force, ϕ is the angle between shear reinforcement and the beam axis perpendicular to the shear force, and z is the inner lever arm and is recommended to be set to $z = 0.9d$.

– Design guideline JSCE (2006)

This recommendation considers the contributions of the cement matrix and the steel fibres to the shear strength of the ultrahigh-strength fibre-reinforced concrete members. According the recommendation, the nominal shear strength V_n is given as

$$V_n = V_c + V_F + V_{ped}, \tag{11}$$

where V_c is the contribution of the cement matrix to the shear strength of a member that has no shear reinforcement (stirrups), V_F is the contribution of the reinforced fibres, and V_{ped} is the component of effective tensile force of the longitudinal tendons.

V_c is calculated as

$$V_c = \frac{0.18\sqrt{f'_{cd}}\, b_w d}{\gamma_b}, \tag{12}$$

where f'_{cd} [MPa] is the design compressive strength, b_w is the web width, d is the effective depth, and γ_b (= 1.3) is the member factor.

V_F is given by

$$V_F = \frac{(f_{vd} / \tan\beta_u) b_w z}{\gamma_b}, \tag{13}$$

where f_{vd} is the design average tensile strength perpendicular to diagonal cracks, β_u (> 30°) is the angle between the member axis and a diagonal crack, z is the inner lever arm and is recommended to be set to d/1.15, and γ_b is the member factor that can be taken as 1.3.

In the recommendation, because of the fibre orientation included in the design models, f_{vd} can be determined as

$$f_{vd} = \frac{1}{w_{\lim}} \int_0^{w_{\lim}} \frac{\sigma_k(w)}{\gamma_c} dw = \frac{1}{w_{\lim}} \int_0^{w_{\lim}} \sigma_d(w) dw, \quad (14)$$

where w is the crack width, $w_{\lim}$ is the limit value of the crack width and generally taken as 0.3, $\sigma_k(w)$ and $\sigma_d(w)$ are tensile softening curves, and γ_c (= 1.3) is the material factor.

V_{ped} in the recommendation is expressed as

$$V_{ped} = \frac{P_{ed} \sin \alpha_p}{\gamma_b}, \quad (15)$$

where P_{ed} is the effective tensile force of the tendons, α_p is the angle formed by the tendons and the member axis, and γ_b (= 1.1) is the member factor.

3. Shear strength of UHPC–concrete composite members

3.1. Overview

The methods of predicting the shear strength of UHPC–concrete composite members proposed in the present study is based on the existing design formulae explained in Section 2 (ACI 318, EC2, JSCE-2007, ACI 544, MC 2010, and JSCE (2006)). In addition, Noshiravani and Brühwiler (2013) and Yin et al. (2017) have reported that the predominant contributor to the shear strength of composite members is the web of the RC members. The results of their studies suggest that the shear contribution of thin UHPC layers may be relatively small. The shear capacity may depend on the tensile strength of the UHPC, which may be dominated by steel fibres, and/or the mechanical weak bond interface between the UHPC and the RC members.

For this purpose, six different methods were individually proposed to compute the nominal shear resistance of UHPC–concrete members. Three of them, named Methods A1, A2, and A3, were based on converting the volume fraction of steel fibres to the equivalent longitudinal steel ratio. The remaining three methods, named Methods B1, B2, and B3, involve summing the two contributions V_c and V_{UHPC} to the shear resistance, where V_c is the contribution of the RC members and V_{UHPC} is the contribution of the UHPC layer. It should be mentioned that because the specimens used in this study had no shear reinforcement, the shear strength of the reinforcement was omitted. In addition, although Methods A1, A3, and B1 have been presented previously (Yin et al. 2018), prediction from other existing codes were investigated in this study to further demonstrate their accuracy.

3.2. Methods of converting the volume fraction of steel fibres

Methods A1, A2, and A3 for the UHPC–concrete composite members were based on the current design codes for RC members ACI 318, EC2, and JSCE-2007, respectively. The composite members were modelled as equivalent RC members by considering the contribution of the steel fibres in the UHPC to the equivalent longitudinal rebar ratio. This approach was adopted because the contribution of the UHPC layer to the shear capacity of the composite members may depend on the tensile strength of the UHPC when the volume fraction of steel fibres is high (Noshiravani, Brühwiler 2013; Yin et al. 2017; Yin et al. 2018).

In the present study, the equivalent rebar ratio ρ was given as

$$\rho = \rho_s + \rho_{eq,F}, \tag{16}$$

where ρ_s is the rebar ratio of the RC members and $\rho_{eq,F}$ is the equivalent ratio of the volume steel fibres. ρ_s is given as

$$\rho_s = \frac{A_s}{b_w d}, \tag{17}$$

where A_s is the area of the longitudinal rebar, d is the effective depth, and b_w is the width of the specimen sections. $\rho_{eq,F}$ is calculated as

$$\rho_{eq,F} = \%\text{Vol.}\left(\frac{f_{ct}}{f_y}\right)\left(\frac{A_{UHPC}}{A_{RC}}\right), \tag{18}$$

where f_{ct} is the tensile stress of UHPC and is taken as $f_{ct} = 0.3(f'_c)^{2/3}$ with f'_c [MPa] the compressive strength of UHPC; f_y is the yield strength of the longitudinal rebar; A_{UHPC} (= $b_w h_U$) and A_{RC} (= $b_w d$) are the areas of the UHPC and RC part, respectively; b_w is the width; h_U is the UHPC thickness; d is the effective depth; and %Vol. is the volume ratio of steel fibres. The effective depth d was assumed to be

$$d = h_c + \frac{h_U}{2}, \tag{19}$$

where h_c is the height of the RC members.

Therefore, the shear strength $V_{n,compos}$ of the UHPC–concrete composite members can be expressed as follows based on the considered design codes.

(a) Method A1: Based on ACI 318

$$V_{n,compos} = \left(0.16\lambda\sqrt{f_c'} + 17(\rho_s + \rho_{eq,F})\frac{V_u d}{M_u}\right) b_w d, \tag{20}$$

where λ is the reduction factor, f'_c [MPa] is the compressive strength of NSC, V_u is the shear force, M_u is the ultimate moment, d is the effective depth, b_w is the web width, ρ_s is the longitudinal ratio, and $\rho_{eq,F}$ is the equivalent volume ratio of steel fibres (Eq. (18)).

(b) Method A2: Based on EC2

$$V_{n,compos} = \left\{\frac{0.18}{\gamma_c} k\left[100(\rho_s + \rho_{eq,F}) f_{ck}\right]^{\frac{1}{3}}\right\} b_w d, \tag{21}$$

where γ_c is the concrete safety factor, k is the size effect factor, b_w is the web width, d is the effective depth, f_{ck} [MPa] is the compressive strength of NSC, ρ_s is the longitudinal ratio, and $\rho_{eq,F}$ is the equivalent volume ratio of steel fibres (Eq. (18)).

(c) Method A3: Based on JSCE-2007

$$V_c = \frac{\beta_d \beta_p \beta_n f_{vcd} b_w d}{\gamma_b}. \tag{22}$$

Here,

$f_{vcd} = 0.2\sqrt[3]{f'_{cd}}$ (f'_{cd} in MPa), where $f_{vcd} \le 0.72$ MPa;

$\beta_d = \sqrt[4]{\frac{1000}{d}}$ (d in mm), where $\beta_d \le 1.5$;

$\beta_p = \sqrt[3]{100\,(p_v + \rho_{eq,F})}$, where $\beta_p \le 1.5$;

$\beta_n = 1 + \frac{2M_0}{M_{ud}} \quad (N'_d \ge 0)$, where $\beta_n \le 2$;

$\beta_n = 1 + \frac{4M_0}{M_{ud}} \quad (N'_d < 0)$, where $\beta_n \ge 0$.

In these formulae, γ_b (= 1.3) is the member factor, N'_d is the design axial compressive force, M_{ud} is the flexural capacity without consideration of the axial force; M_0 is the flexural moment necessary to counteract the stress due to the axial force at the extreme tension fibre, f'_{cd} is the design compressive strength of concrete, b_w is the width, d is the effective depth, A_s is the area of tension reinforcement, p_v (= $A_s/(b_w d)$) is the reinforcing bar ratio, and $\rho_{eq,F}$ is the equivalent ratio of the volume steel fibres (Eq. (18)).

3.3. Methods based on summing the two shear contributions

In Methods B1, B2, and B3, the shear contributions V_c and V_{UHPC} of the UHPC–concrete composite members are independently computed and summed. The RC contribution V_c was obtained using the current design codes for RC members, ACI 318, EC2, and JSCE-2007. For the UHPC contribution V_{UHPC}, the three design guidelines ACI544, MC 2010, and JSCE (2006) were employed. The calculation was based on the assumption that the UHPC–concrete composite members can be considered as two independent parts (the NSC and UHPC components) that simultaneously fail at the same time. Although this assumption may not correspond to the shear patterns of the actual tests on UHPC in the composite members conducted by Yin et al. (2017), for the sake of simplicity and to allow comparison with the other methods, this assumption was adopted. The nominal shear strength $V_{n,compos}$ could then be given as follows based on the considered design codes.

(a) Method B1: Based on ACI 318 and ACI 544

$$V_{n,compos} = V_{c,\mathrm{ACI318}} + V_{UHPC,\mathrm{ACI544}}, \tag{23}$$

where $V_{c,\mathrm{ACI318}}$ is obtained by Eq. (2) for the NSC component and $V_{UHPC,\mathrm{ACI544}}$ for the UHPC component is given as

$$V_{UHPC,\mathrm{ACI544}} = \frac{2}{3} f_{ct} \left(\frac{d}{a} \right)^{0.25} b_w d \,. \tag{24}$$

In these formulae, the tensile strength f_{ct} of the UHPC was taken as $0.3(f'_c)^{2/3}$, where f'_c [MPa] is the compressive strength of UHPC. Additionally, the effective depth d of the UHPC was assumed to be $h_U/2$, h_U is the thickness of UHPC, a is the distance from loading point to support, and b_w is the web width.

(b) Method B2: Based on EC2 and MC 2010

$$V_{n,compos} = V_{c,\mathrm{EC2}} + V_{UHPC,\mathrm{MC2010}}, \tag{25}$$

where $V_{c,\mathrm{EC2}}$ is obtained by Eq. (3) for the NSC component and $V_{UHPC,\mathrm{MC2010}}$ for the UHPC component is given as

$$V_{UHPC,\mathrm{MC2010}} = \left\{ \frac{0.18}{\gamma_c} k \left[100 \rho_s \left(1 + 7.5 \frac{f_{Ftuk}}{f_{ctk}} \right) f_{ck} \right]^{\frac{1}{3}} \right\} b_w d \,. \tag{26}$$

In these formulae, the tensile strength f_{ctk} of the UHPC was calculated as $0.3(f'_c)^{2/3}$, where f'_c [MPa] is the compressive strength of UHPC, and the effective depth of UHPC was set to $d = h_U/2$, where h_U is the thickness of the UHPC. Furthermore, f_{Ftuk} is the characteristic value of the ultimate residual tensile strength for UHPC obtained from the crack opening w_u (= 1.5 mm). Because the experiments on UHPC in this study were not conducted to determine the value of f_{Ftuk}, the f_{Ftuk}/f_{ctk} ratio was taken as approximately 0.62. This estimate was based on the work by Gowripalan and Gilbert (2000), in which the tensile strength of UHPC was related to the crack opening w_u. Additionally, γ_c is the safety factor, k is the size effect factor, ρ_s is the longitudinal ratio, b_w is the web width, and f_{ck} [MPa] is the characteristic compressive strength of UHPC.

(c) Method B3: Based on JSCE-2007 and JSCE (2006)

$$V_{n,compos} = V_{c,\mathrm{JSCE\text{-}2007}} + V_{UHPC,\mathrm{JSCE(2006)}}, \tag{27}$$

where $V_{c,\mathrm{JSCE\text{-}2007}}$ is obtained by Eq. (5) for the NSC component and $V_{UHPC,\mathrm{JSCE(2006)}}$ for the UHPC component is computed as

$$V_{UHPC,\mathrm{JSCE(2006)}} = V_c + V_F \,. \tag{28}$$

Here, V_c and V_F are given by Eqs. (12) and (13), respectively. Substituting V_c and V_F into Eq. (28) yields $V_{UHPC,\mathrm{JSCE(2006)}}$ as

$$V_{UHPC,\mathrm{JSCE(2006)}} = \frac{0.18\sqrt{f'_{cd}}\, b_w d}{\gamma_b} + \frac{\left(f_{vd} / \tan\beta_u \right) b_w z}{\gamma_b} \,. \tag{29}$$

In these formulae, the effective depth d of the UHPC component was assumed to be $d = h_U/2$. In the present study, the angle β_u was taken as 45°; f_{vd} was approximated as $f_{vd} = f_{tk}/\gamma_c$, where f_{tk} was calculated as $f_{tk} = 0.3(f'_{cd})^{2/3}$ with f'_{cd} [MPa] the design compressive strength; γ_b is the member factor; b_w is the web width; z is the inner lever arm; and h_U is the thickness of the UHPC component.

4. Prediction and verification

4.1. Predicted shear strength

The shear force $V_{n,exp}$ was experimentally obtained as $V_{n,exp} = P_u/2$, where P_u is the ultimate load, and the nominal shear force $V_{n,compos}$ was predicted using the methods in Section 3. The experimental-to-predicted shear strength ratio $V_{n,exp}/V_{n,compos}$ for the OV (specimens failed in shear) and RE (specimens mainly failed in flexure) series were calculated and are listed in Tables 3 and 4, respectively. Tables 3 and 4 also provide the means and coefficients of variation (COVs) for the $V_{n,exp}/V_{n,compos}$ ratios of each series.

The predicted shear strength for the OV series specimens, which experimentally failed in shear, shown in Table 3 agreed reasonably well with the experimental results. From Table 3, the predictions based on the converting the volume fraction of steel fibres were found to yield a better accuracy than those obtained using the sum of the two contributions to the shear strength. The modification of ACI 318 (Method A1), EC2 (Method A2), and JSCE-2007 (Method A3) yielded mean $V_{n,exp}/V_{n,compos}$ ratios of 1.18, 1.16, and 1.25 and COVs of 18.8%, 16.1%, and 14.6%, respectively. Regarding the methods adopting the sum of the two shear strength contributions, Methods B1, B2, and B3 yielded mean $V_{n,exp}/V_{n,compos}$ ratios of 1.31, 1.41, and 0.92 and COVs of 15.9%, 30.8%, and 39.7%, respectively. In addition to the OV series, although the RE series specimens failed experimentally in flexure, the shear strengths of these specimens were calculated and are listed in Table 4 for reference. For all adopted design formulae for the RE series, the mean $V_{n,exp}/V_{n,compos}$ ratios and COVs ranged from 0.84 to 1.23 and from 16.1% to 48.6%, respectively.

Table 3. Predicted and experimental shear strength results (OV series including RE-0).

Specimen	Experimental results		Predicted shear strength $V_{n,exp}/V_{n,compos}$					
	$V_{n,exp}$ (kN)	Failure mode	Method A1	Method A2	Method A3	Method B1	Method B2	Method B3
RE-0	30.54	Shear	1.57*	1.48*	1.54*	1.57*	1.48*	1.54*
OV-25	36.78	Shear	1.15	1.13	1.18	1.33	1.78	0.86
OV-25a	38.98	Shear	1.13	1.07	1.17	1.41	0.99	0.91
OV-50	38.99	Shear	1.02	1.00	1.06	1.01	1.88	0.59
OV-50a	47.53	Shear	1.15	1.11	1.29	1.23	0.94	0.72
Mean	**-**	**-**	**1.18**	**1.16**	**1.25**	**1.31**	**1.41**	**0.92**
COV	**-**	**-**	**18.8%**	**16.1%**	**14.6%**	**15.9%**	**30.8%**	**39.7%**

Note:
* $V_{n,compos}$ is obtained from an RC design code (i.e., Eqs. (2), (3) and (5))

The shear forces of the OV series specimens are plotted in Fig. 4. As shown in these plots, all design formulae except Method B3 (Fig. 4(f)) yielded estimates safely below the target line or approximately agreed with the target line representing $V_{n,exp} = V_{n,compos}$. To further compare the predicted and experimental shear forces of each of the OV series specimens, the results were plotted in a bar chart, as shown in Fig. 5. From Fig. 5, all adopted design codes showed

promising results. It is of interest that the formulae for Methods B1 and B3 do not include a term for the ratio of the longitudinal rebar. The predicted shear strengths were the same at the same UHPC thickness, as can be seen by comparing the OV-25 and OV-25a results and the OV-50 and OV-50a results. For Method B2, the prediction greatly underestimated the actual strengths in the cases of OV-25 and OV-50 because no steel rebar was present in the UHPC (i.e., the UHPC shear contribution was zero in Eq. (26)).

Table 4. Predicted and experimental shear strength results (RE series).

Specimen	Experimental results		Predicted shear strength $V_{n,exp}/V_{n,compos}$					
	$V_{n,exp}$ (kN)	Failure mode	Method A1	Method A2	Method A3	Method B1	Method B2	Method B3
RE-0	30.54	Shear	1.57*	1.48*	1.54*	1.57*	1.48*	1.54*
RE-20	28.59	Flexure-shear	1.14	1.05	1.09	1.14	1.48	0.77
RE-32	21.84	Flexure	0.90	0.79	0.88	1.15	0.88	0.74
RE-50	27.69	Flexure	1.21	1.00	1.25	1.07	0.63	0.52
RE-100	56.48	Flexure	1.22**	0.84**	0.61**	1.22**	0.84**	0.61**
Mean	**-**	**-**	**1.21**	**1.03**	**1.07**	**1.23**	**1.06**	**0.84**
COV	**-**	**-**	**19.9%**	**26.4%**	**33.0%**	**16.1%**	**37.0%**	**48.6%**

Note:
* $V_{n,compos}$ is obtained from an RC design code (i.e., Eqs. (2), (3), and (5))
** $V_{n,compos}$ is obtained from an FRC design code (i.e., Eqs. (6), (8), and (11))

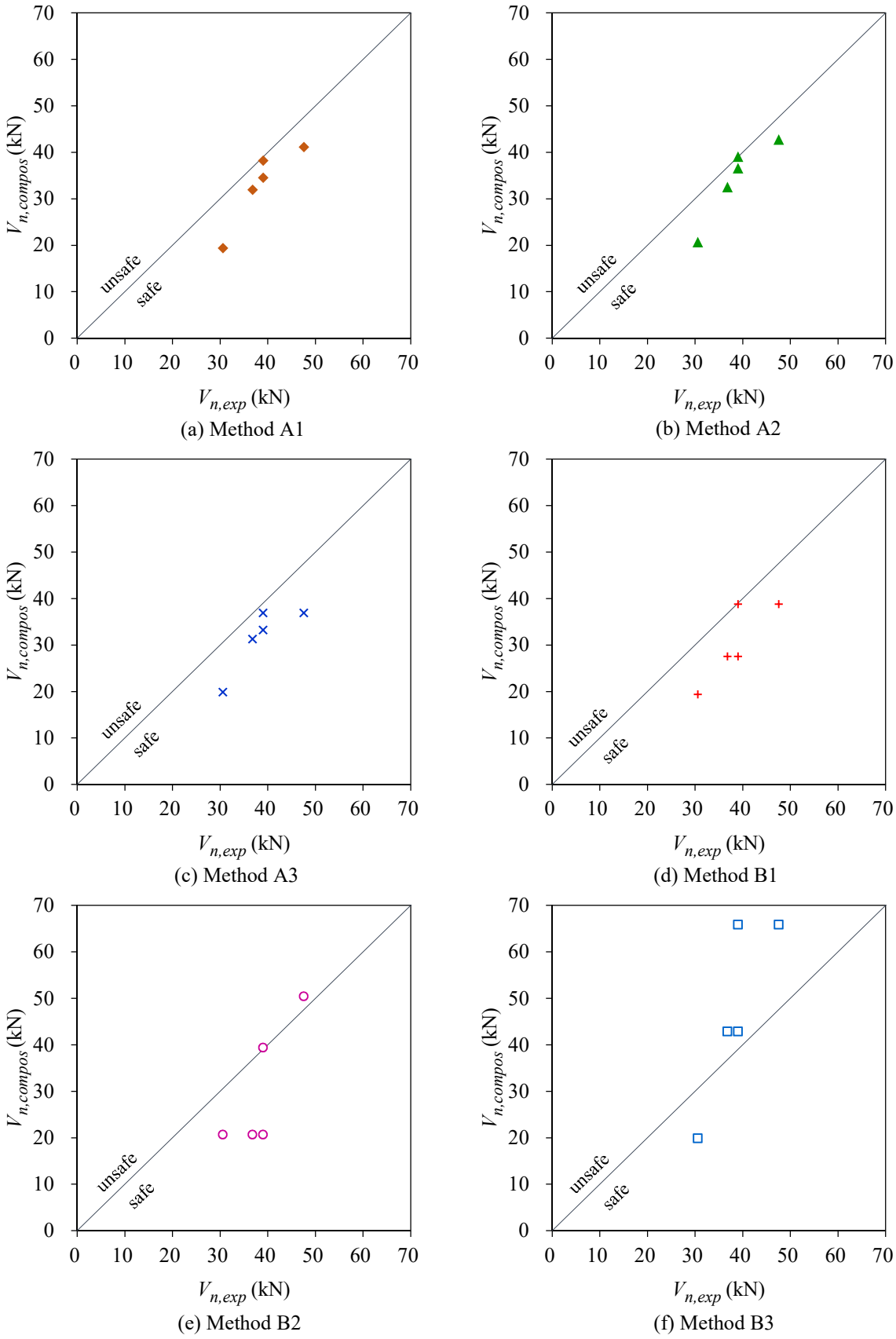

Fig. 4. Predicted shear forces plotted against experimental results for OV series specimens (including RE-0).

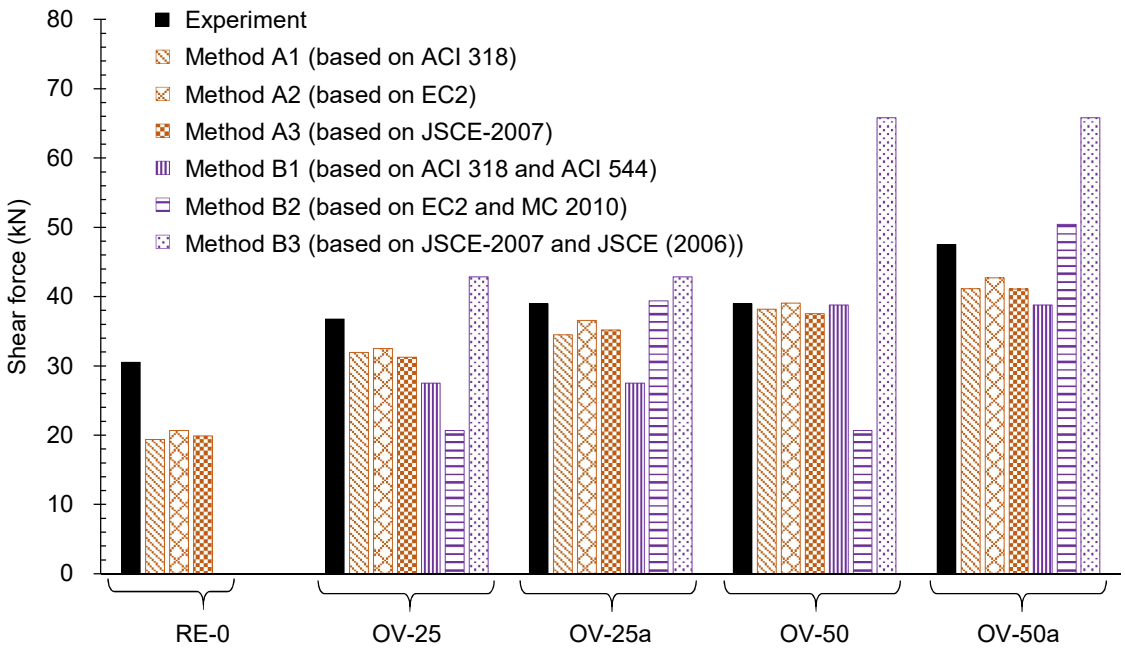

Fig. 5. Shear capacities for OV series specimens (including RE-0).

4.2 Prediction of failure mode

In the present study, failure mode prediction was conducted using the shear force V_{fle} given by the flexural moment M_{fle} computed using the method reported by Shirai et al. (2018). This shear force V_{fle} was compared with those $V_{n,compos}$ obtained using the six methods adopted in the shear strength prediction (Section 4.1). The calculation method and the flexural moment M_{fle} results are summarised as follows:

In accordance with the method by Shirai et al. (2018), the flexural moment of the UHPC–concrete members was computed based on the equilibrium with geometrical compatibility in a section of the members. A representation of the assumed stresses and strains in the UHPC–concrete section is shown in Fig. 6.

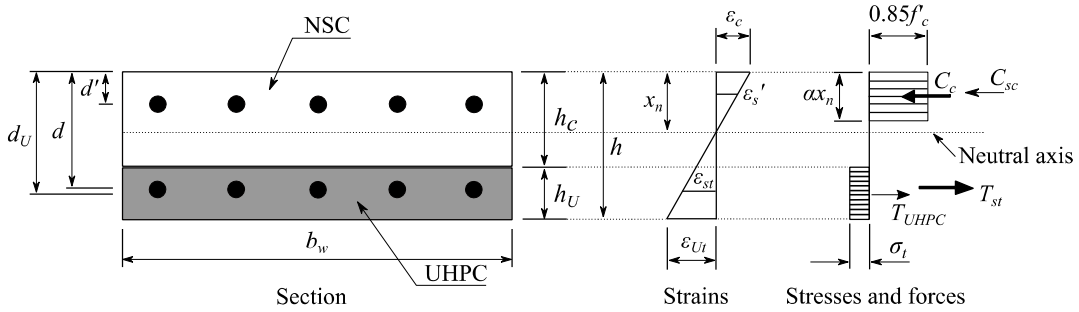

Fig. 6. Calculation assumptions for the flexural strength of the UHPC–concrete members (Shirai et al. 2018).

From Fig. 6, the equilibrium equation is expressed as

$$C_c + C_{sc} = T_{st} + T_{UHPC}\,, \tag{30}$$

where

$C_c = 0.85 f_c^{'} \alpha x_n b_w$

$C_{sc} = A_s^{'} \sigma_s^{'}$

$T_{st} = A_{sU} \sigma_{sU}$

$T_{UHPC} = A_{UHPC} \sigma_t$.

The flexural moment capacity M_{fle} is then given by

$$M_{fle} = A_s \sigma_s \left(d - \frac{\alpha x_n}{2} \right) + A_{UHPC} \sigma_t \left(d_U - \frac{\alpha x_n}{2} \right) + A_s^{'} \sigma_s^{'} \left(\frac{\alpha x_n}{2} - d^{'} \right). \quad (31)$$

b_w = width of the specimen.
d' = distance from the top of the concrete surface to the radial centre of the top rebar.
d = assumed effective depth (Fig. 6).
d_U = distance from the top of the concrete surface to the centre of the UHPC layer ($d_U = h_C + h_U/2$).
h_C = height of RC member.
h_U = thickness of UHPC.
x_n = distance between the top surface and neutral axis (Fig. 6). x_n can be obtained using the strain compatibility and equilibrium condition and checking the strain level in the reinforcement rebar.
f'_c = compressive strength of concrete.
α = factor relating the depth of equivalent rectangular compressive stress block to neutral axis depth and it shall be taken as 0.85 in the present study (ACI 318).
A'_s = area of top rebar.
A_s = area of bottom rebar.
A_{sU} = area of longitudinal rebar in UHPC.
A_{UHPC} = area of UHPC ($A_{UHPC} = b_w h_U$).
σ'_s = stress of top rebar.
σ_s = stress of bottom rebar.
σ_{sU} = stress of longitudinal rebar in UHPC.
σ_t = tensile stress of UHPC obtained by adopting the formulation provided by ACI 544 as

$$\sigma_t = 0.00772 \left(l/d \right) \rho_f F_{be}, \quad (32)$$

where l is the fibre length, d is the effective depth, ρ_f is the volume fraction of steel fibres, and F_{be} is a factor describing the bond efficiency of the fibres. More details can be found in ACI 544.

The experimental-to-predicted moment capacity ratios $M_{u,exp}/M_{fle}$ for specimen RE series are listed in Table 5. For the ratios reported in Table 5, $M_{u,exp}$ is the ultimate moment experimentally obtained as $M_{u,exp} = V_{n,exp} a$, where a is the distance from the loading point to the support. As shown in Table 5, the predicted and experimental flexural moments for the RE series showed good agreement with a mean $M_{u,exp}/M_{fle}$ ratio of 1.01 and a COV of 13.6% (Shirai et al. 2018).

In the present study, the expected failure mode was evaluated from the ratio $V_{n,compos}/V_{fle}$. When $V_{n,compos}/V_{fle} < 1$, the failure mode was expected to be shear failure, and flexure failure was expected otherwise. As shown in Table 5, although the predicted failure modes did not agree

with the experimental modes in all calculation cases, it may be worthwhile to consider these predicted failure modes. Among the considered prediction methods, the most accurate were Methods A2 (based on EC2) and B3 (based on JSCE-2007 and JSCE (2006)).

Table 5. Predicted failure modes for RE series specimens based on the previously computed flexural moment.

Specimen	Experimental results		Predicted flexural strength		Predicted shear strength and failure mode $V_{n,compos}/V_{fle}$ (Predicted failure mode)					
	$M_{u,exp}$ (kNm)	Failure mode	$M_{u,exp}/M_{fle}$	V_{fle} (kN)	Method A1	Method A2	Method A3	Method B1	Method B2	Method B3
RE-0	18.32	Shear	1.18	25.85	0.75 (Shear)	0.80 (Shear)	0.77 (Shear)	0.75 (Shear)	0.80 (Shear)	0.77 (Shear)
RE-20	17.15	Flexure-shear	1.07	26.78	0.94 (Shear)	1.02 (Flexure)	0.98 (Shear)	0.94 (Shear)	0.72 (Shear)	1.39 (Flexure)
RE-32	13.10	Flexure	0.80	27.19	0.89 (Shear)	1.02 (Flexure)	0.91 (Shear)	0.70 (Shear)	0.91 (Shear)	1.09 (Flexure)
RE-50	16.61	Flexure	1.00	27.59	0.83 (Shear)	1.00 (Flexure)	0.80 (Shear)	0.94 (Shear)	1.59 (Flexure)	1.93 (Flexure)
RE-100	33.88	Flexure	0.99	56.91	0.81 (Shear)	1.18 (Flexure)	1.63 (Flexure)	0.81 (Shear)	1.18 (Flexure)	1.63 (Flexure)
Mean	-	-	**1.01**	-	-	-	-	-	-	-
COV	-	-	**13.6%**	-	-	-	-	-	-	-

Note:
V_{fle} = shear force obtained at the calculated flexural moment M_{fle}.

Conclusions

A total of six methods of predicting the shear capacity of UHPC–concrete composite members based on existing design codes were presented in this paper. The predicted shear strength of RC slabs strengthened with various UHPC configurations in the tensile zone were verified against experimental results. From the assessments conducted in this study, the following conclusions were reached.

1. The shear strength of UHPC–concrete members obtained using the methods based on converting the volume fraction of steel fibres generally provided better prediction results than the methods adopting the sum of the two shear strength contributions V_c and V_{UHPC}.

2. The methods based on converting the volume fraction of steel fibres, Methods A1, A2, and A3, yielded predicted shear strengths for the OV series specimens with mean $V_{n,exp}/V_{n,compos}$ ratios of 1.18, 1.16, and 1.25 and COVs of 18.8%, 16.1%, and 14.6%, respectively. The methods summing the two components, Methods B1, B2, and B3, yielded mean $V_{n,exp}/V_{n,compos}$ ratios of 1.31, 1.41, and 0.92 and COVs of 15.9%, 30.8%, and 39.7%, respectively.

3. The failure modes determined from the predicted shear force obtained at the predicted flexural moment and those obtained using the adopted methods for the shear force prediction were compared. The failure modes predicted using Methods A2 and B3 were found to be the most accurate among the six methods.

4. From the present study, the proposed methods for UHPC–concrete members based on modifications to existing design models yielded promising results with reasonable

accuracy. However, a more realistic and accurate model for UHPC–concrete members is needed in future work.

Acknowledgments

The authors gratefully acknowledge the financial support from the Toda Scholarship Foundation 2017 Research Grant for this work.

References

ACI Committee 544. (1988). Design Considerations for Steel Fiber Reinforced Concrete. *ACI Structural Journal*, *85*(5), 563–579.

ACI Committee. (2008). *Building code requirements for structural concrete (ACI 318) and commentary*. American Concrete Institute.

Alaee, F. J., & Karihaloo, B. L. (2003). Retrofitting of reinforced concrete beams with CARDIFRC. *Journal of Composites for Construction*, *7*, 174–186. https://doi.org/10.1061/(ASCE)1090-0268(2003)7:3(174)

Brühwiler, E., & Denarie, E. (2008). Rehabilitation of concrete structures using ultra-high performance fibre reinforced concrete. In *Proceedings of the UHPC-2008*: *The Second International Symposium on Ultra High Performance Concrete* (pp. 05–07).

CEB-FIP Model Code. (2010). *The first draft of the fib Model Code for Concrete Structures*. International Federation for Structural Concrete (fib).

Eurocode 2. (2004). *EN 1992-1-1: Design of Concrete Structures: Part 1-1: General Rules and Rules for Buildings*. British Standards Institution.

Gowripalan, N., & Gilbert, R. (2000). *Design Guidelines for Ductal Prestressed Concrete Beams. Design Guide*. University of New South Wales, Sydney, Australia. Retrieved from http://docshare04.docshare.tips/files/20028/200286367.pdf

Graybeal, B. A. (2005). *Characterization of the behavior of ultra-high performance concrete*. PhD Thesis, University of Maryland, USA. http://hdl.handle.net/1903/2365

Graybeal, B. A., & Baby, F. (2013). Development of Direct Tension Test Method for Ultra-High-Performance Fiber-Reinforced Concrete. *ACI Materials Journal*, *110*(2), 177–186.

Habel, K. (2004). *Structural behaviour of elements combining ultra-high performance fibre reinforced concretes (UHPFRC) and reinforced concrete*. PhD Thesis, École Polytechnique Fédérale de Lausanne (EPFL), Switzerland. https://infoscience.epfl.ch//record/33507

Habel, K., Denarié, E., & Brühwiler, E. (2007). Experimental investigation of composite ultra-high-performance fiber-reinforced concrete and conventional concrete members. *ACI Structural Journal*, *104*(1), 93–101.

JSCE Concrete Committee. (2006). *Recommendation for design and construction of ultra high strength fiber reinforced concrete structures (Draft)*. Guidelines for Concrete, No. 9. Japan Society of Civil Engineers (JSCE).

JSCE Concrete Committee. (2010). *Standard specifications for concrete structures - 2007 "Design"*. Guidelines for Concrete, No. 15. Japan Society of Civil Engineers (JSCE). Retrieved from http://www.jsce-int.org/system/files/JGC15_Standard_Specifications_Design_1.0.pdf

Noshiravani, T., & Brühwiler, E. (2013). Analytical model for predicting response and flexure-shear resistance of composite beams combining reinforced ultrahigh performance fiber-reinforced concrete and reinforced concrete. *Journal of Structural Engineering*, *140*(6). https://doi.org/10.1061/(ASCE)ST.1943-541X.0000902

Noshiravani, T., & Brühwiler, E. (2013). Experimental investigation on reinforced ultra-high-performance fiber-reinforced concrete composite beams subjected to combined bending and shear. *ACI Structural Journal*, *110*(2), 251–261.

Oesterlee, C. (2010). *Structural response of reinforced UHPFRC and RC composite members*. PhD Thesis, École Polytechnique Fédérale de Lausanne (EPFL), Switzerland. https://infoscience.epfl.ch/record/169623?ln=en

Shirai, K., Yin, H., & Teo, W. (2018). Flexural strength calculation of the RC members rehabilitated with UHPC. In *Proceedings of the Japan Concrete Institute*, *40*.

Wille, K., El-Tawil, S., & Naaman, A. (2014). Properties of strain hardening ultra high performance fiber reinforced concrete (UHP-FRC) under direct tensile loading. *Cement and Concrete Composites*, 48, 53–66. https://doi.org/10.1016/j.cemconcomp.2013.12.015

Yin, H., Shirai, K., & Teo, W. (2018). Shear capacity prediction of reinforced concrete members strengthened with ultra-high performance concrete overlay. In *Proceedings of the Japan Concrete Institute*, *40*.

Yin, H., Teo, W., & Shirai, K. (2017). Experimental investigation on the behaviour of reinforced concrete slabs strengthened with ultra-high performance concrete. *Construction and Building Materials*, *155*, 463–474. https://doi.org/10.1016/j.conbuildmat.2017.08.077

Yoo, D. Y., & Banthia, N. (2016). Mechanical properties of ultra-high-performance fiber-reinforced concrete: A review. *Cement and Concrete Composites*, *73*, 267–280. https://doi.org/10.1016/j.cemconcomp.2016.08.001

Yoo, D. Y., & Yoon, Y. S. (2016). A review on structural behavior, design, and application of ultra-high-performance fiber-reinforced concrete. *International Journal of Concrete Structures and Materials*, *10*(2), 125–142. https://doi.org/10.1007/s40069-016-0143-x

Chapter VII

Paper VI

Prediction of flexural strength of UHPC-concrete composite members based on existing design models

Prediction of flexural strength of UHPC-concrete composite members based on existing design models

Abstract

Ultra-high performance concrete (UHPC) is an advancement in concrete technology. UHPC can be defined by its exceptional properties including high strength, high stiffness, and high ductility. Recently, UHPC have been studied for strengthening conventional reinforced concrete (RC) structural members. Owing to the excellent properties of UHPC, the strengthened members or UHPC-concrete composite members have significantly improved the structural performance in previous studies. However, methods to predict the capacity of the UHPC-concrete composite members are very limited in the past. In the present study, a simple method based on the existing design models for the prediction of the flexural strength of the composite RC members strengthened with UHPC at the tension zone was presented. The rectangular stress block diagrams for compression and tension zone of the conventional concrete and UHPC layer in the composite section were assumed, respectively. The prediction results showed good agreement with the experimental results. This demonstrated that the proposed method was able to predict the flexural strength of UHPC-concrete composite members.

Keywords: Flexural moment capacity, strength prediction, design code, RC structures, UHPC strengthening, rehabilitating, composite behaviour

Introduction

Over the last decades, ultra-high performance concrete (UHPC), which was initially developed by Richard and Cheyrezy (1995), has been applied to the construction field either by cast in-situ or by prefabricated panels. UHPC, a cementitious concrete material, is defined by its superior mechanical properties such as high strength (> 150 MPa in compression and > 8 MPa in tension), strain hardening, low permeability, and energy absorption (Wille et al. 2014; Graybeal, Baby 2013; Alkaysi et al. 2016).

Recently, several studies on conventional RC members strengthened with UHPC layer have been conducted (Brühwiler, Denarie 2008; Habel et al. 2007; Noshiravani, Brühwiler 2013; Yin et al. 2017). According to Brühwiler and Denarie (2008), UHPC has been applied to strengthen parts of reinforced concrete (RC) structures in full-scale applications. It showed that UHPC development is mature to be used as a suitable material for strengthening RC structures. In addition, many UHPC-concrete composite members were experimentally tested (Habel et al. 2007; Noshiravani, Brühwiler 2013; Yin et al. 2017). Results showed that UHPC layer enhances the structural performance.

Although the structural performance of UHPC-concrete composite members is significantly enhanced by UHPC strengthening, the analytical models of the flexural strength are very limited (Alaee, Karihaloo 2003; Habel et al. 2006; Noshiravani, Brühwiler 2013). Those models were based on moment-curvature relationships through the cross-sectional analysis; however, several analytical steps were required.

For RC members or fibre reinforced concrete (FRC) members, the flexural strength can be obtained from the existing design models (ACI Committee 318 2008; ACI Committee 544 1998). According to ACI Committee 318 (2008), the moment capacity can be computed using a simplified stress block diagram. Whereas, the tensile stress of normal strength concrete (NSC)

is generally negligible, that of FRC or UHPC should be taken into account because UHPC has high tensile strength (> 8 MPa).

However, no design models have been made available for UHPC-concrete composite members. Therefore, development of analytical models for composite models is certainly needed. Use with modification of the existing design models for non-composite RC or FRC members would be useful because they are simple and easy to use.

For this purpose, in the present study, a simple method based on modification of existing design models for the flexural strength calculation for UHPC-concrete composite members is proposed. This paper was organised as follows. Experimental data tested by previous study (Yin et al. 2017), which was used to verify the proposed method is briefly described in Section 1. Section 2 reviews the existing design models for non-composite RC or FRC members. The proposed method for the flexural strength of UHPC-concrete composite members is presented in Section 3. Sections 4 and 5 shows the discussion on the flexural moment calculation results and predicted failure modes, respectively. Furthermore, the present paper expands on a previous study (Shirai et al. 2018) by adding new results and findings.

1. Database description and results

1.1. Specimen details

Nine specimens tested by Yin et al. (2017) were used to verify the flexural strength calculation in the present study. Two of them were non-composite specimens made of NSC and UHPC; namely, RE-0 and RE-100, respectively. The remaining seven specimens were UHPC-concrete composite specimens, which were strengthened with various UHPC configurations in the tension zone as shown in Fig. 1. The overall of test system was illustrated in Fig. 1(a).

The specimens were grouped into two series. The first series labelled as RE series was consisted of five specimens and the second was OV series consisted of four specimens as shown in Fig. 1(b) and (c), respectively. For RE series, the composite specimens were strengthened with UHPC as patch material for repair and rehabilitation of structural members. In practice, when the deterioration in RC structures occurs, the deteriorated concrete was often removed and repair material are applied to the concrete substrate. For OV series, two additional thicknesses of UHPC overlay of 25 mm and 50 mm were applied onto the tension zone of the specimen RE-0. Two specimens were prepared for each UHPC thickness. One was not reinforced, while the other was reinforced with five 10-mm diameter high tensile strength steels. Details of the longitudinal steel arrangement and geometry of the specimens are shown in Fig. 1 and Table 1.

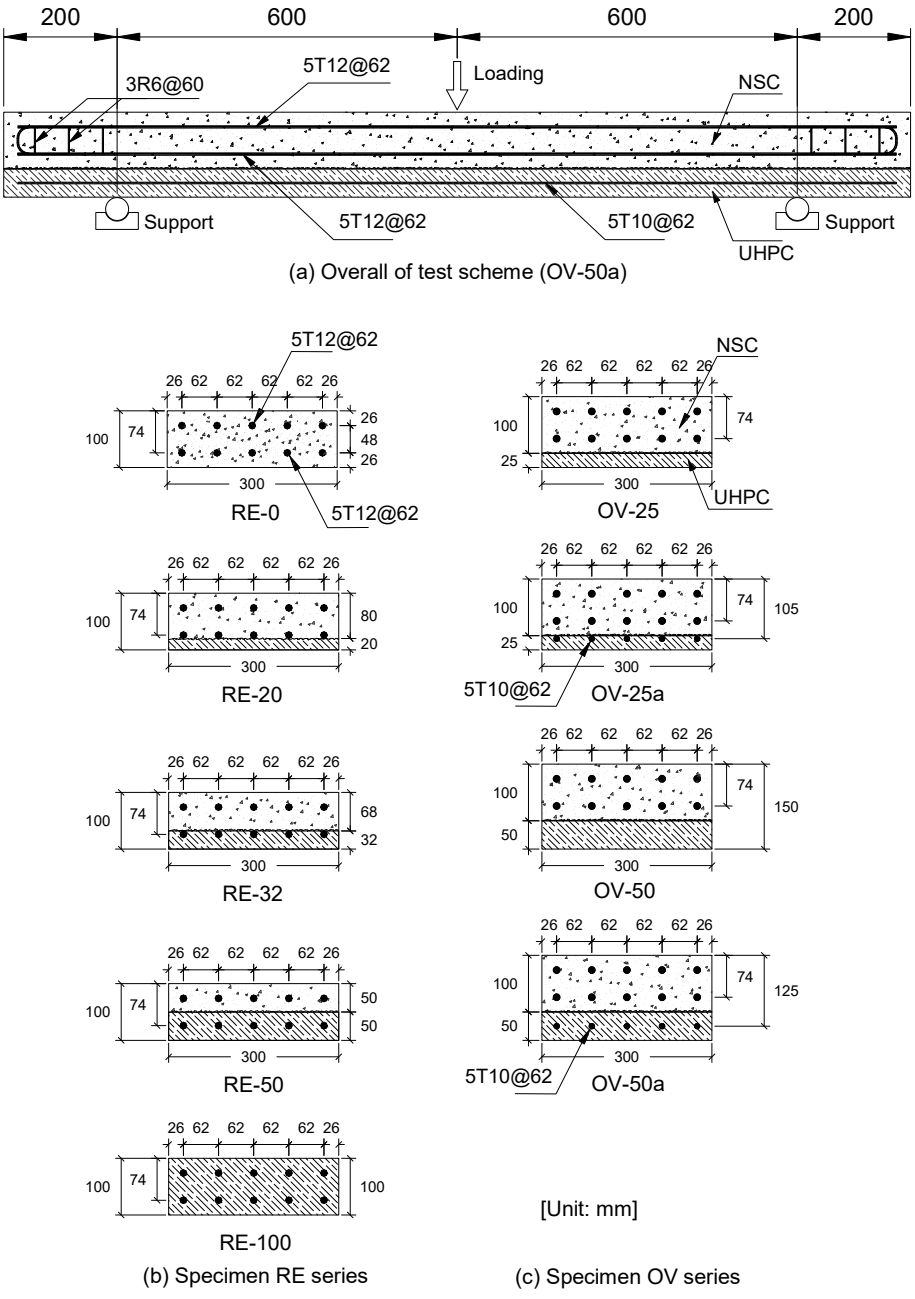

Fig. 1. Overall of test scheme and details of specimens (Yin et al. 2017).

Table 1. Geometric details of the specimens (Yin et al. 2017).

Specimen	b (mm)	h (mm)	h_U (mm)	a (mm)
RE-0	300	100	-	600
RE-20	300	100	20	600
RE-32	300	100	32	600
RE-50	300	100	50	600
RE-100	300	100	100	600
OV-25	300	125	25	600
OV-25a	300	125	25	600
OV-50	300	150	50	600
OV-50a	300	150	50	600

Note:
b: width of the specimens
h: height of the specimens
h_U: thickness of the UHPC layer
a: distance between loading point and support.

1.2. Material properties of the specimens

Table 2 shows the properties of NSC and UHPC materials. The compressive and flexural strength were tested at day 28. For NSC, ready-mixed concrete was used. For UHPC, it was manually mixed. The steel fibres of 13 mm in length and 0.2 mm in diameter and the tensile strength of 2300 MPa was added in UHPC mixtures. More details of UHPC can be found in the original document (Yin et al. 2017).

Table 2. Concrete properties of the specimens (Yin et al. 2017).

Material	Compressive strength (MPa)	Flexural strength (MPa)	Young's modulus[§] (GPa)
NSC	23	-	22.5
UHPC	153	27.4	58.1

[§]: calculated using $E_c = 4700(f'_c)^{0.5}$ where f'_c is the compressive strength in MPa (ACI Committee 318 2008).

Table 3 shows the properties of longitudinal rebar of the specimens. Two diameters 12 mm and 10 mm were used; namely T12 and T10, respectively. The tensile yield strength of T12 and T10 rebar was experimentally obtained as shown in Table 3.

Table 3. Longitudinal reinforcement properties of the specimens (Yin et al. 2017).

Reinforcement	Diameter (mm)	Area (mm^2)	Yield strength (MPa)	Young's modulus (GPa)
T12	12	113.1	502	200
T10	10	78.5	475	200

1.3. Brief description of test results

Crack patterns of the specimens after tests are illustrated in Fig. 2. For the non-composite specimens, NSC specimen RE-0 and UHPC specimen RE-100 showed shear and flexural failure, respectively. All specimens strengthened with UHPC in RE series mainly failed in

flexures, except specimen RE-20 showing debonding and inclined shear cracks (Fig. 2(a)). For OV series, all specimens failed in shear along with debonding of UHPC overlay (Fig. 2(b)).

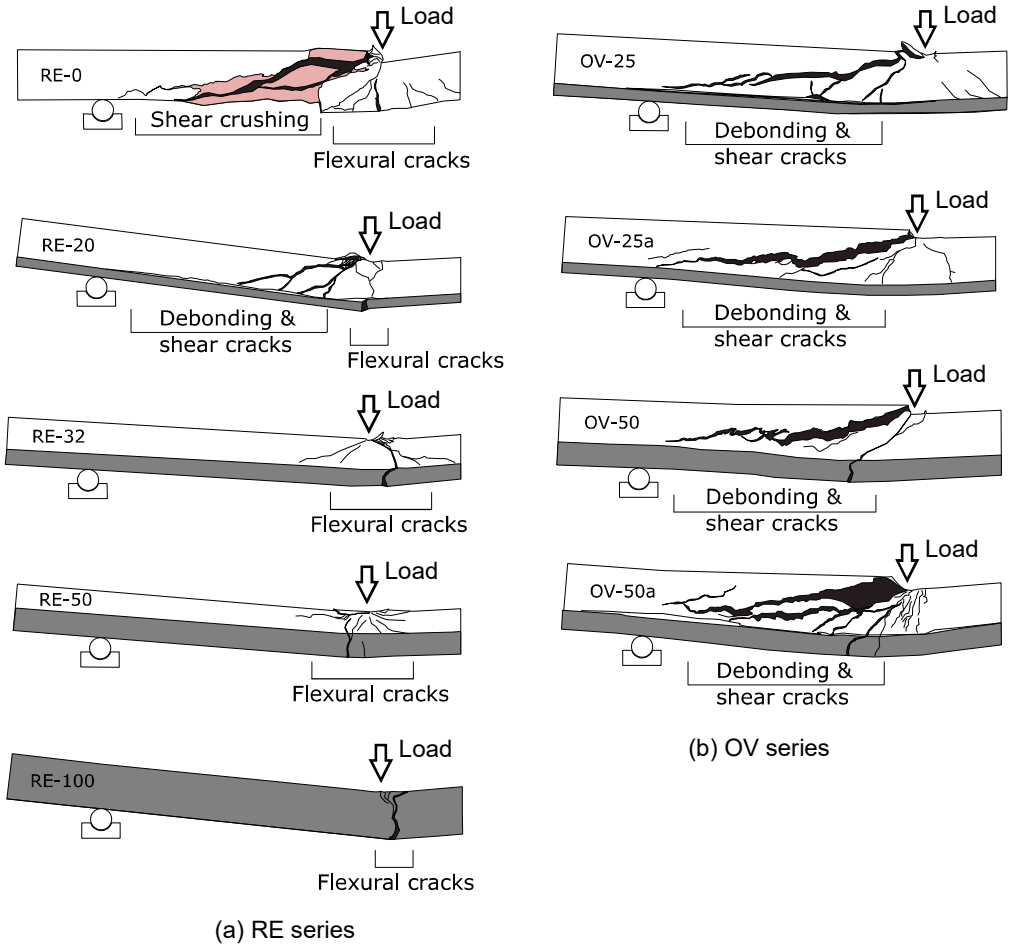

Fig. 2. Experimentally tested crack patterns (Yin et al. 2017).

Fig. 3(a) and (b) depict the load-deflection curves of the specimen RE series and OV series, respectively. Besides improvement in failure modes, the overall behaviour of the strengthened slab change completely as well. As shown in Fig. 3(a), all UHPC-concrete composite slabs (RE-20, RE-32 and RE-50) exhibited extensive deflection hardening and ductility during the post cracking range. Although no strength enhancement was attained in any of the strengthened slabs compared with non-composite NSC specimen RE-0, it could easily be offset by their excellent energy absorption capabilities. It was obvious that the non-composite UHPC RE-100 showed the highest ultimate load (Fig. 3(a)).

From Fig. 3(b), for OV series, owing to strengthening effect including the increase of the total height of the specimens, UHPC-concrete composite specimens enhanced overall performance such as stiffness and ultimate load compared to specimen RE-0. In addition, it was noted that composite specimen OV-50a reinforced with five 10-mm diameter high-tensile-strength steels in UHPC did not seem to differ from specimen OV-50 without rebar in initial stiffness. However, reinforcing bars in UHPC helped increase the ultimate load of the specimen. Full detailed discussion can be found in the original article (Yin et al. 2017).

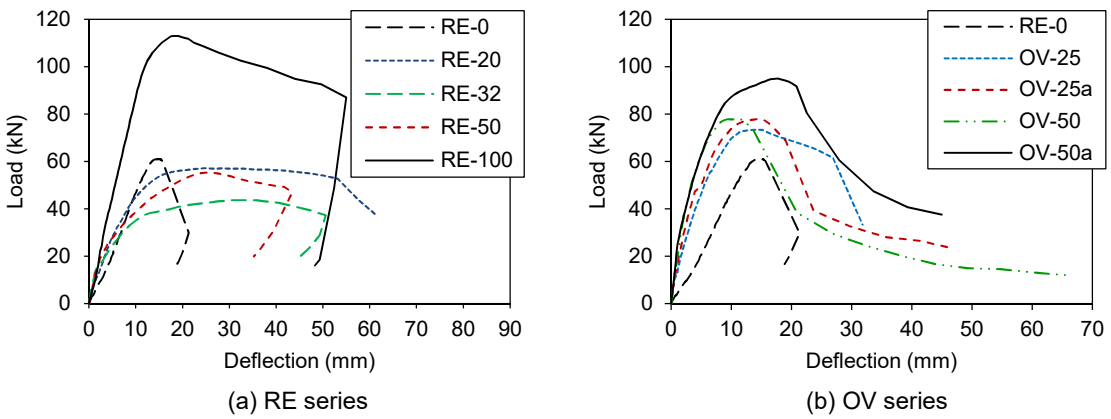

Fig. 3. Load-deflection curves of the test specimens (Yin et al. 2017).

2. Review of existing design models for flexural members

2.1. Design code ACI 318 for RC members

According to the current design code ACI 318 (ACI Committee 318 2008) for RC structures, the moment resistant capacity of rectangular RC members can be calculated using the simplified stress block diagram and the concrete tensile stress is neglected as shown in Fig. 4. Based on this diagram, the moment resistance of the members M_n can be expressed as:

$$M_n = A_s f_y \left(d - \frac{a}{2} \right) \tag{1}$$

where A_s is the area of longintudinal rebar; f_y is the yield strength of longitudinal rebar; d is the effective depth; and a is the depth of compressive stress block (see Fig. 4).

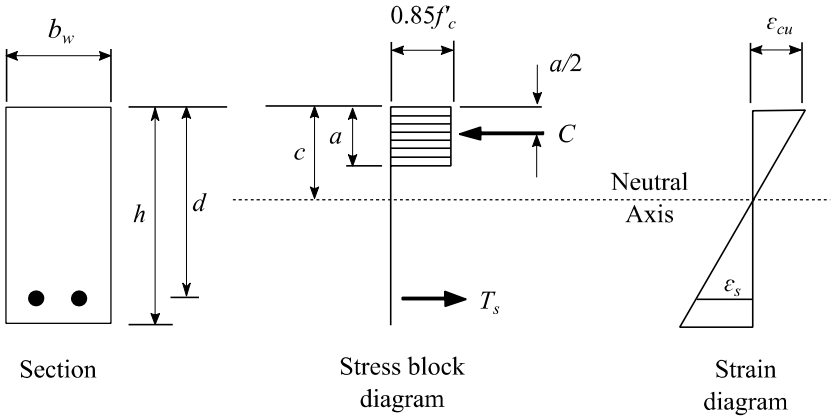

Fig. 4. Diagrams of stresses and strains in a section of RC members (ACI Committee 318 2008).

2.2. Design code ACI 544 for FRC members

The design guideline ACI 544 (ACI Committee 544 1988) for FRC members recommends that the moment resistant capacity can be calculated based on simplified assumptions of stress and strain diagrams as shown in Fig. 5. The tensile stress of the concrete of FRC members is accounted for the design calculation whereas that of NSC of RC members is generally negligible. From Fig. 5, the moment resistance M_n can be expressed as:

$$M_n = A_s f_y \left(d - \frac{a}{2} \right) + \sigma_t b_w (h - e) \left(\frac{h}{2} + \frac{e}{2} - \frac{a}{2} \right) \tag{2}$$

where A_s is the area of longitudinal rebar; f_y is the yield strength of longitudinal rebar; d is the effective depth; a is the depth of compressive rectangular stress block; c is the neutral axis depth; b_w is the web width; h is the total height; σ_t is the tensile stress in fibrous concrete; and e is the distance from extreme compression fibre to the top of tensile stress block of fibrous concrete (see Fig. 5).

The distance e is given by:

$$e = \left[\varepsilon_s (\text{Fibres}) + 0.003 \right] \left(\frac{c}{0.003} \right) \tag{3}$$

where ε_s(Fibres) is the tensile strain in fibres; and c is the depth of neutral axis.

The tensile stress σ_t (in MPa) can be given by:

$$\sigma_t = 0.00772 \left(\frac{l}{d} \right) \rho_f F_{be} \tag{4}$$

where l is the fibre length; d is the effective depth; ρ_f is the percent by volume of steel fibres; and F_{be} is the factor of bond efficiency of the fibre (F_{be} =1.0 was used in the present study).

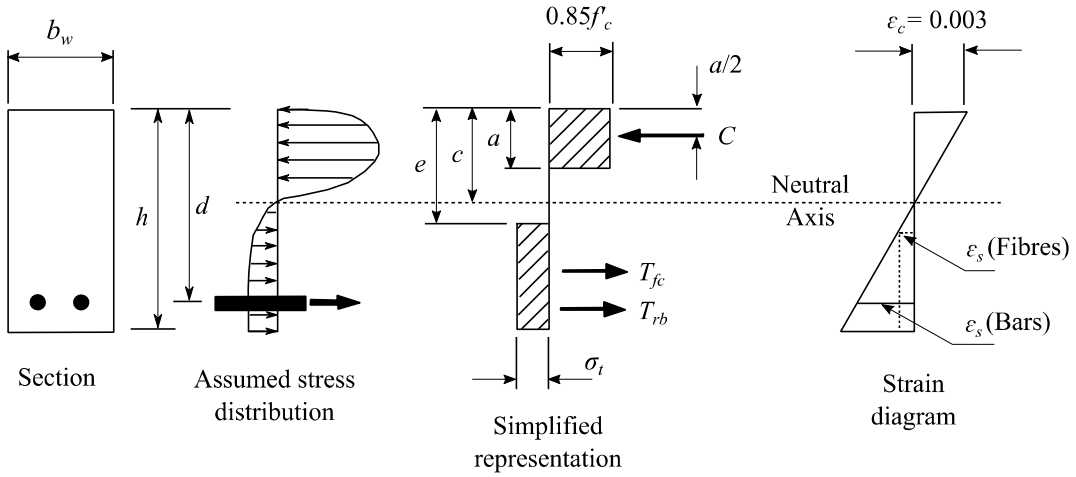

Fig. 5. Diagrams of stresses and strains in a section of FRC members (ACI Committee 544 1988).

3. Flexural strength of UHPC-concrete composite members

3.1. Overview

In the present study, the flexural moment of UHPC-concrete composite members was predicted based on the equilibrium with geometrical compatibility in a section of the members. An assumed representation of stresses and strains in UHPC-concrete composite sections is depicted in Fig. 6.

Assumptions employed in the flexural moment calculation are as follows:

- NSC and UHPC parts of the composite members were assumed to fail simultaneously.
- Assumed strain (ε_c) corresponding to ultimate compressive stress was 0.003 for NSC.
- The tensile stress, σ_t, used for FRC members (see Fig. 5), was adopted for UHPC.
- Since UHPC layer at the tension chord is relatively thin thickness, it may be reasonable to assume that the distance, $h - e$, (see Fig. 5) shall be taken as the UHPC thickness, ($h - e = h_U$) as depicted in Fig. 6. h is the total height of the section.
- A tensile force for the UHPC, T_{UHPC}, was then computed as a production of the stress, σ_t, obtained from Eq. (4), and the corresponding UHPC area A_{UHPC} (= $b_w \times h_U$).

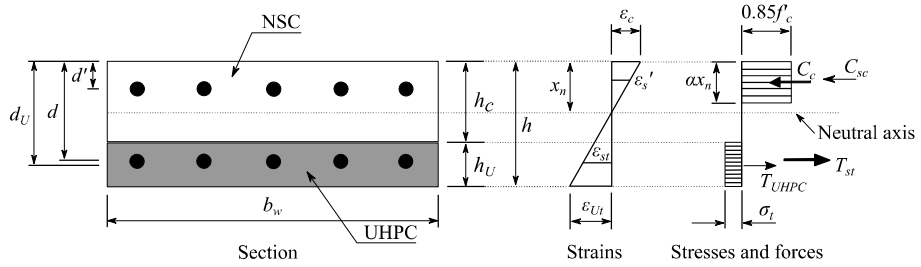

(a) Stresses and strains in a typical UHPC-concrete section for RE series

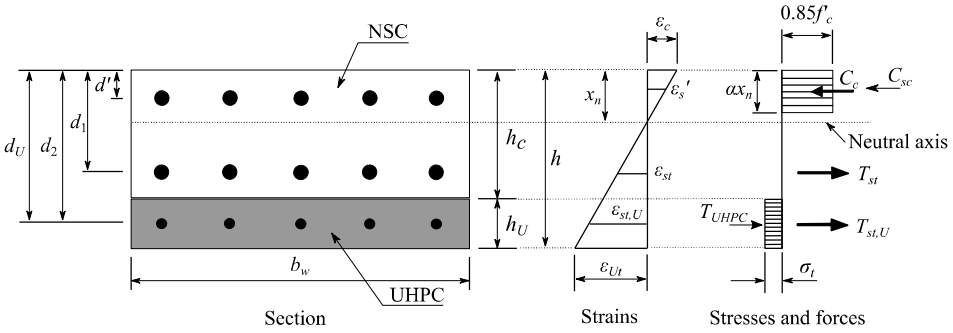

(b) Stresses and strains in a typical UHPC-concrete section for OV series

Fig. 6. Calculation assumptions for flexural strength of UHPC-concrete members.

3.2. Equilibrium conditions

As widely accepted in the current design models, in the present study, an equilibrium equation is derived from the compatibility condition, which the strain varies linearly along the cross-section as shown in Fig. 6. At the equilibrium condition, the equations could be expressed as:

For specimen RE series, except specimen RE-0:

$$C_c + C_{sc} = T_{st} + T_{UHPC} \tag{5a}$$

For specimen OV series:

$$C_c + C_{sc} = T_{st} + T_{st,U} + T_{UHPC} \tag{5b}$$

where:

$C_c = 0.85 f'_c \alpha x_n b_w$

$$C_{sc} = A_s^{'}\sigma_s^{'}$$
$$T_{st} = A_s\sigma_s$$
$$T_{st,U} = A_{sU}\sigma_{sU}$$
$$T_{UHPC} = A_{UHPC}\sigma_t$$

The flexural moment capacity M_{fle} is then given by:

For specimen RE series, except specimens RE-0:

$$M_{fle} = A_s\sigma_s\left(d - \frac{\alpha x_n}{2}\right) + A_{UHPC}\sigma_t\left(d_U - \frac{\alpha x_n}{2}\right) + A_s^{'}\sigma_s^{'}\left(\frac{\alpha x_n}{2} - d^{'}\right) \quad (6a)$$

For specimen OV series:

$$M_{fle} = A_s\sigma_s\left(d_1 - \frac{\alpha x_n}{2}\right) + A_{sU}\sigma_{sU}\left(d_2 - \frac{\alpha x_n}{2}\right) + A_{UHPC}\sigma_t\left(d_U - \frac{\alpha x_n}{2}\right) + A_s^{'}\sigma_s^{'}\left(\frac{\alpha x_n}{2} - d^{'}\right) \quad (6b)$$

where the notations of Eqs. (5) and (6) are as follows:
b_w = web width.
d' = distance from extremely top concrete surface to centre of diameter of top rebar.
d = assumed effective depth (Fig. 6(a)).
d_1 = distance from extremely top concrete surface to centre of T12 rebar (Fig. 6(b)).
d_2 = distance from extremely top concrete surface to centre of T10 rebar (Fig. 6(b)).
d_U = distance from extremely top concrete surface to centre of UHPC layer ($d_U = h_C + h_U/2$).
h_C = height of RC member.
h_U = thickness of UHPC.
x_n = distance between extremely top surface and neutral axis. The x_n can be calculated using strain compatibility and equilibrium condition, and checking the strain level in the reinforcement rebar.
f'_c = compressive strength of NSC.
α = factor relating depth of equivalent rectangular compressive stress block to neutral axis depth and it shall be taken as 0.85 in the present study due to f'_c = 23 MPa (Fig. 7).

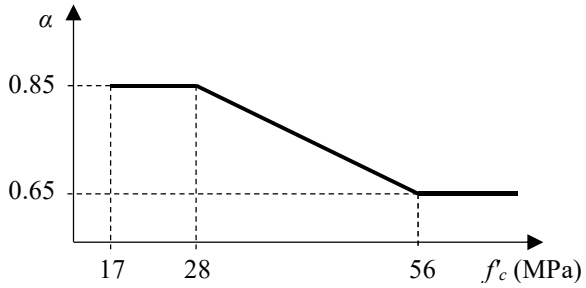

Fig. 7. Value of factor α according to ACI Committee 318 (2008).

A'_s = area of top rebar (5T12 = 565 mm^2).
A_s = area of bottom rebar (5T12 = 565 mm^2).
A_{sU} = arear of longitudinal rebar in UHPC overlay (5T10 = 363 mm^2).
A_{UHPC} = area of UHPC ($A_{UHPC} = b_w \times h_U$).

σ'_s = stress of top rebar.
σ_s = stress of bottom rebar.
σ_{sU} = stress of longitudinal rebar in UHPC overlay.
σ_t = tensile stress of UHPC obtained using Eq. (4).

In the analysis, the situations can be classified as follows:

- No reinforcement yielded ($\sigma'_s < f_y$, and $\sigma_s < f_y$), where f_y is the yield strength of rebar.
- Tension reinforcement (bottom rebar) yielded and compression reinforcement (top rebar) did not yield ($\sigma_s = f_y$, and $\sigma'_s < f_y$).
- Both tension and compression reinforcement yielded ($\sigma_s = f_y$, and $\sigma'_s = f_y$).

It should be mentioned that the flexural moment of NSC specimen RE-0 in this study was obtained based on the current design code ACI Committee 318 (2008). For UHPC specimen RE-100, the flexural moment was obtained using the Eq. (6a), where the distance $h - e$ (see Fig. 5) and the d_U in Eq. (6a) were assumed 50 mm and 75 mm, respectively. In addition, the flexural strength calculation results for the specimens (RE-0, -32, -50, and -100) were previously reported (Shirai et al. 2018).

4. Prediction results and verification

Table 4 shows the predicted flexural moment capacities for all specimens described in Section 1.1. In this table, the predicted flexural moment, M_{fle}, was obtained using the adopted calculation approach (Section 3), and the ultimate moment, $M_{u,exp}$, was experimentally obtained as $M_{u,exp} = V_{n,exp} \times a$, where a is the distance from loading point to support. The $V_{n,exp}$ is the shear force and obtained as $V_{n,exp} = P_u/2$, where P_u is the experimental ultimate load. Some statistic values of the experimental-to-predicted moment capacity ratio $M_{u,exp}/M_{fle}$ was calculated for both RE and OV series as shown in Table 4.

As seen in Table 4, the predicted moment capacity in RE series showed good agreement with experimental results with mean $M_{u,exp}/M_{fle}$ ratio and coefficient of variation (COV) of 1.01 and 13.6%, respectively. In OV series, due to the occurrence of shear failure, the specimens might not reach their maximum moment capacity. The flexural moment for OV series was additionally calculated and shown in Table 4 for reference. As a result, the flexural moment for specimen OV series showed a large variation with the mean $M_{u,exp}/M_{fle}$ ratio of 1.08 and COV of 25.7% in comparison to RE series where the specimens mainly failed in flexure.

It should be noticed that for composite members, as the thickness of UHPC layer increased, the calculated moment slightly increased. This result indicated that the contribution of tension fracture of UHPC layer was not significant for the specimens used in this study. However, when the prediction was plotted against the experimental results for RE series as shown in Figs. 8 and 9, it clearly showed that the data points of flexural moment greatly gathered along the target line representing $M_{u,exp} = M_{fle}$ (Fig. 8), and good agreement observed (Fig. 9).

Among all specimens in RE series, UHPC specimen RE-100 showed high flexural moment in both the calculation and experiment. The main reason to this is that only RE-100 had UHPC in the compression zone and the high compressive strength of UHPC significantly influenced the increase of the flexural capacity (Shirai et al. 2018).

Table 4. Comparison between predicted and experimental results.

Specimen	Experimental results		Predicted flexural moment
	$M_{u,exp}$ (kNm)	Failure mode	$M_{u,exp}/M_{fle}$
RE-0	18.32	Shear	1.18
RE-20	17.15	Flexure-shear	1.07
RE-32	13.10	Flexure	0.80
RE-50	16.61	Flexure	1.00
RE-100	33.88	Flexure	0.99
Mean	-	-	**1.01**
COV	-	-	**13.6%**
RE-0	18.32	Shear	1.18
OV-25	22.07	Shear	1.34
OV-25a	23.39	Shear	0.77
OV-50	23.39	Shear	1.32
OV-50a	28.52	Shear	0.80
Mean	-	-	**1.08**
COV	-	-	**25.7%**

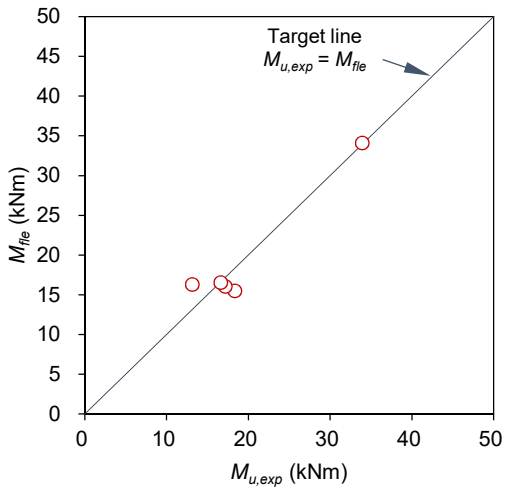

Fig. 8. Comparison between predicted flexural moments and experimental results of specimen RE series.

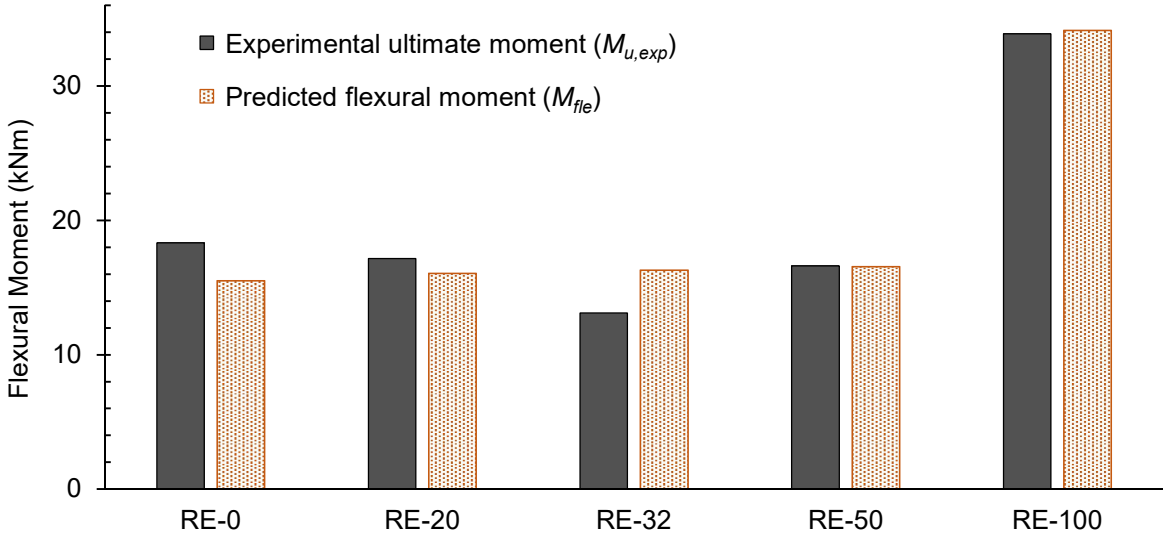

Fig. 9. Prediction and experimental results of the flexural moment capacities of specimen RE series.

5. Prediction of failure mode

In the present study, the failure mode prediction was conducted based on the shear force V_{fle} given by the computed flexural moment M_{fle} described in Section 4. This shear force V_{fle} was compared with those ($V_{n,compos}$) obtained from the six methods for the shear strength calculation reported by Yin et al. (2018). Full details of the six methods (Methods A1, A2, A3, B1, B2, and B3), shown in Table 5, could be found in the open document by Yin et al. (2018).

Table 5. Predicted failure mode based on previously computed flexural moment.

Specimen	Experimental results		Predicted flexural strength		Predicted shear strength and failure mode					
					$V_{n,compos}/V_{fle}$ (Predicted failure mode)					
	$M_{u,exp}$ (kNm)	Failure mode	$M_{u,exp}/M_{fle}$	V_{fle} (kN)	Method A1	Method A2	Method A3	Method B1	Method B2	Method B3
RE-0	18.32	Shear	1.18	25.85	0.75 (Shear)	0.80 (Shear)	0.77 (Shear)	0.75 (Shear)	0.80 (Shear)	0.77 (Shear)
RE-20	17.15	Flexure-shear	1.07	26.78	0.94 (Shear)	1.02 (Flexure)	0.98 (Shear)	0.94 (Shear)	0.72 (Shear)	1.39 (Flexure)
RE-32	13.10	Flexure	0.80	27.19	0.89 (Shear)	1.02 (Flexure)	0.91 (Shear)	0.70 (Shear)	0.91 (Shear)	1.09 (Flexure)
RE-50	16.61	Flexure	1.00	27.59	0.83 (Shear)	1.00 (Flexure)	0.80 (Shear)	0.94 (Shear)	1.59 (Flexure)	1.93 (Flexure)
RE-100	33.88	Flexure	0.99	56.91	0.81 (Shear)	1.18 (Flexure)	1.63 (Flexure)	0.81 (Shear)	1.18 (Flexure)	1.63 (Flexure)
OV-25	22.07	Shear	1.34	27.44	31.98 (Flexure)	32.55 (Flexure)	31.17 (Flexure)	27.65 (Flexure)	20.66 (Shear)	42.77 (Shear)
OV-25a	23.39	Shear	0.77	50.73	34.50 (Shear)	36.43 (Shear)	33.32 (Shear)	27.65 (Shear)	39.37 (Shear)	42.84 (Shear)
OV-50	23.39	Shear	1.32	29.48	38.23 (Flexure)	38.99 (Flexure)	36.78 (Flexure)	38.60 (Flexure)	20.74 (Shear)	66.08 (Flexure)
OV-50a	28.52	Shear	0.80	59.57	41.33 (Shear)	42.82 (Shear)	36.84 (Shear)	38.64 (Shear)	50.56 (Shear)	66.01 (Flexure)

Note:
V_{fle}: shear force obtained at the calculated flexural moment M_{fle}.
$V_{n,compos}$: predicted shear force based work done by Yin et al. (2018).

The failure mode was evaluated by mean of the ratio of $V_{n,compos}/V_{fle}$. When $V_{n,compos}/V_{fle} < 1$, the failure mode was expected to be shear failure, or flexure failure in the contrary. Table 5 shows the predicted failure mode for all specimens. From Table 5, the most accurate predicted failure mode was given by Method A2.

Conclusions

The flexural strength prediction for UHPC-concrete composite members based on the existing design models were presented. From this study, the following conclusions can be drawn.

(1) The adopted method was able to predict the ultimate moment in good agreement with experimental results for UHPC-concrete composite members. As clearly shown in RE series, the flexural moment capacity was predicted with mean $M_{u,exp}/M_{fle}$ ratio and COV of 1.01 and 13.6%, respectively.

(2) In OV series, due to the occurrence of shear failure, the specimens might not reach their maximum moment capacity. The computed flexural moment showed a large COV of 25.7% while in RE series COV was 13.6%.

(3) The failure modes defined by the predicted shear force given at the predicted flexural moment and those obtained from the adopted methods for the shear force prediction were presented. It was observed that the failure modes observed from Method A2 was found to be the most accurate prediction.

(4) Although the flexural strength prediction demonstrated reasonable agreement with the experimental results, further studies should be conducted to develop and improve the adopted method for UHPC-concrete composite members.

Acknowledgments

The authors are grateful for the financial support of this work by the Toda Scholarship Foundation 2017 Research Grant.

References

ACI Committee 544. (1988). Design Considerations for Steel Fiber Reinforced Concrete. *ACI Structural Journal*, *85*(5), 563–579.

ACI Committee. (2008). *Building code requirements for structural concrete (ACI 318) and commentary*. American Concrete Institute.

Alaee, F.J., & Karihaloo, B.L. (2003). Retrofitting of reinforced concrete beams with CARDIFRC. *Journal of Composites for Construction*, *7*, 174–186. https://doi.org/10.1061/(ASCE)1090-0268(2003)7:3(174)

Alkaysi, M., El-Tawil, S., Liu, Z., & Hansen, W. (2016). Effects of silica powder and cement type on durability of ultra high performance concrete (UHPC), *Cement and Concrete Composites*. 66, 47–56. https://doi.org/10.1016/j.cemconcomp.2015.11.005

Brühwiler, E., & Denarie, E. (2008). Rehabilitation of concrete structures using ultra-high performance fibre reinforced concrete. In *Proceedings of the UHPC-2008*: *The Second International Symposium on Ultra High Performance Concrete* (pp. 05–07).

Graybeal, B.A., & Baby, F. (2013). Development of direct tension test method for ultra-high-performance fiber-reinforced concrete. *ACI Materials Journal*, *110*(2), 177–186.

Habel, K., Denarié, E., & Brühwiler, E. (2006). Structural response of elements combining ultrahigh-performance fiber-reinforced concretes and reinforced concrete. *Journal of Structural Engineering, 132*(11), 1793–1800. https://doi.org/10.1061/(ASCE)0733-9445(2006)132:11(1793)

Noshiravani, T., & Brühwiler, E. (2013). Analytical model for predicting response and flexure-shear resistance of composite beams combining reinforced ultrahigh performance fiber-reinforced concrete and reinforced concrete. *Journal of Structural Engineering*, *140*(6). https://doi.org/10.1061/(ASCE)ST.1943-541X.0000902

Richard, P., & Cheyrezy, M. (1995). Composition of reactive powder concretes. *Cement and concrete research, 25*(7), 1501–1511. https://doi.org/10.1016/0008-8846(95)00144-2

Shirai, K., Yin, H., & Teo, W. (2018). Flexural strength calculation of the RC members rehabilitated with UHPC. In *Proceedings of the Japan Concrete Institute*, *40*.

Wille, K., El-Tawil, S., & Naaman, A. (2014). Properties of strain hardening ultra high performance fiber reinforced concrete (UHP-FRC) under direct tensile loading. *Cement and Concrete Composites*, 48, 53–66. https://doi.org/10.1016/j.cemconcomp.2013.12.015

Yin, H., Teo, W., & Shirai, K. (2017). Experimental investigation on the behaviour of reinforced concrete slabs strengthened with ultra-high performance concrete. *Construction and Building Materials*, *155*, 463–474. https://doi.org/10.1016/j.conbuildmat.2017.08.077

Yin, H., Shirai, K., & Teo, W. (2018). Prediction of shear capacity of UHPC-concrete composite structural members based on existing codes. *Journal of Civil Engineering and Management*, (under review).

Chapter VIII
Conclusions and recommendations

Conclusions and recommendations

1. Conclusions

From this study, the following conclusions could be reached:

(1) The structural behaviour of composite RC members strengthened with UHPC under static loading through the experimental study was investigated. The UHPC strengthening layer improves the performance of composite UHPC-concrete slabs showing an excellent energy absorption with extensive deflection hardening and ductility during the post cracking range.

(2) An FE model of the flexural behaviour of non-composite UHPC members under static loading was developed. The accurately simulated results demonstrated the effectiveness and adequacy of the developed FE model and modelling technique.

(3) The behaviour of composite UHPC-concrete slabs under static loading was sucessfully predicted using an improved FE model with modelling technique using equivalent beam elements at the interface.

(4) The numerical response of composite UHPC-concrete members subjected to dynamic loading was figured out. The effectiveness of UHPC layer of UHPC-concrete composite members was demonstrated through comparing the results with reference non-composite RC and UHPC members under same blast loading. It showed that UHPC strengthening layer significantly improves the blast resistance of the members as compared to the conventional RC members.

(5) The prediction of composite UHPC-concrete members using existing design models was evaluated. The proposed method was found to be able to fairly predict the structural capacity of composite UHPC-concrete members compared to the experimental results.

2. Recommendations for the future study

– *Static loading*

(1) More experimental studies on UHPC-concrete composite members should be suggestible be conducted because some factors affecting the structural behaviour were not included in the present study such as size effect of specimens and effect of longitudinal reinforcement ratio.

(2) An improvement of numerical simulation results should be carried by employing statistic analysis for determining the most appropriate model parameters. In addition, the bond strength interface between concrete and longitudinal reinforcement should also be considered.

(3) Further study on analytical models for predicting the structural capacity of UHPC-concrete composite should be developed and improved.

– *Dynamic loading (blast)*

(1) To validate the FE model for the blast response, test data on UHPC-concrete composite members subjected to blast loading are needed for the future study.

(2) An analytical model for blast resistant of UHPC-concrete members should be conducted.

(3) Pressure–impulse (P–I) diagrams, which is commonly used in the preliminary design of structures to establish safe response limits at given blast loading scenarios, should be developed for UHPC-concrete composite members.

– *Construction methods*

Procedures and techniques that are used in the constructing process for the application of composite UHPC-concrete structural elements should be investigated. For instance, methods would be the prefabricated UHPC-concrete elements or half-precast application.

LIST OF RELATED PUBLISHED PAPERS

■ International peer-reviewed journal

(1) **Hor Yin**, Wee Teo, Kazutaka Shirai, "Experimental investigation on the behaviour of reinforced concrete slabs strengthened with ultra-high performance concrete," Construction and Building Materials, 155, 463–474, 2017.

■ International peer-reviewed conference proceedings

(2) **Hor Yin**, Kazutaka Shirai, Wee Teo, "Response of UHPC-concrete composite structural members using implicit and explicit finite element method," In: 2018 The 3rd International Conference on Advanced Functional Materials (ICAFM 2018), San Francisco, United States, August 3 – 5, 2018.

(3) Wee Teo, Kazutaka Shirai, **Hor Yin**, "Retrofitting and strengthening interventions of RC members using ultra high performance concrete (UHPC)," In: IABSE Conference – Engineering the Developing World, 726–731, Kuala Lumpur, Malaysia, April 25 – 27, 2018.

(4) **Hor Yin**, Kazutaka Shirai, Wee Teo, "Numerical assessment of ultra-high performance concrete material," In: 2016 IEEE International Conference on Innovative Engineering Materials (ICIEM 2016), Singapore, August 20 – 22, 2016. (Online open: IOP Conference Series, Materials Science and Engineering, 241, 2017, 012004)

■ Domestic peer-reviewed conference proceedings

(5) **Hor Yin**, Kazutaka Shirai, Wee Teo, "Shear capacity prediction of reinforced concrete members strengthened with ultra-high performance concrete overlay," Proceedings of the Japan Concrete Institute, 40(2), 1243–1248, June 2018.

(6) Kazutaka Shirai, **Hor Yin**, Wee Teo, "Flexural strength calculation of the RC members rehabilitated with UHPC," Proceedings of the Japan Concrete Institute, 40(2), 1237–1242, June 2018.

■ Domestic non-peer-reviewed conference proceedings

(7) **Hor Yin**, Kazutaka Shirai, "Investigation of implicit and explicit FEM analysis for RC members strengthened with UHPC under static loading," Architectural Institute of Japan (AIJ), Technical Paper of Annual Meeting, Japan, September 4 – 6, 2018. (in print)

(8) **Hor Yin**, Kazutaka Shirai, Wee Teo, "Model simulation on flexural behavior of ultra-high performance fiber reinforced concrete," Architectural Institute of Japan (AIJ), Technical Paper of Annual Meeting, Japan, August 31 – September 5, 2017.